



Claus Weiland

Aerodynamic Data of Space Vehicles



Springer

Aerodynamic Data of Space Vehicles

Claus Weiland

Aerodynamic Data of Space Vehicles



Springer

Dr. Ing. Claus Weiland
83052 Bruckmühl
Föhrenstr.90
Germany
E-mail: claus.weiland@t-online.de

ISBN 978-3-642-54167-4 ISBN 978-3-642-54168-1 (eBook)
DOI 10.1007/978-3-642-54168-1
Springer Heidelberg New York Dordrecht London

Library of Congress Control Number: 2014930025

© Springer-Verlag Berlin Heidelberg 2014

This work is subject to copyright. All rights are reserved by the Publisher, whether the whole or part of the material is concerned, specifically the rights of translation, reprinting, reuse of illustrations, recitation, broadcasting, reproduction on microfilms or in any other physical way, and transmission or information storage and retrieval, electronic adaptation, computer software, or by similar or dissimilar methodology now known or hereafter developed. Exempted from this legal reservation are brief excerpts in connection with reviews or scholarly analysis or material supplied specifically for the purpose of being entered and executed on a computer system, for exclusive use by the purchaser of the work. Duplication of this publication or parts thereof is permitted only under the provisions of the Copyright Law of the Publisher's location, in its current version, and permission for use must always be obtained from Springer. Permissions for use may be obtained through RightsLink at the Copyright Clearance Center. Violations are liable to prosecution under the respective Copyright Law.

The use of general descriptive names, registered names, trademarks, service marks, etc. in this publication does not imply, even in the absence of a specific statement, that such names are exempt from the relevant protective laws and regulations and therefore free for general use.

While the advice and information in this book are believed to be true and accurate at the date of publication, neither the authors nor the editors nor the publisher can accept any legal responsibility for any errors or omissions that may be made. The publisher makes no warranty, express or implied, with respect to the material contained herein.

Printed on acid-free paper

Springer is part of Springer Science+Business Media (www.springer.com)

for Silvia

Preface

Since their appearance on the Earth men have thought about the environment, in which they live. Over a long period of time they asked of what nature the movement of the Earth, the Sun, the Moon and the stars is. The outcome was that up to the fifteenth century the geocentric world view (the Aristotelian system¹) with the Earth at the center was the matter of common knowledge. Then with the observations and cognitions of Nikolaus Kopernikus (1473 – 1543) and Galileo Galilei (1564 – 1642) a new world view was constructed and introduced, the so called heliocentric system (Copernican system) with the Sun at its center.

The description of our planetary system with the Sun at its center is true up to the present. It can be conjectured that the people also believed at that time that all the other stars circuit the Sun. Further observations, however, have brought the awareness that there exist a tremendous number of other planetary systems forming galaxies and further that a large number of galaxies form the universe. This means the Earth is only a very small particle in the universe and this is true also for our planetary system.

N. Kopernikus and G. Galilei have created a model of the kinematic movement of the planets in our planetary system, but they did not know, if there exist laws, which mathematically describe the mechanics of the motion of planets. This gap was filled by the work of Johannes Kepler (1571 – 1630). His three laws are fundamental down to the present day for the understanding of orbital movement of planets in a planetary system. But on the other hand this wonderful work was also not able to explain why the planets move along such orbits, which means to identify and describe the forces which are acting on the masses in the universe.

The fundamental step, by which the discipline of mechanics was borne, made Isaac Newton (1643 – 1727). He formulated the three principles of mechanics (inertia, action, reaction) and the law of gravitation. Since then the motions of masses in gravitational fields can be predicted in the case that the action (force) law², valid in an inertial coordinate system, can be

¹ Aristotle: 384 - 322 B.C..

² Force is equal to the product of mass times acceleration: $F = m \cdot a$.

transformed to the relevant non-inertial coordinate systems, which could be, for example, either a flight path or a body-fixed system³.

Of course the determination of the motions of masses in gravitational fields is not restricted to natural objects (stars, suns, planets, moons, etc.), but is valid also for man-made bodies, like space vehicles (probes, capsules, winged spacecrafts, etc.). With that the mechanics of space flight could be generated.

During the cold war humans began with the flight of man-made vehicles into the space. The first orbital⁴ flight of a space vehicle was accomplished by the Soviet Union (Russia) with the launch of the SPUTNIK capsule in 1957.

Space vehicles in the frame of this book are atmospheric re-entry and entry vehicles. Generally they are non-winged or winged re-entry vehicles. To them come airbreathing hypersonic flight vehicles, either as Single-Stage-To-Orbit (SSTO) space transportation systems or as the lower stages of Two-Stage-To-Orbit (TSTO) systems.

Although the flight of space vehicles began in the second half of the 1950s, design and operational experience and data of the vehicles under consideration are scarce compared to that of aircraft. There an abundance of data is available for the designer of a new aircraft and also for the student of aeronautics. The approach to a new design is always made in view of former approaches, simply in order to reduce technical and operational risks. If, however, a large technological step is to be performed, the risks must be taken. Experimental vehicles can be a step in between, like the well-known X-planes of the USA.

Regarding space vehicles, exactly this situation is given. Several of the X-planes were and are experimental space vehicles. The experience gained with them, however, led only to a few operational capsules and vehicles, in particular APOLLO, SOYUZ and the SPACE SHUTTLE Orbiter. Not only the classical spacefaring nations, the USA and the Soviet Union (Russia), but also other nations did at least extended technological and project work on capsules, winged re-entry vehicles and also airbreathing systems.

The total number of space plane studies, projects and operational vehicles is not large. Related data is partly available, in particular of the SPACE SHUTTLE Orbiter. The "Lessons Learned", published in 1983 by the NASA, are an excellent and valuable example how experience can be conveyed to the technical community at large.

Today, there are no real projects pursued for the development of new space transportation systems. Probably we are in a transition phase. The author is convinced that the time for new advanced space transportation systems will come.

³ Of course, we consider only the classical mechanics, where due to the relatively low velocities of the space vehicles, -compared to the speed of light-, relativistic effects can be neglected.

⁴ Orbital space flight means that the vehicle is accelerated to the circular speed necessary for the residence in an Earth orbit.

This book presents a collection of aerodynamic data sets of non-winged re-entry vehicles (RV-NW), winged re-entry vehicles (RV-W) and airbreathing hypersonic flight vehicles (CAV). Some of the data were freely available, several were made available by the originators, and a lot of them stem from the work of the author and his colleagues. He has worked for almost three and a half decades in the aerospace field at an university, a research institute and in industry. He was involved in a lot of programs, projects, technology studies and scientific works mostly with emphasis on space applications.

The book is written for graduate and doctoral students, as well as design and development engineers, in particular when the latter are going to start with new projects and need support and a guideline for the first configurational and aerodynamic design approach.

January 24, 2014

Claus Weiland

Acknowledgements

The author is much indebted to his colleagues E.H. Hirschel, who read several times all the chapters of the book, and W. Staudacher, who read parts of the book. Their suggestions and input were highly appreciated and have definitely enhanced the readability of the book.

Further the author wishes to thank S. Borrelli, K. Bosselmann, A. Gülhan, J.M.A. Longo, W. Schröder, who have made available the aerodynamic data sets of several space vehicles and some other material.

Last but not least I wish to thank my wife for her support and patience.

Claus Weiland

Contents

1	Introduction	1
1.1	Short Historical Overview	1
1.2	Milestones of Space Flight	4
1.3	The Contents of the Book	6
	References	7
2	The Discipline Aerodynamics	9
2.1	Introduction	9
2.2	Steady or Unsteady Aerothermodynamics?	10
2.3	Aerodynamic Coefficients	11
2.4	Examples of Aerodynamic Models	16
2.4.1	The SAENGER Vehicle (CAV).....	16
2.4.2	The X-38 Vehicle (RV-W)	18
2.4.3	The PRORA Vehicle (RV-W)	19
	References	21
3	Classification and Project Data of Space Vehicles	23
3.1	Overview	23
3.2	Re-entry Vehicles - Non-winged (RV-NW): Space Probes and Capsules	25
3.3	Re-entry Vehicles - Non-Winged (RV-NW): Cones and Bicones	30
3.4	Re-entry Vehicles -Winged (RV-W)	33
3.5	Cruise and Acceleration Vehicles (CAV)	37
	References	39
4	Aerodynamic Data of Non-Winged Re-entry Vehicles (RV-NW) - Capsules and Probes -	41
4.1	Introduction	41
4.2	APOLLO (USA)	43
4.2.1	Configurational Aspects	43
4.2.2	Aerodynamic Data of Steady Motion	44
4.2.3	Aerodynamic Data of Unsteady Motion	48
4.2.4	Peculiarities	49
4.3	SOYUZ (Russia)	51
4.3.1	Configurational Aspects	51

4.3.2	Aerodynamic Data of Steady Motion	53
4.3.3	Aerodynamic Data of Unsteady Motion	53
4.3.4	Peculiarities	57
4.4	ARD (Aerodynamic Re-entry Demonstrator) (Europe)	58
4.4.1	Configurational Aspects	58
4.4.2	Aerodynamic Data of Steady Motion	58
4.4.3	Aerodynamic Data of Unsteady Motion	61
4.4.4	Peculiarities	61
4.5	HUYGENS (Cassini Orbiter) (Europe)	66
4.5.1	Configurational Aspects	66
4.5.2	Aerodynamic Data of Steady Motion	66
4.5.3	Aerodynamic Data of Unsteady Motion	69
4.6	BEAGLE2 (UK)	70
4.6.1	Configurational Aspects	70
4.6.2	Aerodynamic Data of Steady Motion	71
4.6.3	Aerodynamic Data of Unsteady Motion	75
4.7	OREX (Japan)	76
4.7.1	Configurational Aspects	76
4.7.2	Aerodynamic Data of Steady Motion	77
4.7.3	Aerodynamic Data of Unsteady Motion	79
4.8	VIKING-Type (Europe)	80
4.8.1	Configurational Aspects	80
4.8.2	Aerodynamic Data of Steady Motion	81
4.8.3	Aerodynamic Data of Unsteady Motion	95
4.9	CARINA (Italy)	96
4.9.1	Configurational Aspects	96
4.9.2	Aerodynamic Data of Steady Motion	98
4.9.3	Aerodynamic Data of Unsteady Motion	100
4.10	AFE (Aeroassist Flight Experiment) (USA-Europe)	101
4.10.1	Configurational Aspects	102
4.10.2	Aerodynamic Data of Steady Motion	103
4.10.3	Aerodynamic Data of Unsteady Motion	108
4.11	VIKING (USA)	111
4.11.1	Configurational Aspects	111
4.11.2	Aerodynamic Data of Steady Motion	112
4.11.3	Aerodynamic Data of Unsteady Motion	117
	References	118
5	Aerothermodynamic Data of Non-Winged Re-entry Vehicles (RV-NW) - Cones and Bicones -	123
5.1	Introduction	123
5.2	BLUFF-BICONE (Germany)	124
5.2.1	Configurational Aspects	124
5.2.2	Aerodynamic Data of Steady Motion	124
5.2.3	Aerodynamic Data of Unsteady Motion	127

5.3	SLENDER-BICONE (Russia)	132
5.3.1	Configurational Aspects	132
5.3.2	Aerodynamic Data of Steady Motion	132
5.3.3	Aerodynamic Data of Unsteady Motion	135
5.4	BENT-BICONE (USA)	138
5.4.1	Configurational Aspects	138
5.4.2	Aerodynamic Data of Steady Motion	138
5.4.3	Aerodynamic Data of Unsteady Motion	139
5.5	COLIBRI (Germany)	142
5.5.1	Configurational Aspects	142
5.5.2	Aerodynamic Data of Steady Motion	144
5.5.3	Aerodynamic Data of Unsteady Motion	147
5.6	IRDT (Inflatable Re-entry Demonstrator) (Russia-Germany)	149
5.6.1	Configurational Aspects	149
5.6.2	Aerodynamic Data of Steady Motion	149
5.6.3	Aerodynamic Data of Unsteady Motion	157
5.7	EXPERT (Europe)	159
5.7.1	Configurational Aspects	159
5.7.2	Aerodynamic Data of Steady Motion	161
5.7.3	Aerodynamic Data of Unsteady Motion	166
	References	169
6	Aerothermodynamic Data of Winged Re-entry Vehicles (RV-W)	171
6.1	Introduction	171
6.2	SPACE SHUTTLE Orbiter (USA)	174
6.2.1	Configurational Aspects	176
6.2.2	Aerodynamic Data of Steady Motion	179
6.2.3	Aerodynamic Data of Unsteady Motion	190
6.3	X-33 Vehicle (USA)	198
6.3.1	Configurational Aspects	198
6.3.2	Aerodynamic Data of Steady Motion	200
6.3.3	Aerodynamic Data of Unsteady Motion	202
6.4	X-34 Vehicle (USA)	207
6.4.1	Configurational Aspects	208
6.4.2	Aerodynamic Data of Steady Motion	209
6.4.3	Aerodynamic Data of Unsteady Motion	216
6.5	X-37 Vehicle (USA)	217
6.5.1	Configurational Aspects	217
6.5.2	Aerodynamic Data of Steady and Unsteady Motions	217
6.6	X-38 Vehicle (USA-Europe)	220
6.6.1	Configurational Aspects	221
6.6.2	Aerodynamic Data of Steady Motion	222

6.6.3	Aerodynamic Data of Unsteady Motion	233
6.7	PHOENIX Demonstrator (Germany)	235
6.7.1	Configurational Aspects	238
6.7.2	Aerodynamic Data of Steady Motion	238
6.7.3	Aerodynamic Data of Unsteady Motion	248
6.8	HOPE-X (Japan).....	253
6.8.1	Configurational Aspects	253
6.8.2	Aerodynamic Data of Steady Motion	255
6.8.3	Aerodynamic Data of Unsteady Motion	260
6.9	Facetted DS6 Configuration (Germany)	264
6.9.1	Configurational Aspects	264
6.9.2	Aerodynamic Data of Steady Motion	267
6.9.3	Aerodynamic Data of Unsteady Motion	267
6.10	PRORA (Italy)	269
6.10.1	Configurational Aspects	270
6.10.2	Aerodynamic Data of Steady Motion	270
6.10.3	Aerodynamic Data of Unsteady Motion	276
6.11	HERMES (Europe)	280
6.11.1	Configurational Aspects	281
6.11.2	Aerodynamic Data of Steady Motion	284
6.11.3	Aerodynamic Data of Unsteady Motion	293
	References	296
7	Aerothermodynamic Data of Cruise and Acceleration Vehicles (CAV)	301
7.1	Introduction	301
7.2	SAENGER (Germany)	303
7.2.1	Configurational Aspects	305
7.2.2	Aerodynamic Data of Steady Motion	305
7.2.3	Aerodynamic Data of Unsteady Motion	316
7.3	ELAC (Germany)	319
7.3.1	Configurational Aspects	319
7.3.2	Aerodynamic Data of Steady Motion	322
7.3.3	Aerodynamic Data of Unsteady Motion	328
	References	331
8	Coordinate Systems	333
	References	337
	Appendix A : Wind Tunnels	339
	Appendix B: Abbreviations, Acronyms	343
	Name Index	347
	Subject Index	351

Introduction

Humans have started to capture the space after World War II. To leave the Earth atmosphere and its gravitational field requires an appropriate propulsion system, which is primarily up to these days given by rocket based systems. Further a flying device is needed, whereby men and payload can be transported to space and back to the Earth surface. These devices are space vehicles like probes, capsules and winged re-entry vehicles. The determination of the aerodynamics of such space vehicles is a challenging task and a selection of results will be presented in this book.

1.1 Short Historical Overview

After World War II space transportation began in the late fifties and the early sixties of the last century in the Soviet Union (UdSSR) and the United States of America (USA) and initially has used vehicles with very simple shapes. When these countries started to transport men into space (suborbital) or even into orbits of the Earth, the main challenge was to bring them back to the Earth's surface by a safe re-entry process. At that time the selected vehicles were very blunt and had an axisymmetric geometry. They performed re-entries into the Earth atmosphere either by ballistic or low lift flights. The final approach towards the Earth surface was always initiated by parachute systems. The landing process, which was not very comfortable for the crew members, was conducted either at sea, for example the pacific ocean, or on land supported by mechanical dampers, for example in the Kazakh desert. These re-entry vehicles were called capsules. Later, when extra-terrestrial fly-by and entry missions came into play, for example to the planets Mercury, Mars, Venus, Jupiter, Saturn and Saturn's moon Titan, etc., similar configurations, although unmanned, were taken into account. These vehicles are called probes. Capsules and probes together with cones and bicones form the group of non-winged re-entry vehicles (RV-NW).

For this group (RV-NW) we present in this book the aerodynamic data sets of the nine capsules and probes: APOLLO, SOYUZ, ARD, BEAGLE2, OREX, VIKING-type, CARINA, AFE and VIKING (Chapter 4) and the six cones and bicones: BLUFF-BICONE, SLENDER-BICONE, BENT-BICONE, COLIBRI, IRDT and EXPERT (Chapter 5).

In the seventieth the question arose, whether the manned space transport could be made cheaper (reduction of the cost per kg payload mass), more comfortable for the crew and more reliable with respect to the terminal approach and landing process. The only answer at the time of these questions was given through the development of a partly reusable and winged space vehicle, the U.S. SPACE SHUTTLE Orbiter¹.

Two of the above-mentioned improvements for the manned space transport became true, but a reduction of the payload cost could not be achieved.

There were a lot of further projects and system studies worldwide at that time aiming at the development of winged space flight and/or re-entry vehicles of the SPACE SHUTTLE Orbiter-type, for example in

Japan	⇒ HOPE-X,
USA	⇒ X-33, X-34, X-37, etc.,
USA - Europe	⇒ X-38,
Europe	⇒ HERMES, PHOENIX/HOPPER, etc..

However, up to now, none of these became operational. We call this group of space planes winged re-entry vehicles (RV-W). The aerodynamic coefficients are presented for the ten RV-W vehicles: SPACE SHUTTLE Orbiter, X-33, X-34, X-37, X-38, PHOENIX, HOPE-X, Facetted Configurations, PRORA and HERMES (Chapter 6).

In the ninetieth worldwide discussions took place to develop an advanced space transportation system with the capabilities

- to launch on demand,
- of full reusability,
- to start either vertically or horizontally and to land horizontally,
- to reduce drastically the cost for transporting payload into space.

Detailed studies of such kind of systems were carried out, for example, in the frame of the Future European Space Transportation Investigations Program (FESTIP), [1]. There, a lot of Single-Stage-To-Orbit (SSTO) and Two-Stage-To-Orbit (TSTO) systems were investigated and compared in order to

- select the concept which would become technically feasible in the near future,
- identify the technology requirements for the realization of such a concept,
- determine whether the concept would be economically viable.

SSTO concepts were studied, for example, in the U.K. with HOTOL and in the U.S. with the NASP² program³.

¹ The UdSSR has developed some years later a very similar vehicle system, called BURAN, which had flown just one demonstration flight, before the project was cancelled, due to technical and budgetary problems, [1].

² NASP ⇒ National Aerospace Plane.

³ The classification is sometimes not unique, so one could add also the X-33 vehicle to this class!

The TSTO systems consist in general of a lower stage, which transports the upper stage to a certain altitude, where the stage separation takes place. The lower stages are often hypersonic airplanes, propelled by a system of airbreathing engines, as it was the case in the German SAENGER project and the French STAR-H concept⁴, [1]. The upper stages are SHUTTLE-like orbiters propelled by rocket motors. The lower stages build the group of cruise and acceleration vehicles (CAV), [2, 3]. The group of CAV's considered in this book consists of the two vehicles SAENGER and ELAC (Chapter 7).

What is today's situation regarding the development of advanced space transportation vehicles?

First, we should have in mind, that a lot of the global communication systems, like television, mobile phones, internet data transfer, Earth observation including weather prediction, global positioning system etc., are based on the elements of space transportation. These elements are satellites, capsules, space stations, winged space orbiters etc.. Most of them are launched by rockets or rocket-like systems, which were developed essentially in the seventieth and eightieth of the last century. The drawbacks of such systems we have already discussed above.

On the other hand all the activities regarding the RV-W's and CAV's listed above were terminated or cancelled. Most of them due to budgetary reasons, but also some of them simply because the technological barrier was too high. Does that mean, that there is no necessity in the future for advanced space transport systems in the sense discussed before? The answer is definitely no, in particular with respect to the above-mentioned communication systems, which have to be up-dated, serviced and repaired, and that needs man in space, although robotic systems are advancing.

It seems that mankind always needs a period of consolidation after the dramatic evolutions in areas of its daily life regarding technological, social, commercial and political aspects. The evolutions are sometimes too fast, so that people have problems to assimilate them. Likewise new movements in space vehicle evolution will not occur soon, in particular when only the commercial success stands in the foreground. Nevertheless men's thirst for knowledge and their curiosity are strong incentives and the history has shown that new evolutions will always come.

Approximately in the last twenty years there was no real (or industrial) project pursued regarding the development of advanced space transportation systems in the sense discussed above, despite the fact that some minor system studies or demonstration activities, like the U.S. X-43 and X-51A scramjet propulsion system tests, have taken place.

⁴ There were other concept studies of TSTO systems with CAV-type lower stages like the French PREPHA study or MIGAKS of the Russian Oryol program. But for these studies the author had neither information about the existence of aerodynamic data nor any access to it.

Obviously the time is not ripe for advanced systems. But the author believes in the sentence “No idea is so powerful, then that, whose time has come”, and such an idea will come.

1.2 Milestones of Space Flight

The successful exploration of our planetary system requires more advanced transport systems supplying near Earth space stations as outpost for manned travel to other planets of our solar system and beyond.

It may be of interest to study the list below, where milestones⁵ of the exploration of space, conducted with manned or unmanned vehicles, since the fiftieth of the last century are summarized.

- | | | |
|--------------------------|---|--------|
| 4. Oct. 1957 SPUTNIK 1: | first flight in an Earth orbit, | UdSSR, |
| 1957 SPUTNIK 2: | first living creature,
the dog Laika in Earth orbit, | UdSSR, |
| 3. Sept. 1959 LUNIK 2: | first flight to the Moon, the
vehicle is shattered on its surface, | UdSSR, |
| 12. April 1961 WOSTOK 1: | first man in Earth orbit,
Juri Gagarin, | UdSSR, |
| 1962 MARINER 2: | first probe passing the planet
Venus, | USA, |
| 2. March 1965 | first walk outside a capsule
in space, Alexej Leonow, | UdSSR, |

⁵ This is not a complete list of events, but reflects the interest of the author.

4. July 1965 MARINER 4: first probe passing the planet Mars, USA,
15. Dec. 1966 LUNA9: flight to the Moon and first successful landing on its surface, UdSSR,
20. July 1969 APOLLO 11: first man on the Moon, Neil Armstrong, USA,
15. Dec. 1970 VERENA 7: flight to the planet Venus and first successful landing on its surface, UdSSR,
19. April 1971 SALJUT 1: first space station in Earth orbit, UdSSR,
3. Dec. 1973 PIONEER 10: first probe passing the planet Jupiter, USA,
- 1974 MARINER 10: first probe passing the planet Mercury, USA,
1. Sept. 1979 PIONEER 11: first probe passing the planet Saturn, USA,
- 1981 first flight of a winged space vehicle, the SPACE SHUTTLE Orbiter, USA,
- 1986 VOYAGER 2: first probe passing the planet URANUS, USA,
24. Aug. 1989 VOYAGER 3: first probe passing the planet Neptun, USA,
- 1997 PATHFINDER: flight to the planet Mars and first successful landing on its surface, USA,
- Nov. 2000 ISS: start of the installation of the International Space Station ISS,
14. Jan. 2005 HUYGENS: flight to planet Saturn's moon Titan and first successful landing on its surface, Europe

1.3 The Contents of the Book

The capacity and quality of the atmospheric flight performance of space flight vehicles⁶ is characterized by the aerodynamic data bases. The tools to establish aerodynamic data bases are

- semi-empirical design methods,
- wind tunnel tests,
- numerical simulations,
- free flight tests.

The results of these tools are harmonized and consolidated and form the aerodynamic data base. Of course the numerical simulations methods have this role only since approximately twenty years.

A complete aerodynamic data base would encompass the coefficients of the static longitudinal and lateral motions and the related dynamic coefficients (Chapter 2). The whole data base has to be verified by free flight tests.

In this book the aerodynamics of 27 vehicles are considered. Only a few of them did really fly. Therefore the aerodynamic data bases are often not complete, in particular when the projects or programs were more or less abruptly stopped, often due to political decisions. Then, during the run-down phases the interests of the engineers involved are often strongly reduced. A proper reporting of the actual status of the projects usually does not take place, which concerns also the aerodynamic data bases.

Configurational design studies or the development of demonstrators usually happen with reduced or incomplete aerodynamic data sets. Therefore some data sets base just on the application of one or two of the above mentioned tools, either semi-empirical design methods, wind tunnel tests or numerical simulations. In so far a high percentage of the data presented here is incomplete and would have to be verified.

Flight mechanics needs the aerodynamic coefficients as function of a lot of variables (in general more than ten), [4]. The allocation of the aerodynamic coefficients for a particular flight operation at a specific trajectory point is conducted by an aerodynamic model. The establishment of such models is described in Chapter 2.

A summary of the vehicles considered in this book is given in Chapter 3. Chapters 4 to 7 give the data sets of the different vehicle classes.

Finally, Chapter 8 deals with the definitions of the various coordinate systems used for the different vehicle types presented in the related chapters.

⁶ Of course, that is true for all aerospace vehicles.

References

1. Kuczera, H., Sacher, P.: Reusable Space Transportation Systems. Springer, Heidelberg (2011)
2. Hirschel, E.H.: Basics of Aerothermodynamics, vol. 204. Springer, Heidelberg; Progress in Astronautics and Aeronautics. AIAA, Reston (2004)
3. Hirschel, E.H., Weiland, C.: Selected Aerothermodynamic Design Problems of Hypersonic Flight Vehicles, vol. 229. Springer, Heidelberg; Progress in Astronautics and Aeronautics. AIAA, Reston (2009)
4. Weiland, C.: Computational Space Flight Mechanics. Springer, Heidelberg (2010)

The Discipline Aerodynamics

The flight performance of any flying object (airplanes, spaceplanes, space vehicles, etc.) is primarily determined by their aerodynamic behavior. In general the mission of flight vehicles ascertain the configurational shape and with that the aerodynamics during flight. We therefore deal now with the discipline aerodynamics.

2.1 Introduction

The main task of this book is to present the aerodynamic data bases of 27 space vehicles. When we talk about space vehicles we have to be aware, that only three of them (category one) were really operational, namely the capsules APOLLO and SOYUZ and the winged re-entry vehicle SPACE SHUTTLE Orbiter¹. All the other configurations and shapes have either demonstrator status (category two) or were only technology and systems studies (category three). Most of the vehicles of the second category have undertaken just one demonstration flight (or mission), while the third category encompasses only paper work and ground based experimental investigations.

Nevertheless, there are candidates of the third category, like HERMES, where the aerodynamic data have a well substantiated status. This is due to the fact that extensive experimental and numerical work was performed by the European industrial companies, research institutes and universities involved in the program.

When we talk about a classical aerodynamic data base, for example for civil or military aircraft, we are aware that the coefficients of the forces and moments are completely driven by fluid mechanical effects. This is true for vehicle speeds up to Mach numbers around 3. Beyond this edge thermodynamic effects come into play.

When vehicles fly beyond $M_\infty \approx 3$ actually an aerothermodynamic data base is established, which consists normally of aerodynamic coefficients, temperatures and heat fluxes in particular at the vehicle's surface. The temperature and heat flux distributions at the vehicle's surface are called thermal loads.

¹ Of course, there are space probes, like HUYGENS or VIKING, which have been developed and built for just one or two missions.

In this book we only consider the “aerodynamic coefficients”, although one should properly call them “aerothermodynamic coefficients”. In the following we will explain why.

As already mentioned when flight Mach numbers exceed the value of $M_\infty \approx 3$, thermodynamic effects come into the game the stronger as the speed increases. In the following we explain what physically happens, when the vehicle speed arrives at hypersonic Mach numbers, and what that means for the “aerodynamic coefficients”.

As is well known space vehicles flying with Mach numbers larger than one generate so-called bow shocks which are normally detached, because such vehicles have in general blunt noses. With increasing Mach number the temperature in the air between the bow shock and the vehicle surface grows dramatically. This leads to the situation that the air loses its ideal behavior and so-called thermodynamic effects (hot or real gas effects) arise, influencing the molecular and atomic structure of the air.

Essentially these effects are, [1, 2]:

- vibrational excitation of the molecules,
- dissociation of oxygen ($O_2 \rightarrow O + O$),
- dissociation of nitrogen ($N_2 \rightarrow N + N$),
- chemical reactions (e.g. $NO \leftrightarrow N + O$),
- ionization of atoms.

These effects change the pressure (except for the first item) and the shear stress fields and in particular the values at the vehicle’s surface. Normally the pressure field (pressure drag) is only slightly influenced, whereas the shear stress field (viscous drag) can change considerably due to the change of the viscosity with temperature. For example the skin friction at a hot surface generates a lower viscous drag than the skin friction at a cold surface, [3].

Therefore we have besides the fluid mechanical influences also thermodynamic influences on the “aerodynamic coefficients”. That is the reason why one should rather use the term “aerothermodynamic coefficients” for this kind of data. But unfortunately in the literature no differentiation is made between these notations. Therefore we also keep the term “aerodynamic coefficients” for data bases covering the hypersonic flight regime.

2.2 Steady or Unsteady Aerothermodynamics?

The flight of a Re-entry Vehicle (RV) is an unsteady flight throughout. A CAV nominally may fly in a steady mode, but actually it flies more or less in an unsteady mode. For an introduction in flight trajectories of RV’s and CAV’s, see, e.g., [1, 4].

The mechanical loads summated over the vehicle surface show up as the aerodynamic properties of the vehicle: lift, drag, pitching moment etc., called in their totality the aerodynamic data set of the vehicle.

A well established approach of the aeronautical community is also employed in the space community: the aerodynamic data of a vehicle are –with one exception– steady motion data. This approach is permitted as long as the flight of the vehicle can be considered as quasi-steady². The actual flight path –with steady and/or unsteady flight– then is described with the help of three or six degrees of freedom trajectory determinations, see, e.g., [4], with appropriate systems and operational and control variables, [1].

A reliable criterium, which defines, when the flight can be considered as being quasi-steady, is not known. Nevertheless, the experience indicates that one can assume RV and CAV flight to be quasi-steady. This is the reason why the aerodynamic data are always obtained in a steady-state mode (steady motion), experimentally and computationally.

The mentioned exception is an aerodynamic vehicle property which is truly time-dependent: the dynamic stability, see, e.g., [5]. The dynamic stability is the damping behavior once a disturbance of the vehicle's flow field has happened, for instance an angle of attack disturbance. The time dependence indicates, whether the unsteady –in general oscillatory– motion due to the disturbance is damped or not. Although very important, the dynamic stability can be considered as being not a primary aerodynamic data set item.

There are other phenomena which are truly unsteady. One is due to the thermal inertia of a thermal protection system. The surface temperature distribution will not always adapt the value which belongs to the instant state of flight. Another example is the processes in propulsion systems. We will not pursue this topic further.

We close this section with a remark regarding the nomenclature in aerothermodynamics. In the space community the aerodynamic data are –at least sometimes– called “data of static longitudinal stability”. This obviously stems from the rocket launch technology. During the launch process the rocket flies longitudinally unstable and must be controlled with appropriate means, either aerodynamical or thruster related.

It appears to be advisable to use for RV's and CAV's the term “aerodynamic data set” which is used in the aeronautical community instead of “data of static longitudinal stability”.

2.3 Aerodynamic Coefficients

In general the aerodynamic forces and moments are defined in two coordinate frames, namely the body-fixed (body-axis) system and the air-path (wind-axis) system.

The definition of the forces and moments in the body-fixed system is (see Chapter 8):

² Changes of the free-stream conditions are so slow that the flow field around the vehicle is approximately steady. This means that the mechanical and thermal values along the whole vehicle surface are to a greater or lesser extent instantaneously steady.

X	axial force	l	rolling moment,
Z	normal force	m	pitching moment,
Y	side force	n	yawing moment,

and in the air-path system (the moments are defined as before):

L	lift force,
D	drag force,
Y_a	side force.

When forces are normalized with the dynamic pressure of the free-stream $q_\infty = 0.5\rho_\infty v_\infty^2$ and a reference area S_{ref} , and the moments in addition with a reference length b_{ref} (often the span width), we get the aerodynamic coefficients:

$$C_X = \frac{X}{q_\infty S_{ref}}, \quad C_Z = \frac{Z}{q_\infty S_{ref}}, \quad C_Y = \frac{Y}{q_\infty S_{ref}},$$

$$C_l = \frac{l}{q_\infty S_{ref} b_{ref}}, \quad C_m = \frac{m}{q_\infty S_{ref} c}, \quad C_n = \frac{n}{q_\infty S_{ref} b_{ref}},$$

and

$$C_L = \frac{L}{q_\infty S_{ref}}, \quad C_D = \frac{D}{q_\infty S_{ref}}, \quad C_{Y_a} = \frac{Y_a}{q_\infty S_{ref}}.$$

For airplanes, cruise and acceleration vehicles (CAV) and winged re-entry vehicles (RV-W) usually the air-path coordinate system is used, while the body-fixed system is often applied to capsules, probes, cones and bicones, see Chapters 4 to 7.

There are a lot of independent variables which influence the aerodynamic coefficients³. In the following we specify the most important ones:

$$M, Re, \alpha, \dot{\alpha}, \beta, \delta_e, \delta_a, \delta_{bf}, \delta_r, \delta_{sb}, p, q, r, \quad (\text{list of independent variables})$$

where

³ We mention here that the flight control of space vehicles is not only done by aerodynamic control surfaces, but also by rocket based Reaction Control Systems (RCS), in particular when during the re-entry phase the aerodynamic control surfaces are not effective. This is the case during the first part of the re-entry trajectory, where the density of the atmosphere is low. For the SPACE SHUTTLE Orbiter the RCS system is active down to an altitude of approximately 30 km ($M_\infty \approx 5$), [1].

M	flight Mach number	Re	Reynolds number,
α	angle of attack	$\dot{\alpha}$	time derivative of α ,
β	angle of side slip, yaw angle,	δ_a	aileron setting,
δ_e	elevon deflection	δ_r	rudder deflection,
δ_{bf}	body flap deflection	q, p, r	angular velocities,
δ_{sb}	speed break deflection		

and⁴

$$\delta_e = \frac{1}{2} (\delta_e^R + \delta_e^L) \quad \text{elevon deflection ,}$$

$$\delta_a = \frac{1}{2} (\delta_e^R - \delta_e^L) \quad \text{aileron setting ,}$$

$$\delta_e^L \quad \text{left wing flap deflection, positive downward ,}$$

$$\delta_e^R \quad \text{right wing flap deflection, positive downward .}$$

Of course, not all of the independent variables are appropriate or important for the various space vehicles. For example, CAV's do not have body flaps or RV-NW's have no aerodynamic controls and in the case that the RV-NW vehicles are axisymmetric no lateral forces and moments are acting.

Experience has shown that the aerodynamic coefficients, representing the longitudinal motion C_X, C_Z, C_m (or C_L, C_D, C_m), depend for the static stability mainly on the variables $M, \alpha, \delta_e, \delta_{bf}, \delta_{sb}$ and for the dynamic stability on $\dot{\alpha}, q$, whereas the lateral coefficients C_Y, C_l, C_n (or C_{Ya}, C_l, C_n) are up to the static variables $\beta, \delta_a, \delta_r$ and to the dynamic variables p, r .

The establishment of the aerodynamic data base, mainly driven by wind tunnel tests and numerical simulations, occurs with fixed settings of the aerodynamic control surfaces and at a constant flight Mach number, while changing either the angle of attack α (with constant β) or the angle of side slip β (with constant α). This yields a complex dependency of the aerodynamic coefficients on all those independent variables, which cannot be described analytically. This means that the aerodynamic coefficients at a particular operating point during the flight along a prescribed trajectory have to be determined by a multi-dimensional interpolation inside the aerodynamic data base, which in general is a highly sophisticated and expensive task.

In order to have a working basis for the determination of the aerodynamic coefficients, to be used in flight mechanical computations, an aerodynamic model has to be generated. With the experience made during the development of civil and military aircraft as well as space flight vehicles, two assumptions can be formulated. Firstly, that the aerodynamic impacts based on the longitudinally acting independent variables are decoupled from those acting in the lateral direction. This is obviously valid for small angles of attack and

⁴ R denotes right hand, L left hand side.

side slip. Secondly, that the aerodynamic impacts can be piecewise linearly approximated.

In that sense the following “aerodynamic derivatives” are built:

a) longitudinal stability

$$\begin{aligned} \frac{\partial C_X}{\partial M}, \quad \frac{\partial C_Z}{\partial M}, \quad \frac{\partial C_L}{\partial M}, \quad \frac{\partial C_D}{\partial M}, \quad \frac{\partial C_m}{\partial M}, \\ \frac{\partial C_X}{\partial Re}, \quad \frac{\partial C_Z}{\partial Re}, \quad \frac{\partial C_L}{\partial Re}, \quad \frac{\partial C_D}{\partial Re}, \quad \frac{\partial C_m}{\partial Re}, \\ \frac{\partial C_X}{\partial \alpha}, \quad \frac{\partial C_Z}{\partial \alpha}, \quad \frac{\partial C_L}{\partial \alpha}, \quad \frac{\partial C_D}{\partial \alpha}, \quad \frac{\partial C_m}{\partial \alpha}, \\ \frac{\partial C_X}{\partial \delta_e}, \quad \frac{\partial C_Z}{\partial \delta_e}, \quad \frac{\partial C_L}{\partial \delta_e}, \quad \frac{\partial C_D}{\partial \delta_e}, \quad \frac{\partial C_m}{\partial \delta_e}, \\ \frac{\partial C_X}{\partial \delta_{bf}}, \quad \frac{\partial C_Z}{\partial \delta_{bf}}, \quad \frac{\partial C_L}{\partial \delta_{bf}}, \quad \frac{\partial C_D}{\partial \delta_{bf}}, \quad \frac{\partial C_m}{\partial \delta_{bf}}, \\ \frac{\partial C_X}{\partial \delta_{sb}}, \quad \frac{\partial C_Z}{\partial \delta_{sb}}, \quad \frac{\partial C_L}{\partial \delta_{sb}}, \quad \frac{\partial C_D}{\partial \delta_{sb}}, \quad \frac{\partial C_m}{\partial \delta_{sb}}, \\ \frac{\partial C_X}{\partial \dot{\alpha}*}, \quad \frac{\partial C_Z}{\partial \dot{\alpha}*}, \quad \frac{\partial C_L}{\partial \dot{\alpha}*}, \quad \frac{\partial C_D}{\partial \dot{\alpha}*}, \quad \frac{\partial C_m}{\partial \dot{\alpha}*}, \\ \frac{\partial C_X}{\partial q*}, \quad \frac{\partial C_Z}{\partial q*}, \quad \frac{\partial C_L}{\partial q*}, \quad \frac{\partial C_D}{\partial q*}, \quad \frac{\partial C_m}{\partial q*}, \end{aligned}$$

b) lateral stability

$$\begin{aligned} \frac{\partial C_Y}{\partial \beta}, \quad \frac{\partial C_{Ya}}{\partial \beta}, \quad \frac{\partial C_l}{\partial \beta}, \quad \frac{\partial C_n}{\partial \beta}, \\ \frac{\partial C_Y}{\partial \delta_a}, \quad \frac{\partial C_{Ya}}{\partial \delta_a}, \quad \frac{\partial C_l}{\partial \delta_a}, \quad \frac{\partial C_n}{\partial \delta_a}, \\ \frac{\partial C_Y}{\partial \delta_r}, \quad \frac{\partial C_{Ya}}{\partial \delta_r}, \quad \frac{\partial C_l}{\partial \delta_r}, \quad \frac{\partial C_n}{\partial \delta_r}, \\ \frac{\partial C_Y}{\partial p*}, \quad \frac{\partial C_{Ya}}{\partial p*}, \quad \frac{\partial C_l}{\partial p*}, \quad \frac{\partial C_n}{\partial p*}, \\ \frac{\partial C_Y}{\partial r*}, \quad \frac{\partial C_{Ya}}{\partial r*}, \quad \frac{\partial C_l}{\partial r*}, \quad \frac{\partial C_n}{\partial r*}, \end{aligned}$$

where the variables $\dot{\alpha}$, p , q , r are made dimensionless with \bar{c} being the mean chord⁵ and v_∞ the free-stream velocity, and we then have $\dot{\alpha}^* = \dot{\alpha} \bar{c}/v_\infty$, $p^* = p \bar{c}/v_\infty$, $q^* = q \bar{c}/v_\infty$, $r^* = r \bar{c}/v_\infty$.

The following derivatives are known as, [5, 6]:

yaw stiffness	$C_{n\beta}$	weathercock stability, directional stability
yaw control	$C_{n\delta_r}$	
roll stiffness	$C_{l\beta}$	dihedral effect
roll control	$C_{l\delta_a}$	
damping in roll	C_{lp^*}	
damping in yaw	C_{nr^*}	
cross derivative	C_{np^*}	yawing moment due to roll
cross derivative	C_{lr^*}	rolling moment due to yaw
damping in pitch	C_{mq^*}	
damping in pitch	$C_{m\dot{\alpha}^*}$	due to angle of attack change
yaw-lateral force	C_{Yr^*}	
roll-lateral force	C_{Yp^*}	

As already mentioned the establishment of the aerodynamic model depends on the aerospace vehicle considered, the measured and numerically simulated aerodynamic data and the experience of the design engineers, who decide and estimate which aerodynamic characteristics are important and which ones are negligible.

A possible aerodynamic model could be built as follows. First, the dependence of the aerodynamic coefficients on the main parameters M , Re and α is determined. Then all the other influences are added by an incremental consideration. Therefore one obtains in general for the k^{th} -aerodynamic coefficient:

$$\begin{aligned} C_k = & C_k^0(M, Re, \alpha) + \Delta C_k^\beta(M, Re, \alpha, \beta) + \Delta C_k^{\delta_e}(M, \alpha, \delta_e) + \\ & + \Delta C_k^{\delta_{bf}}(M, \alpha, \delta_{bf}) + + \Delta C_k^{\delta_{sb}}(M, \alpha, \delta_{sb}) + \Delta C_k^{\delta_a}(M, \alpha, \delta_a) + \\ & + \Delta C_k^{\delta_r}(M, \alpha, \delta_r) + + \Delta C_k^{\dot{\alpha}}(M, Re, \alpha, \dot{\alpha}) + \Delta C_k^q(M, Re, \alpha, q) + \\ & + \Delta C_k^p(M, Re, \alpha, p) + \Delta C_k^r(M, Re, \alpha, r), \end{aligned}$$

where the term $C_k^0(M, Re, \alpha)$ denotes the aerodynamic coefficient, when all the control surfaces are in neutral position and the angle of yaw is $\beta = 0^\circ$.

Of course for individual coefficients some of the increments can be neglected as the two examples, namely the lift coefficient C_L and the rolling moment coefficient C_l show.

⁵ The mean chord is defined by $\bar{c} = S/b$, with S the planform area and b the span of the wing.

$$C_L = C_L^0(M, Re, \alpha) + \Delta C_L^\beta(M, Re, \alpha, \beta) + \Delta C_L^{\delta_e}(M, \alpha, \delta_e) + \\ + \Delta C_L^{\delta_{bf}}(M, \alpha, \delta_{bf}) + + \Delta C_L^{\dot{\alpha}}(M, Re, \alpha, \dot{\alpha}) + \Delta C_L^q(M, Re, \alpha, q),$$

and

$$C_l = \Delta C_l^\beta(M, Re, \alpha, \beta) + \Delta C_l^{\delta_a}(M, \alpha, \delta_a) + \Delta C_l^{\delta_r}(M, \alpha, \delta_r) + \\ + \Delta C_L^p(M, Re, \alpha, p) + \Delta C_L^r(M, Re, \alpha, r).$$

The increments are determined by:

$$\Delta C_k^\Sigma(M, Re, \alpha, \Sigma) = C_k^\Sigma(M, Re, \alpha, \Sigma) - C_k(M, Re, \alpha),$$

where Σ denotes any variable specified in the list presented above.

When the aerodynamic design engineers decide, after inspection of the aerodynamic data, that the influence of the independent variables are small and that their behavior in general is linear, an aerodynamic model in the type of a Taylor series can be generated. Therefore we get, for example, for the lift coefficient⁶

$$C_L = C_L^0(M) + \frac{\partial C_L}{\partial \alpha} \delta(\alpha) + \left(\frac{\partial C_L}{\partial \beta} \delta(\beta) \right) + \frac{\partial C_L}{\partial \delta_e} \delta(\delta_e) + \frac{\partial C_L}{\partial \delta_{bf}} \delta(\delta_{bf}) + \\ \frac{\partial C_L}{\partial \delta_{sb}} \delta(\delta_{sb}) + \frac{\partial C_L}{\partial \dot{\alpha}^*} \delta(\dot{\alpha}^*) + \frac{\partial C_L}{\partial q^*} \delta(q^*),$$

where the term in brackets is mostly negligible, and for the rolling moment coefficient

$$C_l = \frac{\partial C_l}{\partial \beta} \delta(\beta) + \frac{\partial C_l}{\partial \delta_a} \delta(\delta_a) + \frac{\partial C_l}{\partial \delta_r} \delta(\delta_r) + \frac{\partial C_l}{\partial p^*} \delta(p^*) + \frac{\partial C_l}{\partial r^*} \delta(r^*).$$

2.4 Examples of Aerodynamic Models

2.4.1 The SAENGER Vehicle (CAV)

In Section 7.2 we deal with the aerodynamics of the SAENGER vehicle, the reference concept of a German technology program. In the following we describe the aerodynamic model for this airbreathing vehicle, which is reported in [7]. The sketch in Fig. 2.1. shows the notations used in the model.

$$C_L(M, \alpha, \delta_e) = C_L(M, \alpha) + \Delta C_L(M, \alpha, \delta_e) + \Delta C_{L,book}(M, \alpha),$$

⁶ The Reynolds number dependency is omitted in this example.

$$\begin{aligned}
C_D(M, \alpha, \delta_e, H) &= C_{D0,pressure}(M, \alpha) + C_{D0,friction}(M, H) \\
&\quad + \Delta C_{D,induced}(M, \alpha) + \Delta C_D(M, \alpha, \delta_e) \\
&\quad + \Delta C_{D,book}(M, \alpha) + \Delta C_{D,friction,book}(M, H), \\
C_m(M, \alpha, \delta_e) &= C_m(M, \alpha) + \Delta C_m(M, \alpha, \delta_e) + \Delta C_{m,book}(M, \alpha), \\
C_Y(M, \beta, \delta_r) &= \frac{\partial C_Y}{\partial \beta}(M) \beta + \frac{\partial C_Y}{\partial \delta_r}(M) \delta_r, \\
C_l(M, \alpha, \beta, \delta_r, \delta_a) &= \frac{\partial C_l}{\partial \beta}(M, \alpha) \beta + \frac{\partial C_l}{\partial \delta_r}(M) \delta_r + \frac{\partial C_l}{\partial \delta_a}(M) \delta_a, \\
C_n(M, \alpha, \beta, \delta_r) &= \frac{\partial C_n}{\partial \beta}(M, \alpha) \beta + \frac{\partial C_n}{\partial \delta_r}(M) \delta_r.
\end{aligned}$$

The variable H denotes the flight altitude. For longitudinal coefficients the increment method is used, whereas for the lateral coefficients the derivative method is applied indicating the expectation of a linear behavior. The terms with the subscript “book” contain primarily the influence of the propulsion system including the inlet and the expansion nozzle⁷.

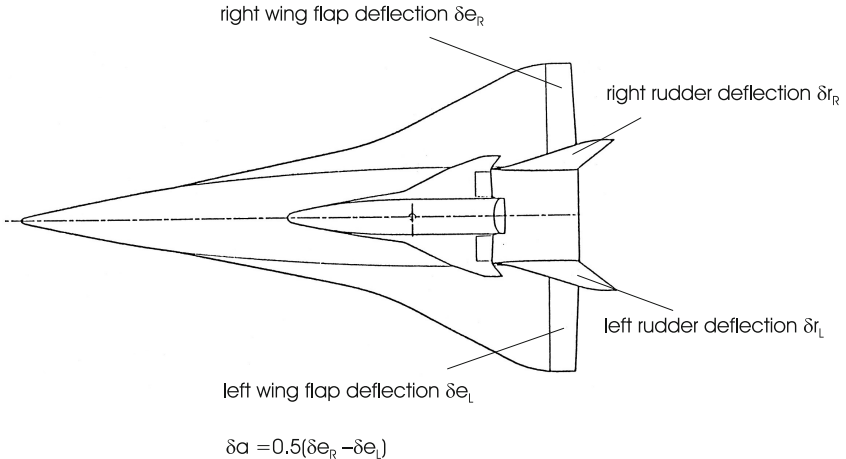


Fig. 2.1. SAENGER top view: notations of the aerodynamic control deflections

⁷ For the book keeping of the aerodynamic and propulsion forces see, e.g., [1].

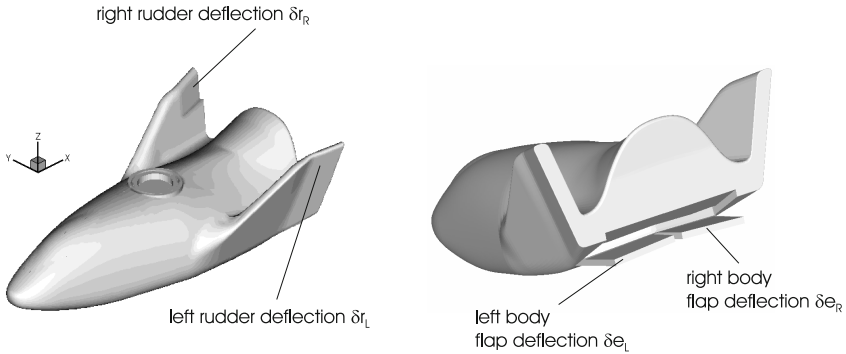
2.4.2 The X-38 Vehicle (RV-W)

The X-38 spacecraft, a European-US project (Section 6.6), was designed as a crew rescue vehicle (CRV) for the evacuation of the crew members of the International Space Station ISS. This was for the case that they become injured or fall ill, and further in the case of an ISS disaster. Many European institutions (aerospace companies, research institutes and universities) were involved in establishing the aerodynamic data base (ADB). The responsibility for this ADB was with the French company DASSAULT AVIATION. Therefore this company, with the support of some NASA engineers, had generated the aerodynamic model, which we describe below, [8].

$$\begin{aligned}
 C_L &= C_L^0(M) + \frac{\partial C_L}{\partial \alpha} \delta(\alpha) + \frac{\partial C_L}{\partial \delta_e} \delta(\delta_e) + \frac{\partial C_L}{\partial \delta_{sb}} \delta(\delta_{sb}), \\
 C_D &= C_D^0(M) + \frac{\partial C_D}{\partial \alpha} \delta(\alpha) + \frac{\partial C_D}{\partial \delta_e} \delta(\delta_e) + \frac{\partial C_D}{\partial \delta_{sb}} \delta(\delta_{sb}), \\
 C_m &= C_m^0(M) + \frac{\partial C_m}{\partial \alpha} \delta(\alpha) + \frac{\partial C_m}{\partial \delta_e} \delta(\delta_e) + \frac{\partial C_D}{\partial \delta_{sb}} \delta(\delta_{sb}) + \frac{\partial C_m}{\partial q^*} \delta q^*, \\
 C_Y &= \frac{\partial C_Y}{\partial \beta} \delta(\beta) + \frac{\partial C_Y}{\partial \delta_a} \delta(\delta_a) + \frac{\partial C_Y}{\partial \delta_r} \delta(\delta_r) + \frac{\partial C_Y}{\partial \delta_{sb}} \delta(\delta_{sb}), \\
 C_l &= \frac{\partial C_l}{\partial \beta} \delta(\beta) + \frac{\partial C_l}{\partial \delta_a} \delta(\delta_a) + \frac{\partial C_l}{\partial \delta_r} \delta(\delta_r) + \frac{\partial C_l}{\partial \delta_{sb}} \delta(\delta_{sb}) + \\
 &\quad \frac{\partial C_l}{\partial p^*} \delta(p^*) + \frac{\partial C_l}{\partial r^*} \delta(r^*), \\
 C_n &= \frac{\partial C_n}{\partial \beta} \delta(\beta) + \frac{\partial C_n}{\partial \delta_a} \delta(\delta_a) + \frac{\partial C_n}{\partial \delta_r} \delta(\delta_r) + \frac{\partial C_n}{\partial \delta_{sb}} \delta(\delta_{sb}) + \\
 &\quad \frac{\partial C_n}{\partial p^*} \delta(p^*) + \frac{\partial C_n}{\partial r^*} \delta(r^*).
 \end{aligned}$$

As one can see, the model above is based on the derivative method indicating the assumption that the aerodynamic coefficients have primarily a linear dependency on the related independent variables.

Note that the elevon and aileron deflections are based on the split body flap and that the speed brake deflection is due to the appropriate rudder setting as is shown in Fig. 2.2.



$$\begin{aligned}
 \text{elevator deflection} \quad & \delta e = 0.5 (\delta e_l + \delta e_r) \\
 \text{aileron deflection} \quad & \delta a = 0.5 (\delta e_l - \delta e_r) \\
 \text{rudder deflection} \quad & \delta r = 0.5 (\delta r_l + \delta r_r) \\
 \text{spade brake deflection} \quad & \delta_{sb} = 0.5 (\delta r_l - \delta r_r)
 \end{aligned}$$

Fig. 2.2. X-38 vehicle: notations used in the aerodynamic model

2.4.3 The PRORA Vehicle (RV-W)

The aerodynamics of the demonstrator vehicle PRORA, an Italian project, are discussed in Section 6.10. PRORA is primarily a re-entry vehicle, however with a certain ascent capability. The aerodynamic model presented below is a combination of the increment method and the derivative method, whereby the derivative terms are only used for the time dependent variables $\dot{\alpha}, p, q, r$, indicating the assumption that their influence on the aerodynamic coefficients is linear, [9].

$$\begin{aligned}
 C_L = & C_L^{BL}(M, Re, \alpha) + \Delta C_L^\beta(M, Re, \alpha, \beta) + \Delta C_L^{\delta_e}(M, \alpha, \delta_e) + \\
 & \Delta C_L^{\delta_r}(M, \alpha, \delta_r) + \frac{\partial C_L}{\partial \dot{\alpha}^*}(M, Re, \alpha) \dot{\alpha}^* + \frac{\partial C_L}{\partial q^*}(M, Re, \alpha, cog) q^*,
 \end{aligned}$$

$$\begin{aligned}
 C_D = & C_D^{BL}(M, Re, \alpha) + \Delta C_D^\beta(M, Re, \alpha, \beta) + \Delta C_D^{\delta_e}(M, \alpha, \delta_e) + \\
 & \Delta C_D^{\delta_r}(M, \alpha, \delta_r),
 \end{aligned}$$

$$\begin{aligned}
 C_m = & C_m^{BL}(M, Re, \alpha) + \Delta C_m^\beta(M, Re, \alpha, \beta) + \Delta C_m^{\delta_e}(M, \alpha, \delta_e) + \\
 & \Delta C_m^{\delta_r}(M, \alpha, \delta_r) + \frac{\partial C_m}{\partial \dot{\alpha}^*}(M, Re, \alpha) \dot{\alpha}^* + \frac{\partial C_m}{\partial q^*}(M, Re, \alpha, cog) q^*,
 \end{aligned}$$

$$C_Y = \Delta C_Y^\beta(M, Re, \alpha, \beta) + \Delta C_Y^{\delta_e}(M, \alpha, \delta_e) + \Delta C_Y^{\delta_r}(M, \alpha, \beta, \delta_r) +$$

$$\frac{\partial C_Y}{\partial p^*} (M, Re, \alpha, cog) p^* + \frac{\partial C_Y}{\partial r^*} (M, Re, \alpha, cog) r^*,$$

$$C_l = \Delta C_l^\beta(M, Re, \alpha, \beta) + \Delta C_l^{\delta_e}(M, \alpha, \delta_e) + \Delta C_l^{\delta_r}(M, \alpha, \beta, \delta_r) +$$

$$\frac{\partial C_l}{\partial p^*} (M, Re, \alpha, cog) p^* + \frac{\partial C_l}{\partial r^*} (M, Re, \alpha, cog) r^*,$$

$$C_n = \Delta C_n^\beta(M, Re, \alpha, \beta) + \Delta C_n^{\delta_e}(M, \alpha, \delta_e) + \Delta C_n^{\delta_r}(M, \alpha, \beta, \delta_r) +$$

$$\frac{\partial C_n}{\partial p^*} (M, Re, \alpha, cog) p^* + \frac{\partial C_n}{\partial r^*} (M, Re, \alpha, cog) r^*.$$

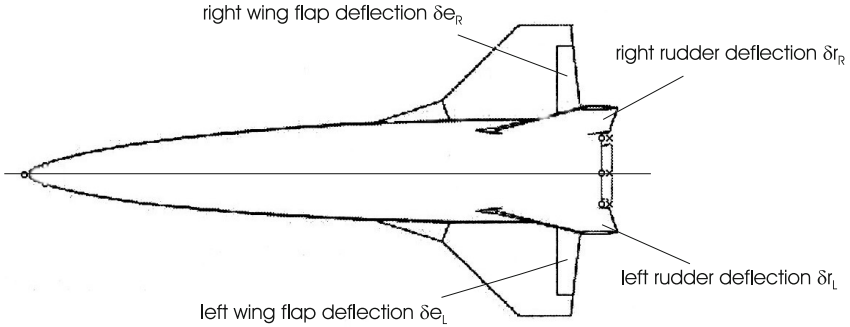


Fig. 2.3. PRORA vehicle: notations used in the aerodynamic model

Remarkable in this model are on the one hand the Reynolds number and the center-of-gravity (*cog*) dependencies, and on the other hand that no aileron influence is explicitly accounted for. Fig. 2.3 shows the notations used in the model.

References

1. Hirschel, E.H., Weiland, C.: Selected Aerothermodynamic Design Problems of Hypersonic Flight Vehicles, vol. 229. Springer, Heidelberg; Progress in Astronautics and Aeronautics. AIAA, Reston (2009)
2. Hirschel, E.H.: Basics of Aerothermodynamics, vol. 204. Springer, Heidelberg; Progress in Astronautics and Aeronautics. AIAA, Reston (2004)
3. Hirschel, E.H., Weiland, C.: Design of hypersonic flight vehicles: some lessons from the past and future challenges. CEAS Space Journal 1(1), 3–22 (2011)
4. Weiland, C.: Computational Space Flight Mechanics. Springer, Heidelberg (2010)
5. Etkin, B.: Dynamics of Atmospheric Flight. John Wiley & Sons, New York (1972)
6. Brockhaus, R.: Flugregelung. Springer, Heidelberg (2001)
7. Kraus, M.: Aerodynamische Datensätze für die Konfiguration SÄNGER 4-92. Deutsche Aerospace, DASA-LME211-TN-HYPAC-290 (1992)
8. Preaud, J.-P.: Dassault preliminary ADB in Gemass Format, Formulation and Description. Industrial Communication (1998)
9. Rufolo, G.C., Roncioni, P., Marini, M., Votta, R., Palazzo, S.: Experimental and Numerical Aerodynamic Data Integration and Aerodatabase Development for the PRORA-USV-FTB-1 Reusable Vehicle. AIAA-Paper 2006-8031 (2006)

Classification and Project Data of Space Vehicles

The development of space vehicles is an evolutionary process, like so many other objects and instruments humans have evolved. The first space vehicles, the capsules and probes (RV-NW), had very simple shapes. These were followed by the more complex shapes of the winged re-entry vehicles (RV-W) SPACE SHUTTLE Orbiter and BURAN Orbiter. The next step, which was mainly conceived in order to overcome the pure rocket based propulsion system, was to transport space vehicles, at least partly, with the support of airbreathing propulsion systems into space. Unfortunately the consideration of some of these systems, -Single-Stage-To-Orbit, Two-Stage-To-Orbit (CAV)-, up to now has only the status of technology and system study work.

3.1 Overview

In this book we present the aerodynamic coefficients of a large number of space vehicles. This comprises vehicles with such a level of maturity that they became operational, like APOLLO, SOYUZ, SPACE SHUTTLE Orbiter, etc., industrial projects, which were cancelled, but had already established a high degree of aerodynamic data, like HERMES, X34, etc., demonstrator projects, like PHOENIX, PRORA, OREX, etc., as well as paperwork projects, like SAENGER, ELAC, CARINA, etc., all performed by work-shares of industrial companies, research institutes and universities. Further, space vehicles executing extra terrestrial missions, like VIKING, HUYGENS, etc., are also considered.

We arrange these vehicles in the following three classes, which were already defined in [1, 2]:

- Non-winged vehicles (RV-NW) with the subclasses capsules and probes as well as cones and bicones,
- Winged re-entry vehicles (RV-W),
- Cruise and acceleration vehicles (CAV).

The transport of payload into space and its return to the Earth's surface is known to require the development and construction of suitable vehicles which are able to withstand the very severe thermal and mechanical (pressure and shear stress, [1]) loads encountered during such a mission. In the early days of

space exploration the designers had the feeling that the vehicle shape should be as simple and compact as possible. So, capsules and probes as the most important types of the non-winged re-entry vehicles (RV-NW) were born. Basic properties and details of the aerothermodynamic design problems of such vehicles are treated in [1].

In general the class of RV-NW's comprises ballistic entry probes (also for entry into extra terrestrial atmospheres), traditional capsules and blunted cones and bicones. Whereas, normally, the capsules and probes do not have aerodynamic control surfaces, the cones and bicones may have some, in particular body flaps for longitudinal trim. To this may come split body flaps, inclined to the lateral axis for roll control and lateral stability¹. The aerodynamics of capsules and probes are treated in Chapter 4 and of cones and bicones in Chapter 5.

A positive aerodynamic performance of the lift-to-drag ratio L/D for capsules and probes can be achieved only with negative angle of attack. The reason for that is described in detail in [1]. In contrast to this cones and bicones behave, regarding the aerodynamic performance, like conventional airplanes or winged space planes, namely that L/D is positive for positive angles of attack.

A winged re-entry vehicle is heavier and more complex than a non-winged vehicle (capsule), but in principle is a re-usable vehicle. Its relatively high lift-to-drag ratio L/D leads to in a large cross-range capability. The aerodynamic design of RV-W's is driven by the wide Mach number and altitude range of these vehicles, the structural design is driven by the large thermal loads², which are present on the atmospheric high speed segment of the re-entry trajectory.

Winged re-entry vehicles basically fly a braking mission during return from orbit or sub-orbit to the surface of Earth. They are, therefore, on purpose blunt and compact vehicles. They fly on the largest part of their trajectory at high angle of attack, which is in contrast to airbreathing CAV's.

The high angle of attack of the vehicle with a more or less flat windward side increases the “effective” bluntness, and thus increases further the (wave) drag of the vehicle. On the other hand, the large bluntness permits a very effective surface radiation cooling, [2].

The small aspect ratios of RV-W's, as for all hypersonic flight vehicles, causes difficulties in low speed control, such as during approach and landing. In Chapter 6 the aerodynamic coefficients of RV-W vehicles are presented for the whole trajectory including the low speed segment.

To date, there does not exist a fully reusable space transportation system with the capability of taking off horizontally or vertically and landing horizontally. As we have mentioned before, the SPACE SHUTTLE Orbiter is launched vertically like a rocket with the support of solid rocket boosters

¹ Of course, the guidance and flight control of RV-NW's is also conducted in a wide field by Reaction Control Systems (RCS).

² Usually cold primary structures and thermal protection systems (TPS).

attached to the expendable tank. The re-entry process into the Earth's atmosphere consists of a gliding unpowered flight and a horizontal landing on a conventional runway.

All of the capsules, which have transported and still transport men to and from space, were and are single-use vehicles, launched vertically on top of rockets. The landing, either at sea or on ground, is usually performed with the aid of a parachute system.

Although the above-mentioned systems represent reliable means of space transportation, the cost of delivering payloads into space remains much too high and a launch on demand is not possible. Consequently, at the end of the 1980s and during the 1990s, numerous activities all over the world aimed for the developments of fully reusable space transportation systems. These were to have the capability of launch on demand and preferable the ability to take-off and land horizontally.

Conceptual design studies covered Single-Stage-To-Orbit (SSTO) and Two-Stage-To-Orbit (TSTO) systems. An overview about these studies can be found in [3].

The class of cruise and acceleration vehicles (CAV's) consists essentially of hypersonic spacecrafts which fly with small angles of attack and minimized drag. Parts of the ascent and descent trajectories which are to be flown by SSTO concept vehicles are in accordance with the definition of CAV's. Other parts of those trajectories are more RV-W like. The lower part of a TSTO system is a pure hypersonic spacecraft and thus a CAV. Candidates of that are, for example, the German SAENGER system and the French STAR-H system. For both systems only preliminary design and technology work was performed before the projects were cancelled during the mid of the 1990s.

The aerodynamic data bases of two of such systems are partly available and can be found in Chapter 7.

Below we have listed in four sections in a comparative manner the vehicles considered in this book. Summarized in short are the most relevant development items and mission features, as well as the vehicle shapes.

3.2 Re-entry Vehicles - Non-winged (RV-NW): Space Probes and Capsules

Capsules and probes typically have a lift-to-drag ratio of $0.3 \lesssim L/D \lesssim 0.4$, [1].

Ascent:

Capsules and probes are launched generally on top of rockets which accelerate them to the speeds necessary for stays in the various Earth orbits or in the case of extra-terrestrial mission the speed to leave the Earth's gravity field. For more information concerning the velocity laws of flight in space, see [4].

Descent and landing:

After flying along a ballistic or low L/D entry trajectory the final deceleration takes place by parachute systems either in water or on ground.

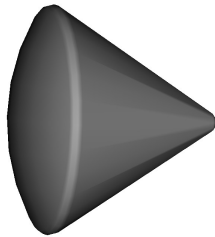
APOLLO capsule: Section 4.2.

Fig. 3.1. Non-winged
re-entry vehicle

- United States flight project,
- several vehicles were developed and manufactured,
- lunar missions, APOLLO project,
- flown during 1966 - 1973,
- aerodynamic data of steady longitudinal motion available,
- axisymmetric shape,
- dynamic stability data available.

Details of aerodynamics: page 43 ff.

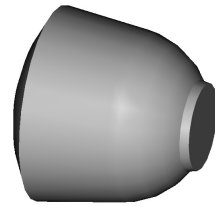
SOYUZ capsule: Section 4.3.

Fig. 3.2. Non-winged
re-entry vehicle

- Soviet Union space project,
- several vehicles were developed and manufactured,
- low Earth orbit missions,
- flown during 1965 - until now,
- aerodynamic data of steady longitudinal motion available,
- axisymmetric shape,
- dynamic stability data available.

Details of aerodynamics: page 51 ff.

ARD capsule: Section 4.4.

- European demonstrator project,
- one vehicle was developed and manufactured,
- sub-orbital flight,
- project duration: 1993 - 1998, one flight in 1998,
- flight data of steady longitudinal motion available,
- axisymmetric shape,
- dynamic stability data available.

Details of aerodynamics: page 58 ff.

Fig. 3.3. Non-winged re-entry vehicle

HUYGENS probe: Section 4.5.

- European space flight project for Saturn moon Titan,
- one vehicle was developed and manufactured,
- passenger space flight to Titan,
- launch on Oct. 1997, arrived at Saturn on July 2004 and land on Titan on Jan. 2005,
- no access to aerodynamic data of steady longitudinal motion,
- axisymmetric shape,
- no access to dynamic stability data.

Fig. 3.4. Space probe

Details of aerodynamics: page 66 ff.

BEAGLE2 probe: Section 4.6.

- Great Britain project,
- one vehicle was developed and manufactured,
- passenger space flight to Mars,
- launch on June 2003, landing on Martian surface Dec. 2003, landing failed,
- rough aerodynamic data of steady longitudinal motion available,
- axisymmetric shape,
- dynamic stability data not available.

Details of aerodynamics: page 70 ff.

Fig. 3.5. Space probe

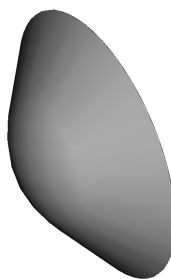
OREX demonstrator: Section 4.7.

Fig. 3.6. Technology demonstrator

- Japan's Hope-X project,
- one vehicle was developed and manufactured,
- flight in low Earth orbit (LEO),
- launch in 1994, one complete orbital cycle performed,
- ballistic re-entry flight, drag coefficients available,
- axisymmetric shape,
- dynamic stability data not available.

Details of aerodynamics: page 76 ff.



Fig. 3.7. Configurational study

VIKING-type : Section 4.8.

- European design study in the Crew Rescue Vehicle (CRV) project,
- extensive theoretical and experimental data available,
- low Earth orbit mission,
- not flown,
- aerodynamic data of steady longitudinal motion available,
- axisymmetric shape,
- dynamic stability data available.

Details of aerodynamics: page 80 ff.

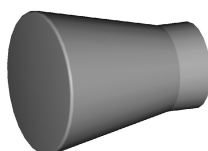


Fig. 3.8. Capsule system study

CARINA probe: Section 4.9.

- Italian project,
- some theoretical and experimental data available,
- low Earth orbit mission,
- not flown,
- rough aerodynamic data of steady longitudinal motion available,
- axisymmetric shape,
- dynamic stability data not available.

Details of aerodynamics: page 96 ff.

AFE probe: Section 4.10.

Fig. 3.9. Capsule system study

- Joint U.S. (AOTV) - Europe (MSRO) project,
- detailed theoretical and experimental data available,
- orbital transfer mission,
- not flown,
- aerodynamic data of steady longitudinal motion available,
- aerodynamic data of steady lateral motion available,
- dynamic stability data not available.

Details of aerodynamics: page 101 ff.

VIKING : Section 4.11.

Fig. 3.10. Space probe

Details of aerodynamics: page 111 ff.

Remark: The denotations of the abbreviations used in the description of the AFE probe are

AOTV \Rightarrow Aero-assisted Orbital Transfer Vehicle,

MSRO \Rightarrow Mars Sample Return Orbiter.

3.3 Re-entry Vehicles - Non-Winged (RV-NW): Cones and Bicones

Cones and bicones have typically a lift-to-drag ratio of $0.6 \lesssim L/D \lesssim 1.2$. Actually there is and was no space flight project, which has used cones or bicones despite their apparent advantages, see, e.g., [1].

Ascent:

Cones and bicones would be probably launched on top of rockets which then accelerate them up to the speeds corresponding to their missions. For more information concerning the velocity laws of flights in space, see, e.g., [4].

Descent and landing:

The re-entry process of cones and bicones would be very similar to the one of capsules and probes, except that their cross-range capability is somewhat higher, which enables them to fly more precisely to the landing area.

The final deceleration could take place by parachute or paraglider systems again either in water or on ground.

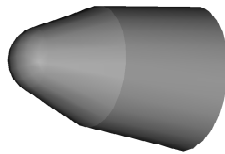


Fig. 3.11. Configurational study

BLUFF-BICONE : Section 5.2.

- German design study in the frame of the European Crew Rescue Vehicle (CRV) project,
- detailed theoretical and experimental data available,
- low Earth orbit missions,
- not flown,
- aerodynamic data of steady longitudinal motion available,
- axisymmetric shape,
- dynamic stability data not available.

Details of aerodynamics: page 124 ff.

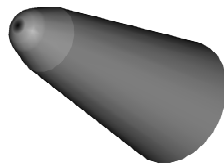
SLENDER-BICONE : Section 5.3.

Fig. 3.12. Configurational study

Details of aerodynamics: page 132 ff.

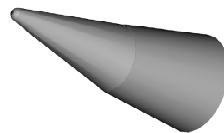
BENT-BICONE : Section 5.4.

Fig. 3.13. Configurational study

Details of aerodynamics: page 138 ff.

COLIBRI: Section 5.5.

Fig. 3.14. Configurational study

Details of aerodynamics: page 142 ff.

IRDT: Section 5.6.

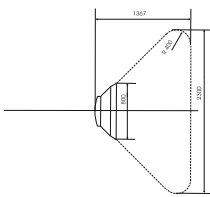


Fig. 3.15. Flight demonstrator

- Russia - Germany space flight project,
- theoretical and experimental data are available,
- sub-orbital flight,
- qualification flight in Feb. 2000,
- aerodynamic data of steady longitudinal motion available,
- axisymmetric body,
- some dynamic stability data available.

Details of aerodynamics: page 149 ff.

EXPERT: Section 5.7.

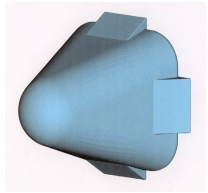


Fig. 3.16. Technology demonstrator

- European flying test bed project,
- theoretical and experimental data are available,
- sub-orbital flight,
- three ballistic re-entry flights are planned,
- aerodynamic data of steady longitudinal motion available,
- aerodynamic data of steady lateral motion not available,
- dynamic stability data not available.

Details of aerodynamics: page 159 ff.

3.4 Re-entry Vehicles -Winged (RV-W)

RV-W have typically an untrimmed lift-to-drag ratio of $L/D \approx 2.0$ in the high Mach number regime. For the approach and landing process the magnitude of the aerodynamic performance L/D must be at least 4.5 in the low subsonic regime.

Ascent:

Winged re-entry vehicles (RV-W) are either launched vertically with the help of rockets, or - in the case of Two-Stage-To-Orbit systems (TSTO) - horizontally from a carrier vehicle, the lower stage of the system. Other launch modes have been considered, viz. the horizontal launch from a sled, [1, 2].

Descent and landing:

The return to the Earth surface in any case is made with an unpowered gliding flight, followed by the horizontal landing on a runway.

SPACE SHUTTLE Orbiter: Section 6.2.



- United States' space flight project,
- detailed aerodynamic data base available,
- flights in low Earth orbit,
- 135 flights between 1981 and 2011,
- aerodynamic data of steady motion (longitudinal and lateral) available,
- dynamic stability data available.

Fig. 3.17. Space and re-entry vehicle

Details of aerodynamics: page 174 ff.

X-33 space vehicle: Section 6.3.

Fig. 3.18. Demonstrator vehicle

- United States' technology and flight demonstrator project,
- experimental and numerical data for hypersonic flight available,
- sub-orbital flight,
- project: begin in 1996 cancelled in 2001,
- aerodynamic data of steady motion (longitudinal and lateral) available,
- dynamic stability data not available.

Details of aerodynamics: page 198 ff.

X-34 space vehicle: Section 6.4.

Fig. 3.19. Demonstrator vehicle

- United States' technology and flight demonstrator project,
- experimental and numerical data available,
- flight with $M_{\infty} = 8$ up to an altitude of 76 km,
- project: begin in 1996, cancelled in 2001,
- aerodynamic data of steady motion (longitudinal and lateral) available,
- dynamic stability data not available.

Details of aerodynamics: page 207 ff.

X-37 space vehicle: Section 6.5.

Fig. 3.20. Demonstrator vehicle

- United States' technology and flight demonstrator project,
- no access to aerodynamic data,
- project: begin in 1999,
- first flight took place in 2010 and two further ones in 2011 and 2012,
- aerodynamic data of steady motion (longitudinal and lateral) not available,
- dynamic stability data not available.

Details of aerodynamics: page 217 ff.

X-38 re-entry vehicle: Section 6.6.

Fig. 3.21. Re-entry vehicle on lifting body basis

- Europe - U.S. crew rescue vehicle project,
- experimental and numerical data for the whole Mach number range available,
- two flights for parafoil landing demonstration,
- project: begin in 1996, cancelled in June 2002,
- aerodynamic data of steady motion (longitudinal and lateral) available,
- some dynamic stability data available.

Details of aerodynamics: page 220 ff.

PHOENIX re-entry demonstrator: Section 6.7.

Fig. 3.22. Space flight demonstrator

- Germany's space flight demonstrator project,
- detailed experimental and numerical data for the whole Mach number range available,
- some flights demonstrating automatic landing capability,
- project: begin in 2000, terminated in 2004,
- aerodynamic data of steady motion (longitudinal and lateral) available,
- dynamic stability data not available.

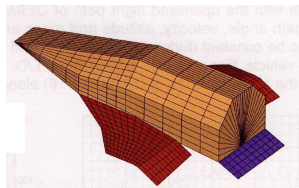
Details of aerodynamics: page 235 ff.

HOPE-X re-entry vehicle: Section 6.8.

Fig. 3.23. Space and re-entry vehicle

- Japan's space flight project,
- some experimental and numerical data of the aerodynamic data base available,
- not flown,
- project: begin 1980s, cancelled in 2003,
- aerodynamic data of steady motion (longitudinal and lateral) available,
- dynamic stability data not available.

Details of aerodynamics: page 253 ff.

Facetted DS6 configuration: Section 6.9.**Fig. 3.24.** Technology demonstrator vehicle

- Germany's configurational study,
- some experimental and numerical data available,
- demonstration flights: SHEFEX I in 2005 and SHEFEX II, in 2012, no flight of DS6,
- project: begin in the 1990s,
- some aerodynamic data of steady motion (longitudinal) available,
- dynamic stability data not available.

Details of aerodynamics: page 264 ff.**PRORO-USV demonstrator vehicle: Section 6.10.****Fig. 3.25.** Technology demonstrator vehicle

- Italy's flight demonstrator program,
- experimental and numerical data for transonic flight available,
- one transonic demonstrator flight in Feb. 2007,
- project: begin in 2000,
- aerodynamic data of steady motion (longitudinal and lateral) available,
- dynamic stability data not available.

Details of aerodynamics: page 269 ff.**HERMES re-entry vehicle: Section 6.11.****Fig. 3.26.** Re-entry vehicle

- Re-entry vehicle as part of Europe's access to space program,
- detailed experimental and numerical data for the whole Mach number range,
- no demonstration flight,
- project: begin in 1984, cancelled 1993,
- aerodynamic data of steady motion (longitudinal and lateral) available,
- dynamic stability data not available.

Details of aerodynamics: page 280 ff.

3.5 Cruise and Acceleration Vehicles (CAV)

CAV's possess as aircraft-like vehicles a high lift-to-drag ratio L/D . For example, the lower stage of the TSTO system SAENGER possesses for hypersonic Mach numbers a $L/D \approx 4.5$ to 5.0 , and in the low subsonic regime a $L/D \approx 11$.

Ascent:

Most complex are the SSTO vehicles³. Their propulsion systems could be described as follows:

1. only conventional rocket motors \implies HOPPER,
2. only linear aerospike rocket motor \implies X-33,
3. turbojet for aeroassisted flight⁴ in the first part of the trajectory (up to altitudes of 15-18 km) and rocket motors for flight in the second part of the trajectory \implies HOTOL⁵ concept I,
4. combination of turbojet-ramjet/scramjet propulsion in the first part of the trajectory (up to altitudes of 42-46 km) and rocket motors for flight in the second part of the trajectory \implies HOTOL concept II, [3].

For the SSTO concept cases 3) and 4) the flight during the first part of the ascent trajectory was to be aeroassisted, where the vehicle behaves like a CAV⁶.

Descent and landing:

TSTO systems have a clear distinction between the tasks of the upper stage and the lower stage. The lower stage is a CAV with an airbreathing propulsion system, which transports the upper stage to the altitude, where the stage separation takes place. The upper stage is rocket propelled and behaves like a RV-W.

SSTO's execute the descent like a RV-W, which means unpowered in a straight deceleration mode, gliding to the runway. The descent of TSTO's is split. The lower stage operates like a powered hypersonic spacecraft (CAV)

³ ESA initiated the program “Future European Space Transportation Investigation Program” (FESTIP), (1994-1998). In this program a large variety of different SSTO and TSTO concepts were investigated and their potentials were worked out, [3, 5].

⁴ Aeroassisted flight means flight with an airbreathing propulsion system and lift generated by aerodynamic surfaces like wings, winglets and parts of fuselages.

⁵ The “Horizontal Take-Off and Landing” concept HOTOL was a British project, which was considered during the years 1982-1991, [3].

⁶ There were other CAV-type concept studies, for example the U.S. NASP National Aerospace Plane concept, the French concepts STAR-H and PREPHA as well as the Russian concept MIGAKS. All these studies were cancelled. The author had no access to any aerodynamic data of these vehicles.

and flies back to its destination. The upper stage conducts the re-entry and landing process like a RV-W.

**SAENGER TSTO system,
lower stage: Section 7.2.**



Fig. 3.27. Hypersonic vehicle

- Germany's Hypersonic Technology Program,
- detailed experimental and numerical data of the lower stage for the whole Mach number range available,
- no demonstration flight,
- project: begin in 1986, cancelled 1993,
- aerodynamic data of steady motion (longitudinal and lateral) available,
- dynamic stability data not available.

Details of aerodynamics: page 303 ff.

**ELAC technology demonstrator,
lower stage: Section 7.3.**

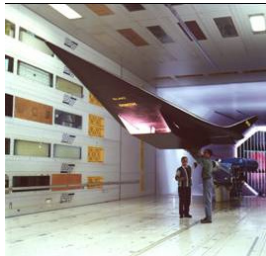


Fig. 3.28. Hypersonic vehicle

- TSTO design study of three German DFG Centers of Excellence,
- experimental and numerical data for the whole Mach number range,
- no demonstration flight,
- project: begin in 1989, finished 2003,
- aerodynamic data of steady motion (longitudinal and lateral) available,
- dynamic stability data not available.

Details of aerodynamics: page 319 ff.

References

1. Hirschel, E.H., Weiland, C.: Selected Aerothermodynamic Design Problems of Hypersonic Flight Vehicles, vol. 229. Springer, Heidelberg; Progress in Astronautics and Aeronautics. AIAA, Reston (2009)
2. Hirschel, E.H.: Basics of Aerothermodynamics, vol. 204. Springer, Heidelberg; Progress in Astronautics and Aeronautics. AIAA, Reston (2004)
3. Kuczera, H., Sacher, P.: Reusable Space Transportation Systems. Springer, Heidelberg (2011)
4. Weiland, C.: Computational Space Flight Mechanics. Springer, Heidelberg (2010)
5. FESTIP System Concept Team. Concept Selection Workshop. Conclusions and recommendations handout distributed to all participants, Lenggries, Germany, September 15-16 (1998)

Aerodynamic Data of Non-Winged Re-entry Vehicles (RV-NW)

- Capsules and Probes -

The Soviet Union (now Russia) and the United States of America were the first, who had developed capsules and probes and had brought them into space. Later other countries or union of countries (Germany, Japan, Great Britain, France, Italy, Europe, etc.) developed and sometimes launched similar vehicles as demonstrators, often in order to improve their competence in space transportation technology.

The shapes were very simple, axisymmetric configurations, which were equipped for the re-entry process with a heat shield consisting of ablative materials. Ballistic or low lift flight trajectories were devised for the re-entry process. The flight control of such vehicles was exclusively conducted by Reaction Control Systems (RCS).

4.1 Introduction

In order to understand some of the aerodynamic properties of capsules and probes we describe in the following some effects which are inherent in this kind of vehicles.

- Angle of attack:

Blunt configurations like capsules and probes have a positive lift only for negative angles of attack. The reason for that is, that bluff bodies have a large axial force coefficient C_X and a small normal force coefficient C_Z . Hence the lift coefficient, eq. (8.7), changes sign when $C_X \sin \alpha$ becomes larger than $C_Z \cos \alpha$. For an explanation in more detail see [1]. Therefore all aerodynamic coefficients in this chapter are plotted versus negative angles of attack.

- Flow field past axisymmetric bodies:

For a flow field around an axisymmetric body there can always be found a plane of symmetry whatever the values of the angles of attack α and angle of side slip β are. This means that the aerodynamic data sets of such

vehicles consists only of the longitudinal coefficients. Lateral coefficients are unessential.

- Banking:

Banking a vehicle around an angle μ means to roll the vehicle around the free-stream velocity vector. The result is that the flow is not changed, but the lift acts now in the lift-drag plane, which is turned by the angle μ . For more information see Chapter 6 in [2].

- Trim line:

With the general formulations of forces, moments, center-of-pressure and trim conditions, as they are derived for example in Chapter 7 of [1], we find the relations

$$C_{m_j} = C_{m_{ref}} - C_Z(x_{ref} - x_j) + C_X(z_{ref} - z_j), \quad (4.1)$$

$$x_{cp} = -\frac{C_{m_j}}{C_Z} \quad \text{with} \quad (x_{ref} = z_{ref} = z_{cp} = 0), \quad (4.2)$$

$$z_{cog} - z_{cp} = \frac{C_Z}{C_X}(x_{cog} - x_{cp}), \quad (4.3)$$

where the subscripts cp and cog mean center-of-pressure and center-of-gravity.

With eq. (4.1) the pitching moment coefficient is transformed from the nominal reference point to the reference point positioned in the tip of the vehicle. With eq. (4.2) the center-of-pressure position along the x-coordinate ($z_{cp} = 0$) is calculated. Then with eq. (4.3) the line of the center-of-gravity positions can be determined, where the vehicle flies trimmed. Trim lines can be found in Figs. 4.20, 4.60, 4.61, 5.21.

- The role of the z-offset value for trimmed flight of axisymmetric shapes:

A z-offset of the center-of-gravity (z_{cog}) is very important for the trim condition of axisymmetric shapes. Since the axial force coefficient C_X is much higher than the normal force coefficient C_Z , the trim angle α_{trim} can be considerably influenced by a small change of the z-offset value, which is in contrast to the influences of changes of the x_{cog} values. For more information see Chapter 5 in [1].

4.2 APOLLO (USA)

The APOLLO program was launched with the goal to bring American astronauts to the Moon at the latest by the end of the 1960s. It was part of NASA's continuing program of space exploration following the MERCURY and GEMINI projects. The first successful manned flight (in the frame of the APOLLO program) into space took place in October 1968 with the APOLLO 7 capsule. The mission was to operate inside a low Earth orbit and to test the re-entry process. Ten month later, in July 1969, the first flight to the Moon, performed with APOLLO 11, had happened, which was a striking success. After the first triumphant Moon landing further lunar missions (APOLLO 12,14,15,16,17) were conducted. The lunar program was ended with the successful flight of APOLLO 17 in December 1972.

There is no doubt that the aerodynamics of the APOLLO capsule are one of the best known. Due to the large number of flights in the 1960s and 1970s either in low Earth orbit or to the Moon, the free flight data base is remarkable. During the design of APOLLO, most of the aerodynamic data was obtained from wind tunnel tests, [3] - [7].

Due to the trim behavior of the APOLLO capsule its nominal angle of attack regime is placed between $-30^\circ < \alpha < 0^\circ$. In this regime the aft part of the capsule configuration lies in the "hypersonic shadow" of the flow. The term "hypersonic shadow" is used in analogy to Newton's method for hypersonic flows. There, every surface element, which does not see the free-stream velocity vector has a zero pressure coefficient c_p and does not contribute to the aerodynamic forces, see, e.g., [8]. Of course, this is not completely true for realistic flows, but the experience says that in hypersonic flow the contributions of such surface elements are indeed rather low.

That is the reason why the aerodynamic forces and moments of the capsule are mainly governed by the front part (heatshield) of the configuration. Of course, it could happen, due to uncertainties during the re-entry process, that the capsule enters the atmosphere with other than the nominal angle of attack values. Therefore it is necessary to investigate whether there exist trim points in other angle of attack regimes. Indeed capsules possess often so called parasite trim points, which are usually also Mach number dependent like the nominal ones. For the APOLLO capsule we present an example of this behavior in Sub-Section 4.2.4 (peculiarities).

4.2.1 Configurational Aspects

In Fig. 4.1 typical events and images of the APOLLO program are given. In Fig. 4.2 three-dimensional versions of the APOLLO shape are presented whereas in Fig. 4.3 the geometrical relations are drawn, [3, 4]. The heatshield or front part of the configuration consists of a sphere shell, whereas the aft part of the shape is built by a right circular cone, which is blunted at its apex by a sphere with a small radius.

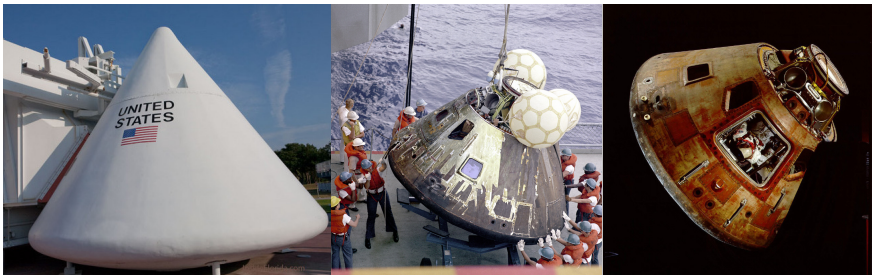


Fig. 4.1. APOLLO mock-up (left); APOLLO 13 during sea recovery (middle); APOLLO 11 after the lunar mission (right). Pictures from NASA gallery.

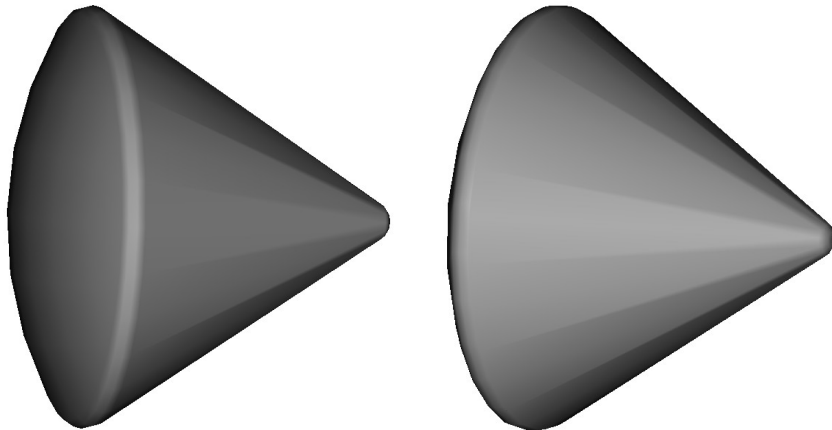


Fig. 4.2. 3D shape presentation of the APOLLO capsule

4.2.2 Aerodynamic Data of Steady Motion

In general the aerodynamic performance data, reported here, was found by wind tunnel tests. During the 1960s the numerical methods for integration of the governing equations were not in a state for generating reliable results of three-dimensional inviscid or viscous flow fields past realistic configurations. This situation has changed during the 1980s with the advent of robust Computational Fluid Dynamics (CFD) codes, whereby the quality of the results was growing every year. At that time these codes could be successfully applied for reliable inviscid and viscous flow fields computations around simple 3-D shapes like capsules and probes. Of course, in parallel progress was

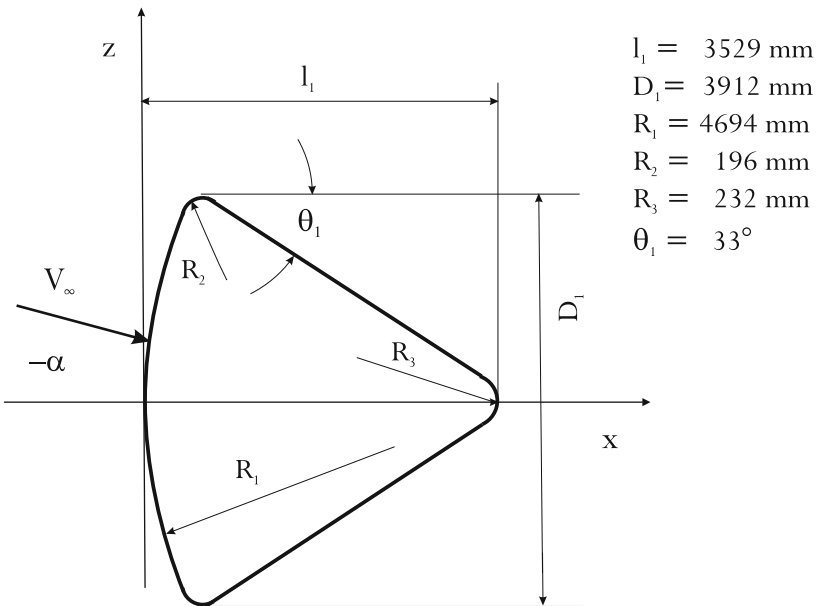


Fig. 4.3. Shape definition of the APOLLO capsule, [3, 4]

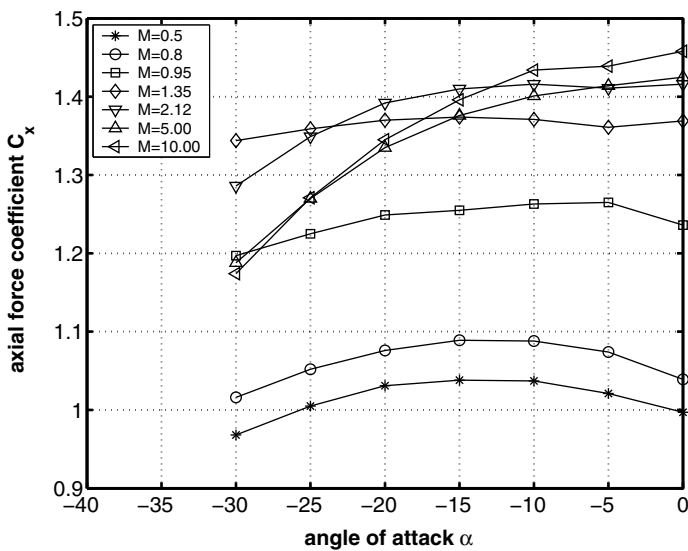


Fig. 4.4. Axial force coefficient C_x as function of the angle of attack α , [4, 7]

necessary also for grid generation strategies and computer capability, what indeed happened. An example of 3-D flow field computations around the APOLLO capsule is given in [9].

Longitudinal Motion

For the axial force C_x and the pitching moment C_m (Figs. 4.4 and 4.7) we have values for the Mach numbers $M_\infty = 0.5, 0.8, 0.95, 1.35, 2.12, 5, 10$, whereas for the normal force C_z , and therefore for the aerodynamic performance L/D (Figs. 4.5 and 4.6), for $M_\infty = 0.95$ no values are available.

Generally we discern that for the prescribed moment reference point static stability is given throughout the whole Mach number regime. The trim angle of attack in the hypersonic flow regime is approximately $\alpha_{trim} \approx -23^\circ$, which increases in the vicinity of the Mach number $M_\infty = 2$ to $\alpha_{trim} \approx -27^\circ$, (Fig. 4.8 (above)). The corresponding aerodynamic performance quantities range between $0.275 \lesssim L/D_{trim} \lesssim 0.325$, (Figs. 4.8 (below)).

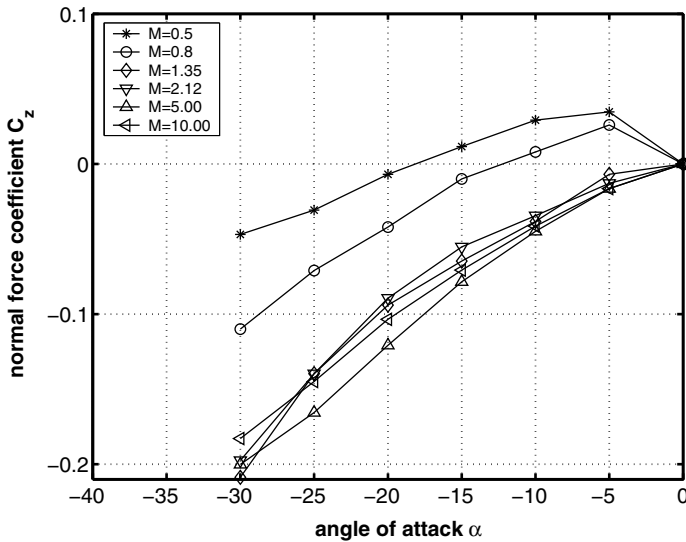


Fig. 4.5. Normal force coefficient C_z as function of the angle of attack α , [4, 7]

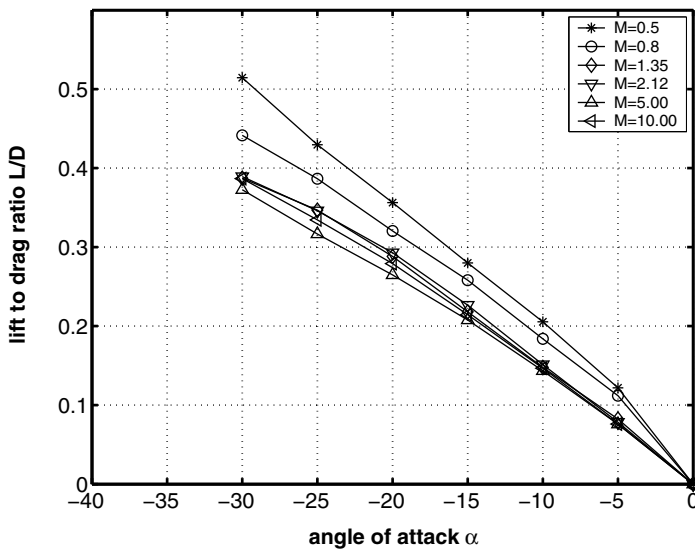


Fig. 4.6. Aerodynamic performance L/D as function of the angle of attack α , [4, 7]

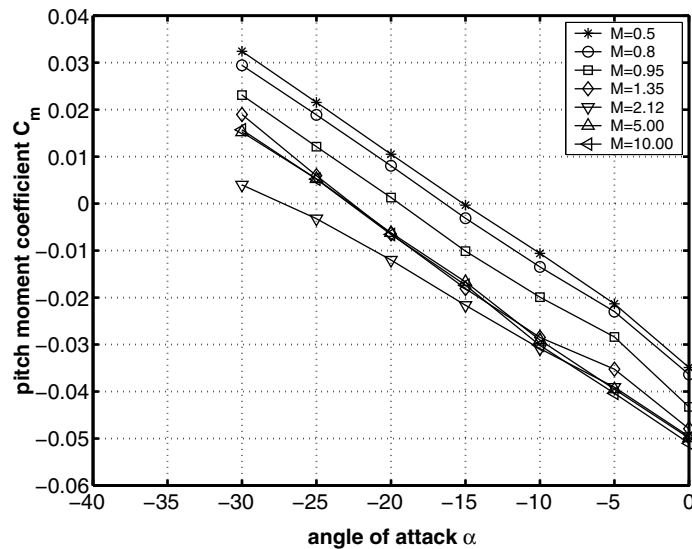


Fig. 4.7. Pitching moment coefficient C_m as function of the angle of attack α . Moment reference point: $x_{ref} = 0.265 D_1$, $z_{ref} = 0.035 D_1$, [4, 7].

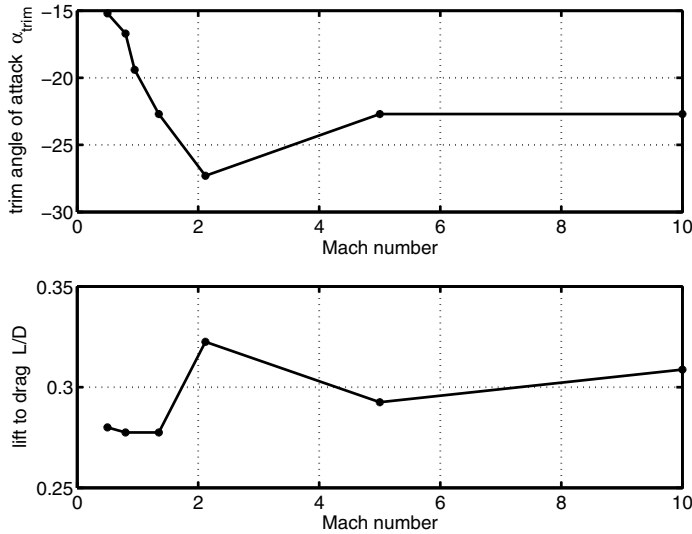


Fig. 4.8. Trim angle of attack as function of Mach number (above), taken from Fig. 4.7. Aerodynamic performance (L/D) at the trim angle of attack as function of the Mach number (below), taken from Fig. 4.6.

Lateral Motion

The APOLLO capsule is an axisymmetric configuration. Because of that no lateral aerodynamic characteristics exist.

4.2.3 Aerodynamic Data of Unsteady Motion

Pitch Motion

The data in Fig. 4.9 are measured with the free-to-tumble test method, [1], applied to an APOLLO command module with protuberances as they are the umbilical fairing, the vent and the surviving antenna. For the Mach number $M_\infty = 0.8$ dynamic pitch stability is guaranteed in the angle of attack regime $-3^\circ \gtrapprox \alpha \gtrapprox -30^\circ$, whereas the vehicle becomes dynamically unstable in that α regime for $M_\infty = 0.5$.

Others Motions

The APOLLO capsule is an axisymmetric configuration. Because of that only the dynamic derivative of pitch motion is relevant.

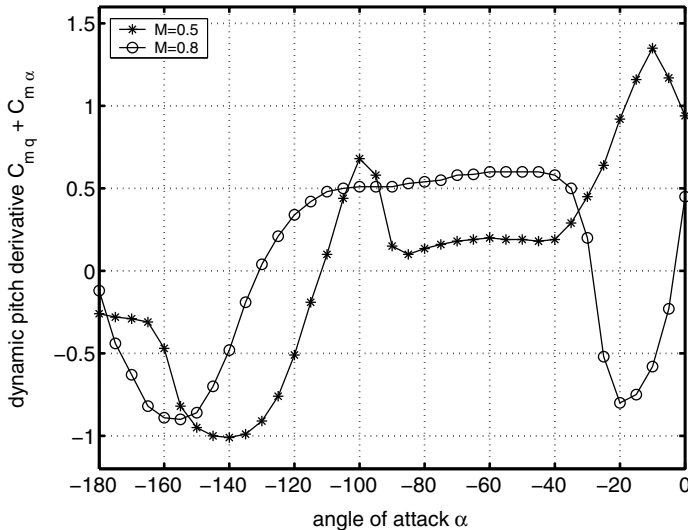


Fig. 4.9. Dynamic derivative of pitch motion $C_{mq} + C_{m\dot{\alpha}}$ as function of the angle of attack α , [4]

4.2.4 Peculiarities

During the development and testing of the APOLLO capsule, it was observed that the pitching moment C_m could meet the trim and stability conditions ($C_m = 0$, $\partial C_m / \partial \alpha < 0$) also at other points besides the nominal one. These points are called “parasite trim points”, [1]. There are at least three reasons why the vehicle must be prevented from entering into such non-nominal trim positions:

- the re-entry process can only be successfully conducted with the heat shield pointing forward in order to cope with the mechanical and thermal loads,
- the parachute landing system can be deployed only if the apex cover can be jettisoned properly, which could be a problem in the case, that the apex is exposed to the high pressure regime. Therefore this requires the heat shield pointing forward, too,
- in the launch abort case the escape procedure requires definitely a capsule heat shield in pointing-forward attitude.

The best solution of this problem would be given by a change to the vehicle shape which prevents the existence of parasite trim points. But this seems to be a demanding design challenge. For the APOLLO capsule this problem could not be solved satisfactorily, [10].

The APOLLO capsule possesses one parasite trim point over the whole Mach number range, which is somewhat fluctuating in the subsonic-transonic-low supersonic regimes. For higher Mach numbers, this trim point becomes

independent of the Mach number, Fig. 4.10. The evaluation was conducted for the center-of-gravity location $x_{cog}/D_1 = 0.657$ (measured from the apex) and $z_{cog}/D_1 = 0.035$.

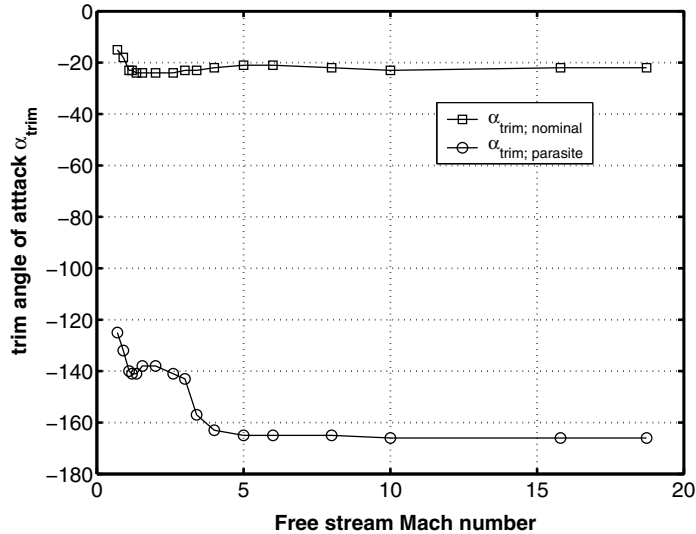


Fig. 4.10. Nominal and parasite trim points of the APOLLO capsule as function of the Mach number. Center-of-gravity: $x_{cog}/D_1 = 0.657$ and $z_{cog}/D_1 = 0.035$. Data source: [4].

4.3 SOYUZ (Russia)

The SOYUZ spacecraft was developed in the 1960s in the frame of the Soviet Union's space program. Its mission profile was in the past to carry people to and from the Soviet space stations SALYUT and MIR. It is still in these days the crew carrier for the International Space Station ISS. Further, the original planning had foreseen SOYUZ to be a part of the Soviet Union's Manned Lunar program, which never came true. The first successful manned flight has taken place in Oct. 1968, subsequent to a manned flight in 1967, which ended with a crash-landing and the death of the cosmonauts. Since then the SOYUZ capsule has conducted the re-entry missions of persons from low Earth orbit flights and the ISS very reliably.

The mass of the SOYUZ capsule is approximately 3000 kg. All the launches of the SOYUZ spacecrafts are carried out with SOYUZ rockets. The transport capability and launch security of these rockets are continuously advanced since the 1960s.

4.3.1 Configurational Aspects

Fig. 4.11 shows some images of the SOYUZ capsule as part of the SOYUZ spacecraft. In Fig. 4.12 three-dimensional versions of the SOYUZ capsule shape are presented whereas in Fig. 4.13 the geometrical relations are drawn, [11]. The SOYUZ spacecraft is composed of three parts, the orbital module, the re-entry module (SOYUZ capsule) and the service module. The shape of the SOYUZ capsule consists of a front part, which is built as a spherical segment, and an aft body in the form of a blunted circular cone, Fig. 4.12. The last part of the descent of the SOYUZ capsule after re-entry in the atmosphere is performed with the help of a parachute system and the subsequent landing always takes place in the desert of Kazakhstan. This is in contrast to the procedure for APOLLO, which was designed for a water landing.



Fig. 4.11. SOYUZ spacecraft with the re-entry module in the middle of the spacecraft structure (left); SOYUZ spacecraft mock-up (middle); SOYUZ capsule after landing in the desert of Kazakhstan (right). Pictures from NASA and ESA galleries.

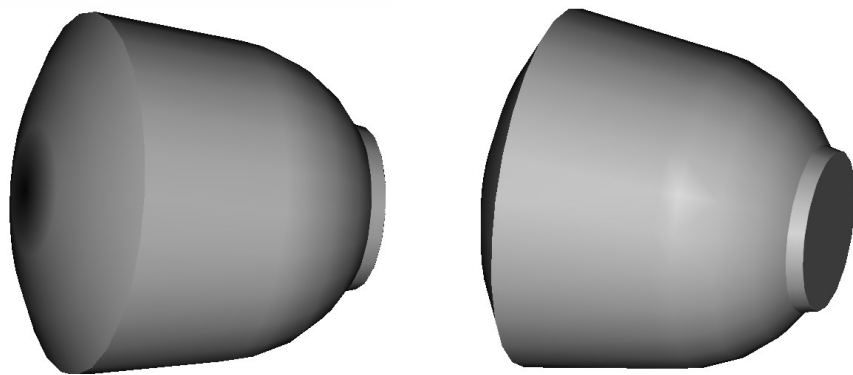


Fig. 4.12. 3D shape presentation of the SOYUZ capsule

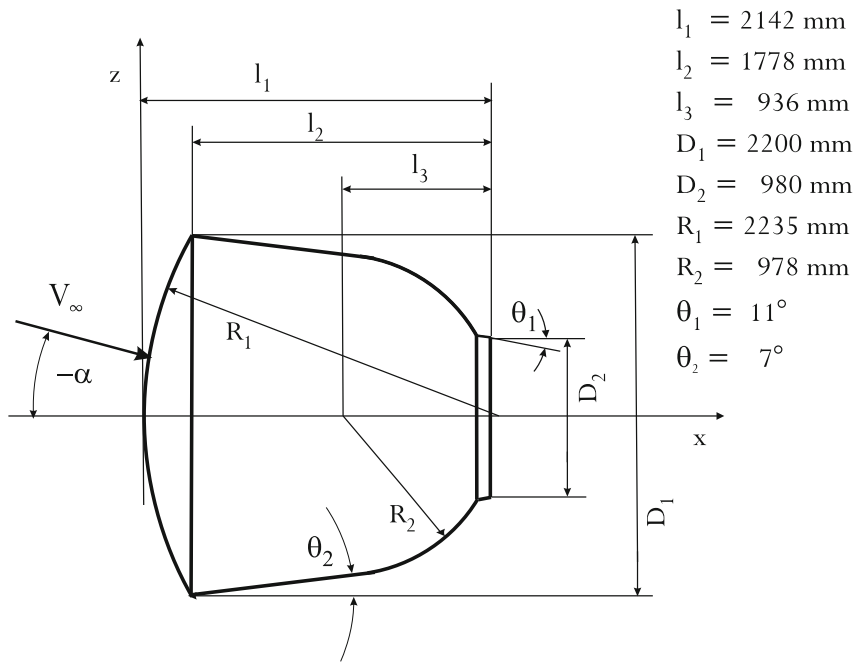


Fig. 4.13. Shape definition of the SOYUZ capsule, [11]

4.3.2 Aerodynamic Data of Steady Motion

Most of the aerodynamic performance data were obtained by experiments in the wind tunnels of TSNIIMASH and TSAGI. Both institutions are located near Moscow, Russia. Certainly some data were measured using a free flying large scale model with a diameter of 1 m.

Longitudinal Motion

The aerodynamic coefficients C_X , C_Z , C_m and L/D are given for the Mach numbers $M_\infty = 0.60, 0.95, 1.10, 1.78, 2.52, 5.96$, Figs. 4.14 - 4.17. The design goal was to attain in the hypersonic flight regime for the given trim angle $\alpha_{trim} \approx -25^\circ$ an aerodynamic performance value of $L/D = 0.3$, which indeed was met, see Figs. 4.16 and 4.17. The vehicle behaves statically stable in the whole Mach number range presented here and the angle of attack regime $-30^\circ \leq \alpha \leq 0^\circ$. It is conspicuous that the axial force coefficient C_X has for all plotted Mach numbers its maximum at $\alpha = 0^\circ$ and decreases with increasing negative angle of attack. This behavior is different from that of APOLLO, where the maximum of the force coefficients are Mach number dependent, with the highest negative α value for the lowest Mach number ($M_\infty = 0.5 \Rightarrow C_{Xmax}(\alpha \approx -15^\circ)$, see Fig. 4.4). The trim angle of attack course as function of the Mach number is exhibited in Fig. 4.18 and indicates the same characteristics as the APOLLO one (see Fig. 4.8), namely to increase from subsonic Mach numbers to a local maximum at $M_\infty \approx 1.8 - 2$, followed by a moderate decrease up to Mach numbers $M_\infty \approx 4$ and a slight growing when the Mach number approaches the hypersonic regime.

Lateral Motion

The SOYUZ capsule is an axisymmetric configuration. Because of that no lateral aerodynamic characteristics exist.

4.3.3 Aerodynamic Data of Unsteady Motion

Pitch Motion

The dynamic derivative of pitch motion¹ $m_z^{\bar{\omega}_z}$ as function of the angle of attack ($-180^\circ \lesssim \alpha \lesssim 0^\circ$) is plotted in Fig. 4.19. Generally for $-83^\circ \lesssim \alpha \lesssim -3^\circ$ dynamic stability is given, but there exists a small sector ($-23^\circ \lesssim \alpha \lesssim -17^\circ$) where this stability is suspended and that is just the range where the SOYUZ capsule for $M_\infty = 0.9$ conducts its trimmed flight ($\alpha_{trim}^{M_\infty=0.9} \approx -18.1^\circ$).

Other Motions

¹ In the Russian literature the dynamic derivative of pitch motion is indicated by $m_z^{\bar{\omega}_z}$ which is proportional to $C_{m\dot{\alpha}} + C_{m\dot{\alpha}}$.

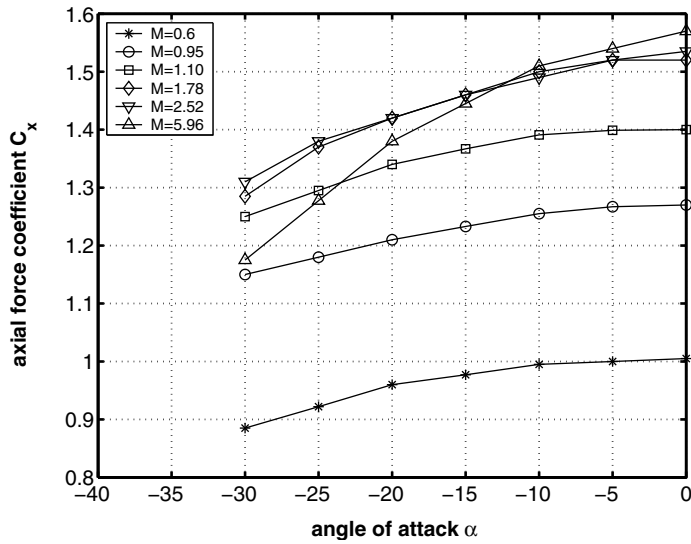


Fig. 4.14. Axial force coefficient C_x as function of the angle of attack α , [11]

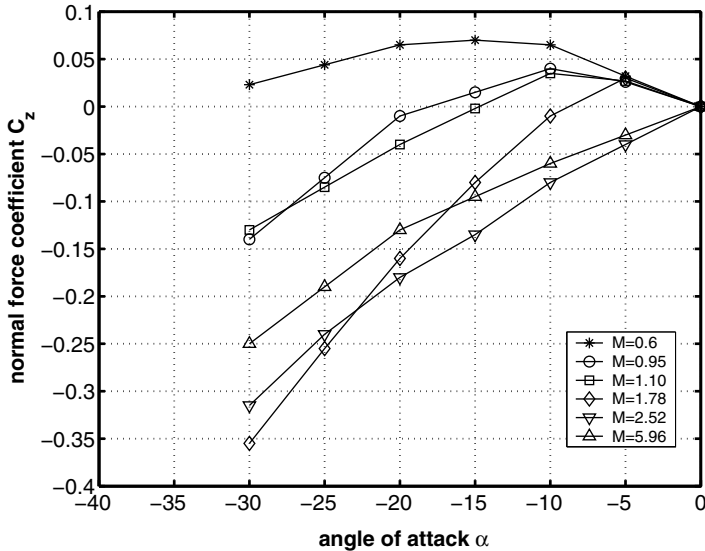


Fig. 4.15. Normal force coefficient C_z as function of the angle of attack α , [11]

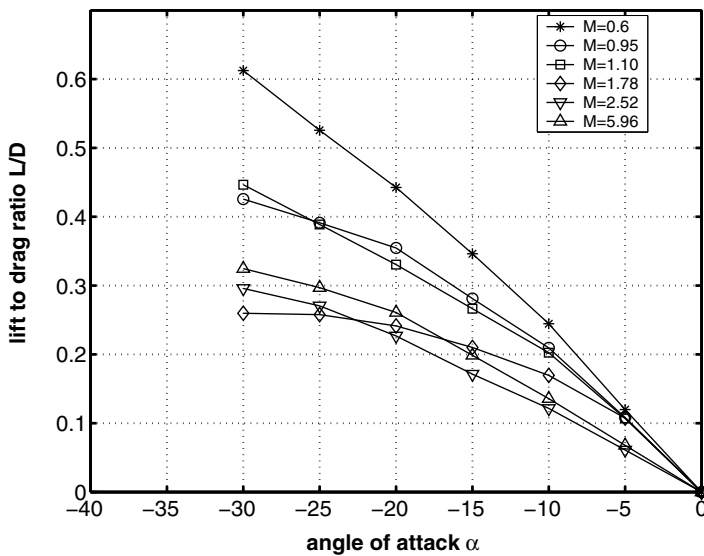


Fig. 4.16. Aerodynamic performance L/D as function of the angle of attack α , [11]

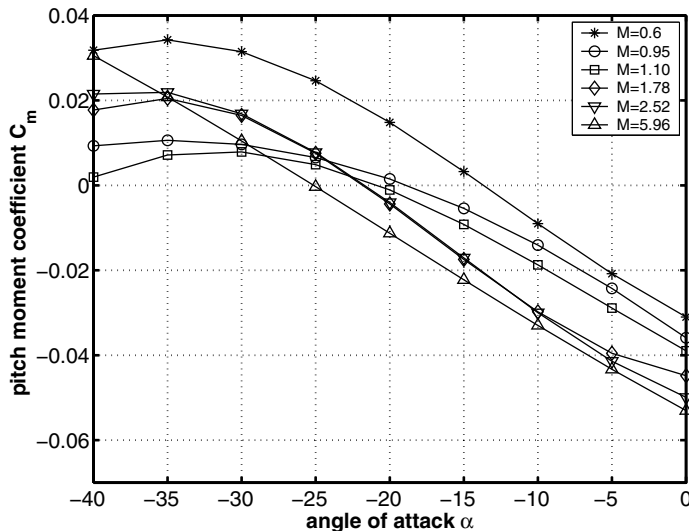


Fig. 4.17. Pitching moment coefficient C_m as function of the angle of attack α , [11]. Moment reference point: $x_{ref} = 0.37 D_1$, $z_{ref} = 0.039 D_1$.

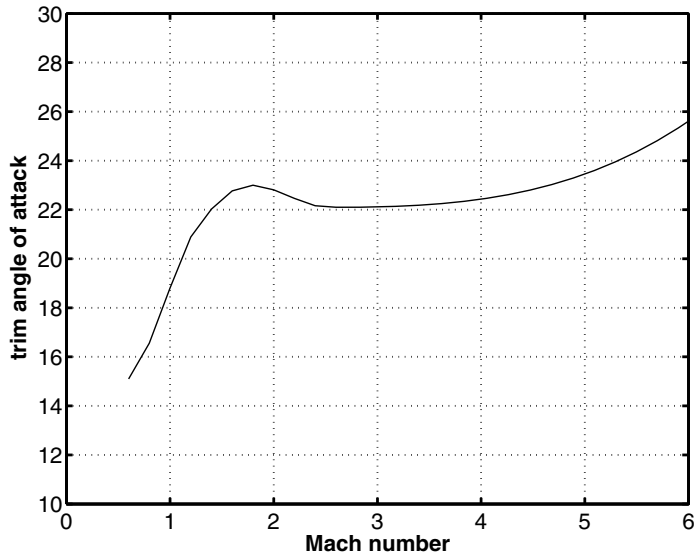


Fig. 4.18. Trim angle of attack α_{trim} as function of the freestream Mach number

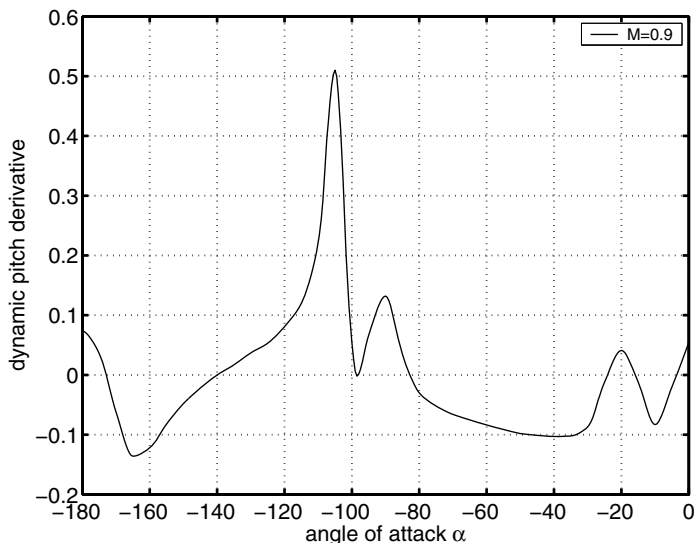


Fig. 4.19. Dynamic derivative of pitch motion $m_z^{\tilde{\omega}}$ as function of the angle of attack α for freestream Mach number $M_\infty = 0.9$, [11]

The SOYUZ capsule is an axisymmetric configuration. Because of that only the dynamic derivative of pitch motion is relevant.

4.3.4 Peculiarities

In the following we describe the determination of a trim line in the way mentioned in Section 4.1. For a given trajectory point the coordinates x_{cp}, z_{cp} can be computed from a numerical solution² of the governing equations by the set of equations, which describes the general formulation of the center of pressure and which can be found in [1]. Then trimmed flight for a prescribed trajectory point is feasible for all the center-of-gravity positions which meet eq. (4.3).

As an example we extract for hypersonic flight ($M_\infty = 5.96$) from Figs. 4.14 and 4.15 for $\alpha_{trim} = -25^\circ$ the axial and normal force coefficients $C_{X,trim} = 1.28$ and $C_{Z,trim} = 0.20$. Further we take over the center of pressure coordinates reported in [11], which are set to $x_{cp} = 0.60D_1$ and $z_{cp} = 0.0D_1$. For these values the evaluation of eq. (4.3) is plotted in Fig. 4.20.

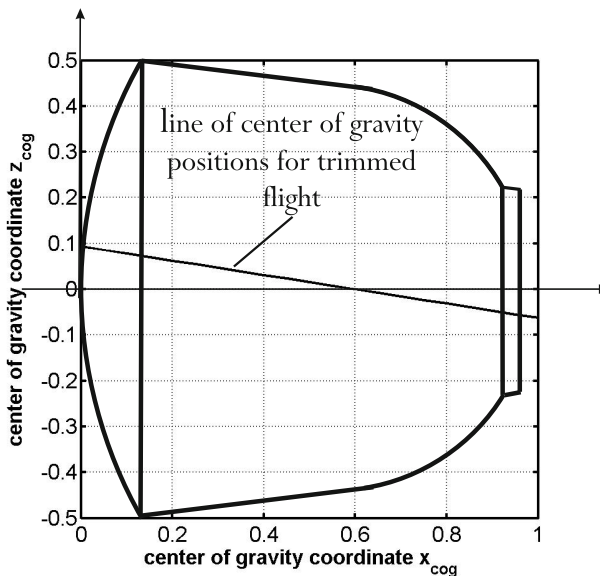


Fig. 4.20. Center-of-gravity locations for trimmed flight in the hypersonic Mach number regime. Data taken from Figs. 4.14 and 4.15 for $\alpha_{trim} = -25^\circ$ and $M_\infty = 5.96$.

² Of course, the center of pressure is also subject of measurements.

4.4 ARD (Aerodynamic Re-entry Demonstrator) (Europe)

After the cancellation of the European HERMES project³ in 1993 due to budget constraints and political uncertainties the European Space Agency ESA decided to develop a non-winged space vehicle in order to demonstrate European's capability for mastering the atmospheric re-entry process on the basis of the know-how gained by the intensive technological activities in the frame of the HERMES program. For supporting this objective further technological work was defined and conducted in the frame of ESA's MSTP⁴ program, which has accompanied the non-winged space vehicle project.

Due to the low budgeting a space vehicle was selected having the shape of a down-scaled APOLLO capsule, [12]. It was foreseen to bring this capsule into space on top of the ARIANE V launcher for performing a suborbital flight. A main topic for the subsequent re-entry mission was to measure and generate reliable aerothermodynamic and thermal flight data as much as possible for the validation and calibration of the theoretical and numerical design and prediction methods. Therefore this capsule got the name Atmospheric Re-entry Demonstrator ARD. The total mass of the ARD capsule has amounted to 2717 kg, [13]. Its one and only (successful) flight took place on October 21. 1998.

4.4.1 Configurational Aspects

Fig. 4.21 shows typical events and images of the ARD program. As already mentioned, due to a limited budget, the configuration of the ARD capsule was a down-scaled APOLLO shape (Fig. 4.22), where in the aft part some configurational differences are available (compare Fig. 4.3 with Fig. 4.23).

4.4.2 Aerodynamic Data of Steady Motion

One of the reasons for the selection of a APOLLO type shape for the ARD capsule was, that the aerodynamics are very similar in both cases. It can be expected that this is true at least for angles of attack $\alpha \gtrapprox -33^\circ$, because then the aft part of the capsule lies in the "hypersonic shadow" of the free-stream, see Section 4.2.

Therefore the basic aerodynamic data base is given by the diagrams Figs. 4.4 - 4.7. From the APOLLO project it was known that the trim angle of attack in hypersonic flow regime measured during flight was approximately 3° lower than the predicted one. During the technology work in the frame

³ The HERMES project was an European program for realizing Europe's autonomous access to space by a winged re-entry vehicle to be launched on top of the ARIANE V rocket, [14].

⁴ MSTP: Manned Space Transportation Programme.



Fig. 4.21. ARD: Capsule recovery after landing in the Pacific ocean on October 21, 1998 (left); the heatshield after flight (middle), [15]; skin friction lines of a numerical Navier-Stokes solution (right), [16].

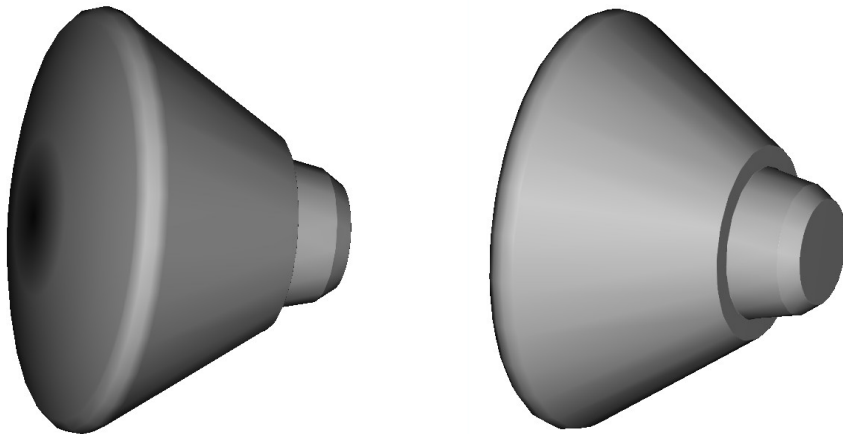


Fig. 4.22. 3D shape presentation of the ARD capsule

of the MSTP program it could be shown that this behavior was mainly due to real gas effects of the heated air streaming around the vehicle, [17]. This was proved by numerical solutions of the Euler and Navier-Stokes equations, which had included the physical description of the equilibrium as well as the non-equilibrium thermodynamics of real gases, and further by a limited number of investigations in the high-enthalpy facilities F4 of ONERA in France and HEG of DLR in Germany. With these results the APOLLO data base was updated, [12, 19].

Longitudinal Motion

In Fig. 4.24 we consider the pitching moment as function of the angle of attack for hypersonic Mach numbers, where the data of APOLLO for $M_\infty = 5$ and 10 are compared with values of the updated APOLLO data base (ARD data

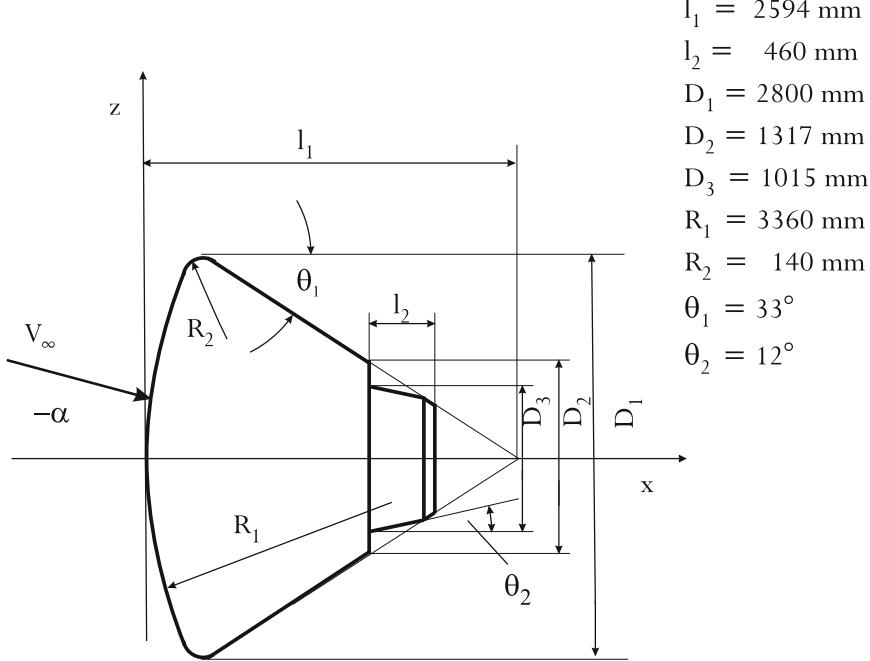


Fig. 4.23. Shape definition of the ARD capsule, [18, 19]

base) for $M_\infty = 10$ and 29 , [19]. Three of the curves give more or less the same trim angle, while for $M_\infty = 29$ the negative trim angle is somewhat lower. This reflects the cognition that with increasing hypersonic Mach number the negative trim angles decrease.

Free flight data measured along the re-entry trajectory, which are extracted from the diagrams reported in [12, 13] and [19], are plotted in Fig. 4.25. The diagram above shows the trim angle of attack α_{trim} , whereas the axial and normal force coefficients C_X and C_Z are drawn in the remaining diagrams. It is to be mentioned that the C_X and C_Z data points have as a parameter the trim angles given in the upper diagram. The general trend is that with increasing negative trim angle the force coefficients C_X and C_Z diminish which is in agreement with Figs. 4.4 and 4.5.

Lateral Motion

The ARD capsule is an axisymmetric configuration. Because of that no lateral aerodynamic characteristics exist.

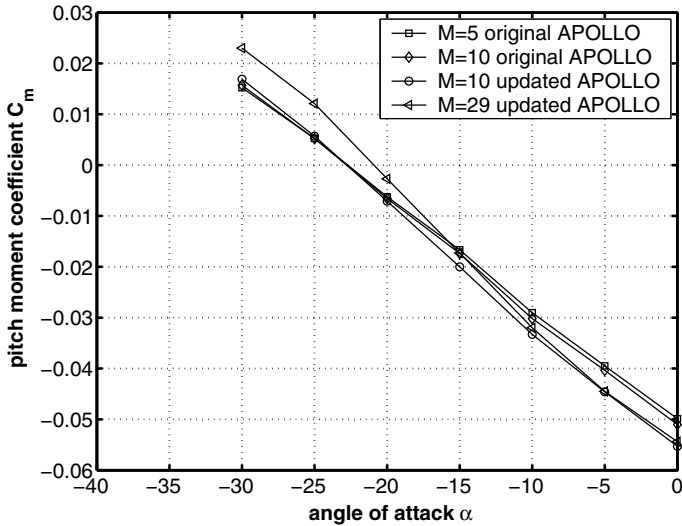


Fig. 4.24. Pitching moment of the original APOLLO data base for $M_\infty = 5$ and 10 compared with values of an updated APOLLO data base (ARD data base) for $M_\infty = 10$ and 29. Moment reference point: $x_{ref} = 0.26D_1$ and $z_{ref} = 0.0353D_1$.

4.4.3 Aerodynamic Data of Unsteady Motion

Pitch Motion

The dynamic pitch derivative $C_{mq} + C_{m\dot{\alpha}}$ as function of the Mach number and with α_{trim} as parameter is plotted in Fig. 4.26. This data is taken from [19]. It can be seen that just below $M_\infty = 1$ the vehicle becomes dynamically unstable ($C_{mq} + C_{m\dot{\alpha}} > 0$) and the degree of instability grows up to $M_\infty \approx 0.5$.

This behavior is somewhat in contradiction to the APOLLO data. Considering for example the $M_\infty = 0.8$ case, which has a trim angle of attack of $\alpha_{trim} \approx -15.5^\circ$ (Fig. 4.27(below)), we find from Fig. 4.26 $C_{mq} + C_{m\dot{\alpha}} \approx 0.2$ for the ARD capsule, which means that the vehicle is dynamically unstable, and from Fig. 4.9 $C_{mq} + C_{m\dot{\alpha}} \approx -0.7$ for APOLLO indicating strong dynamic stability. We have no explanation for that.

4.4.4 Peculiarities

As mentioned earlier the trim angles of attack measured during the re-entry flight are lower than the predicted ones. We demonstrate this in Fig. 4.27, where the ARD free flight data in the hypersonic flow regime are compared with the values of the updated APOLLO data base (diagram above), [13].

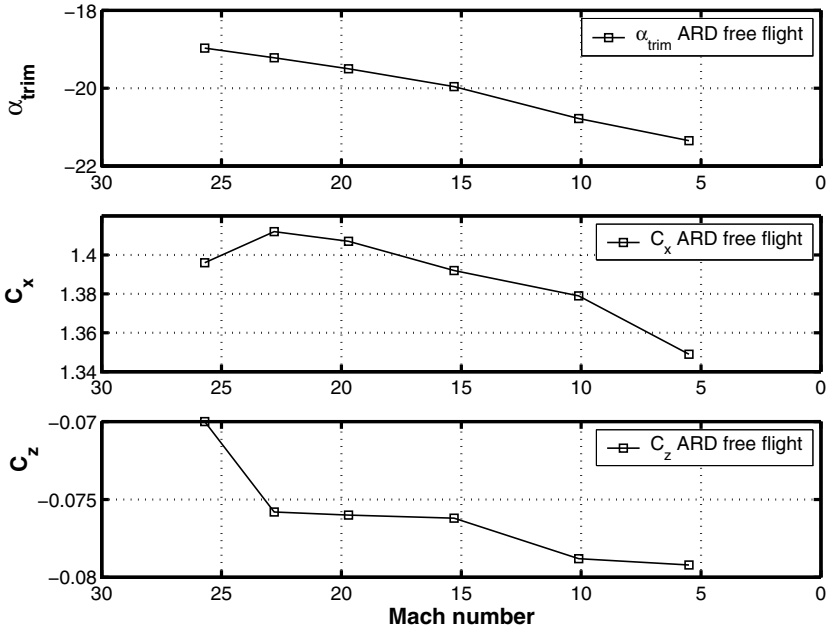


Fig. 4.25. ARD free flight data, [12, 13]. Trim angle of attack α_{trim} (above), axial force coefficient C_X (middle) and normal force coefficient C_Z (below) as function of the Mach number. Moment reference point: $x_{ref} = 0.26D_1$ and $z_{ref} = 0.0353D_1$. Note: The Mach number values on the abscissa decrease from left to right. This improves the understanding since the re-entry process starts at the highest Mach number.

As expected the free flight values are approximately 2° lower than the data of the updated APOLLO data base, which is definitely due to the influence of the real gas effects in the flow, [12, 17]. The diagram below presents the ARD free flight trim angles of attack including super- and subsonic values. A maximum of the negative trim angles is reached in low supersonic flow.

On the basis of the ARD free-stream trim angles plotted in Fig. 4.27 the aerodynamic force coefficients C_X and C_Z of the ARD measurements are compared with the C_X and C_Z values of the original APOLLO data⁵, taken from Figs. 4.4 and 4.5.

The ARD free flight data of the axial force coefficient C_X are higher than the values of the original APOLLO data base, Fig. 4.28 (above), which is a clear indication for the influence of the real gas effects. In order to corroborate this hypothesis more than 120 numerical solutions of Euler and Navier-Stokes

⁵ The angle of attack interpolation is carried out for the $M_\infty = 10$ curve. This can be partly justified by the Mach number independence principle of aerodynamic variables in hypersonic flow (see [1]).

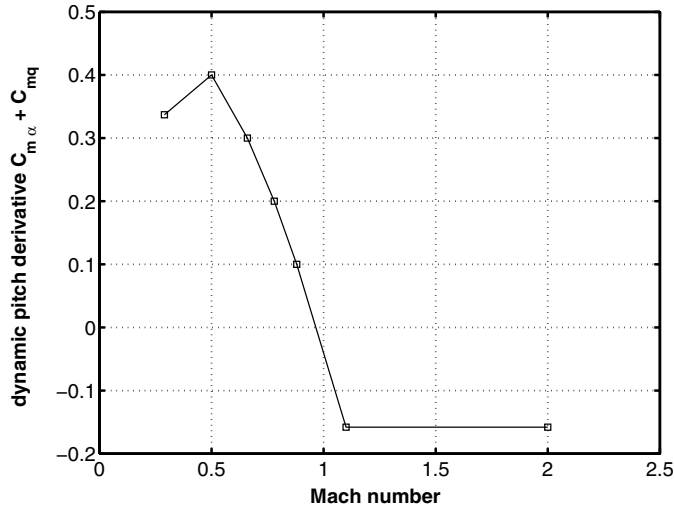


Fig. 4.26. Dynamic pitch derivative $C_{mq} + C_{m\alpha}$ as function of the Mach number and with α_{trim} as parameter. Moment reference point: $x_{ref} = 0.26D_1$ and $z_{ref} = 0.0353D_1$.

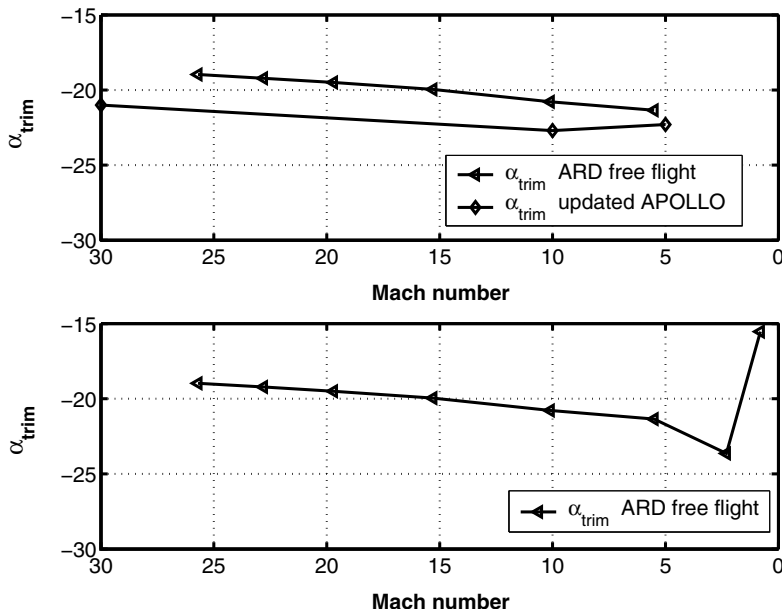


Fig. 4.27. ARD free flight trim angle of attack, [13]. Comparison with updated APOLLO data in the hypersonic regime (above). Total Mach number regime of data (below). Moment reference point: $x_{ref} = 0.26D_1$ and $z_{ref} = 0.0353D_1$.

equations with perfect gas, equilibrium and non-equilibrium real gas thermodynamics were conducted in the frame of the MSTP program as well as the ARD postflight analysis activities. As is exhibited in Fig. 4.29 the C_X values based on the numerical solutions with real gas thermodynamics, either equilibrium or non-equilibrium, correlate much better with the free flight data than the perfect gas solutions do, [17, 20]. The normal force coefficients C_Z (ARD free flight) are lower (negative values!) than the original APOLLO data, Fig. 4.28 (below), where in that case the correlation with the hot gas physics is not so unambiguous.

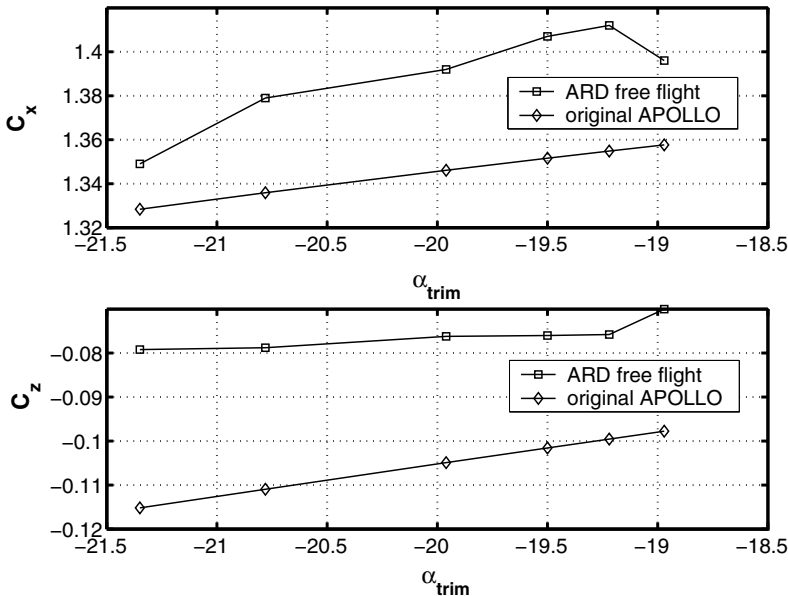


Fig. 4.28. ARD free flight aerodynamic force coefficients. Comparison with the original APOLLO data, taken from Figs. 4.4 and 4.5.

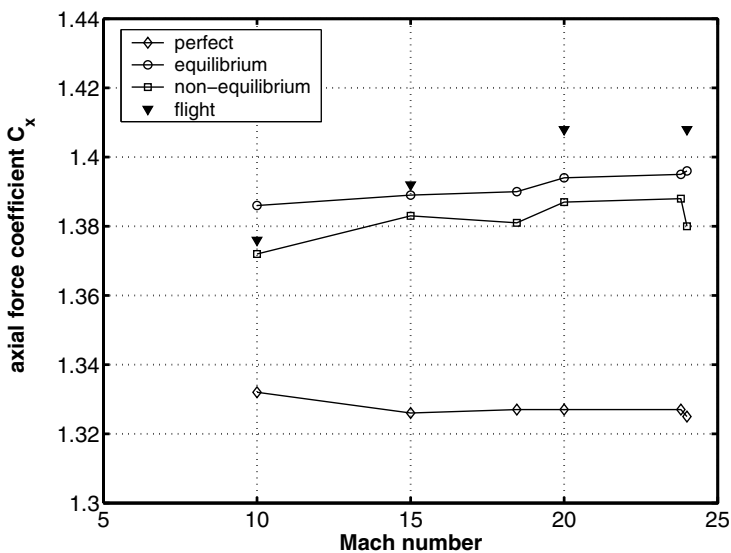


Fig. 4.29. Influence of real gas effects in hypersonic flow on the axial force coefficient C_x . Comparison of ARD free flight data with numerical solutions of Euler and Navier-Stokes equations with hot gas thermodynamics, [17, 20].

4.5 HUYGENS (Cassini Orbiter) (Europe)

There was the joint European - U.S. (ESA / NASA) enterprise for a space flight to the planet Saturn with the spacecraft “Mariner-Mark II Cassini Saturn Orbiter”. This space vehicle consisted of the two elements:

- The Cassini laboratory for the investigation of the features of the planet Saturn including its rings,
- the HUYGENS probe as a passenger experiment of the Cassini Orbiter, see Fig. 4.30, with the mission to investigate the composition of the atmosphere of the largest Saturn moon Titan including the landing on its surface, [21, 22].

The Cassini Saturn Orbiter was launched in Oct. 1997. After a 6.7 year flight using the technique of gravity assist⁶ the orbiter arrived at Saturn in July 2004. The passenger device HUYGENS was released from the Cassini Orbiter on 25. Dec. 2004. On 14. Jan. 2005 HUYGENS had conducted successfully a parachute supported landing on the surface of Saturn's moon Titan, Fig. 4.31.

One of the purposes of the HUYGENS Titan mission was to increase the knowledge about the composition of Titan's atmosphere. Before the launch of the Cassini Orbiter in 1997 it was assumed that the Titan atmosphere consists of Ar , CH_4 and N_2 , where the related mole fractions depend on the altitude in this atmosphere. Yelle, [23], supposed a nominal atmosphere of 2% Ar , 3% CH_4 and 95% N_2 .

Today, we know that in the stratosphere of Titan the composition of the atmosphere consists of $Ar \approx 0\%$, $CH_4 \approx 1.4\%$ and $N_2 \approx 98.4\%$, which changes with decreasing altitude, for example for 32 km, to $Ar \approx 0\%$, $CH_4 \approx 4.9\%$ and $N_2 \approx 95.0\%$, [24].

4.5.1 Configurational Aspects

The HUYGENS probe consists of a blunted cone with a semi-apertural angle of 60° and a nose radius of 1.25 m. The base diameter is 2.7 m. All geometric data are given in Fig. 4.32. Fig. 4.33 shows 3-dimensional views of the configuration.

4.5.2 Aerodynamic Data of Steady Motion

The HUYGENS probe was designed to conduct a ballistic entry into Titan's atmosphere. For such kinds of entry the ballistic factor

⁶ Gravity assist means to fly along trajectories, which “fly by” on several planets in order to get enough orbital energy, due to the related gravity of the planets, for the travel into the deep space. In the case of the Saturn mission the Cassini Orbiter has passed two times the planet Venus, once the Earth and once the planet Jupiter.

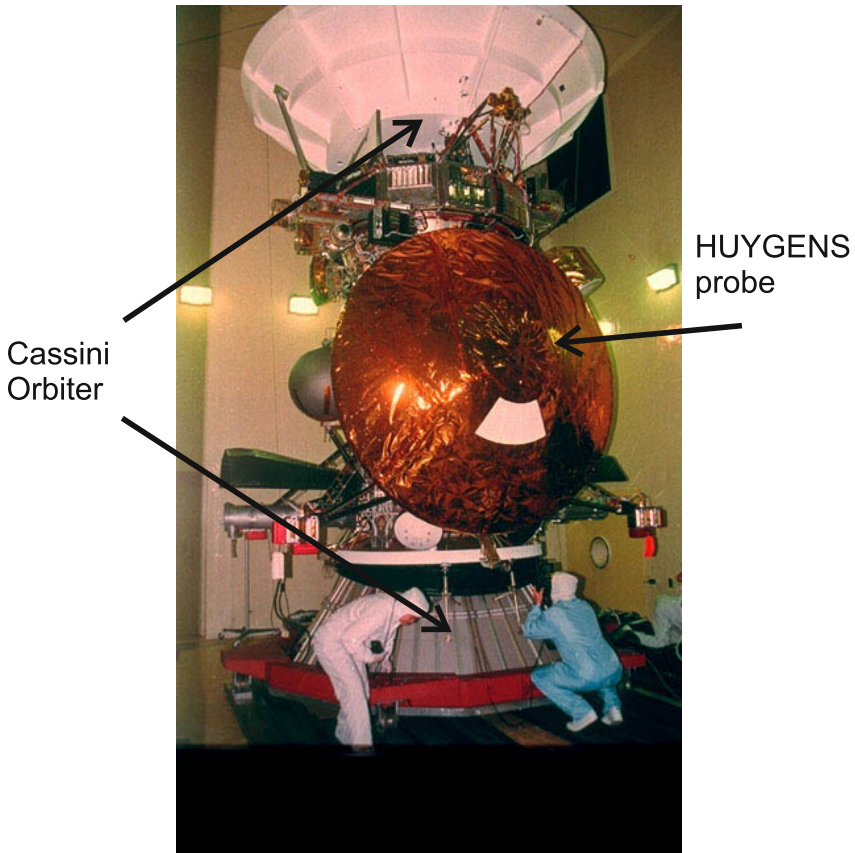


Fig. 4.30. HUYGENS probe as a passenger of the Cassini Orbiter, [24]

$$\beta_m = \frac{m}{S_{ref} C_D}$$

plays a particular role, where m is the vehicle mass, S_{ref} the reference area and C_D the drag, [1]. The ballistic factor is a measure for the manner how probes perform a ballistic entry with a specified landing distortion. Ballistic probes have the advantage that they do not require guidance and control means, in contrary to lifting capsules or probes. Therefore these concepts are less costly than the lifting ones, but they need low ballistic factors.

To ensure a stable ballistic flight and to master the thermal loads during entry in a not well-known atmosphere was the aerothermodynamic challenge of this mission. A proper ballistic entry can be achieved for probes with a ballistic factor $\beta_m \approx 30$, [1, 22]. HUYGENS possess a mass of $m_{HUYGENS} = 318.62$ kg, a reference area of $S_{ref} = 5.725$ m² and it can be assumed that the



Fig. 4.31. HUYGENS probe in the integration hall (left), artist view of the HUYGENS probe during entry in Titan's atmosphere (right), [24]

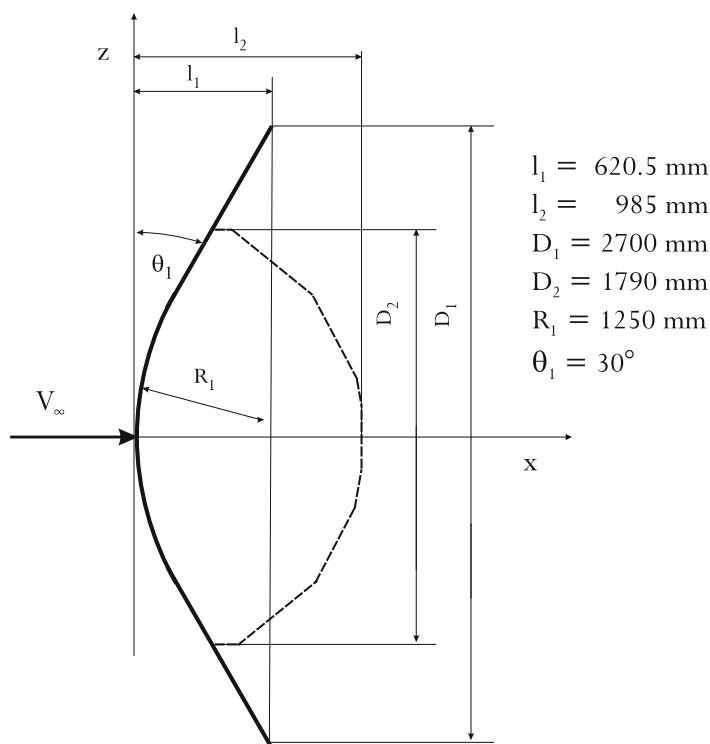


Fig. 4.32. Shape definition of the HUYGENS probe, [21, 22]

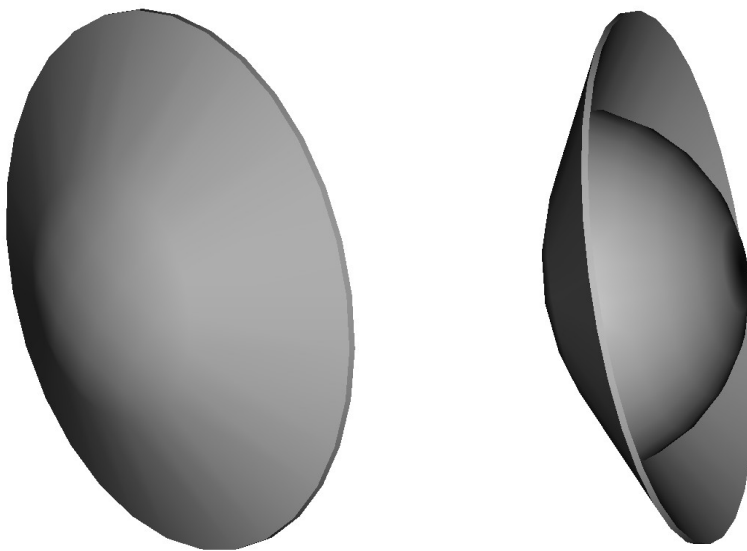


Fig. 4.33. 3D shape presentation of the HUYGENS probe

drag coefficient for high Mach numbers lies approximately between $1.45 \leq C_D \leq 1.50$, which was estimated from the data of BEAGLE2, Section 4.6, and OREX, Section 4.7. In conclusion the ballistic factor of the HUYGENS probe ranges between $39, 38 \geq \beta_m \geq 37.10$, which seems to be an appropriate value.

Longitudinal Motion

The author had no access to the static stability data.

Lateral Motion

The HUYGENS probe is an axisymmetric configuration. Because of that no lateral aerodynamic characteristics exist.

4.5.3 Aerodynamic Data of Unsteady Motion

The author had no access to the dynamic stability data.

4.6 BEAGLE2 (UK)

On June 2, 2003 a space probe called Mars Express was launched on top of a Russian SOYUZ Fregat rocket to fly to the planet Mars. The probe carried besides others a small Mars lander called BEAGLE2. The mission of BEAGLE2 was firstly to perform an autonomous entry into the Mars atmosphere with a subsequent uncontrolled (un-propelled) landing, and secondly to conduct on the Martian surface a couple of scientific experiments. BEAGLE2 was designed, developed and built by a consortium of British Universities and an industrial company. The landing process of BEAGLE2 on the Martian surface was foreseen for December 24, 2003. Unfortunately the landing failed and the lander was lost.

Nevertheless there exists a rough aerodynamic data set which was based on numerical flow field computations for 37 trajectory points (partly considering the particular properties of Mars' CO_2 atmosphere) and on the evaluations and scalings including interpolations and extrapolations of the aerodynamic data of corresponding other probes like HUYGENS and STARDUST, [25, 26].

In Fig. 4.34 some examples of the numerical and experimental data for establishing the aerodynamic data set are displayed.

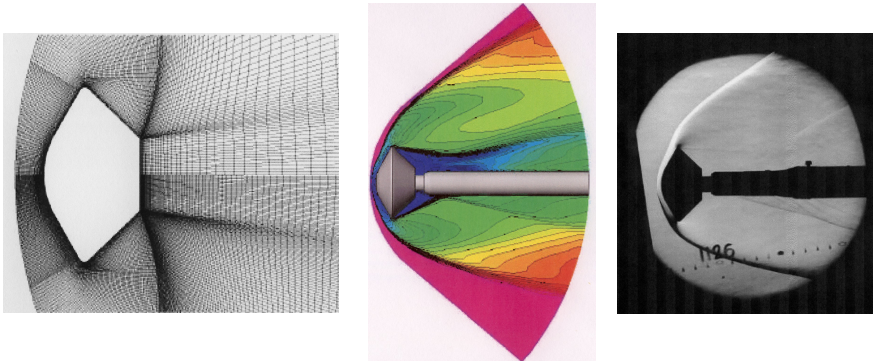


Fig. 4.34. BEAGLE2 shape: grid for the numerical flow field computation with $M_\infty = 3$, $\alpha = 0^\circ$ (left), Mach number contours in the plane of symmetry for a flow field computation with $M_\infty = 6$, $\alpha = 8^\circ$ (middle), Schlieren photograph performed in the Oxford University gun tunnel with the same flow conditions as in the numerical solution (right), [25, 27].

4.6.1 Configurational Aspects

The front part of BEAGLE2 consists of a cone with a semi-apertural angle of 60° , which is blunted by a sphere. The aft part of the configuration is

composed of a truncated cone conversely matched to the front part. The semi-apertural angle of this cone amounts to 46.25° , Figs. 4.35 and 4.36. The front part of BEAGLE2 has some similarities with the HUYGENS (see section 4.5) and the STARDUST shapes. This was the reason why the BEAGLE2 developing team had performed the establishment of the aerodynamic data base partly by a scaling procedure applied to the aerodynamic data sets of these configurations.

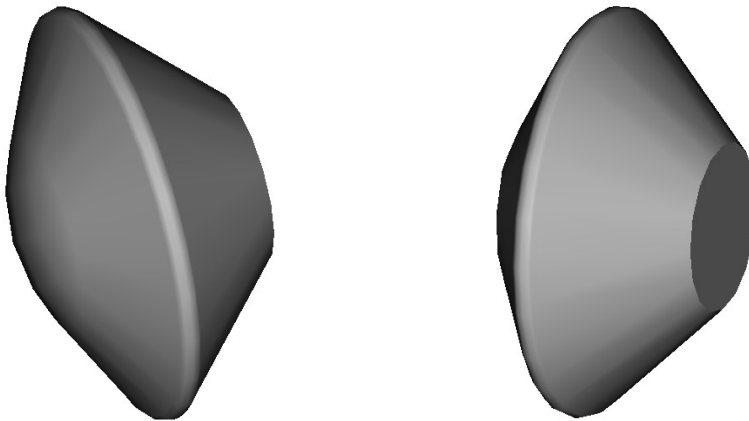


Fig. 4.35. 3D shape presentation of the BEAGLE2 probe

4.6.2 Aerodynamic Data of Steady Motion

The aerodynamic data presented in the following four diagrams come exclusively from [25]. The axial force coefficient C_X is given for $2.5 \leq M_\infty \leq 15$. The angle of attack regime is mainly $-5^\circ \leq \alpha \leq 0^\circ$ except for $M_\infty = 15$ ($-12^\circ \leq \alpha \leq 0^\circ$), Fig. 4.37. There are two Mach numbers ($M_\infty = 6$ and 15) for which the normal force coefficient C_Z is given for angles of attack up to -30° . For all the other Mach numbers just one point ($\alpha = -5^\circ$) of C_Z is available, Fig. 4.38. Since the data for C_X and C_Z are so heterogeneous one can only find few points where the lift-to-drag ratio can be determined, Fig. 4.39. The pitching moment is known for $M_\infty = 15$ in the angle of attack regime $-30^\circ \leq \alpha \leq 0^\circ$, while for all other Mach numbers $M_\infty = 2.5, 5, 7.0$ values are only given for $-5^\circ \leq \alpha \leq 0^\circ$, Fig. 4.40.

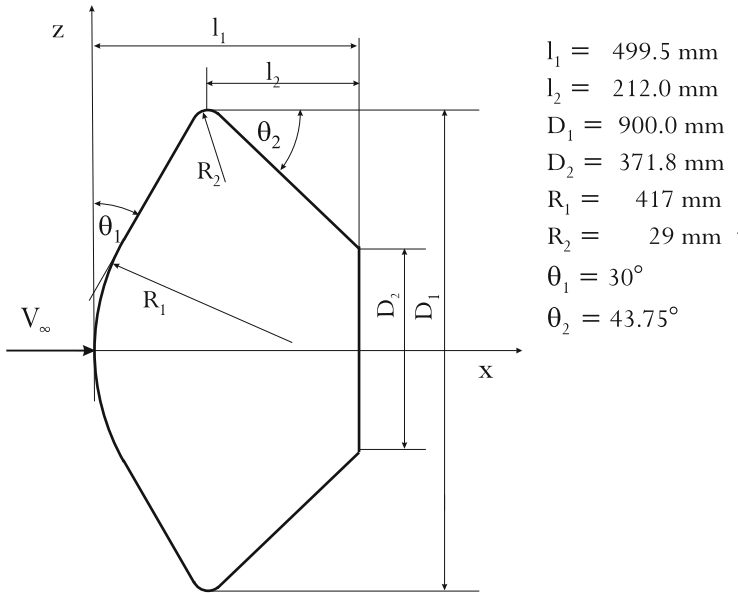


Fig. 4.36. Shape definition of the BEAGLE2 probe, [25, 27]

Longitudinal Motion

One can generally state that the characteristics of the aerodynamic coefficients of the BEAGLE2 probe are similar to most of the other capsules presented in this chapter, like the VIKING type, APOLLO, SOYUZ, HUYGENS or STARDUST configurations. The lift-to-drag ratio seems to be slightly lower compared to other capsules or probes and it is doubtful if L/D reaches 0.3 in hypersonic flight regime for $\alpha = -30^\circ$, Fig. 4.39. Finally, the pitching moment coefficient diagram demonstrates that with $\partial C_m / \partial \alpha < 0$ the shape behaves statically stable despite the fact that the moment reference point is positioned in the nose. The experience from the VIKING2 shape was that through two shifts of the moment reference point (center-of-gravity) along the positive x-axis and the negative z-axis (see Figs. 8.1, 8.2), the configuration can be made trimmable, whereas static stability is retained (compare with Figs. 4.56 - 4.59).

Lateral Motion

The BEAGLE2 probe is an axisymmetric configuration. Because of that no lateral aerodynamic characteristics exist.

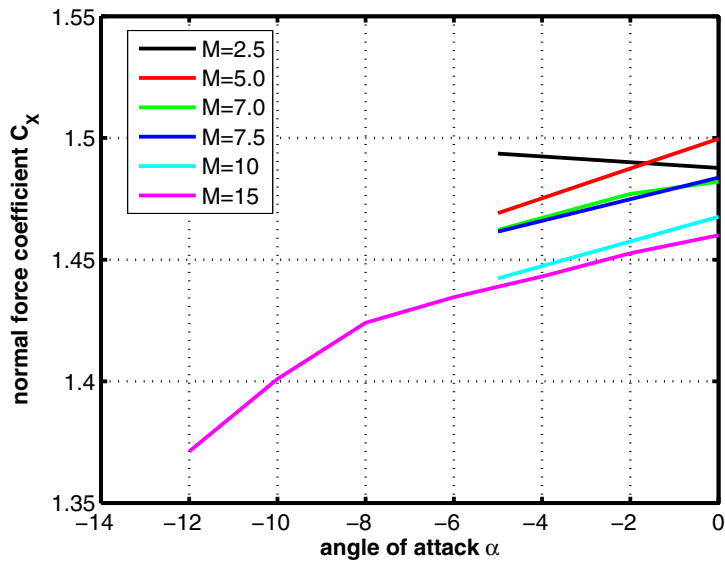


Fig. 4.37. Axial force coefficient C_x as function of the angle of attack α , [25]

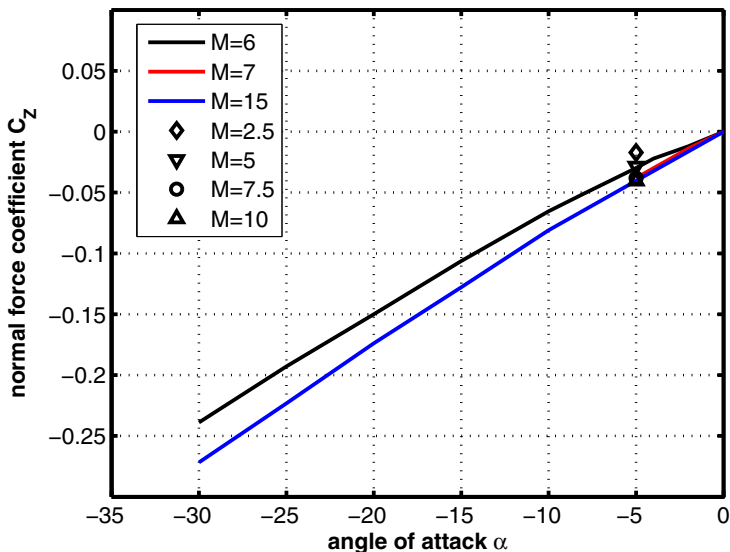


Fig. 4.38. Normal force coefficient C_z as function of the angle of attack α , [25]

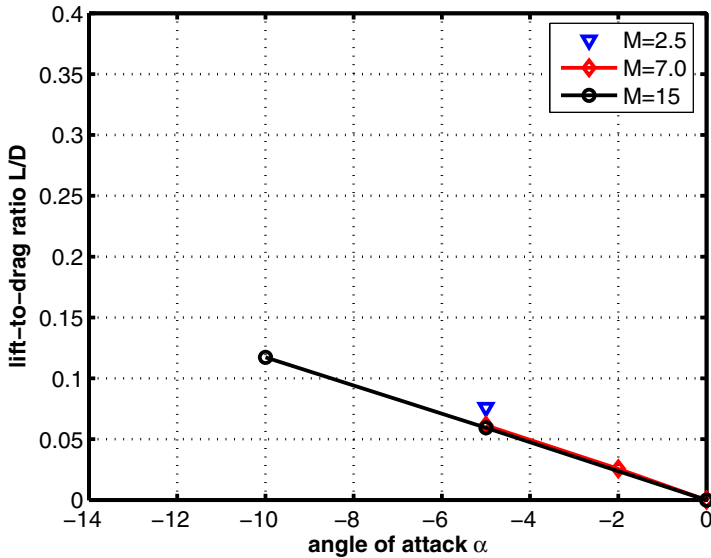


Fig. 4.39. Lift-to-drag ratio L/D as function of the angle of attack α , [25]

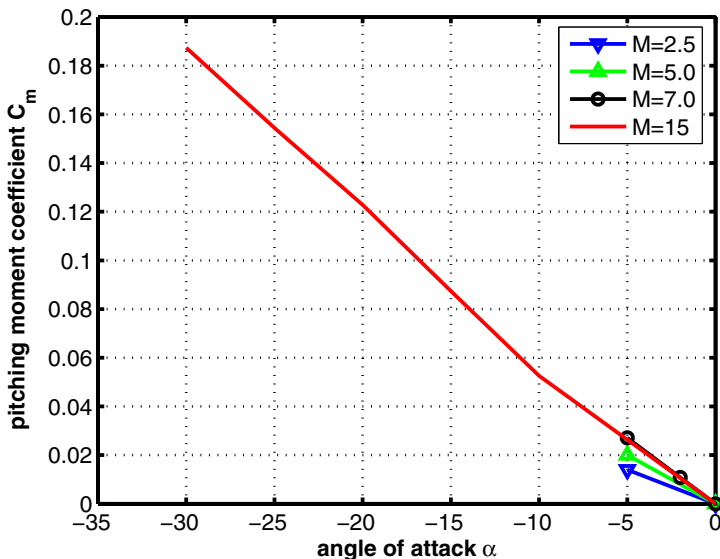


Fig. 4.40. Pitching moment coefficient C_m as function of the angle of attack α , [25]. Moment reference point $x_{ref} = 0.$, $z_{ref} = 0.$

4.6.3 Aerodynamic Data of Unsteady Motion

Dynamic stability data is not available.

4.7 OREX (Japan)

In the second half of the 1980s Japan's government decided to start a program with the intention to allow for an autonomous access to space, as this was already the case in Europe at that time. The main objective of this program was to develop an unmanned winged space vehicle to be launched on top of Japan's H-II rocket. This space vehicle got the name HOPE (H-II Orbiting Plane). In this environment Japan planned the development of some demonstrators with which an analysis of specific parts of flight phases and impacts during the flight along re-entry trajectories could be conducted.

The first demonstrator was the Orbital Re-entry Experiment (OREX), which was a probe flying, after having performed a complete orbit, along a ballistic re-entry path. The purpose of this flight was to provide aerothermal data (wall temperatures and heat transfer rates) for the design of the thermal protection system (TPS) of HOPE, [28].

With the second test vehicle, called ALFLEX (Automatic Landing Flight Experiment), the automatic landing process of HOPE was simulated in particular the guidance, navigation and control system in connection with the identification of the subsonic aerodynamics. The shape of ALFLEX was a down-scaled HOPE vehicle. In July and August 1996 a couple of drop tests were conducted in Woomera, Australia. Thereby ALFLEX was lifted by a helicopter to an altitude of approximately 1500 m and then released.

A third demonstrator vehicle was designed and manufactured with the objective to test the hypersonic flight phase of HOPE. The name of this vehicle was HYFLEX (Hypersonic Flight Experiment). HYFLEX consisted of a slender lifting body shape with two laterally mounted winglets for flight control. This vehicle has performed a suborbital flight with a maximum altitude of 110 km. The objective of this flight was the demonstration of the cross-range capability in the hypersonic flight phase, the delivery of hypersonic aerodynamic data and the examination of guidance and control technologies for the operation along ambitious flight trajectories. HYFLEX has carried out one successful flight in Feb. 1996, but it could not be rescued after its splash into the Pacific Ocean.

In Feb. 1994 OREX was successfully launched on top of a H-II rocket. After performing a complete orbit cycle the re-entry process was initiated by a deorbiting boost of a propulsion system. Fig. 4.41 shows the original OREX probe in an assembly hall (left), an artist' view of the hypersonic flight through Earth' atmosphere (middle) and an engineering drawing presenting some details of the back cover (right).

4.7.1 Configurational Aspects

OREX consisted of a cone with a semi-apertural angle of 50°, which is blunted by a sphere segment with a radius of 1350 mm. The diameter of OREX amounts to 3400 mm. An illustrating three-dimensional presentation



Fig. 4.41. OREX probe: vehicle in the assembly hall (left), synthetic image of the vehicle during re-entry (middle), engineering drawing with some constructional details on the back cover (right), [29]

of OREX is given in Fig. 4.42. Fig. 4.43 exhibits an engineering drawing including measures, [30, 31].

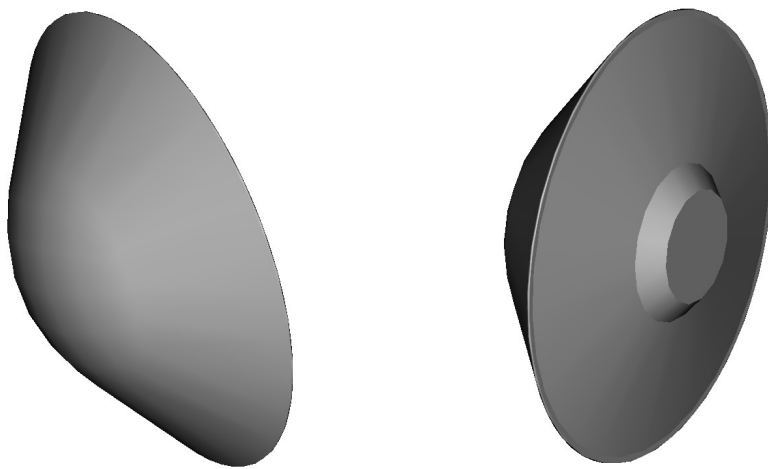


Fig. 4.42. 3D shape presentation of the OREX probe

4.7.2 Aerodynamic Data of Steady Motion

As already mentioned OREX' mission was to measure the temperatures and the heat fluxes in the heat shield area during the most loaded part of the

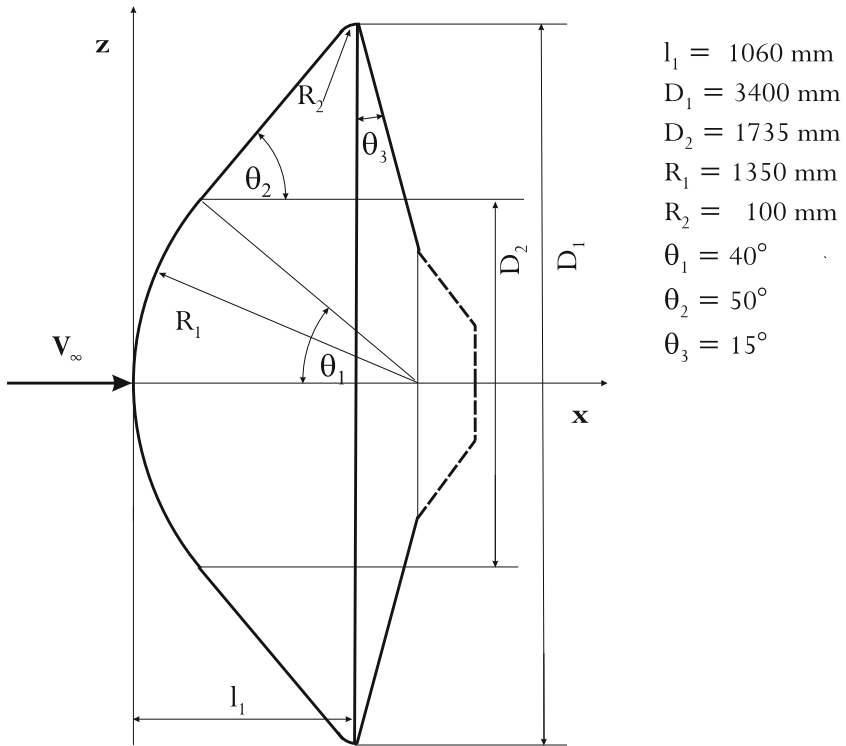


Fig. 4.43. Engineering drawing defining the shape of the OREX probe, [30, 31]

re-entry phase. An evaluation of these measurements and comparison with the results of numerical simulations can be found in [1, 30, 32].

Longitudinal Motion

Since OREX has performed a ballistic flight, this means flight without lift, the flight trajectory is determined only by the aerodynamic drag. The drag data available come from numerical investigations of various probe shapes, where also the OREX configuration was considered, [28]⁷. We present these drag data as function of the Mach number in Fig. 4.44.

⁷ The values of the drag of OREX presented in [28] are relatively high and are denoted as fore-body drag. Unfortunately it is not quite clear, if the base drag is included or not in the given values, because it seems that the drag values of the other shapes (APOLLO, ARD, BEAGLE2, etc.) to which [28] refers, obviously are total drags.

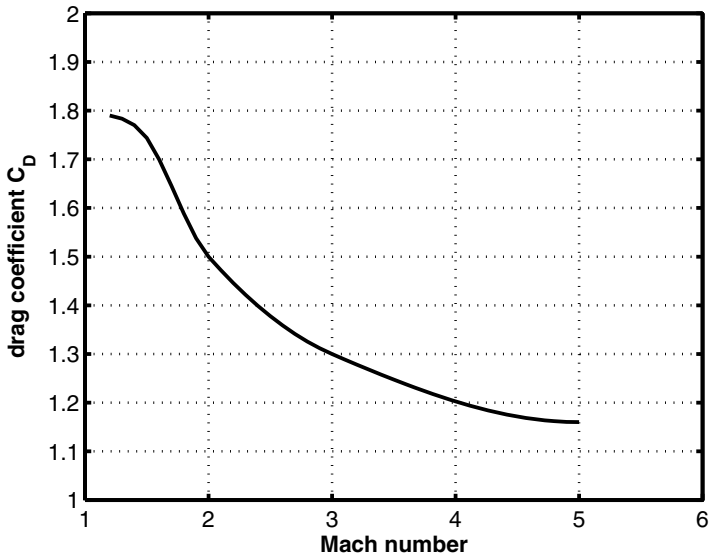


Fig. 4.44. Drag coefficient C_D as function of the free-stream Mach number M_∞ , [33]

Lateral Motion

The OREX probe is an axisymmetric configuration which performs essentially a ballistic flight. This means that it is not envisaged that the flight is assisted by lift. Therefore the mission trajectory embodies no banking and influences through side forces are not expected. Because of that no lateral aerodynamic characteristics exist.

4.7.3 Aerodynamic Data of Unsteady Motion

Dynamic stability data are not available.

4.8 VIKING-Type (Europe)

One part of Europe's activities for an autonomous access to space was the development of the winged re-entry vehicle HERMES (see Chapter 6, Section 6.11). In the beginning of the 1990s Europe's space authority ESA had been aware that due to technical and budgetary reasons a realization of the HERMES project could no longer be pursued. Therefore the project was cancelled. Since the goal of an autonomous access to space at that time was still existing, also in conjunction with Europe's contribution to servicing the International Space Station ISS, a new program⁸ was launched, where a cheaper and technically more reliable solution was aimed for.

In this environment a capsule solution was favored. Therefore the aerospace companies Aerospatiale in France and Dasa in Germany started in 1995 in the frame of some phase A studies, initiated by ESA, investigations of capsule configurations of VIKING-type. VIKING-type shapes are characterized by very blunt front cones (semi-apertural angles θ_1 of approximately 80°) and aft cones with different semi-apertural angles θ_2 . The shape of the front part is in contrast to the well known capsules APOLLO and SOYUZ, which hold spherical caps.

Under the acronym CRV/CTV⁹ Dasa investigated¹⁰ the aerodynamics of VIKING-type shapes with $\theta_2 = 14^\circ, 16^\circ, 18^\circ, 20^\circ, 23^\circ, 25^\circ, 27^\circ$, [34, 35, 36]. Aerospatiale has conducted intensive work on the VIKING-type shape with $\theta_2 = 20^\circ$, [37]. In the course of the investigations the VIKING-type shape with $\theta_2 = 25^\circ$ was called VIKING1 and with $\theta_2 = 20^\circ$ VIKING2.

Besides wind tunnel tests, a great part of the investigations was carried out by numerical simulations. The Figs. 4.45, 4.46, 4.47 exhibit for various trajectory points some evaluations of these computations.

4.8.1 Configurational Aspects

The VIKING-type shape consists of a cone with a semi-apertural angle $\theta_1 = 80^\circ$, which is blunted at the apex by a small sphere segment, followed by a torus segment with a sphere radius of $0.02D_1$ and a reversed aft part cone with various semi-apertural angles θ_2 . In Fig. 4.48 a 3D presentation of the VIKING1 shape is shown. The detailed measures of the VIKING1 and the VIKING2 shapes are given in Fig. 4.49.

⁸ MSTP: Manned Space Transportation Programme.

⁹ CRV: Crew Rescue Vehicle, CTV: Crew Transport Vehicle.

¹⁰ Partly together with the National Aerospace Laboratory NLR of The Netherlands.

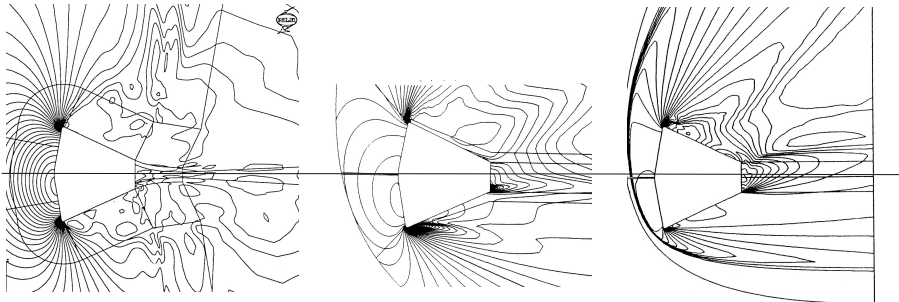


Fig. 4.45. Numerical solutions of flow past the VIKING1 shape. $M_\infty = 0.9$, $\alpha = -10^\circ$ Navier-Stokes solution, [35, 36] (left), $M_\infty = 1.5$, $\alpha = -20^\circ$ Euler solution, [38, 39] (middle), $M_\infty = 3$, $\alpha = -25^\circ$ Navier-Stokes solution, [35, 40] (right). Shown are pressure contours $\log(p/p_\infty)$.

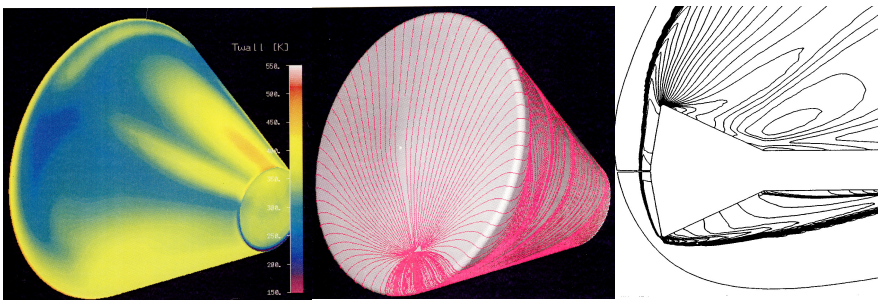


Fig. 4.46. Numerical solutions past the VIKING1 shape. $M_\infty = 3$, $\alpha = -25^\circ$, Navier-Stokes solution, wall temperature rear view (left) and skin friction lines front view (middle), $M_\infty = 18.5$, $\alpha = -25^\circ$ Navier-Stokes solution for the VIKING1 shape with the wind tunnel sting ($\log(p/p_\infty)$), (right), [35].

4.8.2 Aerodynamic Data of Steady Motion

The VIKING2 shape was investigated in the Mach number regime $0.45 \leq M_\infty \leq 3.95$ in the S1 wind tunnel of the von Kármán institute (VKI) in Brussels, Belgium, and the HST and SST wind tunnels of the National Aerospace Laboratory NLR in Amsterdam, The Netherlands. The aerodynamic data for the hypersonic Mach numbers were generated by numerical simulations solving the Euler equations and in one case also the Navier-Stokes equations, [37].

The aerodynamic data base established for the VIKING1 shape was created by approximate design procedures like local inclination methods (e.g., a modified Newton method, [8]) for the supersonic-hypersonic regime, panel methods for the subsonic regime, and numerical simulations on the basis

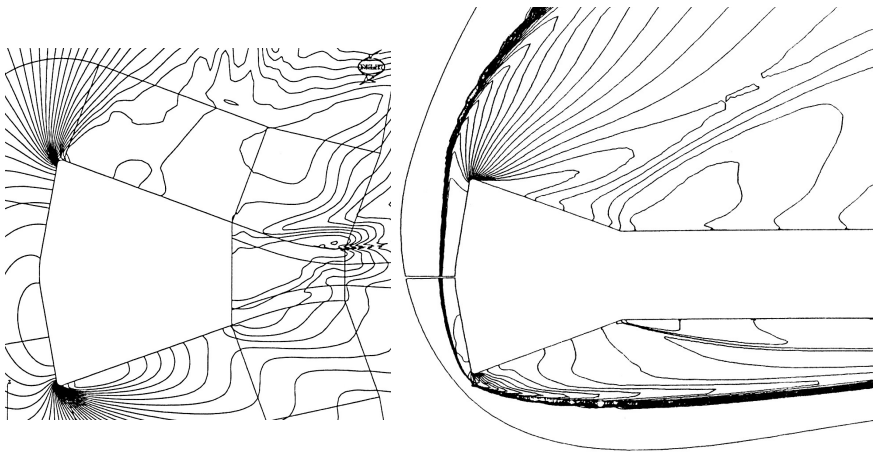


Fig. 4.47. Numerical solutions past the VIKING2 shape. Navier-Stokes solutions. $M_\infty = 1.15$, $\alpha = -20^\circ$ (left), [35, 36], $M_\infty = 19.5$, $\alpha = -17.3^\circ$, shape with the wind tunnel sting (right), [35, 40]. Shown are pressure contours $\log(p/p_\infty)$.

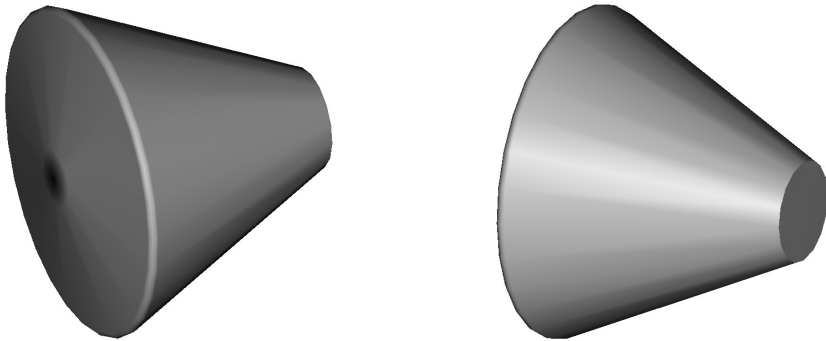


Fig. 4.48. 3D shape presentation of the VIKING1 capsule

of the full Navier-Stokes equations. These numerical simulations have covered the Mach numbers $0.5 \leq M_\infty \leq 2$, [36] , and the Mach numbers $3.0 \leq M_\infty \leq 19.5$, [35].

In the following ten figures (Figs. 4.50 - 4.59) we present the aerodynamic coefficients of the longitudinal motion of the VIKING2 shape. The aerodynamic coefficients, in the angle of attack regime considered here ($-30^\circ \leq \alpha \leq 0^\circ$), are not very much affected by the aft cone angle θ_2 . In

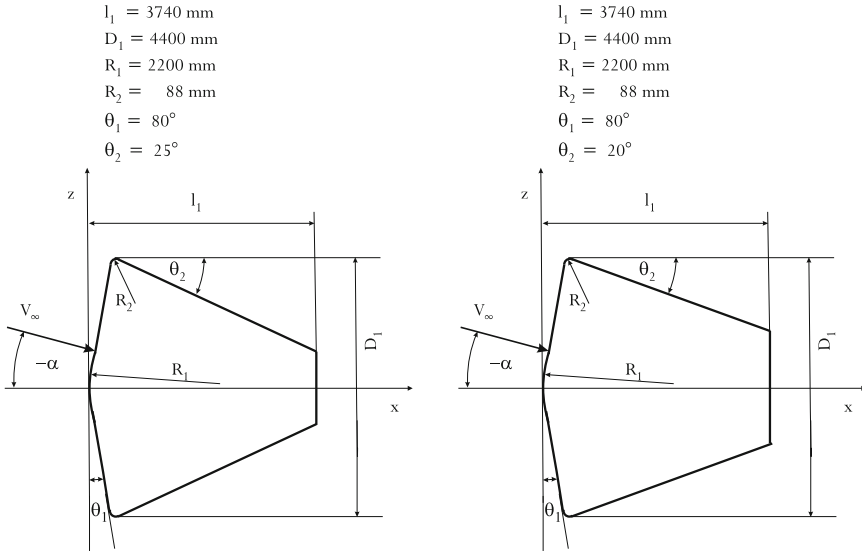


Fig. 4.49. Shape definitions of VIKING1 (left) and VIKING2 (right), [35]

order to quantify the influence of θ_2 on the aerodynamic coefficients we have plotted for some discrete trajectory points these coefficients for the VIKING1 shape within the diagrams of the VIKING2 results (Figs. 4.63 - 4.66).

Longitudinal Motion

The axial force coefficient C_X for the subsonic-transonic and supersonic-hypersonic Mach number regimes is plotted in Figs. 4.50, 4.51. The general tendency of C_X for subsonic-transonic Mach numbers consists in a slight increase of the C_X values with increasing negative angles of attack (local maxima exist around $\alpha \approx -10^\circ$) and an abatement afterwards. For supersonic-hypersonic Mach numbers C_X is highest for $\alpha = 0^\circ$ and decreases then monotonically for growing negative α 's¹¹. The above description of the C_X behavior seems to be characteristic for capsules as can be seen by comparison with the APOLLO data, see Section 4.2.

It is physically obvious that the normal force coefficient C_Z must be zero for $\alpha = 0^\circ$ and negative for larger negative angles of attack α ($\alpha < 0^\circ$), in particular for $\alpha \approx -90^\circ$. But depending on the Mach number C_Z evolves at first positive ($0.45 \leq M_\infty \leq 1.47$) with decreasing α and becomes negative at the latest for $\alpha \lesssim -30^\circ$, Figs. 4.52, 4.53. For higher Mach numbers ($M_\infty \geq 1.5$) C_Z develops always negative.

¹¹ The course of the $M_\infty = 1.47$ curve is untypical and can not be explained physically.

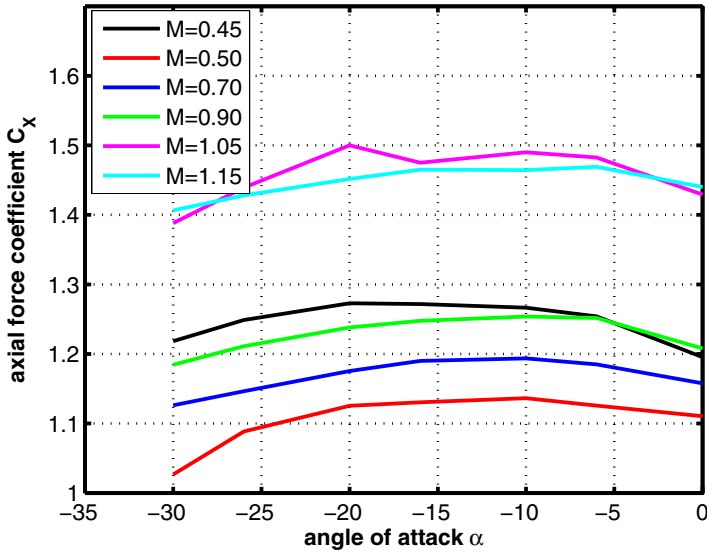


Fig. 4.50. Axial force coefficient C_x as function of the angle of attack α for subsonic-transonic Mach numbers, [37]

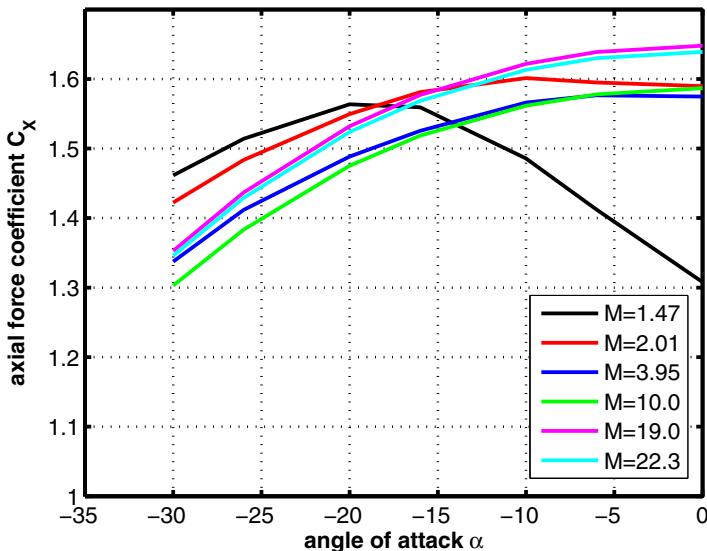


Fig. 4.51. Axial force coefficient C_x as function of the angle of attack α for supersonic-hypersonic Mach numbers, [37]

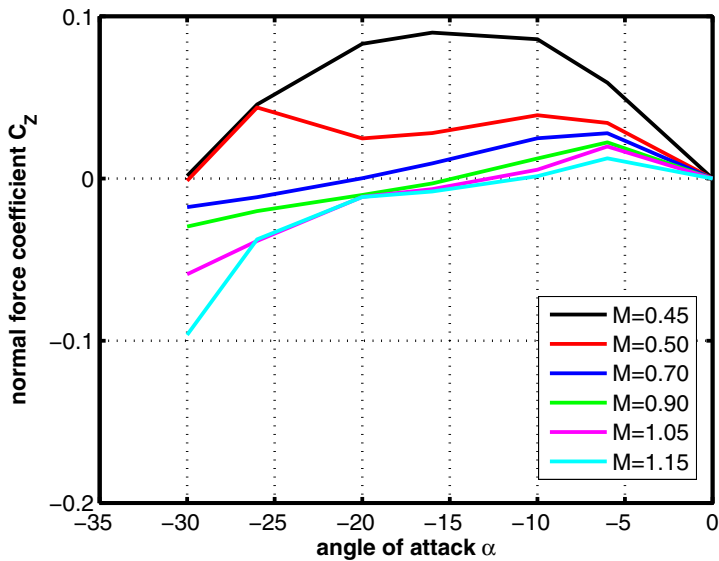


Fig. 4.52. Normal force coefficient C_Z as function of the angle of attack α for subsonic-transonic Mach numbers, [37]

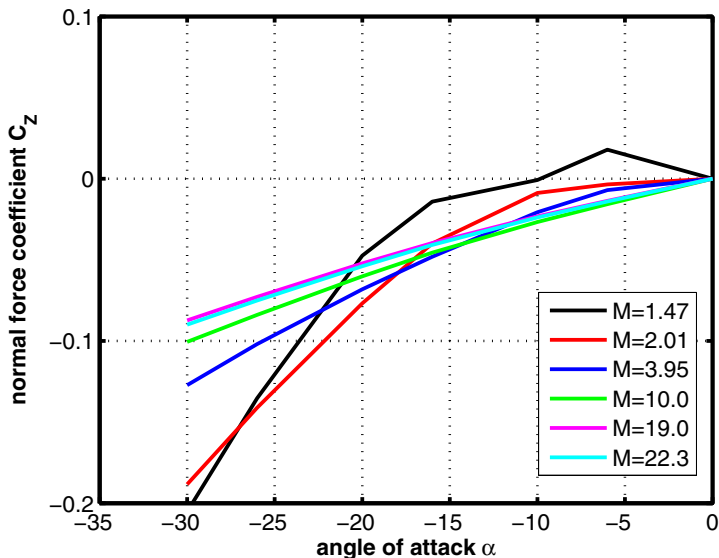


Fig. 4.53. Normal force coefficient C_Z as function of the angle of attack α for supersonic-hypersonic Mach numbers, [37] .

The aerodynamic performance L/D behaves like expected with higher values for subsonic Mach numbers ($M_\infty = 0.45$ and 0.50) and lower values for higher Mach numbers, whereby it is interesting to see that for Mach numbers $M_\infty = 1.47$ and 2.01 L/D is lowest compared to the other supersonic-hypersonic Mach numbers for $|\alpha| \geq 25^\circ$, Figs. 4.54, 4.55. In general the lift-to-drag ratios L/D for the VIKING2 capsule seem to be slightly larger than for the APOLLO capsule.

The data of the pitching moment coefficient C_m , given in [37], are referred to the reference location in the nose tip ($x_{ref} = z_{ref} = 0$), Figs. 4.56, 4.57. Nevertheless they indicate that the vehicle is everywhere statically stable, but cannot be trimmed due to the zero z-offset ($z_{ref} = 0$). A realistic center-of-gravity position, for example, is defined by $x_{cog} = x_{ref} = 0.34 D_1$ and $z_{cog} = z_{ref} = -0.0218 D_1$. Transforming the pitching moment data to this reference position leads obviously to the situation that the vehicle remains statically stable and is now trimmable in the whole Mach number regime, Figs. 4.58, 4.59. The trim angles range from $\alpha_{trim} \approx -10^\circ$ for subsonic Mach numbers until $\alpha_{trim} \approx -25^\circ$ in the hypersonic regime.

As already mentioned earlier it is often difficult for the internal lay-out designer to meet accurately a prescribed center-of-gravity position. Therefore it is of interest to know the trimline as it is defined in Section 4.1, which offers the possibility to shift the coordinates of the center-of-gravity location (x_{cog}, z_{cog}) to some extent, while the trim status is kept.

For three Mach numbers the trim angles of attack are extracted from the diagrams of Figs. 4.58, 4.59, namely $M_\infty = 0.5$, $\alpha_{trim} \approx -10^\circ$, $M_\infty = 0.9$, $\alpha_{trim} \approx -16^\circ$ and $M_\infty = 3.95$, $\alpha_{trim} \approx -22^\circ$. With the associated values for C_X, C_Z and x_{cp} the trim line can be computed. The trim lines for the Mach numbers $M_\infty = 0.5$ and 0.9 indicate always negative z_{cog} values, but for $M_\infty = 3.95$ the trim line crosses at $x_{cog} \approx 0.75$ the $z_{cog} = 0$ barrier denoting positive z-offsets, Fig. 4.60. We have plotted these trim lines into the engineering drawing of the VIKING2 shape in order to have a true to scale impression of the trim line positions, Fig. 4.61.

Of course the usual presentation of the aerodynamic force coefficients for capsules occurs in body fixed coordinates, viz. the axial force coefficient C_X and the normal force coefficient C_Z , but sometimes the depiction of the aerodynamic forces in aerodynamic coordinates, viz. the lift coefficient C_L and the drag coefficient C_D , is also valuable. Therefore we show these data in Fig. 4.62.

The VIKING1 shape has a semi-apertural angle of the aft cone of $\theta_2 = 25^\circ$, Fig. 4.49. We compare now some numerical solutions, mainly on the basis of the Navier-Stokes equations, with VIKING2 data, [35]. The aerodynamic data for the four trajectory points $M_\infty = 0.5$, $\alpha = -3^\circ$, $M_\infty = 0.8$, $\alpha = -5^\circ$, $M_\infty = 0.9$, $\alpha = -10^\circ$ and $M_\infty = 1.15$, $\alpha = -20^\circ$ are considered. These data are plotted together with the VIKING2 results, Figs. 4.63, 4.65, 4.67.

The C_X values of $M_\infty = 0.5$ and 1.15 do not agree well with the VIKING2 data, in contrast to the values for $M_\infty = 0.8$ and 0.9 . For C_Z we have the

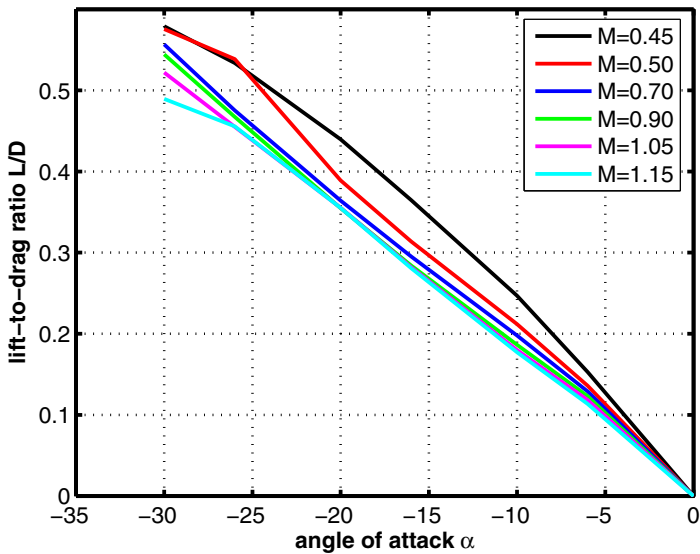


Fig. 4.54. Lift-to-drag ratio L/D as function of the angle of attack α for subsonic-transonic Mach numbers, [37]

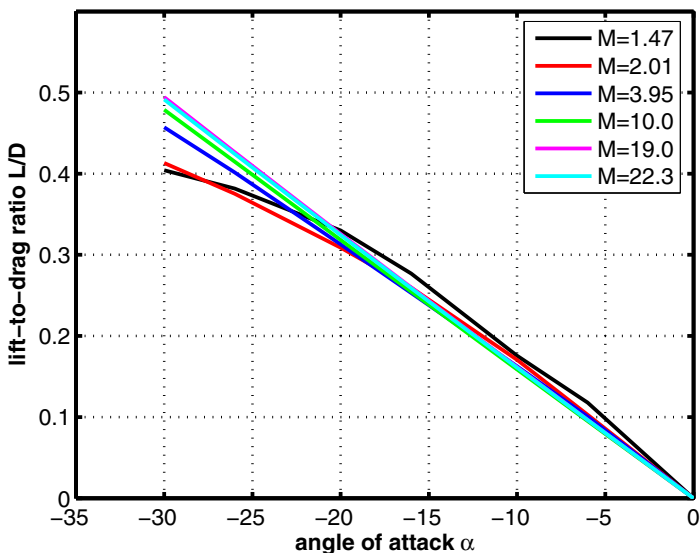


Fig. 4.55. Lift-to-drag ratio L/D as function of the angle of attack α for supersonic-hypersonic Mach numbers, [37]

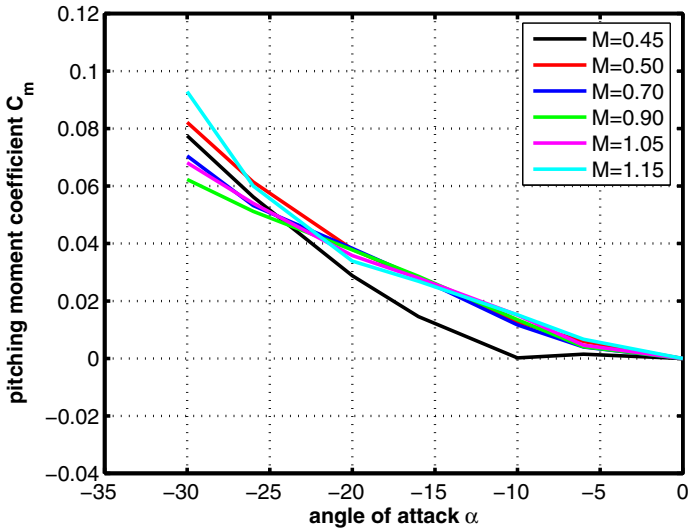


Fig. 4.56. Pitching moment coefficient C_m as function of the angle of attack α for subsonic-transonic Mach numbers, [37]. Moment reference point $x_{ref} = 0.$, $z_{ref} = 0$.

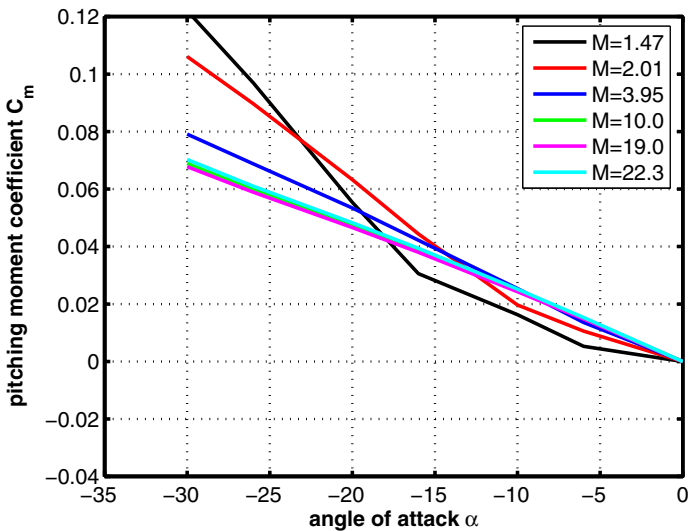


Fig. 4.57. Pitching moment coefficient C_m as function of the angle of attack α for supersonic-hypersonic Mach numbers, [37]. Moment reference point $x_{ref} = 0.$, $z_{ref} = 0$.

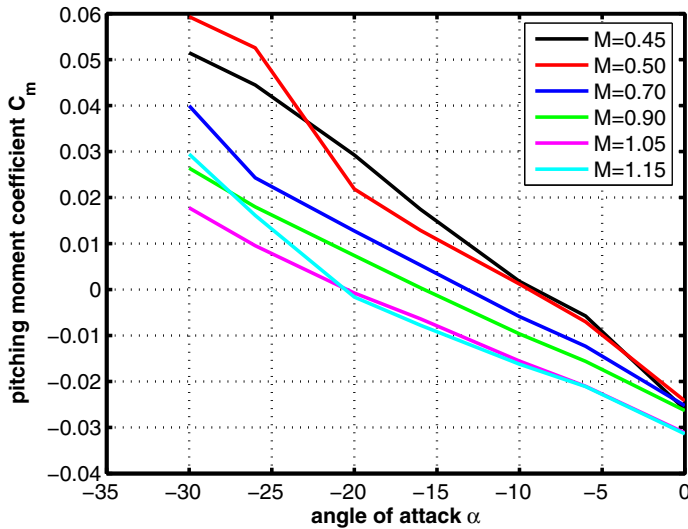


Fig. 4.58. Pitching moment coefficient C_m as function of the angle of attack α for subsonic-transonic Mach numbers, [37]. Moment reference point $x_{ref} = 0.34$, $z_{ref} = -0.0218$.

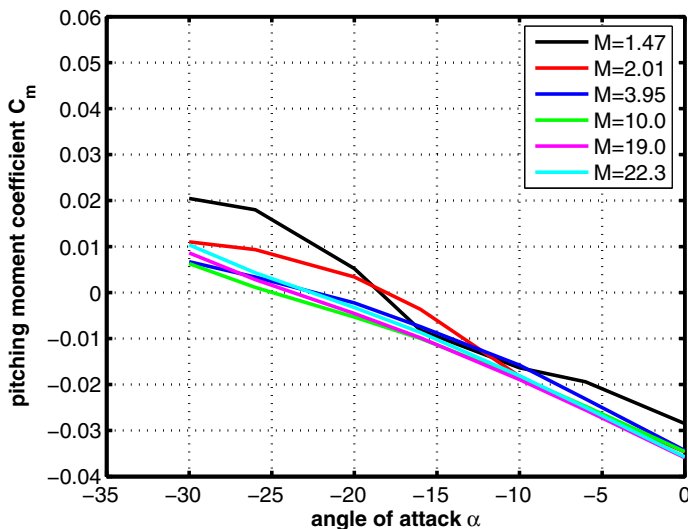


Fig. 4.59. Pitching moment coefficient C_m as function of the angle of attack α for supersonic-hypersonic Mach numbers, [37]. Moment reference point $x_{ref} = 0.34$, $z_{ref} = -0.0218$.

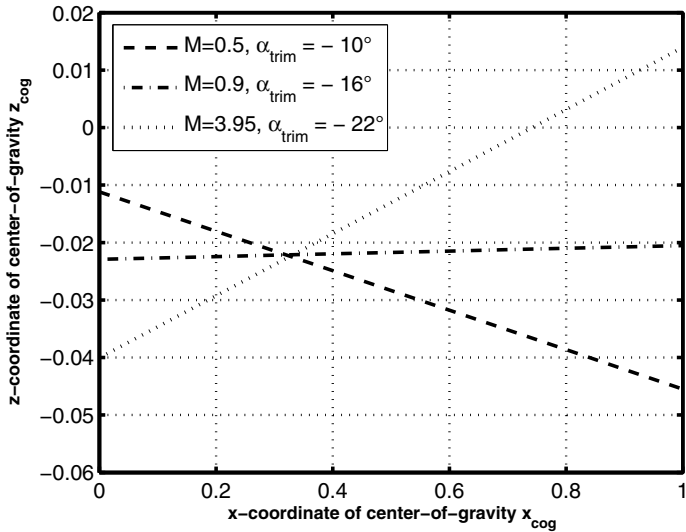


Fig. 4.60. Line of center-of-gravity locations for trimmed flight for the three trajectory points $M_\infty = 0.5$, $\alpha_{trim} = -10^\circ$, $M_\infty = 0.9$, $\alpha_{trim} = -16^\circ$, $M_\infty = 3.95$, $\alpha_{trim} = -22^\circ$ taken from the Figs. 4.58 and 4.59.

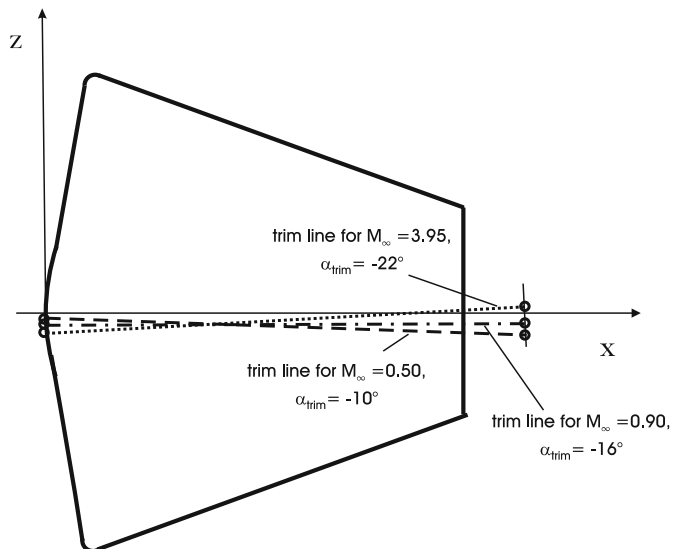


Fig. 4.61. Line of center-of-gravity locations, plotted into the VIKING2 shape, for trimmed flight for the three trajectory points $M_\infty = 0.5$, $\alpha_{trim} = -10^\circ$, $M_\infty = 0.9$, $\alpha_{trim} = -16^\circ$, $M_\infty = 3.95$, $\alpha_{trim} = -22^\circ$. See Fig. 4.60.

picture that the data for $M_\infty = 0.5, 0.9$ and 1.15 compare acceptably with the VIKING2 ones, which is not the case for $M_\infty = 0.8$. Finally the pitching moment data of $M_\infty = 0.5, 0.8$ and 0.9 do not compare sufficiently, in contrast to the one of $M_\infty = 1.15$.

For the supersonic-hypersonic trajectory points $M_\infty = 1.5, \alpha = -20^\circ, M_\infty = 2, \alpha = -20^\circ$ and $-25^\circ, M_\infty = 3, \alpha = -25^\circ, M_\infty = 5, \alpha = -25^\circ, M_\infty = 15, \alpha = -25^\circ$ and $M_\infty = 18.5, \alpha = -25^\circ$, the agreement with the VIKING2 data is much better, except for $M_\infty = 1.5$, Figs. 4.64, 4.66, 4.68.

A conclusion about these data is difficult, since some of the deviations are certainly owing to a lack of accuracy of the numerical solutions.

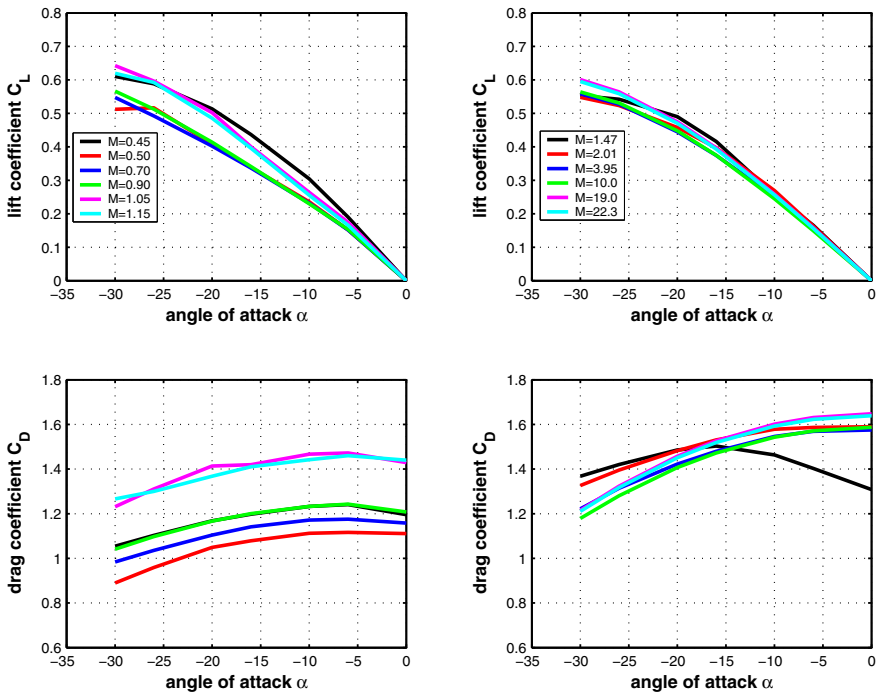


Fig. 4.62. Lift and drag coefficients as function of the angle of attack α , [37]. Subsonic-transonic regime: left plots; supersonic-hypersonic regime: right plots.

Lateral Motion

The VIKING-type capsule is an axisymmetric configuration. Because of that no lateral aerodynamic characteristics exist.

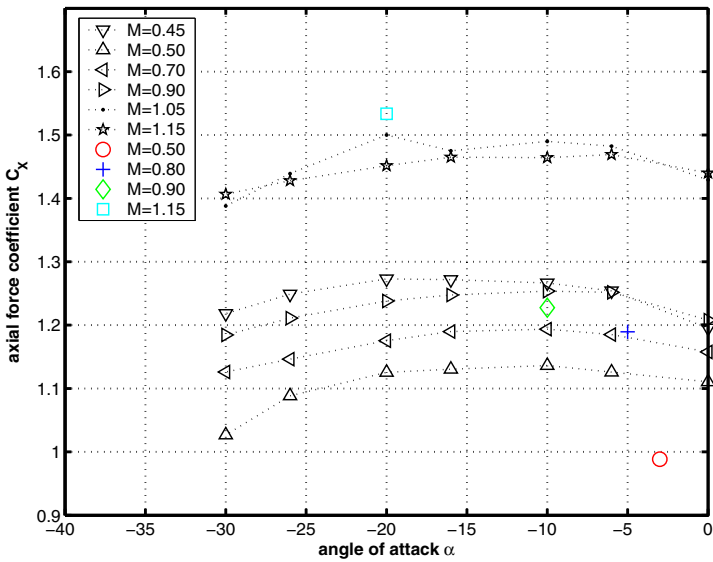


Fig. 4.63. Some axial force coefficients evaluated from numerical flow simulations for the VIKING1 shape embedded into the C_X diagram of Fig. 4.50, [35]. Subsonic-transonic Mach numbers.

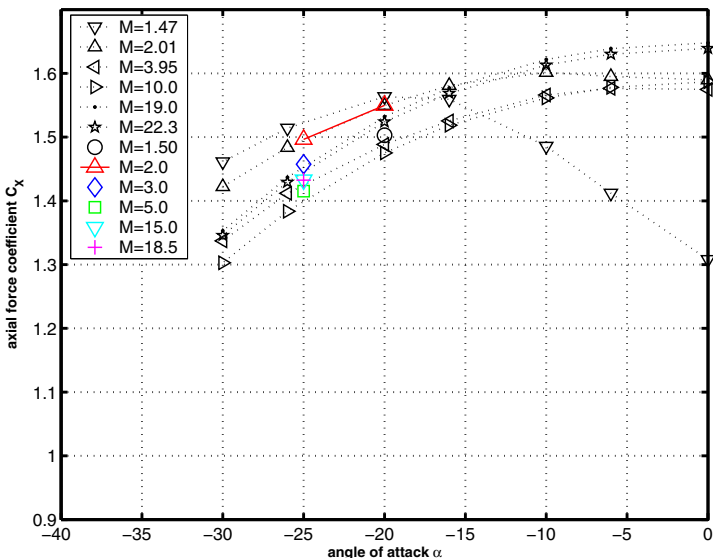


Fig. 4.64. Some axial force coefficients evaluated from numerical flow simulations for the VIKING1 shape embedded into the C_X diagram of Fig. 4.51, [35]. Supersonic-hypersonic Mach numbers.

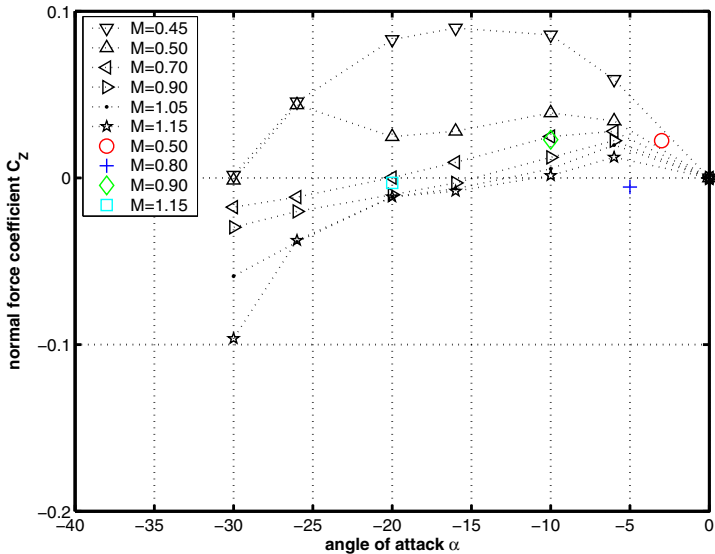


Fig. 4.65. Some normal force coefficients evaluated from numerical flow simulations for the VIKING1 shape embedded into the C_Z diagram of Fig. 4.52, [35]. Subsonic-transonic Mach numbers.

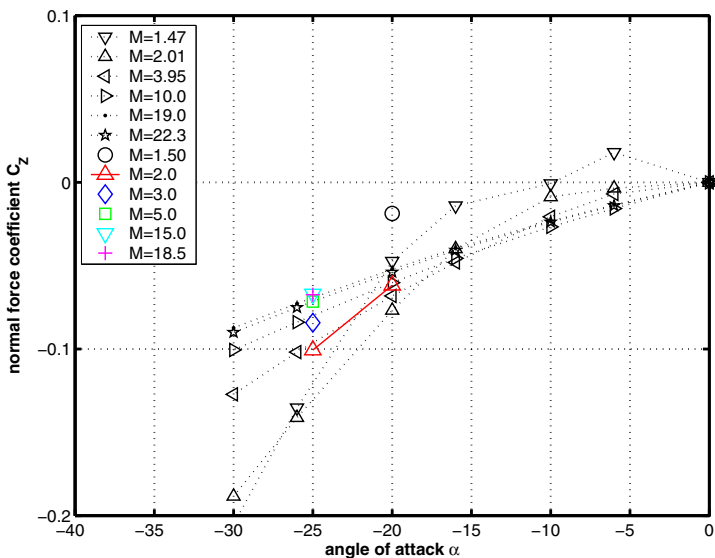


Fig. 4.66. Some normal force coefficients evaluated from numerical flow simulations for the VIKING1 shape embedded into the C_Z diagram of Fig. 4.53, [35]. Supersonic-hypersonic Mach numbers.

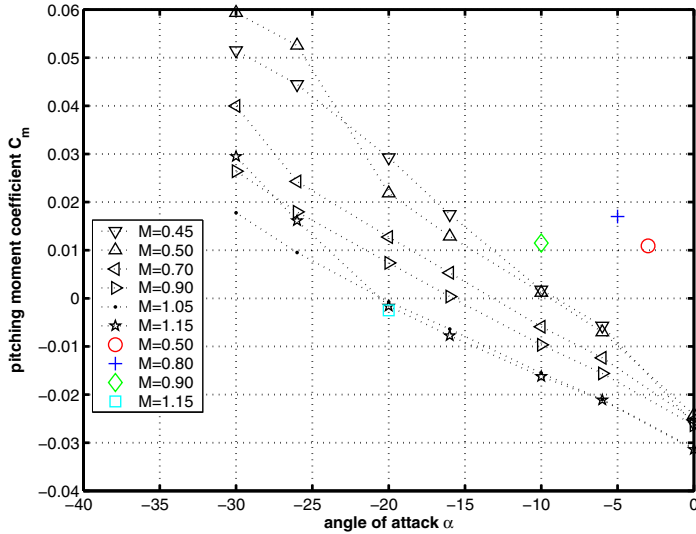


Fig. 4.67. Some pitching moment coefficients evaluated from numerical flow simulations for the VIKING1 shape embedded into the C_m diagram of Fig. 4.58, [35]. Subsonic-transonic Mach numbers. Moment reference point $x_{ref} = 0.34$, $z_{ref} = -0.0218$.

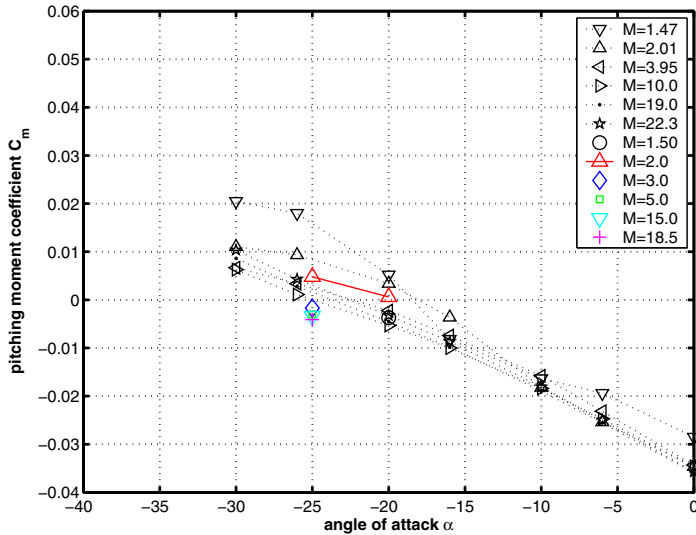


Fig. 4.68. Some pitching moment coefficients evaluated from numerical flow simulations for the VIKING1 shape embedded into the C_m diagram of Fig. 4.59, [35]. Supersonic-hypersonic Mach numbers. Moment reference point $x_{ref} = 0.34$, $z_{ref} = -0.0218$.

4.8.3 Aerodynamic Data of Unsteady Motion

The dynamic stability of the VIKING-type shapes was not investigated. Nevertheless in [37] pitch damping values ($C_{m\dot{\alpha}} + C_{mq}$) are given, which come from the ARD capsule. The idea behind that is, that capsules often have a similar dynamic behavior. For completeness we have plotted these data in Fig. 4.69.

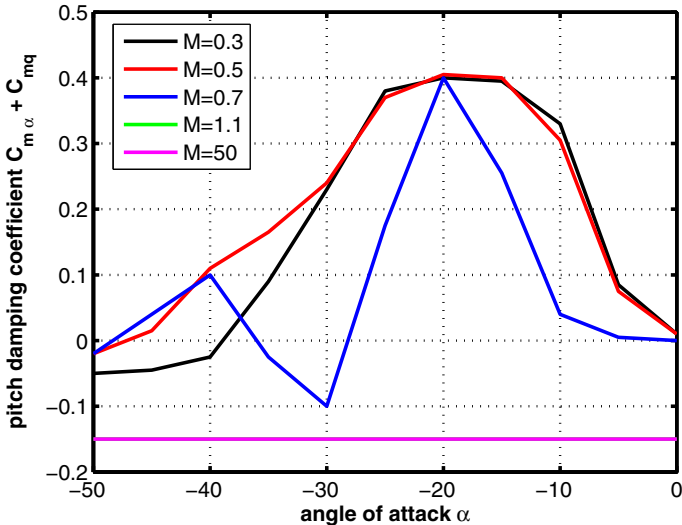


Fig. 4.69. Pitch damping coefficient $C_{m\dot{\alpha}} + C_{mq}$ as function of the angle of attack α [37]. Moment reference point $x_{ref} = 0.34$, $z_{ref} = -0.0218$.

4.9 CARINA (Italy)

In the late 1980s and the early 1990s there was a worldwide renaissance of interests in new space transportation systems as well as space explorations and utilizations. The HERMES program in Europe, the HOPE project in Japan and the NASP and X-33 projects in the United States were some of the activities regarding new space transportation systems. Further, at that time the decision was made to construct and assemble the International Space Station ISS, with which, besides others, the potential was offered for scientific experiments under microgravity conditions.

Some nations in Europe had the impression that their experience and knowledge were not evident enough for taking part in Europe's space programs. Therefore several national activities were launched in order to enhance the research and development basis for a participation in international space programs.

One of these activities was Italy's CARINA project. CARINA was a small system, which was composed of a re-entry module and a service module, [41]. It was planned to launch it by a small rocket or as a piggy-back passenger of a larger space vehicle. CARINA was a testbed for learning more about re-entry technology and microgravity processing. However, the project was cancelled in the middle of the 1990s.

4.9.1 Configurational Aspects

The Italian aerospace company ALENIA SPAZIO was the prime contractor of the CARINA project, [41, 42]. For the re-entry module a GEMINI-like shape was chosen, Fig. 4.70. An engineering drawing of the re-entry module is given in Fig. 4.71. The CARINA configuration, consisting of the re-entry and the service module, is plotted in Fig. 4.72. The gross mass of the CARINA configuration amounts to approximately 450 kg.

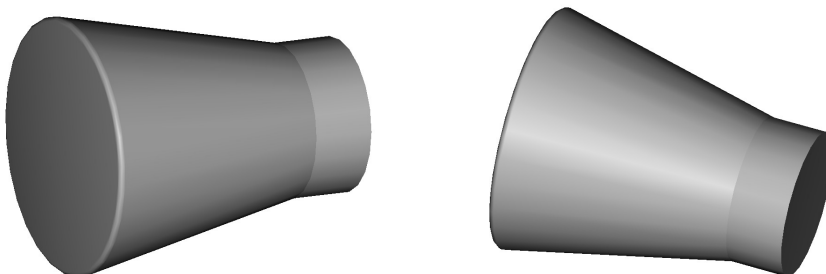


Fig. 4.70. 3D shape presentation of CARINA capsule (re-entry module)

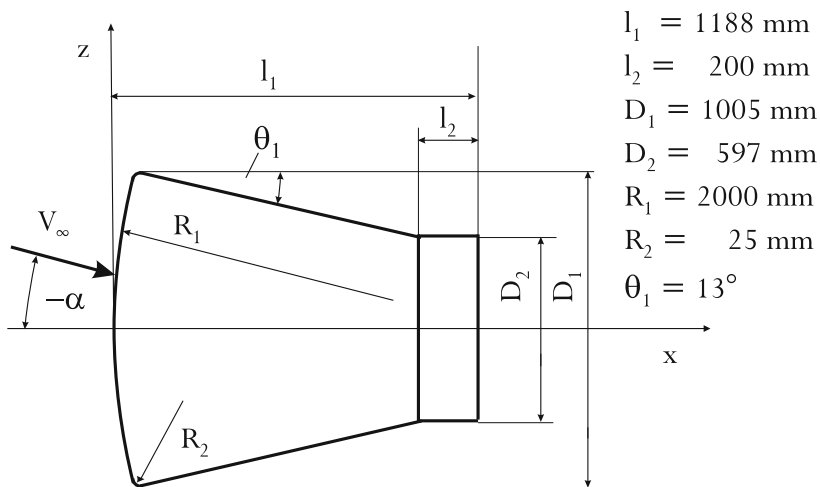


Fig. 4.71. Shape definition of the CARINA capsule (re-entry module), [41]

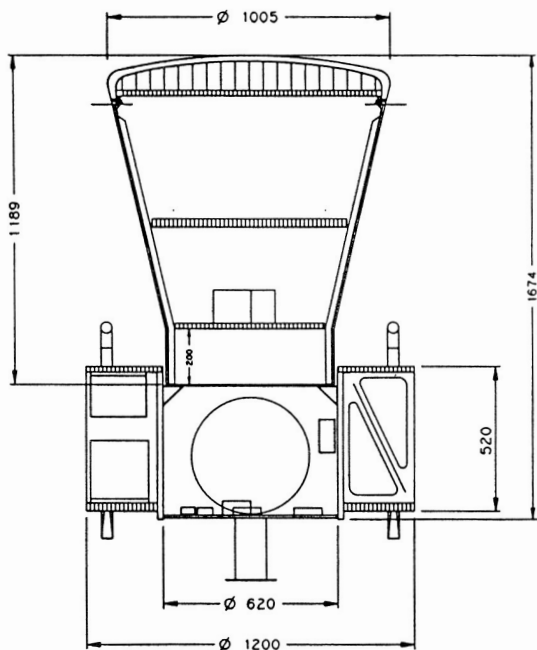


Fig. 4.72. CARINA configuration: Re-entry module and service module, [41]

4.9.2 Aerodynamic Data of Steady Motion

Longitudinal Motion

The aerodynamic coefficients were determined by wind tunnel tests (AEDC (USA) and Lavochkin (Russia)) and by numerical flow field simulations. The flow fields were calculated by using the Euler and the Navier-Stokes equations.

From the literature it is known that data were generated for $0.8 \leq M_\infty \leq 1.6$ and $M_\infty = 8$, [41, 42], but published have been only a few of them. These few data are plotted in Figs. 4.73 - 4.75. The axial force coefficient C_X for $M_\infty = 1.2$ is exhibited in Fig. 4.73. The general trend of this curve is in agreement with the data of other capsules. The same is true for the normal force coefficient C_Z , Fig. 4.74, where the available data for $M_\infty = 1.2$ and 8 are plotted. The pitching moment coefficient C_m displayed for $M_\infty = 0.9$ and 8, indicates static stability, when the moment reference point is given by the center-of-gravity¹².

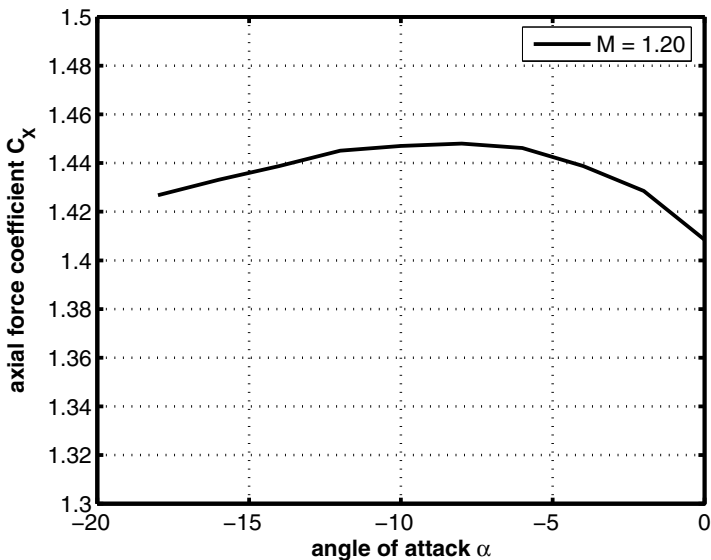


Fig. 4.73. Axial force coefficient C_X as function of the angle of attack α for $M_\infty = 1.2$, [42]

¹² Unfortunately the position of the center-of-gravity is not exactly known. However, since the C_m data are zero for angle of attack $\alpha = 0^\circ$, one knows at least that the z-offset must be zero, which means $z_{cog} = 0$.

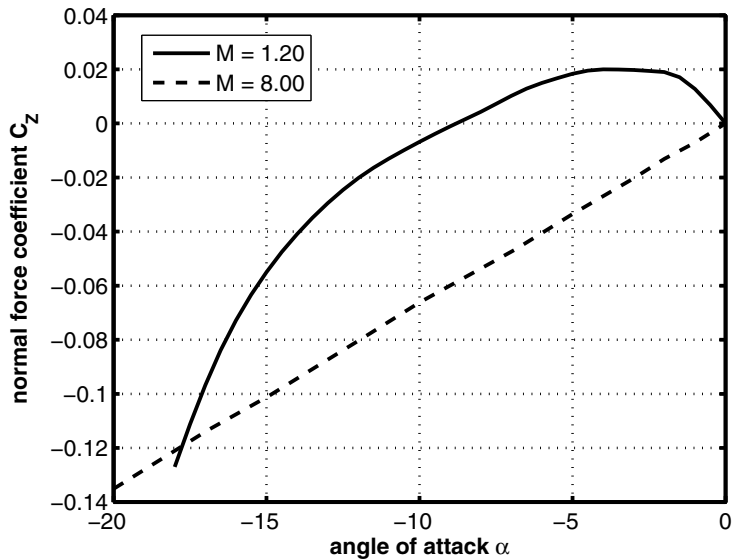


Fig. 4.74. Normal force coefficient C_Z as function of the angle of attack α for $M_\infty = 1.2$ and 8, [41, 42]

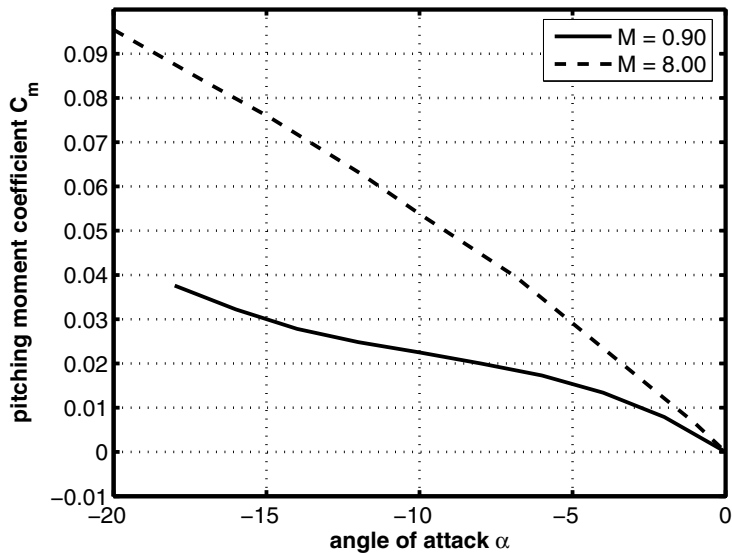


Fig. 4.75. Pitching moment coefficient C_m as function of the angle of attack α for $M_\infty = 0.90$ and 8, [41, 42]. Moment reference point is the center-of-gravity.

Lateral Motion

The CARINA capsule is an axisymmetric configuration. Because of that no lateral aerodynamic characteristics exist.

4.9.3 Aerodynamic Data of Unsteady Motion

Dynamic stability investigations are not known.

4.10 AFE (Aeroassist Flight Experiment) (USA-Europe)

In the late 1980s and the early 1990s the U.S. National Aeronautics and Space Administration NASA has dealt with the idea to design a space vehicle which is able to transport cargo between different orbits. In that frame it was envisaged to develop an economically operating vehicle, which had to meet two basic requirements.

The first one was, that the transfer from a higher to a lower Earth orbit should be conducted without the use of any propulsion system. This class of space vehicles is referred to as Aeroassisted Orbital Transfer Vehicles (AOTV)¹³, [43, 44]. This means to build a vehicle which had aerocapturing capabilities¹⁴. The second condition was, that the devices and the equipment located on the back side (behind the heat shield) of the vehicle should not directly be impinged by high enthalpy flow coming from the stagnation point regime of the heat shield, in order to prevent high thermal loads.

Generally axisymmetric lifting capsules have trim angles in the hypersonic regime of order 20° , which may lead to higher thermal loads at the rear parts of these vehicles. In such cases particular arrangements are necessary to thermally protect these parts. In order to avoid such arrangements NASA developed a configuration where the trim angle of attack in the hypersonic flight regime ranges in the vicinity of $\alpha \approx 0^\circ$. This shape got the name AFE (Aeroassisted Flight Experiment).

About ten years later a renewed interest in this shape arose at the European Space Agency (ESA) in the frame of the Mars Sample Return Orbiter (MSRO) activities, [45, 46, 47], Fig. 4.76.



Fig. 4.76. Mars sample return orbiter (MSRO) with the AFE heat shield. Navier-Stokes solution, $M_\infty = 9.91$, perfect gas (left) [48], model with partial back cover in the high enthalpy wind tunnel F4 of ONERA (middle) [46], synthetic image of the MSRO in aerocapture formation (right) [46].

¹³ Later it was named ASTV \Rightarrow Aeroassisted Space Transfer Vehicle.

¹⁴ Information about the aerocapturing concept can be found in [1].

4.10.1 Configurational Aspects

The AFE shape is complex. It consists of a blunted elliptic cone with a half angle in the symmetry plane of 60° , which is raked off at 73° to the centerline (x -axis) whereby a circular raked plane is generated with a diameter of $D_2 = 3879$ mm. A skirt with a width of $l_1 = 336$ mm is attached to the raked plane¹⁵. The blunt nose is an ellipsoid with an ellipticity of 2.0. The total diameter of the shape, - that is the raked elliptic cone plus the skirt -, amounts to $D_1 = 4267$ mm (≈ 14 ft), Fig. 4.77, [43, 44].

Fig. 4.78 shows a three-dimensional presentation of the shape. In Fig. 4.79 the AFE shape including a possible package of devices and equipments on the back side is exhibited in terms of a three views engineering drawing, [44].

In the frame of the MSRO program the AFE heat shield (Mars premier shield) was scaled down by a factor of 14/12, which means to have a total diameter of $D_1 = 3657$ mm (≈ 12 ft), [45, 46].

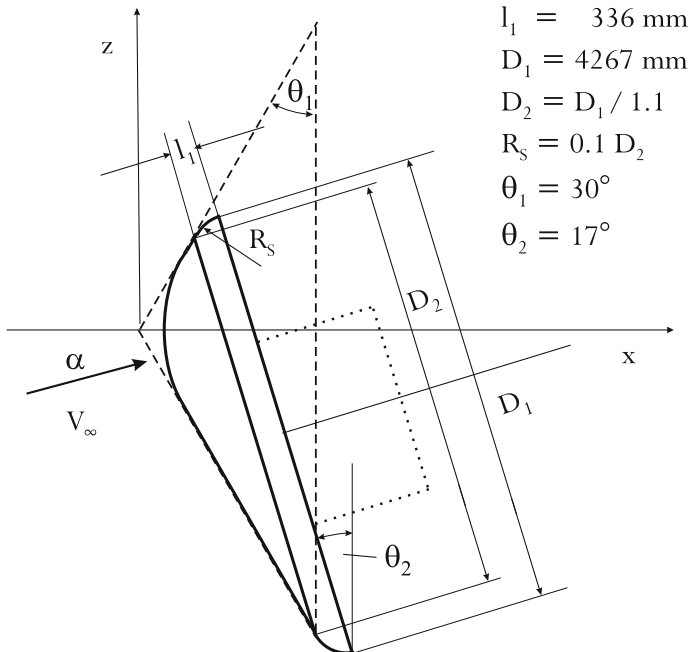


Fig. 4.77. Shape definition of the AFE configuration, [43, 45, 46]

¹⁵ l_1 is calculated by $l_1 = R_S \cos 60^\circ$, where R_S is the skirt radius (see Fig. 4.77) with $R_S = 0.1 D_2$.

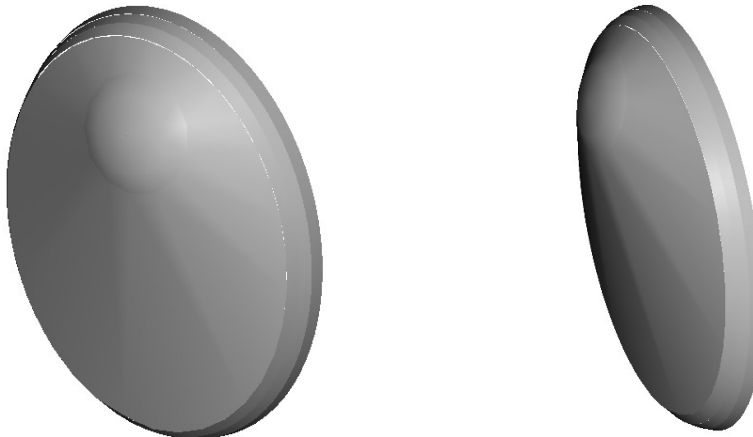


Fig. 4.78. 3D shape presentation of the AFE configuration

4.10.2 Aerodynamic Data of Steady Motion

The mission of an Aeroassisted Orbital Transfer Vehicle (AOTV) consists in transporting cargo from a higher to a lower Earth orbit. This requires the reduction of the orbital energy of the vehicle which takes place by a deep immersion into the Earth atmosphere. When the vehicle enters the atmosphere its velocity is very high. The Mach number is around 30 and reduces normally to approximately 15. Therefore the complete aerocapturing flight occurs in the hypersonic flight regime. This is the reason why the aerodynamic data base, considered here, is given only for hypersonic Mach numbers.

Longitudinal Motion

A first campaign for the establishment of a hypersonic aerodynamic data base was carried out in NASA Langley's cold hypersonic wind tunnels for Mach 6 (Langley 20-Inch Mach 6 Tunnel) and Mach 10 (Langley 31-Inch Mach 10 Tunnel). The gas used in both tunnels was air. Test were also done in Langley's Hypersonic CF₄ Tunnel, [43, 44]. All these tunnels do not fulfill the free flight conditions for temperature, pressure and density, which are usually higher than in these tunnels. The difference between the air tunnels and the CF₄ tunnel consists in the two items, the reservoir temperature T_0 and the effective ratio of specific heats γ_{eff} :

- Langley 20-Inch Mach 6, $T_0 = 611$ K, $\gamma_{eff} = 1.40$,
- Langley CF₄ Mach 6, $T_0 = 850$ K, $\gamma_{eff} = 1.11$,
- Langley 31-Inch Mach 10, $T_0 = 1027$ K, $\gamma_{eff} = 1.34$.

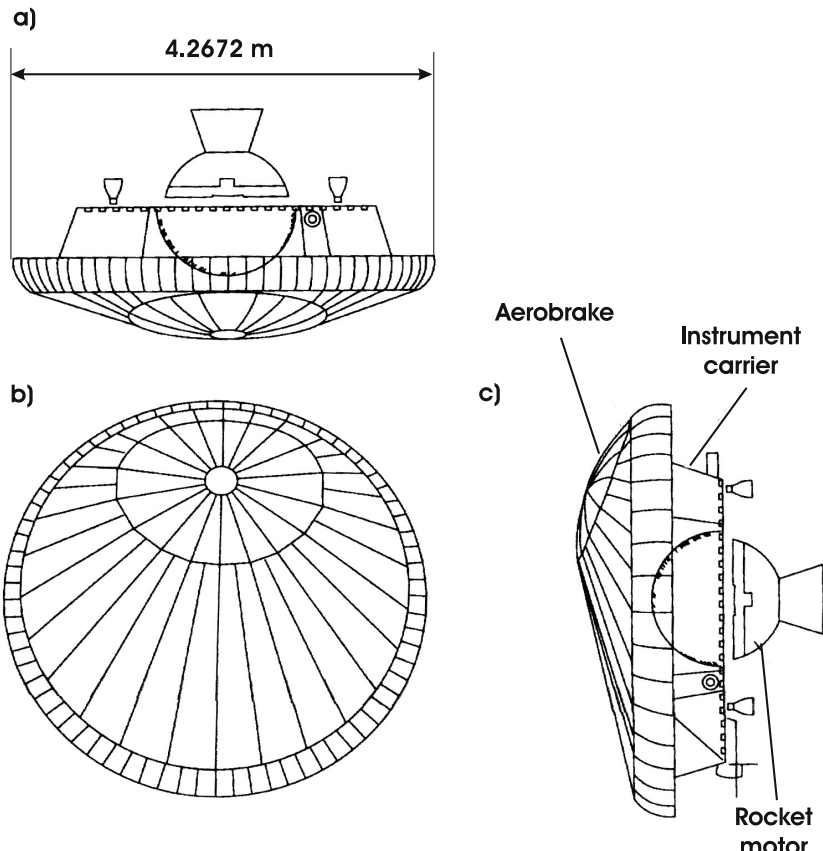


Fig. 4.79. Shape definition of the AFE configuration. Engineering drawings of top view a), front view b) and side view c), [43].

In general the ratio of specific heats is around 20% lower in the CF_4 tunnel than in the air tunnels, [43].

From later investigations for example in the HERMES and ARD projects (see Sections 6.11 and 4.4) it is known that there exists a dependency of the pitching moment, and therefore of the trim angle, on real gas effects. The influence of real gas effects are much lower on the aerodynamic performance L/D .

To overcome these real gas problems NASA's Ames Research Center had built the Hypervelocity Free-Flight Aerodynamic Facility (HFFAF), which follows the gun tunnel concept. A model is shot into a gas at rest with conditions for temperature, pressure and density similar to free flight. The

evaluation of the flight trajectory, by using the flight mechanical equations for six degree of freedom motion, delivers the aerodynamic coefficients.

On this basis the aerodynamic coefficients for two Mach numbers as functions of the angle of attack were determined. An effective ratio of specific heats γ_{eff} was ascertained by comparing shock shapes (shock stand-off distance) of shadowgraphs taken from the HFFAF tunnel with the ones of Navier-Stokes solutions for various γ_{eff} . The outcome was that the real gas effects for these flight conditions could be approximately simulated by using $\gamma_{eff} = 1.2$, [49]. For the γ_{eff} - approach see [1]

From most of the other aerodynamic data bases for hypersonic velocities, discussed in this book, we are aware that a Mach number independency exists in this flight regime. An inspection of the next four figures (Figs. 4.80 - 4.83), showing the axial and normal force coefficients, the lift-to-drag ratio and the pitching moment coefficient, reveals that this is true for the results coming from the conventional Langley tunnels, but not for the HFFAF data. The axial force coefficients of the Langley data agree well with the HFFAF data for $M_\infty = 9.2$, but not with the data for $M_\infty = 11.8$, Fig. 4.80. This is different for the normal force and the lift-to-drag ratio, where the $M_\infty = 11.8$ HFFAF data are better in line with Langley's results than the $M_\infty = 9.2$ ones, Figs. 4.81 and 4.82.

The above mentioned differences are smaller for the pitching moment coefficients, Figs. 4.83. From Langley's results we find a trim angle slightly larger than zero, and from the HFFAF data a trim angle slightly lower than zero.

In the frame of the MSRO project several numerical flow field simulations were conducted with the goal to better understand the influence of real gas effects on the trim angle, [45] - [47]. For the trajectory point $M_\infty = 18.7$, $\alpha = -4^\circ$ the pitching moment coefficient, taken from [45], is shown in Fig. 4.83. It is well in line with the other data.

Lateral Motion

In the next three figures (Figs. 4.84 - 4.86) the coefficients of the side force, the rolling moment and the yawing moment are plotted as function of the side slip angle β . Since the AFE shape is symmetrical in the $x - z$ plane, Fig. 4.77, it is expected that the curves go through the origin ($x = z = 0$). But this is not the case and the shown offset can only be explained, in particular as the magnitude of the values to be measured are very small, by model and balance misalignments, [44]. Further the angle of attack dependencies of the values for $M_\infty = 9.9$ are obviously also not in line with the physics. A better angle of attack behavior seems to be given for Mach number $M_\infty = 5.94$.

Nevertheless the negative derivative of the rolling moment coefficients indicates a damping of the roll motions and the positive derivative of the yawing moment coefficients denotes directional stability.

The three small diagrams of Fig. 4.87 show the lateral coefficients (C_Y, C_l, C_n) as function of angle of attack α for a nearly constant side slip angle β . It is conspicuous that no clear tendency of C_Y, C_l, C_n as function of α can

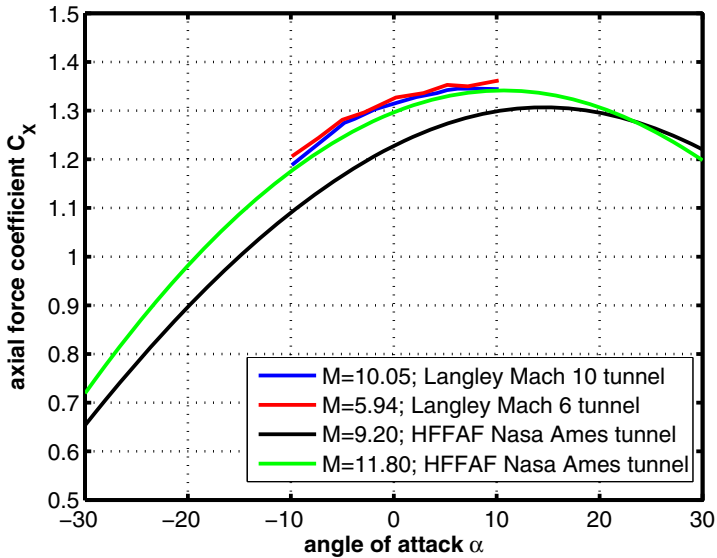


Fig. 4.80. Axial force coefficient C_x as function of the angle of attack α for hypersonic Mach numbers, [43, 49].

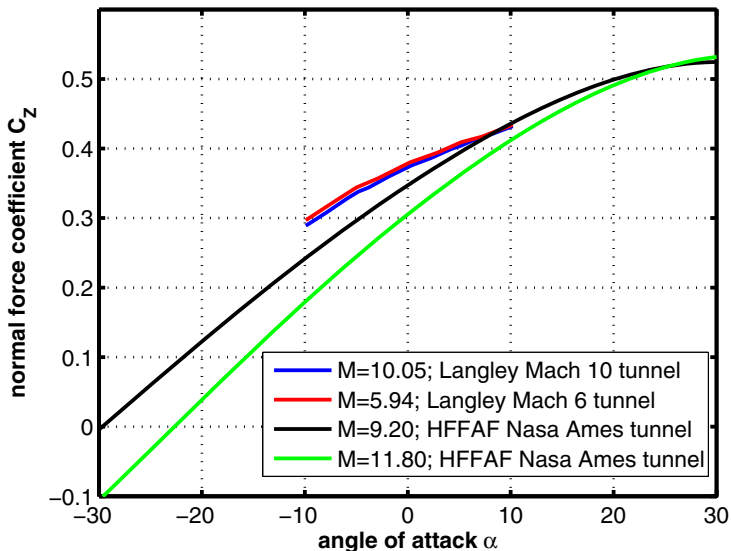


Fig. 4.81. Normal force coefficient C_z as function of the angle of attack α for hypersonic Mach numbers, [43, 49].

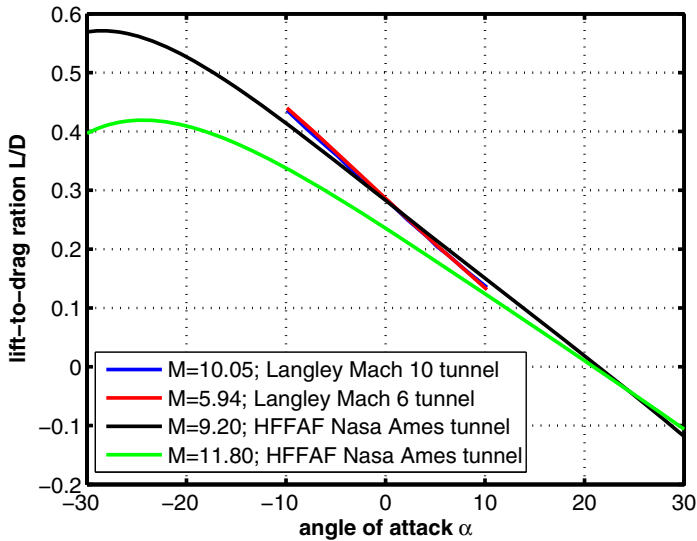


Fig. 4.82. Lift-to-drag ratio L/D as function of the angle of attack α for hypersonic Mach numbers, [43, 49].

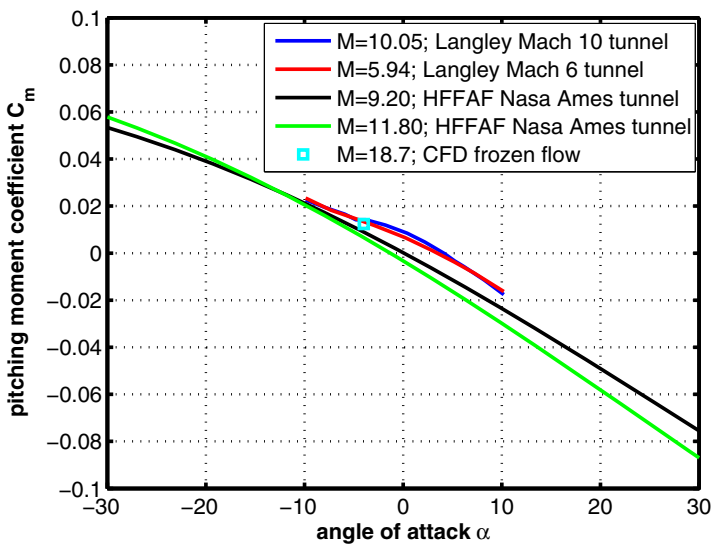


Fig. 4.83. Pitching moment coefficient C_m as function of the angle of attack α for hypersonic Mach numbers, [43, 45, 49]. Moment reference point given by rake-plane center, see Fig. 4.77.

be observed, which emphasizes the difficulties the experimentalists had to measure the lateral characteristics of the AFE shape.

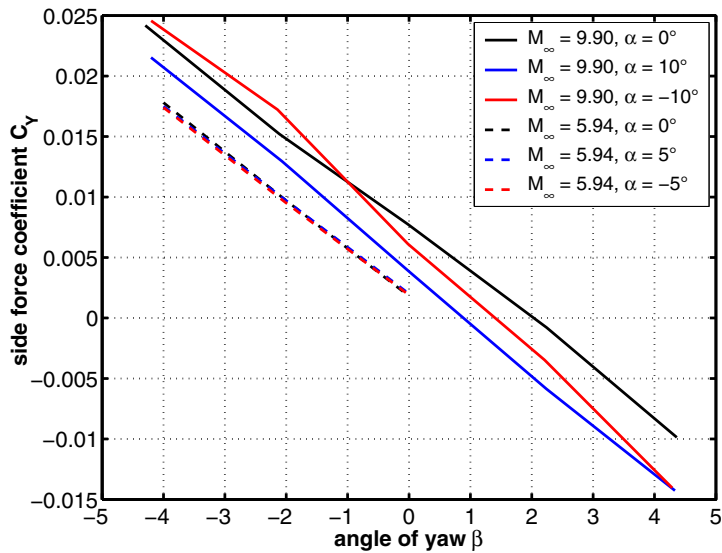


Fig. 4.84. Side force coefficient C_Y as function of the angle of yaw β for hypersonic Mach numbers, [44]

4.10.3 Aerodynamic Data of Unsteady Motion

Data of dynamic stability investigations are not available.

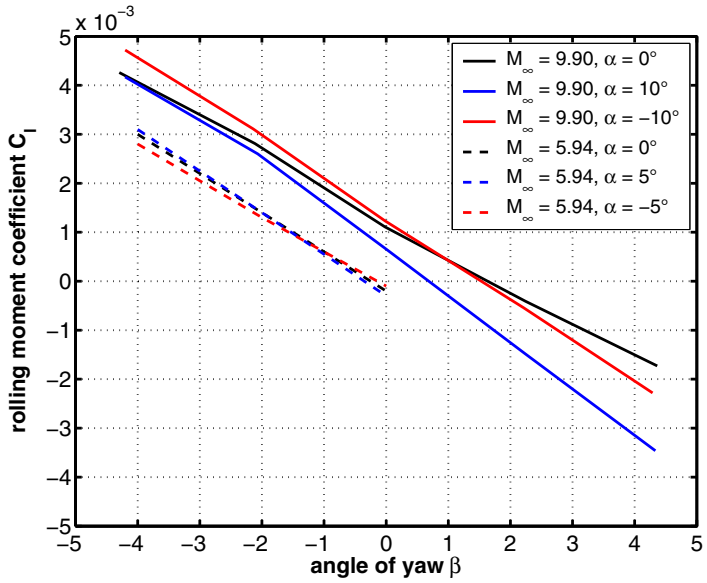


Fig. 4.85. Rolling moment coefficient C_l as function of angle of yaw β for hypersonic Mach numbers, [44]. Moment reference point given by the rake-plane center, see Fig. 4.77.

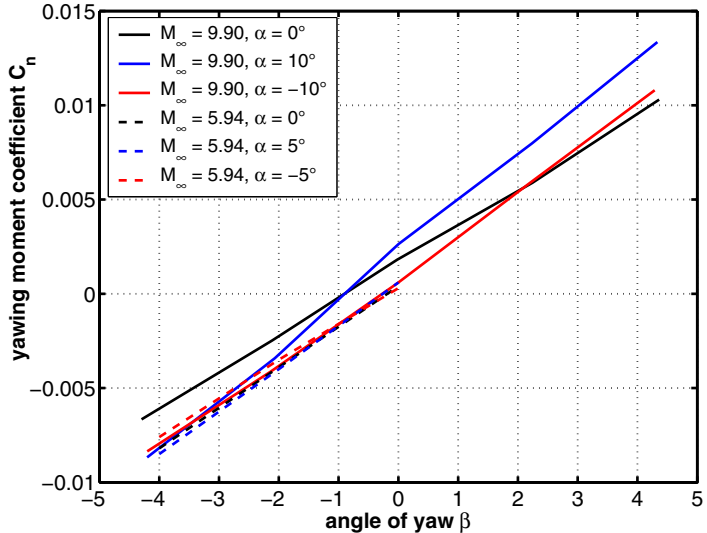


Fig. 4.86. Yawing moment coefficient C_n as function of the angle of yaw β for hypersonic Mach numbers, [44]. Moment reference point given by the rake-plane center, see Fig. 4.77.

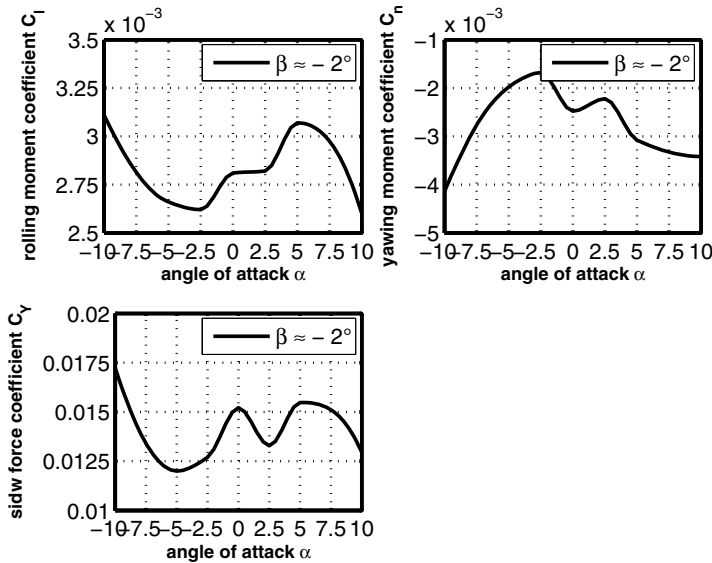


Fig. 4.87. Rolling moment, yawing moment and side force coefficients as function of the angle of attack α at nearly constant yawing angle β for $M_\infty = 9.9$, [44]. Moment reference point given by the rake-plane center, see Fig. 4.77.

4.11 VIKING (USA)

The VIKING mission to Mars, planned, developed and performed by the U.S. space agency NASA, was composed of the two spacecrafts VIKING'1' and VIKING'2'. The primary mission objectives were to obtain images of the Martian surface, to characterize the composition of the atmosphere and to search for evidence of life.

VIKING'1' was launched on Aug. 20, 1975 and arrived at Mars orbit on June 19, 1976 after a 10 month cruise. Approximately one month later (July 20, 1976) landing on the Martian surface took place after the VIKING'1' orbiter had identified an appropriate not too rough landing site by images made out of its orbit position. VIKING'2' was launched on Sept. 9, 1975, entered Mars orbit on Aug. 7, 1976, and its lander touched down on Sep. 3, 1976.

Fig. 4.88 shows the VIKING Orbiter with the entry module as well as the lander configuration.



Fig. 4.88. VIKING Orbiter with the entry module (left), and the lander configuration (right)

4.11.1 Configurational Aspects

A 3D presentation of the entry module is given in Fig. 4.89. The VIKING entry module consists of the aeroshell and the lander plus base cover configuration, [50], which is displayed in Fig. 4.90. The entry module consists of a spherically blunted cone with a semi-apertural angle of $\theta_1 = 70^\circ$. The afterbody consists of two truncated cone segments with the semi-apertural angles $\theta_2 = 40^\circ$ and $\theta_3 = 62.18^\circ$.

Most of the aerodynamic data presented here are taken from [50]. These data were generated by wind tunnel tests¹⁶ using a 0.08 scale model. The measures of the model and the flight configuration, also shown in Fig. 4.91, are displayed in Table 4.1.

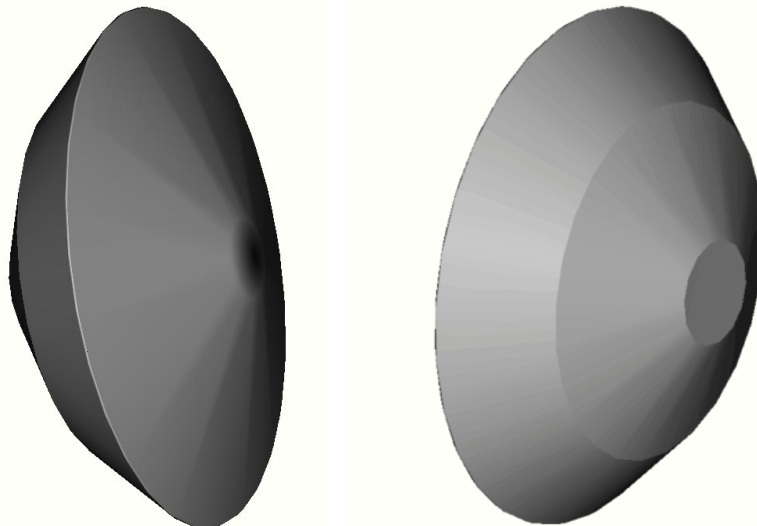


Fig. 4.89. 3D shape presentation of the VIKING entry module, [50]. View of the aeroshell (left) and of the base cover (right).

4.11.2 Aerodynamic Data of Steady Motion

The whole work regarding the establishment of the aerodynamic data base of the VIKING entry module was done in wind tunnels. Approximate design methods were not applied and numerical methods had not the maturity at that time for contributing to the data base as is the case today. Most of the aerodynamic data presented here were attained at NASA Langley's 8-foot transonic windtunnel ($0.4 \leq M_\infty \leq 1.2$), [50], which is operated with air.

Since the Martian atmosphere consists essentially of carbon dioxide (CO_2) some investigations were performed in the NASA Ames Hypervelocity Free-Flight Aerodynamic Facility, which is operated with CO_2 . The general outcome was that the drag coefficients grow about 3% more in the CO_2 medium compared to air, [51].

¹⁶ The tests took place in NASA Langley's 8-foot transonic windtunnel .

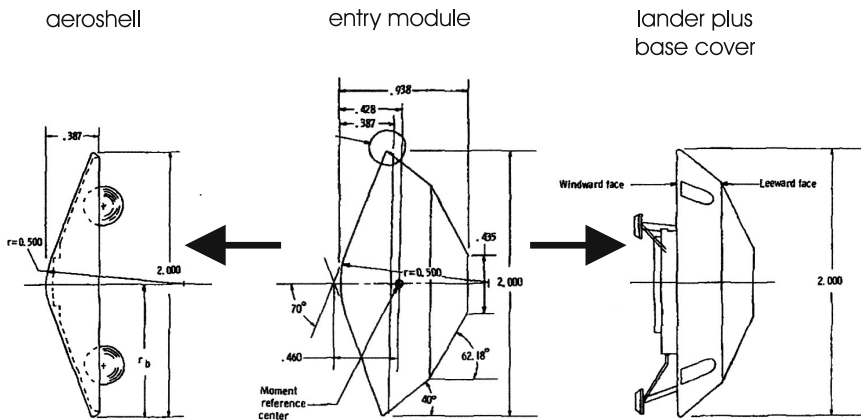


Fig. 4.90. VIKING's entry module (middle) composed of the aeroshell (left) and the lander plus base cover part (right), [50]

Table 4.1. VIKING entry module: dimensions of the 0.08 scale wind tunnel model and of the flight configuration, [50]

	model [cm]	flight configuration [cm]
d_1	28.04	350.05
d_2	6.09	76.23
l_1	13.15	164.38
l_2	6.00	75.00
l_3	6.44	80.61
r_1	7.01	87.62
r_2	0.21	2.62
θ_1	70°	70°
θ_2	40°	40°
θ_3	62.18°	62.18°

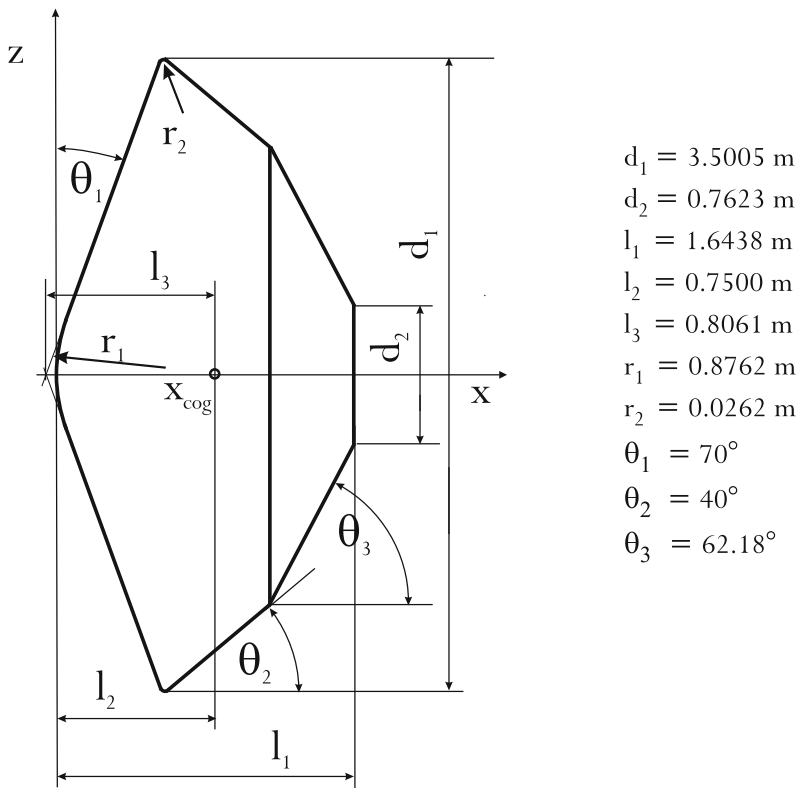


Fig. 4.91. Shape definition of the VIKING capsule (entry vehicle) with measures, [50]

Longitudinal Motion

The axial force coefficient C_X has only a slight dependency on the angle of attack in the subsonic-transonic Mach number regime ($0.4 \leq M_\infty \leq 1.2$). For $M_\infty \geq 2$ C_X decreases with increasing negative angle of attack. The lowest C_X values are given for subsonic speeds which increase monotonically with growing Mach numbers, Fig. 4.92. Most of the curves of the normal force coefficients C_Z start in the positive value regime for increasing negative angles of attack, but turn then ($\alpha \lesssim -5^\circ$) strongly to negative values, Fig. 4.93. The aerodynamic performance L/D shows nearly no Mach number dependency for $0.4 \leq M_\infty \leq 2$, Fig. 4.94. The pitching moment diagram, Fig. 4.95, indicates static stability in the whole Mach number regime presented here.

Generally the behavior of the aerodynamic coefficients of the VIKING entry module is very similar to that of the VIKING-type shapes of Section 4.8.

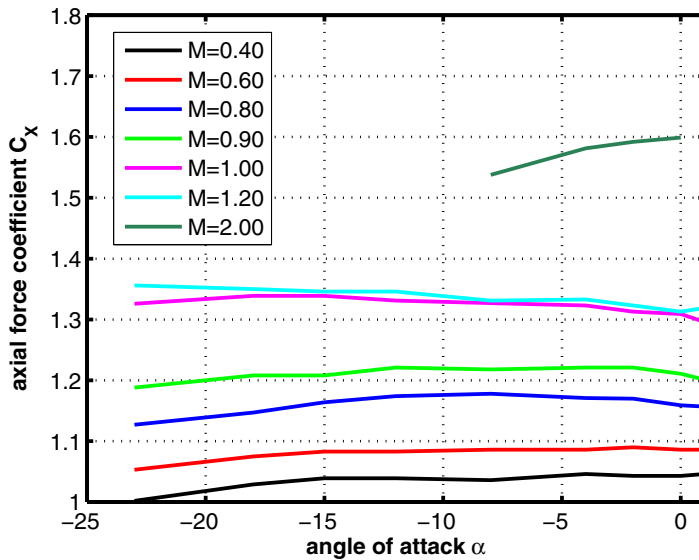


Fig. 4.92. Axial force coefficient C_X as function of the angle of attack α . All data are taken from [50], except the $M_\infty = 2$ ones, which come from [51].

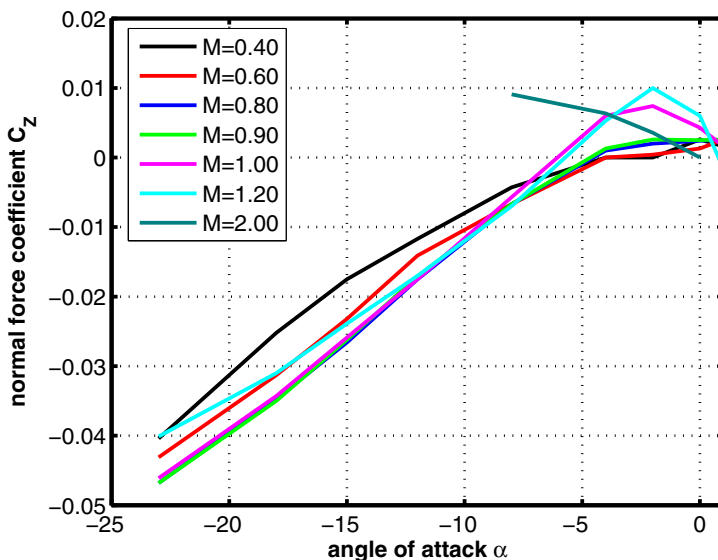


Fig. 4.93. Normal force coefficient C_Z as function of angle of attack α . All data are taken from [50], except the $M_\infty = 2$ ones, which come from [51].

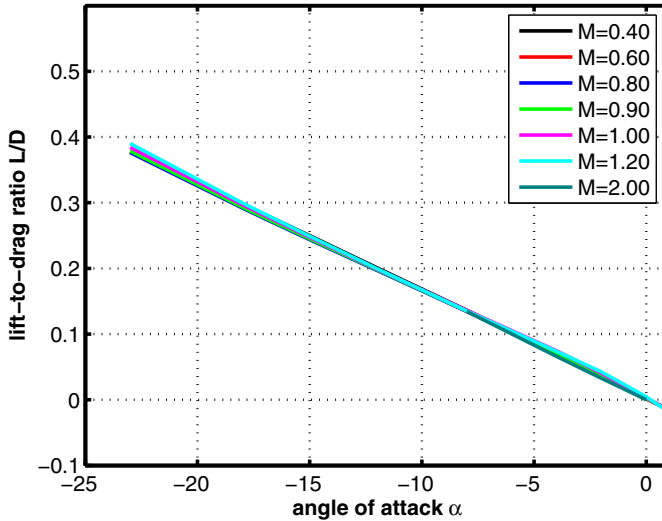


Fig. 4.94. Lift-to-drag ratio L/D as function of angle of the attack α . All data are taken from [50], except the $M_\infty = 2$ ones, which come from [51].

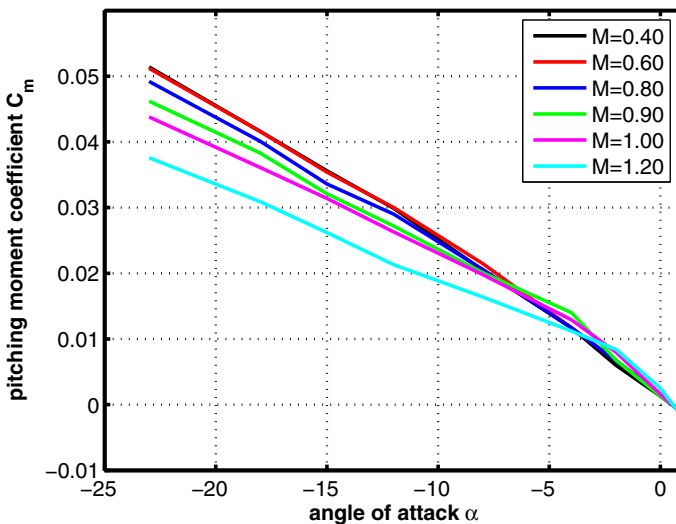


Fig. 4.95. Pitching moment coefficient C_m as function of the angle of attack α . Moment reference point of windtunnel model $x_{ref} \equiv x_{cog} = 0.428 d_1/2$, $z_{ref} = 0$. All data are taken from [50].

Lateral Motion

The VIKING entry module is an axisymmetric configuration. Because of that no lateral aerodynamic characteristics exist.

4.11.3 Aerodynamic Data of Unsteady Motion

Dynamic stability investigations were conducted in ballistic range facilities by data reduction of the flight path, and by forced and free oscillation techniques, [1], in conventional wind tunnels, [51] - [53]. A lot of measured dynamic stability data are inconsistent with each other and depend obviously either on the pitch amplitude angle (ballistic range facility) or the reduced frequency parameter (forced oscillation technique). Regarding the pitch amplitude, tests have shown that the vehicle becomes dynamically more unstable for low pitch oscillation angles, and it seems that these low pitch amplitude data agree acceptably well with the forced oscillation data. In summary the VIKING entry module behaves, as expected, dynamically unstable in the transonic Mach number regime and has also a dynamic instability regime around Mach number 2. From all these dynamic stability data given in [51] to [53], we have plotted in Fig. 4.96 the forced oscillation results of [53] as function of the Mach number, whereby the angle of attack was $\alpha = 0^\circ$ and the pitch amplitude angle $\pm 1.8^\circ$.

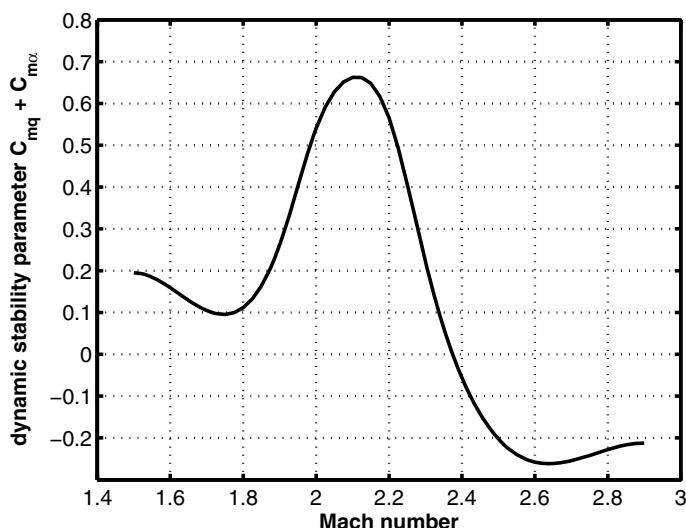


Fig. 4.96. Dynamic pitch damping coefficient $C_{mq} + C_{m\dot{\alpha}}$ as function of the Mach number at angle of attack $\alpha = 0^\circ$ and a pitch amplitude angle of $\pm 1.8^\circ$, [53].

References

1. Hirschel, E.H., Weiland, C.: Selected Aerothermodynamic Design Problems of Hypersonic Flight Vehicles, vol. 229. Springer, Heidelberg; Progress in Astronautics and Aeronautics. AIAA, Reston (2009)
2. Weiland, C.: Computational Space Flight Mechanics. Springer, Heidelberg (2010)
3. Bertin, J.J.: The Effect of Protuberances, Cavities, and Angle of Attack on the Wind Tunnel Pressure and Heat Transfer Distribution for the APOLLO Command Module. NASA TM X-1243 (1966)
4. Moseley, W.C., Moore, R.H., Hughes, J.E.: Stability Characteristics of the APOLLO Command Module. NASA TN D-3890 (1967)
5. Lee, D.B., Bertin, J.J., Goodrich, W.D.: Heat Transfer Rate and Pressure Measurements Obtained During APOLLO Orbital Entries. NASA TN D-6028 (1970)
6. Lee, D.B., Goodrich, W.D.: The Aerothermodynamic Environment of the APOLLO Command Module During Superorbital Entry. NASA TN D-6792 (1972)
7. N.N. APOLLO Data Base. Industrial communication, Aerospatiale - Deutsche Aerospace Dasa (1993)
8. Hirschel, E.H.: Basics of Aerothermodynamics, vol. 204. Springer, Heidelberg; Progress in Astronautics and Aeronautics. AIAA, Reston (2004)
9. Bouslog, S.A., An, M.Y., Wang, K.C., Tam, L.T., Caram, J.M.: Two Layer Convective Heating Prediction Procedures and Sensitivities for Blunt Body Re-entry Vehicles. AIAA-Paper 93-2763 (1993)
10. Moseley, W.C., Martino, J.C.: APOLLO Wind Tunnel Testing Programme – Historical Development of General Configurations. NASA TN D-3748 (1966)
11. Ivanov, N.M.: Catalogue of Different Shapes for Unwinged Reentry Vehicles. Final report, ESA Contract 10756/94/F/BM (1994)
12. Paulat, J.C.: Atmospheric Re-entry Demonstrator: Post Flight Analysis - Aerodynamics. In: Proceedings 2nd Int. Symp. on Atmospheric Re-entry Vehicles and Systems, Arcachon, France (2001)
13. Rolland, J.Y.: Atmospheric Re-entry Demonstrator: Post Flight Restitution. In: Proceedings 2nd Int. Symp. on Atmospheric Re-entry Vehicles and Systems, Arcachon, France (2001)
14. Kuczera, H., Sacher, P.: Reusable Space Transportation Systems. Springer, Heidelberg (2011)
15. Bouilly, J.M., His, S., Macret, J.L.: The ARD Thermal Protection System. In: Proceedings 1st Int. Symp. on Atmospheric Re-entry Vehicles and Systems, Arcachon, France (February 1999)
16. Muylaert, J.: Felici, F., Kordulla, W.: Aerothermodynamics in Europe: ESA Achievements and Challenges. ESA-SP- 487 (2002)

17. Pallegoix, J.F., Collinet, J.: Atmospheric Reentry Demonstrator: Post Flight Analysis, Flight Rebuilding with CFD Control. In: Proceedings 2nd Int. Symp. on Atmospheric Re-entry Vehicles and Systems, Arcachon, France (2001)
18. Tran, P.: ARD Aerothermal Environment. In: Proceedings 1st Int. Symp. on Atmospheric Re-entry Vehicles and Systems, Arcachon, France (1999)
19. Paulat, J.C., Baillion, M.: Atmospheric Re-entry Demonstrator Aerodynamics. In: Proceedings 1st Int. Symp. on Atmospheric Reentry Vehicles and Systems, Arcachon, France (1999)
20. Paulat, J.C.: Synthesis of Critical Points. ESA Manned Space Transportation Programme, Final Report, HT-SF-WP1130-087-AS, Aerospatiale (1997)
21. Baillion, M., Pallegoix, J.F.: HUYGENS Probe Aerothermodynamics. AIAA-Paper 97-2476 (1997)
22. Baillion, M.: Aerothermodynamic Requirements and Design of the HUYGENS Probe. Capsule Aerothermodynamics, AGARD-R-808 (1997)
23. Mazoue, F., Graciona, J., Tournebize, L., Marraffa, L.: Updated Analysis of the Radiative Heat Flux During the Entry of the Huygens Probe in the Titan Atmosphere. ESA SP-563 (2005)
24. (2013), <http://www.esa.int/esasearch?q=Huygens+atmosphere>
25. Burnell, S.I., Liever, P., Smith, A.J., Parnaby, G.: Prediction of the BEAGLE2 Static Aerodynamic Coefficients. In: Proceedings 2nd Int. Symp. on Atmospheric Re-entry Vehicles and Systems, Arcachon, France (2001)
26. Olynick, D.R., Chen, Y.K., Tauber, M.E.: Wake Flow Calculations with Ablation for the Stardust Sample Return Capsule. AIAA-Paper 97-2477 (1997)
27. Smith, A.J., Parnaby, G., Matthews, A.J., Jones, T.V.: Aerothermodynamic Environment of the BEAGLE2 Entry Capsule. ESA-SP-487 (2002)
28. Akimoto, T., Ito, T., Yamamoto, Y., Bando, T., Inoue, Y.: Orbital Re-entry Experiment (OREX) - First Step of Space Return Flight Demonstrations in Japan. IAF Paper 94-V.2.525, Jerusalem Israel (1994)
29. N.N. Activities in the Past. Japan Aerospace Exploration Agency, <http://www.rocket.jaxa.jp/fstr/0c01.html>
30. Yamamoto, Y., Yoshioka, M.: CFD and FEM Coupling Analysis of OREX Aerothermodynamic Flight Data. AIAA-Paper 95-2087 (1995)
31. Murakami, K., Fujiwara, T.: A Hypersonic Flowfield Around a Re-entry Body Including Detailed Base Flow. ESA-SP-367 (1995)
32. Gupta, R.N., Moss, J.N., Price, J.M.: Assessment of Thermochemical Nonequilibrium and Slip Effects for Orbital Re-entry Experiment (OREX). AIAA-Paper 96-1859 (1996)
33. Mehta, R.C.: Aerodynamic Drag Coefficient for Various Reentry Configurations at High Speed. AIAA-Paper No. 2006-3179 (2006)
34. Weiland, C.: Crew Transport Vehicle Phase A, Aerodynamics and Aerothermodynamics. CTV-Programme, HV-TN-3100-X05-DASA, Dasa, Mnchen/Ottobrunn, Germany (1995)
35. Hagmeijer, R., Weiland, C.: Crew Transport Vehicle Phase A, External Shape Definition and Aerodynamic Data Set. CTVProgramme, HV-TN-2100-011-DASA, Dasa, Mnchen/Ottobrunn, Germany (1995)

36. Kok, J.C., Hagmeijer, R., Oskam, B.: Aerodynamic CFD Data for Two Viking-Type Capsule Configurations at Subsonic, Transonic, and Low Supersonic Mach Numbers. CRV/CTV Phase A Study, NLR Contract Report CR 95273 L, NLR Amsterdam, the Netherlands (1995)
37. Blanchet, D., Kilian, J.M., Rives, J.: Crew Transport Vehicle-Phase B, Aerodynamic Data Base. CTV-Programme, HV-TN- 8-10062-AS, Aerospatiale (1997)
38. Menne, S.: Computation of Non-Winged Vehicle Aerodynamics in the Low Supersonic Range. ESA-SP-367 (1995)
39. Weiland, C., Pfitzner, M.: 3-D and 2-D Solutions of the Quasi-Conservative Euler Equations. Lecture Notes in Physics, vol. 264. Springer (1986)
40. Schröder, W., Hartmann, G.: Implicit Solutions of Three-Dimensional Viscous Hypersonic Flows. Computer and Fluids 21(1) (1992)
41. Marzano, A., Solazzo, M., Sansone, A., Capuano, A., Borriello, G.: Aerothermodynamic Development of the CARINA Re-entry Vehicel: CFD Analysis and Experimental Tests. ESA-SP-318 (1991)
42. Solazzo, M., Sansone, A., Gasbarri, P.: Aerodynamic Characterization of the CARINA Re-entry Module in the Low Supersonic Regimes. ESA-SP-367 (1994)
43. Wells, W.L.: Measured and Predicted Aerodynamic Coefficients and Shock Shapes for Aeroassist Flight Experiment Configurations. NASA TP- 2956 (1990)
44. Micol, J.R., Wells, W.L.: Hypersonic Lateral and Directional Stability Characteristics of Aeroassist Flight Experiment in Air and CF4. NASA TM-4435 (1993)
45. Dieudonne, W., Spel, M.: Entry Probe Stability Analysis for the Mars Pathfinder and the Mars Premier Orbiter. ESA-SP-544 (2004)
46. Charbonnier, J.M., Fraysse, H., Verant, J.L., Trainau, J.C., Pot, T., Masson, A.: Aerothermodynamics of the Mars Premier Orbiter in Aerocapture Configuration. In: Proceedings 2nd Int. Symp. on Atmospheric Re-entry Vehicles and Systems, Arcachon, France (2001)
47. Verant, J.L., Pelissier, C., Charbonnier, J.M., Erre, A., Paris, S.: Review of the MSR Orbiter Hypersonic Experimental Campaigns. In: Proceedings 3rd Int. Symp. on Atmospheric Re-entry Vehicles and Systems, Arcachon, France (2003)
48. Chanetz, B., Pot, T., Le Sant, Y., Leplat, M.: Study of the Mars Sample Return Orbiter in the Hypersonic Wind Tunnel R5Ch. In: Proceedings 2nd Int. Symp. on Atmospheric Re-entry Vehicles and Systems, Arcachon, France (2001)
49. Yates, L.A., Venkatapathy, E.: Trim Angle Measurement in Free-Flight Facilities. AIAA-Paper 91-1632 (1991)
50. McGhee, R.J., Siemers, P.M., Pelc, R.E.: Transonic Aerodynamic Characteristics of the Viking Entry and Lander Configuration. NASA TM X-2354 (1971)
51. Sammonds, R.I., Kruse, R.L.: Viking Entry Vehicle Aerodynamics at $M = 2$ in Air and Some Preliminary Test Data for Flight in CO₂ at $M = 11$. NASA TN D-7974 (1975)

52. Whitlock, C.H., Siemers, P.M.: Parameters Influencing Dynamic Stability Characteristics of Viking-Type Entry Configurations at Mach 1.76. *J. of Spacecraft* 9(7) (1972)
53. Uselton, B.L., Schadow, T.O., Mansfield, A.C.: Damping-in-Pitch Derivatives of 120- and 140-Degrees Blunted Cones at Mach Numbers from 0.6 Trough 3. *AEDC-TR-70-49* (1970)
54. Baillion, M., Tran, P., Caillaud, J.: Aerodynamics, Aerothermodynamics and Flight Qualities. *ARCV Programme, ACRVA- TN 1.2.3.-AS*, Aerospatiale (1993)
55. Rochelle, W.C., Ting, P.C., Mueller, S.R., Colovin, J.E., Bouslog, S.A., Curry, D.M., Scott, C.D.: Aerobrake Heating Rate Sensitivity Study for the Aeroassist Flight Experiments. *AIAA-Paper, 89 - 1733* (1989)

Aerothermodynamic Data of Non-Winged Re-entry Vehicles (RV-NW)

- Cones and Bicones -

During the search for simple, appropriate shapes of RV-NW space vehicles the designers discovered the cone, respectively the bicone shapes as possible candidates. In particular the bicone shapes offer the capability to design a mission adapted configuration with specific properties. This is due to their large geometrical possibilities.

5.1 Introduction

Since a long time various blunted cones and bicones were considered for specific manned or unmanned space missions, and some preliminary feasibility studies have been made. Very often the cones and bicones are blunted by spherical pigs. The advantage of cone-based configurations consists in the higher lift-to-drag ratio compared to classical capsules. The family of bicones can be divided into three classes, see, e.g., [1]:

- bluff (fat)-bicones,
- slender-bicones,
- bent-bicones,

Bluff-bicones have in the hypersonic flight regime a maximum lift-to-drag ratio of $L/D_{max} \approx 0.6$, slender-bicones of $L/D_{max} \approx 1.1$ and bent-bicones of $L/D_{max} \approx 1.5$.

In contrast to classical axisymmetric RV-NW's (capsules and probes, see Chapter 4) these shapes generate lift with a positive angle of attack. In general, blunted cones and bicones are appropriate (in the frame of the non-winged vehicle class) for missions where a large cross-range capability, good maneuverability, low landing distortion and low deceleration loads are required, and further when high entry velocities and thin atmospheres are given (for example planetary missions towards Mars or moons of planets).

Despite the obvious advantages of cone-type space vehicles over capsules no operable vehicle of such type was ever built or flown.

In Europe several activities were conducted in the frame of ESA's Crew Transport Vehicle (CTV) studies, [2, 3]. Investigations are also made in the U.S., [4, 5]. In Russia are, besides others, some preliminary studies on biconic shapes, [6].

Fig. 5.1 gives some impressions of biconic shapes studied at Daimler Benz Aerospace (Dasa) in the 1990s.

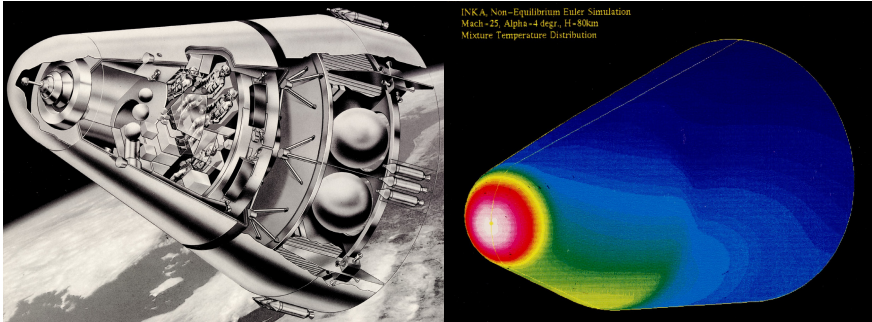


Fig. 5.1. Bicones: Synthetic image taken from a CRV/CTV study performed by Dasa in 1995, initiated by ESA (left), 3D non-equilibrium Euler solution around the bent-bicone configuration INKA, [7], a Dasa study, 1993 (right), free-stream conditions: $M_\infty = 25$, $\alpha = 4^\circ$, $H = 80$ km.

5.2 BLUFF-BICONE (Germany)

5.2.1 Configurational Aspects

A 3D presentation of Dasa's bluff-bicone shape is shown in Fig. 5.2, whereas the drawing in Fig. 5.3 gives the measures which define this configuration. Bluff-bicone shapes have the advantage that the constraints of internal layout (payload accommodation) and of the launch system (usually fairing restrictions of rockets) can better be met than with the other bicone shapes.

5.2.2 Aerodynamic Data of Steady Motion

The aerodynamic data presented below were generated exclusively by the application of approximate design methods like local inclination methods for supersonic and hypersonic Mach numbers and panel methods for subsonic Mach numbers, [8].

Longitudinal Motion

The lift coefficient C_L for the subsonic-transonic and transonic-supersonic flight regimes is plotted in Figs. 5.5 and 5.6. Interesting is the fact, that

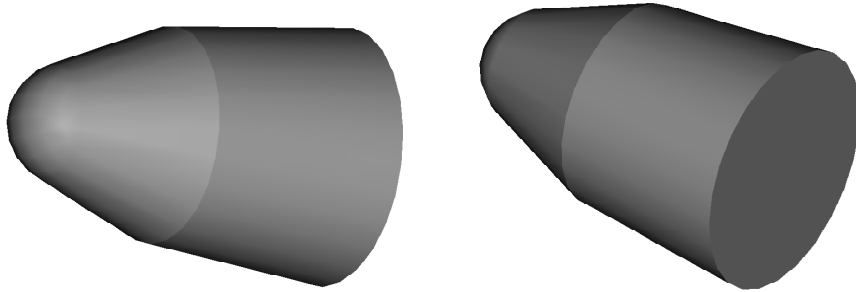


Fig. 5.2. 3D shape presentation of Dasa's BLUFF-BICONE configuration, [3]

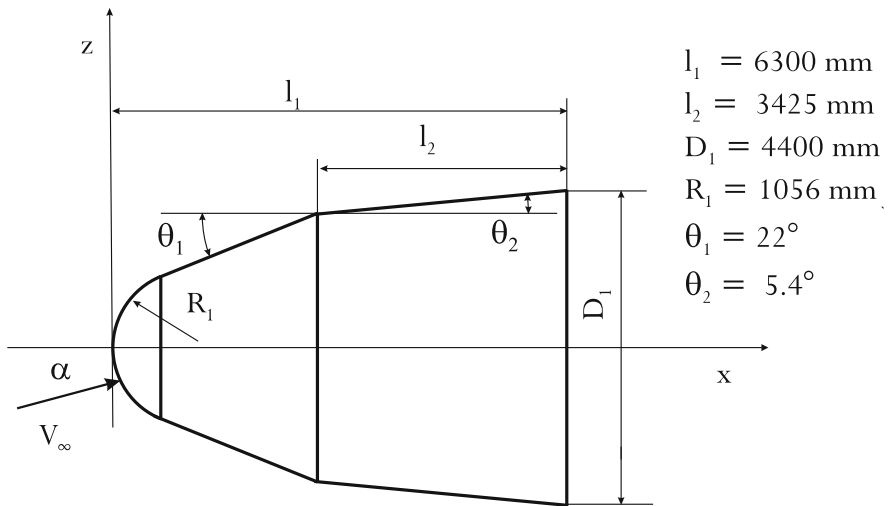


Fig. 5.3. Shape definition of Dasa's BLUFF-BICONE configuration, [3]

the usually found linear behavior of $C_L(\alpha)$ is present only in the transonic regime, whereas for subsonic and super-hypersonic Mach numbers the C_L curves deviate considerably from linearity.

The drag coefficient C_D acts like expected starting with low values in the subsonic regime, then rising to extreme values in the transonic regime and finally again declining to lower values in the supersonic-hypersonic regime, Figs. 5.7, 5.8.

The cross-range capability of a space vehicle is directly related to the lift-to-drag ratio L/D in all speed regimes. This quantity amounts for the bluff-bicone to approximately 0.8 for $\alpha \approx 25^\circ$ in the subsonic regime,

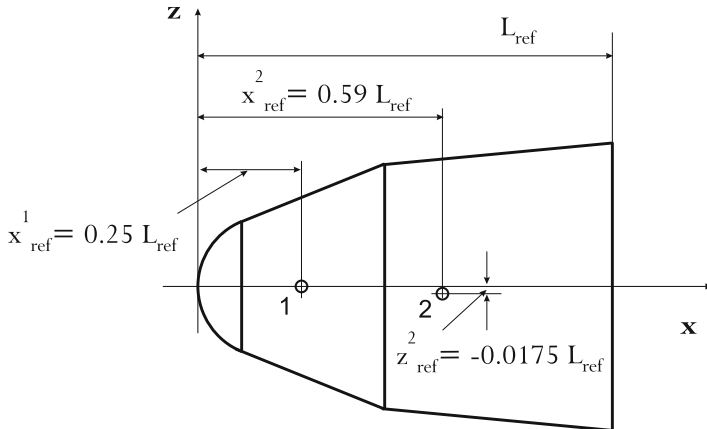


Fig. 5.4. Definition of two moment reference positions used for the presentation of the pitching moment coefficients in Figs. 5.11 - 5.13. **1** $x_{ref} = 0.25 \cdot L_{ref}$, $z_{ref} = 0.0 \cdot L_{ref}$ and **2** $x_{ref} = 0.59 \cdot L_{ref}$, $z_{ref} = -0.0175 \cdot L_{ref}$.

Fig. 5.9, and decreases in the supersonic-hypersonic regime to $L/D \approx 0.65$ for $\alpha \approx 20^\circ$, Fig. 5.10.

Axisymmetric bodies can more efficiently be trimmed, if the center-of-gravity is off the axis of symmetry, [1]. For the nominal moment reference point applied here ($x_{ref} = 0.25 \cdot L_{ref}$, $z_{ref} = 0.0 \cdot L_{ref}$), Fig. 5.4, the vehicle is stable in the whole Mach number regime, but cannot be trimmed, because for all Mach numbers the pitching moment is $C_m \neq 0$ at $\alpha > 0$, Figs. 5.11 and 5.12.

This problem can be overcome either by a suitable selection of the center-of-gravity position (which may be restricted by the internal lay-out of the vehicle) or by employing aerodynamic devices like flaps and brakes (which of course complicates the vehicle design and the control system). As an example for the former approach we have changed the center-of-gravity position to $x_{ref} = 0.59 \cdot L_{ref}$, $z_{ref} = -0.0175 \cdot L_{ref}$ (Fig. 5.4) with the result that for the Mach numbers $M_\infty = 1.35$ and 1.5 the vehicle is still slightly statically stable and can be trimmed at $\alpha \approx 12^\circ$, Fig. 5.13. For higher Mach numbers the pitching moment derivative tends to become zero and no trim is possible.

For two trajectory points ($M_\infty = 1.5$, $\alpha = 20^\circ$ and $\alpha = 25^\circ$) also numerical solutions were generated [9], with the Euler method reported in [10, 11]. Very good agreement was obtained for the drag and the pitching moment, Figs. 5.8 and 5.12, whereas the lift and therefore also the aerodynamic performance L/D deviate somewhat from each other, Figs. 5.6, 5.10, 5.13. Nevertheless the Euler results prove to some extent the reliability of the used engineering methods.

All coefficients approach Mach number independency for $M_\infty \gtrsim 5$.

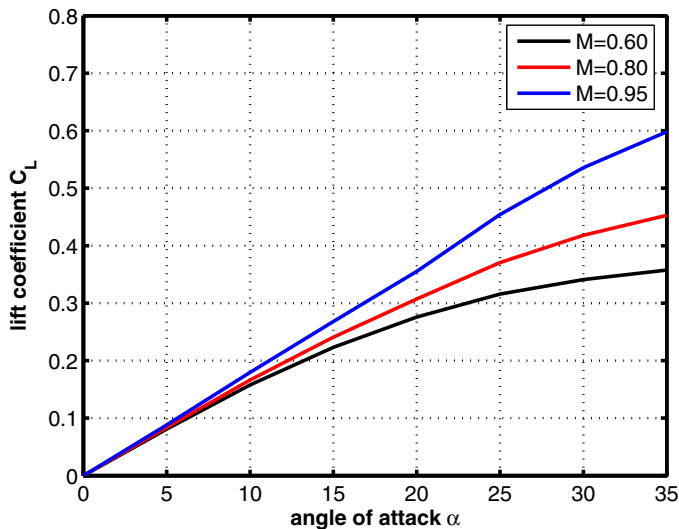


Fig. 5.5. Lift coefficient C_L as function of the angle of attack α for subsonic-transonic Mach numbers, [8]

Lateral Motion

The vehicle is axisymmetric.

5.2.3 Aerodynamic Data of Unsteady Motion

Investigations of dynamic stability were not done.

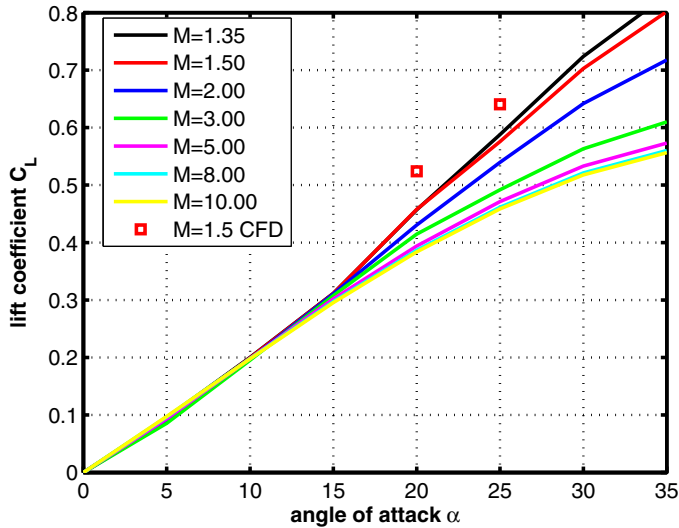


Fig. 5.6. Lift coefficient C_L as function of the angle of attack α for transonic-supersonic Mach numbers, [8]

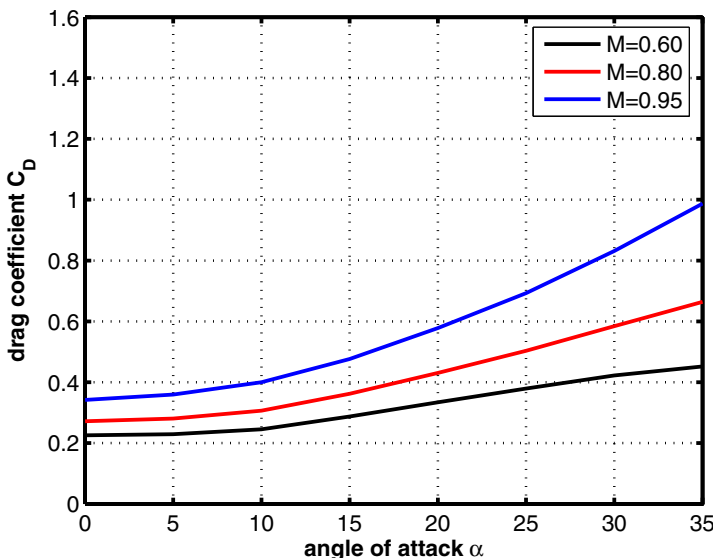


Fig. 5.7. Drag coefficient C_D as function of the angle of attack α for subsonic-transonic Mach numbers, [8].

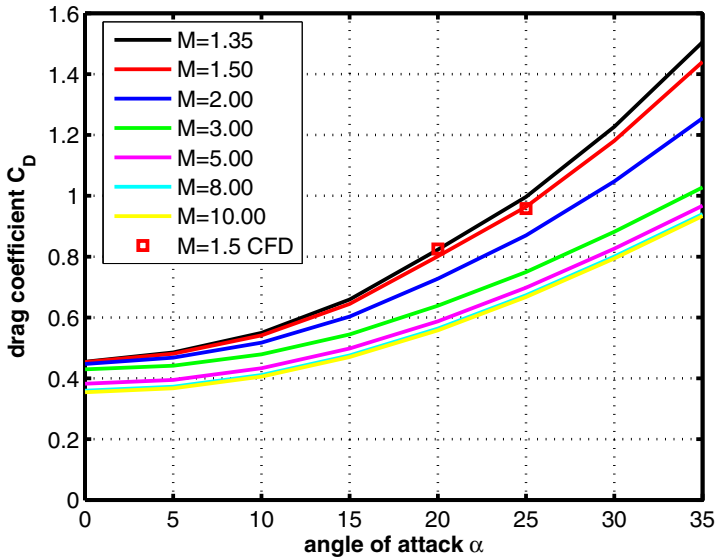


Fig. 5.8. Drag coefficient C_D as function of the angle of attack α for transonic-supersonic Mach numbers, [8].

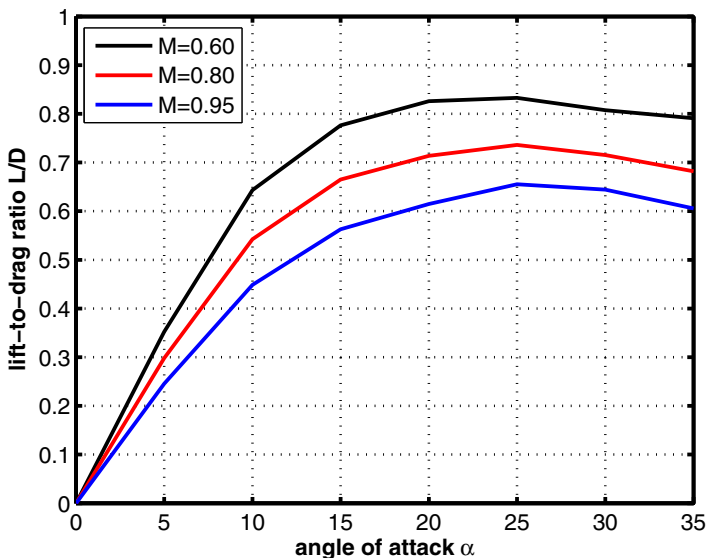


Fig. 5.9. Lift-to-drag ratio L/D as function of the angle of attack α for subsonic-transonic Mach numbers, [8]

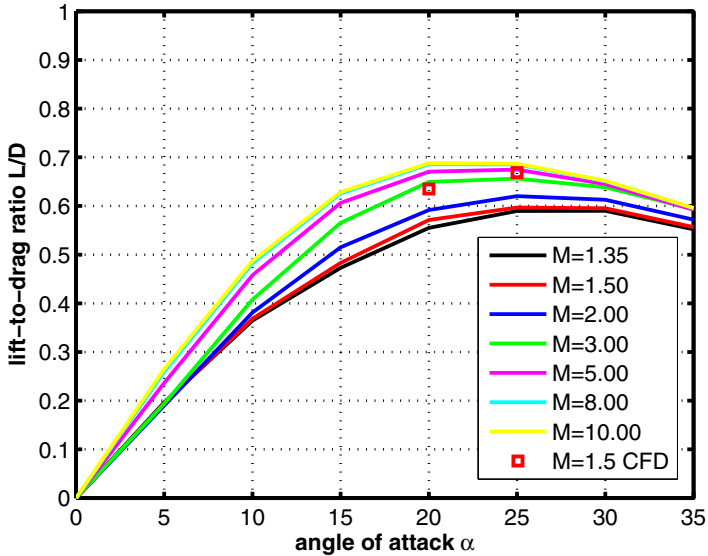


Fig. 5.10. Lift-to-drag ratio L/D as function of the angle of attack α for transonic-supersonic Mach numbers, [8].

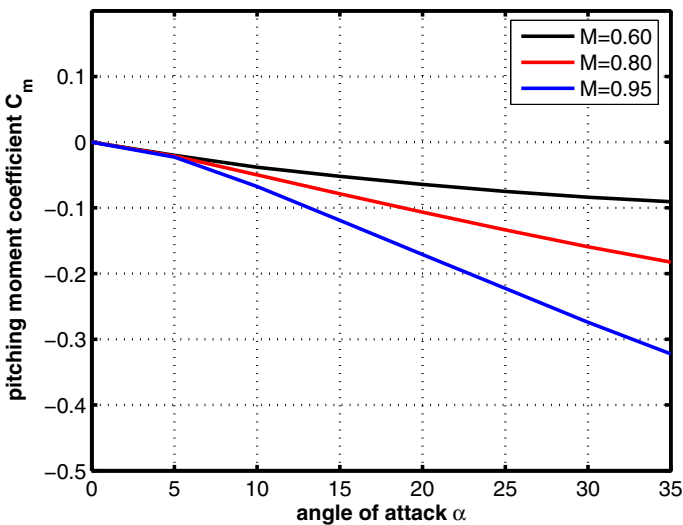


Fig. 5.11. Pitching moment coefficient C_m as function of angle of attack α for subsonic-transonic Mach numbers. Moment reference point $x_{ref} = 0.25 \cdot L_{ref}$, $z_{ref} = 0.0 \cdot L_{ref}$, [8].

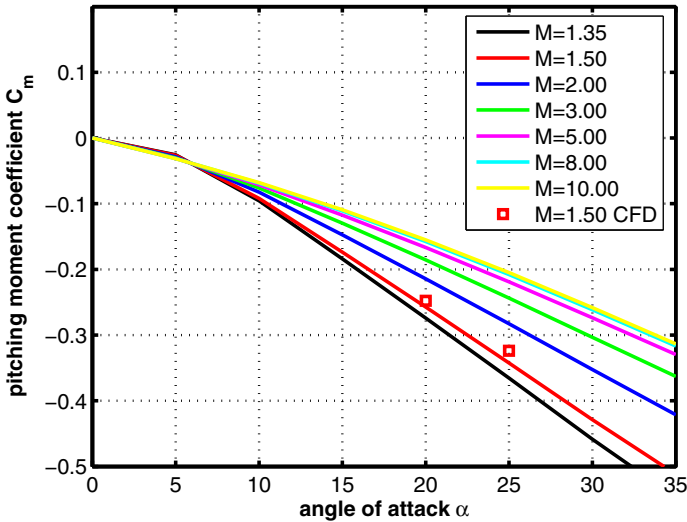


Fig. 5.12. Pitching moment coefficient C_m as function of the angle of attack α for transonic-supersonic Mach numbers. Moment reference point $x_{ref} = 0.25 \cdot L_{ref}$, $z_{ref} = 0.0 \cdot L_{ref}$, [8].

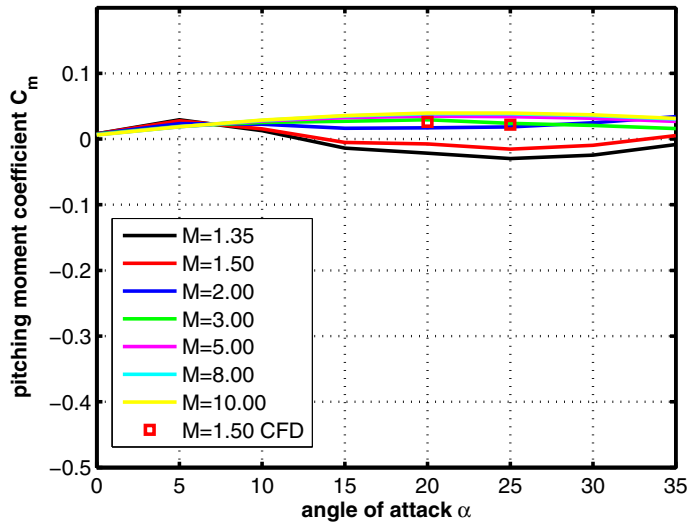


Fig. 5.13. Pitching moment coefficient C_m as function of the angle of attack α for transonic-supersonic Mach numbers. Moment reference point $x_{ref} = 0.590 \cdot L_{ref}$, $z_{ref} = -0.0175 \cdot L_{ref}$, [8].

5.3 SLENDER-BICONIC (Russia)

An increase of the aerodynamic performance L/D can also be attained with a slender-bicone, Fig. 5.14, where the reduction of the diameter D_1 , compared to the bluff-bicone, leads to decreased axial and drag forces and a slight increase of the normal force.

5.3.1 Configurational Aspects

The configuration, which we consider here, was designed at Tsniimash, a Russian Research Institute for space applications located at Kaliningrad near Moscow. The geometric data of the shape are given in Fig. 5.15, [6].

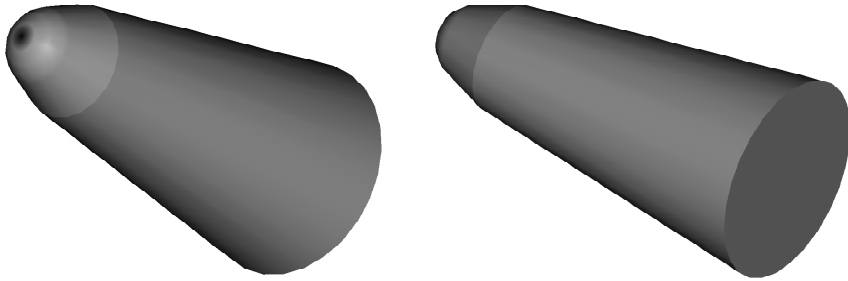


Fig. 5.14. 3D shape presentation of the SLENDER-BICONIC capsule

5.3.2 Aerodynamic Data of Steady Motion

The aerodynamic data discussed below for the Mach numbers $0.60 \leq M_\infty \leq 4$ were obtained by wind tunnel investigations, whereas approximate design methods were applied for the generation of the $M = 5.96$ data, [6].

Longitudinal Motion

The characteristics of the lift coefficient C_L are comparable to the ones of the bluff-bicone, Figs. 5.5 and 5.6. However the slope $\partial C_L / \partial \alpha$ for higher angles of attack is somewhat larger in the transonic regime than in the other flight regimes, Fig. 5.16.

Regarding the drag we expect that it is highest in the transonic regime with a monotonic decrease towards the subsonic as well as supersonic regime. Fig. 5.17 indeed shows this behavior.

The lift-to-drag diagram, Fig. 5.18, exhibits some irregularities, in particular the L/D curve for the Mach number $M_\infty = 5.96$ appears to be somewhat

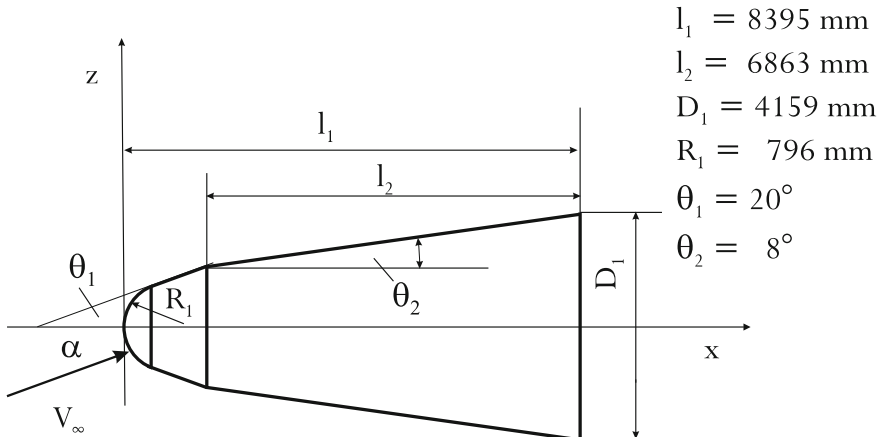


Fig. 5.15. Shape definition of the SLENDER-BICONE capsule, [6]

too high. A possible explanation could be that, as already mentioned above, the aerodynamic values for this Mach number were generated by an approximate design method, whereas the other values were compiled by tests in wind tunnels.

Now we pay our attention to the pitching moment coefficient. The general moment reference point was $x_{ref} = 0.57 \cdot L_{ref}$, $z_{ref} = -0.0667 \cdot L_{ref}$. For this reference point the slender-bicone vehicle behaves unstable for the Mach numbers $M_\infty = 0.6, 0.95, 1.18$. It alters its behavior to a slightly static stability for the Mach numbers $M_\infty = 2.53, 4, 5.96$. In addition for $M_\infty = 2.53$ a trim point is available for an angle of attack value of $\alpha_{trim} \approx 26^\circ$, Fig. 5.19.

The question arises whether there exists a center-of-gravity location where, for all Mach numbers, statically stable and trimmed flight can be secured. In Fig. 5.20 the pitching moment coefficient for such a point ($x_{ref} = 0.42 \cdot L_{ref}$, $z_{ref} = -0.1467 \cdot L_{ref}$) is plotted, but it seems rather doubtful if in practice the lay-out designer can realize such a center-of-gravity location.

In the following we demonstrate in a further example what one has to do in order to trim the vehicle at a specific trajectory point. Let the trajectory point be given by $M_\infty = 5.96$ and $\alpha = 20^\circ$. We then find from Fig. 5.18 a lift-to-drag ratio of $L/D = 1.0707$. Further we use the relations formulated in Section 4.1.

With eq. (4.1) the pitching moment coefficient is transformed from the nominal reference point (P1: $x_{ref} = 0.57 \cdot L_{ref}$, $z_{ref} = -0.0667 \cdot L_{ref}$) to the reference point positioned in the tip of the vehicle ($x_j = 0 \cdot L_{ref}$, $z_j = 0 \cdot L_{ref}$). With eq. (4.2) the center-of-pressure position along the x-coordinate ($z_{cp} = 0$) is calculated to $x_{cp} = 0.5640$. Then with eq. (4.3) the

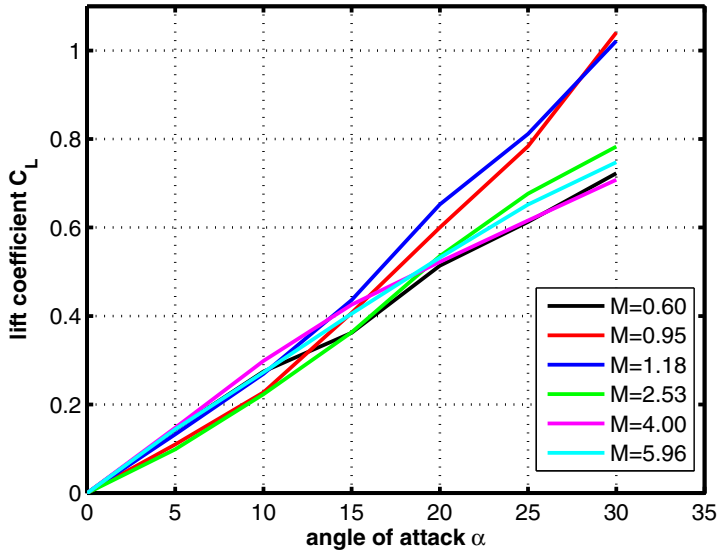


Fig. 5.16. Lift coefficient C_L as function of the angle of attack α , [6]

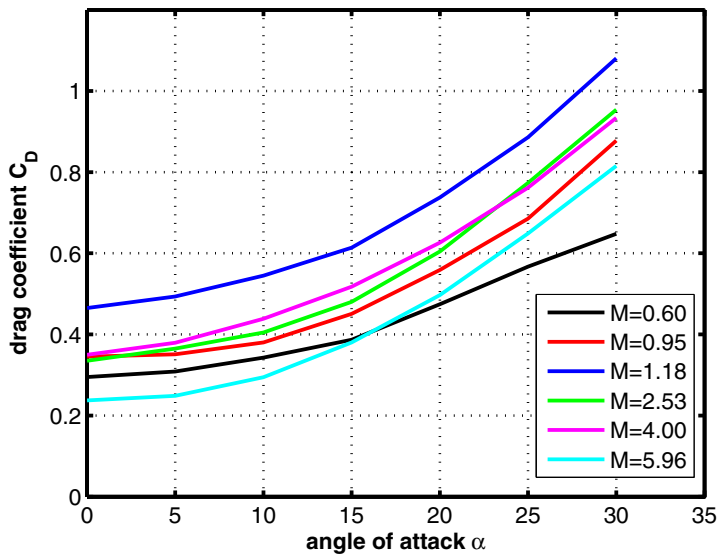


Fig. 5.17. Drag coefficient C_D as function of the angle of attack α , [6]

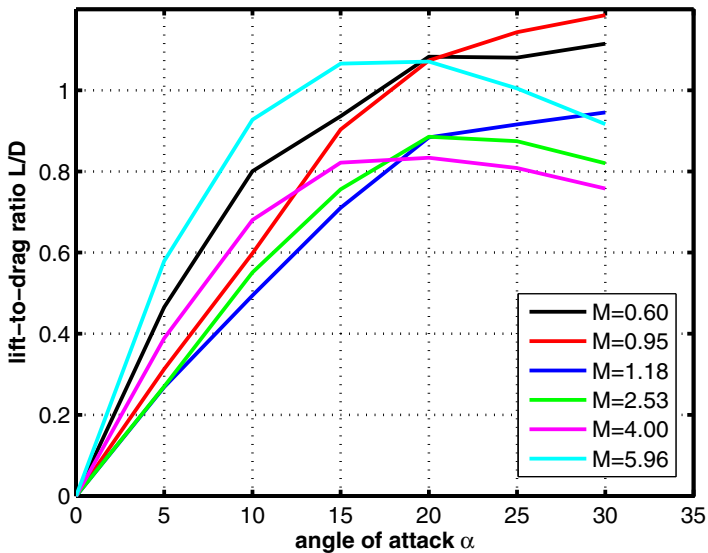


Fig. 5.18. Lift-to-drag ratio L/D as function of the angle of attack α , [6]

line of the center-of-gravity positions is determined, where the vehicle flies trimmed, Fig. 5.21.

We select now two additional trim points on this line, besides the trim point on the x-axis (P3: $x_{ref} = 0.564 \cdot L_{ref}$, $z_{ref} = 0.0 \cdot L_{ref}$), one with a negative z-offset, (P2: $x_{ref} = 0.554 \cdot L_{ref}$, $z_{ref} = -0.0236 \cdot L_{ref}$) and one with a positive z-offset, (P4: $x_{ref} = 0.574 \cdot L_{ref}$, $z_{ref} = +0.0234 \cdot L_{ref}$). This example demonstrates that there exists some margin for the internal vehicle lay-out and the payload accommodation.

Fig. 5.22 shows the pitching moment coefficient for these three trim points and the nominal reference point.

Lateral Motion

The vehicle is axisymmetric.

5.3.3 Aerodynamic Data of Unsteady Motion

Results of investigations of dynamic stability are not available.

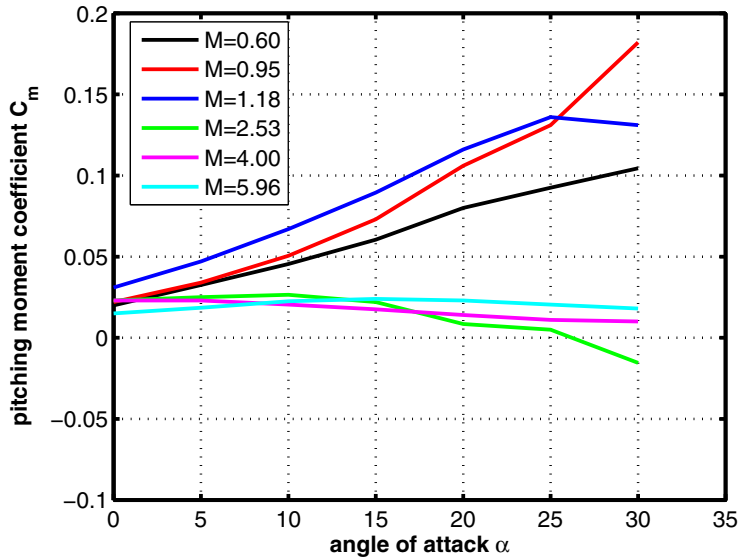


Fig. 5.19. Pitching moment coefficient C_m as function of the angle of attack α . Moment reference point $x_{ref} = 0.57 \cdot L_{ref}$, $z_{ref} = -0.0667 \cdot L_{ref}$, [6].

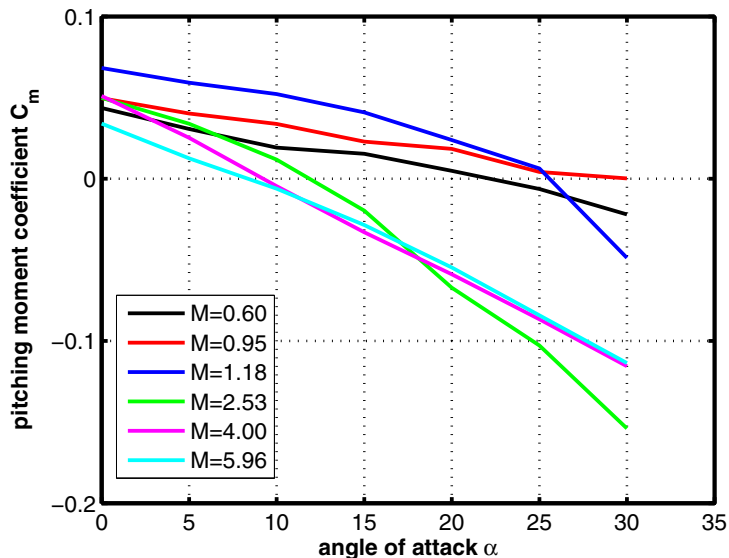


Fig. 5.20. Pitching moment coefficient for stable and trimmed flight. Moment reference point $x_{ref} = 0.42 \cdot L_{ref}$, $z_{ref} = -0.1467 \cdot L_{ref}$, [6].

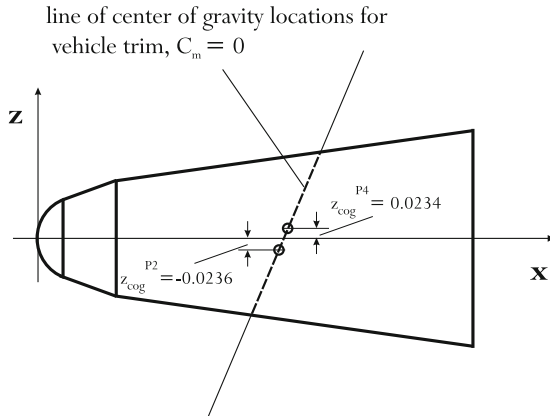


Fig. 5.21. Line of center-of-gravity locations for vehicle trim, $C_m = 0$. $M_\infty = 5.96$, $\alpha_{trim} = 20^\circ$, $x_{cp} = 0.5640$, $L/D_{trim} = 1.0707$ (see Figs. 5.18, 5.22).

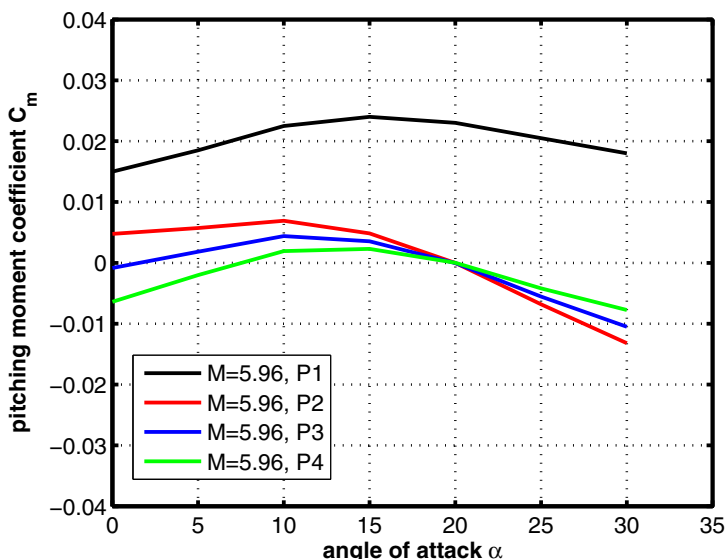


Fig. 5.22. Comparison of pitching moment coefficient C_m as function of angle of attack α for various moment reference points. Mach number $M_\infty = 5.96$.

P1: $x_{ref} = 0.570 \cdot L_{ref}$, $z_{ref} = -0.0667 \cdot L_{ref}$,
 P2: $x_{ref} = 0.554 \cdot L_{ref}$, $z_{ref} = -0.0236 \cdot L_{ref}$,
 P3: $x_{ref} = 0.564 \cdot L_{ref}$, $z_{ref} = -0.0000 \cdot L_{ref}$,
 P4: $x_{ref} = 0.574 \cdot L_{ref}$, $z_{ref} = +0.0234 \cdot L_{ref}$.

5.4 BENT-BICONE (USA)

In the 1980s and 1990s there were some activities in the USA for designing non-winged re-entry vehicles (RV-NW) with relatively high lift-to-drag ratio L/D , [4, 5, 7]. One reason for that was to find a space vehicle with a simple shape, which is able to perform reliably the transfer between orbits of different altitudes using for this operation a more or less deep immersion into Earth's atmosphere. Such vehicles are called Aeroassisted Orbital Transfer Vehicles (AOTV). Another reason was the investigation of space vehicle shapes for the selection of a suitable Crew Transport Vehicle (CTV) in the frame of an ESA study, [7]. The background of this study was an European solution for servicing the International Space Station (ISS).

One group of these configurations was given by bent-bicone shapes, where as an example we consider now the vehicle described in [5].

5.4.1 Configurational Aspects

Figs. 5.23 and 5.24 show the bent-bicone shape, for which aerodynamic data for the two supersonic-hypersonic Mach numbers $M_\infty = 5.9$ and 10.1 exist, [5]. Note: The dimensions of this configuration are those of a wind tunnel model.

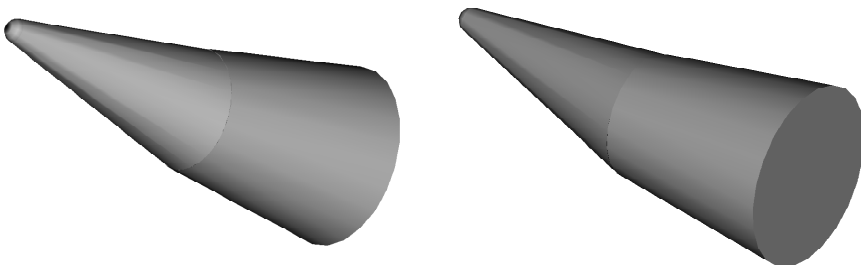


Fig. 5.23. 3D shape presentation of the BENT-BICONE capsule, [5]

5.4.2 Aerodynamic Data of Steady Motion

Longitudinal Motion

The aerodynamic data were established by wind tunnel tests. The lift coefficient C_L is shown in Fig. 5.25. It behaves like expected. The drag coefficient C_D , plotted in Fig. 5.26, holds lower values for small angles of attack

$$\begin{aligned}
 l_1 &= 182.52 \text{ mm} \\
 l_2 &= 80.85 \text{ mm} \\
 l_3 &= 77.32 \text{ mm} \\
 D_1 &= 76.20 \text{ mm} \\
 R_1 &= 5.79 \text{ mm} \\
 \theta_1 &= 7^\circ \\
 \theta_2 &= 12.84^\circ \\
 \theta_3 &= 7^\circ
 \end{aligned}$$

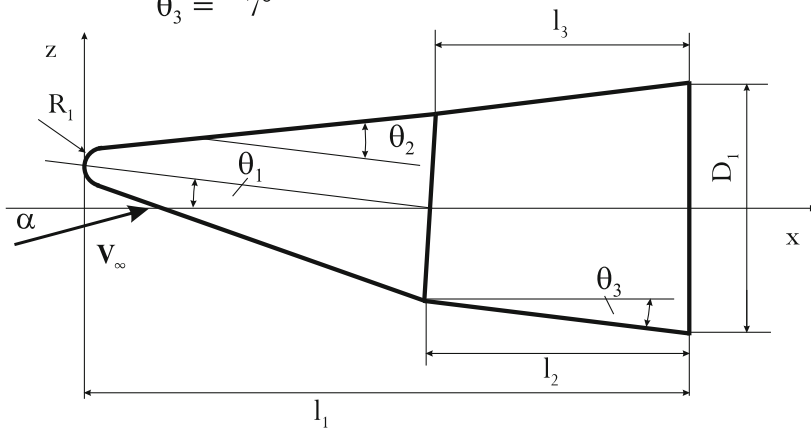


Fig. 5.24. Shape definition of the BENT-BICONE capsule, [5]

($\alpha \leq 10^\circ$) compared to the other bicone shapes, discussed before in this chapter. The aerodynamic performance L/D achieves values in the hypersonic regime of approximately 1.4, Fig. 5.27. Bent-bicones generate asymmetric flow fields even at zero incidence, which supports the trim capacity of the shape, as can be seen in Fig. 5.28. Obviously, in the hypersonic regime statically stable and trimmed flight is possible for realistic center-of-gravity locations and angles of attack ($22^\circ \lesssim \alpha_{trim} \lesssim 24^\circ$).

Lateral Motion

No data are available regarding the lateral motion.

5.4.3 Aerodynamic Data of Unsteady Motion

Results of investigations of dynamic stability are not available.

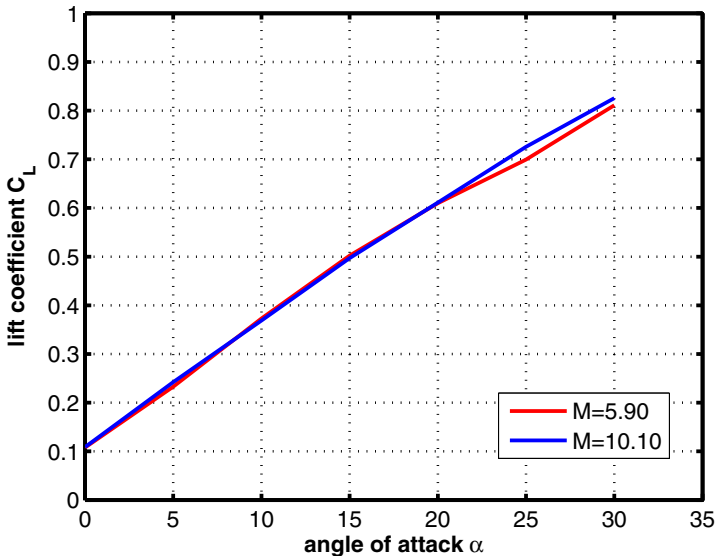


Fig. 5.25. Lift coefficient C_L as function of the angle of attack α , [5]

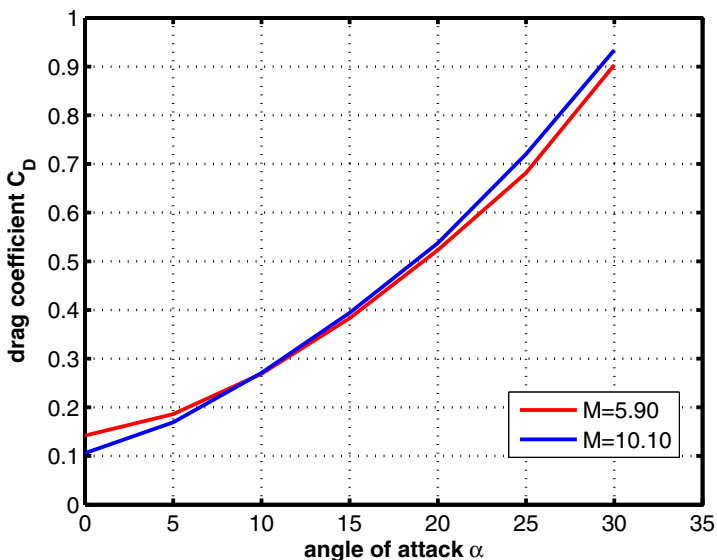


Fig. 5.26. Drag coefficient C_D as function of the angle of attack α , [5]

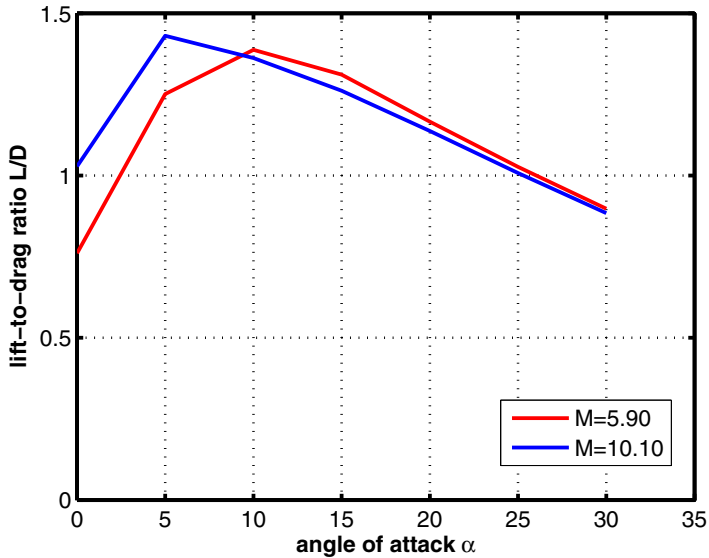


Fig. 5.27. Lift-to-drag ratio L/D as function of the angle of attack α , [5]

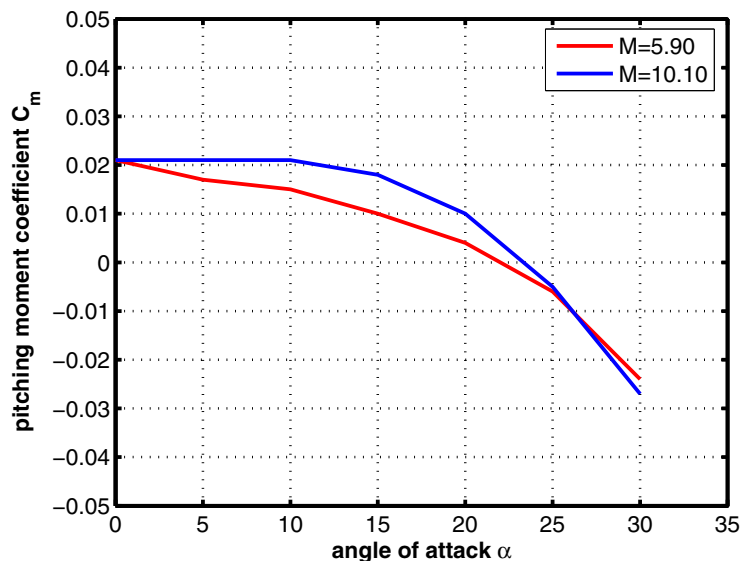


Fig. 5.28. Pitching moment coefficient C_m as function of the angle of attack α . Moment reference point $x_{ref} = 0.554 \cdot L_{ref}$, $z_{ref} = 0.0 \cdot L_{ref}$, [5].

5.5 COLIBRI (Germany)

The utilization of the International Space Station (ISS) as an experimental facility requires a frequent sample return opportunity, which can be provided, for example, by a small, unmanned and controllable re-entry capsule. Therefore the institute of space systems IRS (Institut für Raumfahrtssysteme) of the University of Stuttgart, Germany, proposed a design of a space vehicle on the basis of a simple sphere-cone configuration with a flattened lower surface, where a body flap with two separate parts was mounted. The capsule was named COLIBRI, Figs. 5.29 and 5.30, [12, 13]. In the frame of a small technology program this capsule was also foreseen to serve as a testbed for

- the provision of aerothermodynamic flight data with the goal to verify the aerothermodynamic data base, established by wind tunnel tests and numerical simulation methods (CFD),
- the investigation and test of advanced thermal protection materials,
- the proof of the suitability of a specific re-entry guidance, navigation and control system.

The total mass of the capsule depends on the mission to be performed (number of experiments and/or flight measurement systems, etc.), whereby it was envisaged not to exceed the 300 kg level. Further, it was proposed to perform a demonstrator flight in the early 2000s as a piggy-back payload on the Russian FOTON capsule launched by a Russian SOYUZ rocket. But unfortunately due to budget restrictions this never happened.

5.5.1 Configurational Aspects

Three-dimensional versions of the COLIBRI shape are plotted in Fig. 5.29, where the body flap is not deflected ($\eta = 0^\circ$). The geometrical relations are shown in Fig. 5.30, [12, 13]. In the frame of the configurational design work other configurations were also tested where in particular the flattened part of the lower surface was varied, [12]. The reason for this was that the trim angle of attack α_{trim} of the nominal shape was relatively small ($\alpha_{trim} > 10^\circ$), leading to low L/D values.

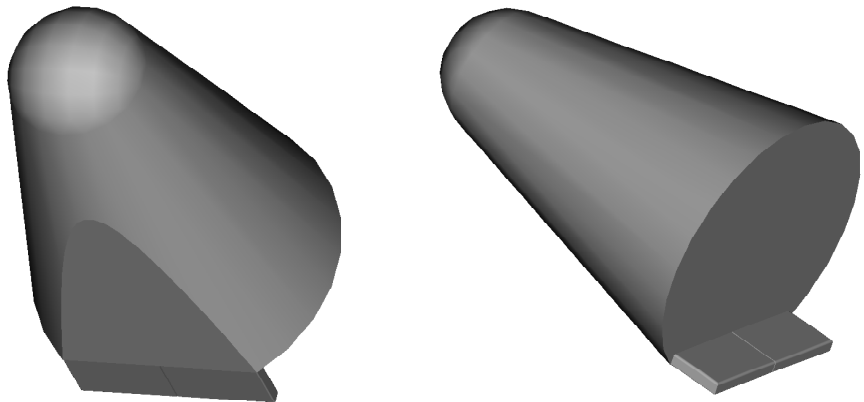


Fig. 5.29. 3D shape presentation of the COLIBRI vehicle

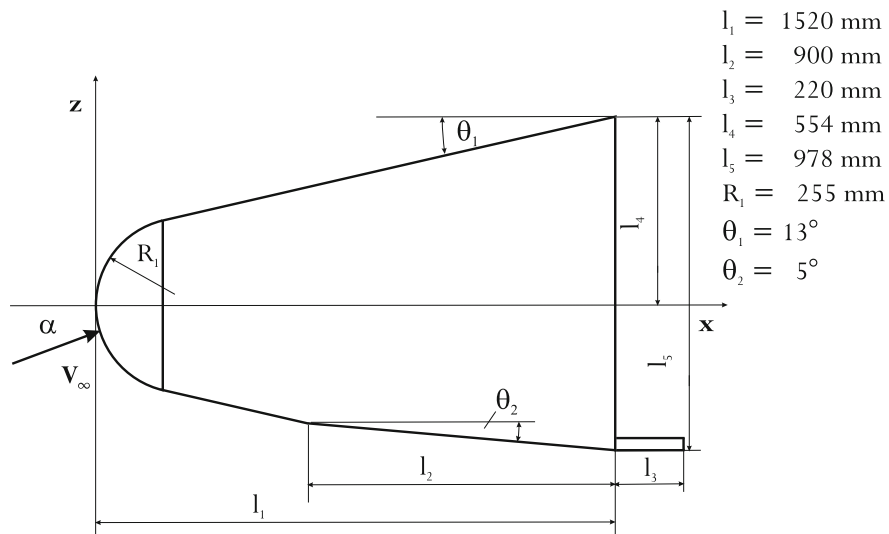


Fig. 5.30. Shape definition of the COLIBRI vehicle, [12, 13]

5.5.2 Aerodynamic Data of Steady Motion

Longitudinal Motion

The performance data presented were generated by measurements in the wind tunnels TMK and H2K of the German Aerospace Center DLR at Cologne. Euler computations around the COLIBRI configuration without the body flap device were also conducted for some trajectory points and can be found in [13]. The data of the following four figures (Figs. 5.33 - 5.35) were obtained for a COLIBRI shape with a body flap deflection of $\eta = 10^\circ$, see Fig. 5.31. A positive (downward) body flap deflection increases the longitudinal static stability. For the drag coefficient C_D values for the Mach numbers $M_\infty = 0.4, 0.6, 1.05, 1.4, 2, 3, 4, 8.7$ are available, Fig. 5.33. Unfortunately for the lift coefficient C_L , and therefore also for the aerodynamic performance L/D , we find in [12] only values for $M_\infty = 1.4, 2, 3, 4$, Figs. 5.32 - 5.34. The original reference point for the pitching moment was $x_{ref}/l_1 = 0.58$, $z_{ref}/l_1 = -0.028$ for Mach number values $M_\infty = 1.4, 2, 3, 4$. Due to problems with the directional stability the reference point was moved forward to $x_{ref}/l_1 = 0.51$. For that value the pitching moment coefficient for $M_\infty = 8.7$ is also plotted in Fig. 5.35. The trim angle α_{trim} lies between $2^\circ \lesssim \alpha_{trim} \lesssim 5^\circ$ for the $M_\infty = 2, 3, 4$ curves but no positive trim angle is available for $M_\infty = 1.4$. The trim angle increases with decreasing body flap deflection, but decreases when the reference point is moved forward. All together it seems difficult with this configuration to attain L/D values of 0.6 or larger, because the trim angle tends to be at the maximum $\alpha_{trim} \approx 10^\circ$.

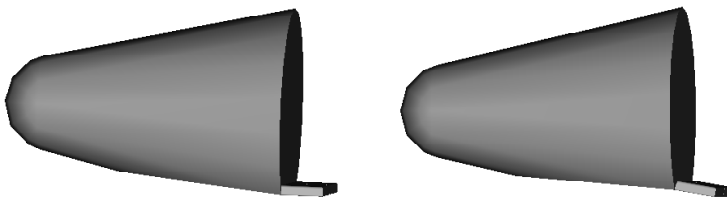


Fig. 5.31. Comparison of 3D shapes of COLIBRI vehicle with different body flap deflections: $\eta = 0^\circ$ (left), $\eta = 10^\circ$ (right)

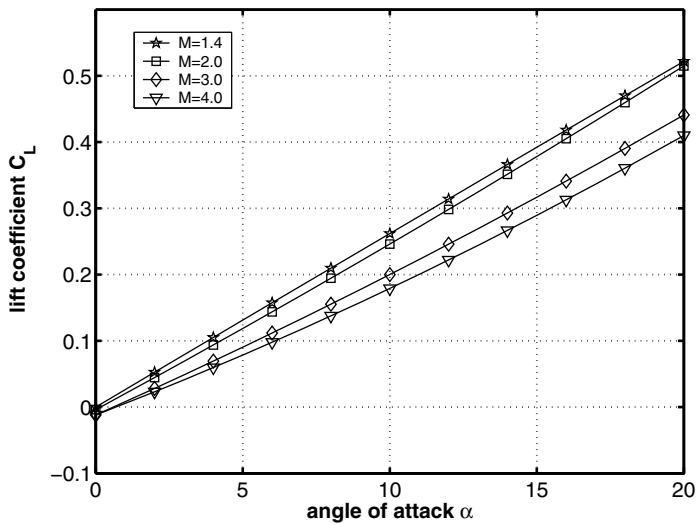


Fig. 5.32. Lift coefficient C_L as function of the angle of attack α , [12]. Body flap deflection $\eta = 10^\circ$.

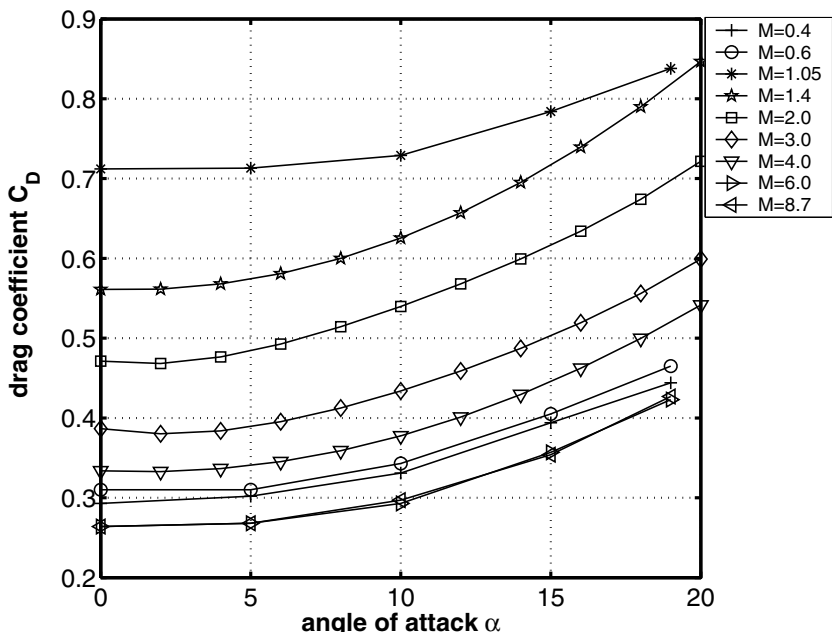


Fig. 5.33. Drag coefficient C_D as function of the angle of attack α , [12]. Body flap deflection $\eta = 10^\circ$.

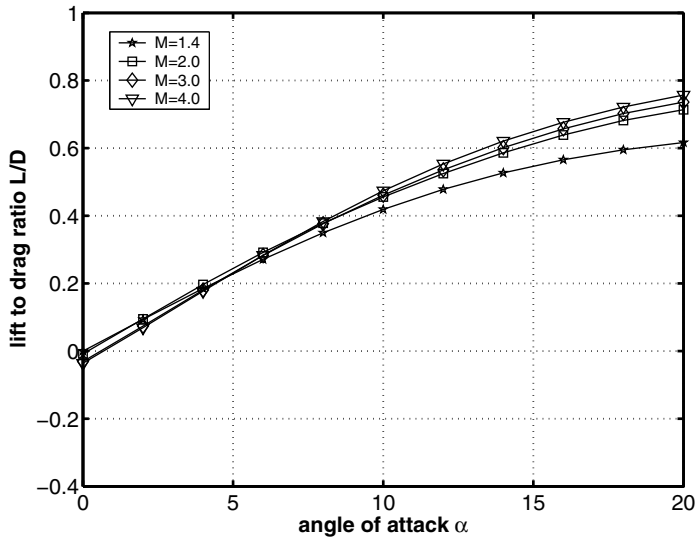


Fig. 5.34. Lift to drag ratio L/D as function of the angle of attack α , [12]. Body flap deflection $\eta = 10^\circ$.

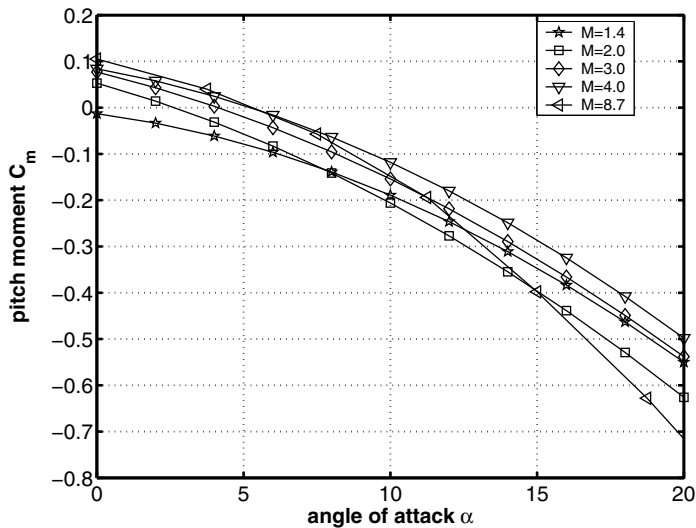


Fig. 5.35. Pitching moment coefficient C_m as function of the angle of attack α , [12]. Body flap deflection $\eta = 10^\circ$. Moment reference point for $M_\infty = 1.4, 2, 3, 4$ curves $x_{ref}/l_1 = 0.58$, $z_{ref}/l_1 = -0.028$, and for the $M_\infty = 8.7$ curve $x_{ref}/l_1 = 0.51$, $z_{ref}/l_1 = -0.028$.

Lateral Motion

As mentioned before the nominal moment reference point $x_{ref}/l_1 = 0.58$, $z_{ref}/l_1 = -0.028$ generates a directional instability in the subsonic flight domain. This was the reason for moving the reference point forward to the x -position $x_{ref}/l_1 = 0.51$, which unfortunately leads on the other hand to lower trim angles with the consequence of a lower aerodynamic performance L/D , as Fig. 5.34 exhibits. For the adjusted reference point the directional stability is indifferent for $M_\infty = 0.6$, whereas for $M_\infty = 1.4$ and 4 stability ($\partial C_n/\partial\beta > 0$) is ensured, Fig. 5.36. The roll moment coefficient was only measured for $M_\infty = 4$. Fig. 5.37 demonstrates that for this Mach number roll stability is given ($\partial C_l/\partial\beta < 0$).

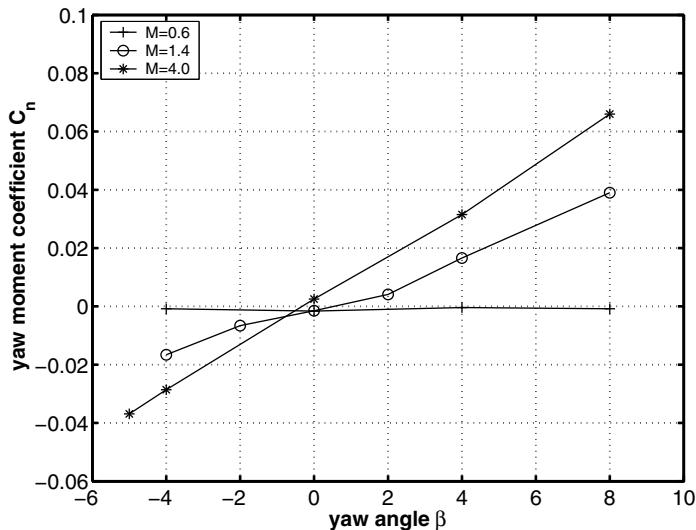


Fig. 5.36. Yawing moment coefficient C_n as function of the angle of yaw β , [12]. Moment reference point $x_{ref}/l_1 = 0.51$, $z_{ref}/l_1 = -0.028$. Body flap deflection $\eta = 0^\circ$.

5.5.3 Aerodynamic Data of Unsteady Motion

Dynamic stability data are not available.

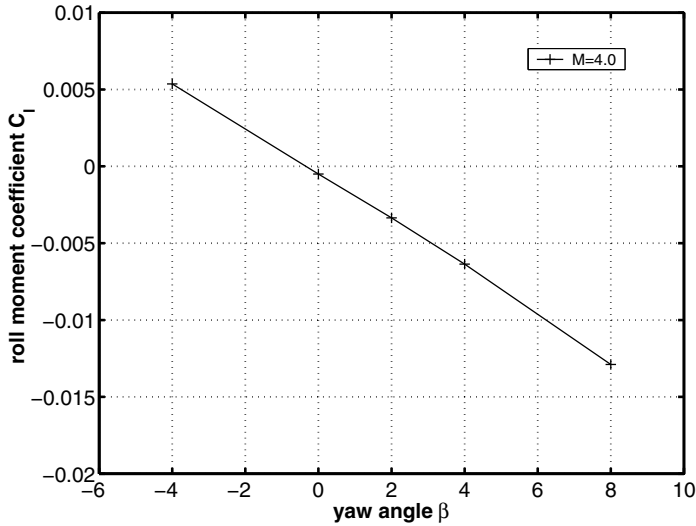


Fig. 5.37. Rolling moment coefficient C_l as function of the angle of yaw β , [12]. Moment reference point $x_{ref}/l_1 = 0.51$, $z_{ref}/l_1 = -0.028$. Body flap deflection $\eta = 0^\circ$.

5.6 IRDT (Inflatable Re-entry Demonstrator) (Russia-Germany)

The Inflatable Re-entry and Descent Technology (IRDT) concept was developed by the Russian space research organization NPO Lavoshkin. The classical non-winged re-entry vehicles (RV-NW) need for the re-entry process a heat shield and for the landing procedure a parachute or parafoil system. Instead, the IRDT system deploys before re-entry the first stage of an inflatable braking unit (IBU) which is able to withstand the extreme flow conditions in hypersonic flight. This envelope increases the vehicle diameter from 0.80 m to 2.30 m, Figs. 5.38 and 5.40. Further, for the landing procedure, a second stage of the inflatable braking unit is deployed. This takes place, when the flight Mach number approaches approximately $M_\infty \approx 0.8$. Thereby the vehicles' diameter is increased to 3.80 m. The main advantage of the IRDT system consists in the considerably lower launch volume and mass compared to the extensive and heavy thermal protection and landing systems of classical capsules.

In Fig. 5.38 the mission sequence from de-orbiting to landing is illustrated, showing the small rigid capsule as orbital configuration, the vehicle, when the first stage of IBU is deployed at an altitude of $H = 100$ km, and the vehicle in landing configuration having the second stage of IBU unfolded, [14, 15].

A qualification flight was carried out on Feb. 9, 2000. For a safe landing (touch down on the ground) the deployed second stage of the IBU system should decelerate the velocity of the vehicle to $v_\infty = 13 - 15$ m/s. Measured were velocities of approximately 60 m/s, which substantiate the suspicion, that the second stage of the IBU was not deployed correctly. Therefore the flight has to be considered as not completely successful, [14, 15]. There were several plans for further demonstration flights, but up to the year 2012 none of these were realized.

5.6.1 Configurational Aspects

The orbital configuration contains the stowed IBU system and the equipment container, where the payload is accommodated. This orbital configuration is the rigid part of the IRDT system consisting of a blunt heat shield and a cone with a semi-apertural angle of 45°, Fig. 5.39.

The technical dimensions of the rigid part (orbital configuration) and of the configuration with deployed first stage of the inflatable braking unit are exhibited in Fig. 5.40.

5.6.2 Aerodynamic Data of Steady Motion

The aerodynamic coefficients presented below were made basically available by NPO Lavoshkin, [17]. In the frame of a cooperation the Deutsche

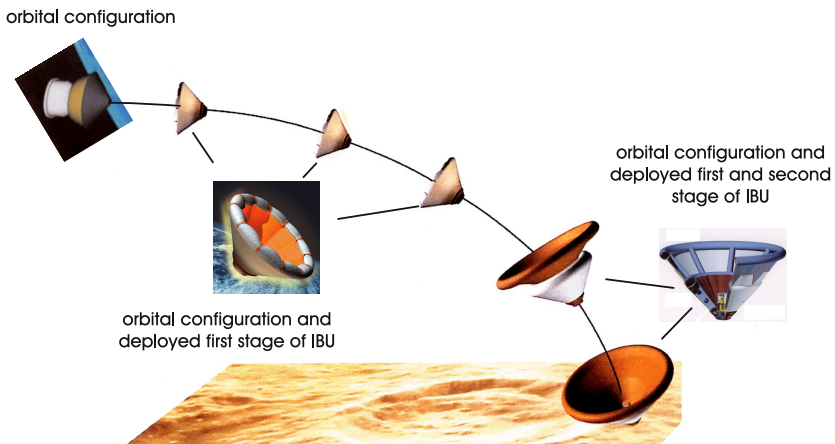


Fig. 5.38. IRDT: Schematic of the de-orbiting, the re-entry and the landing process, [14, 15]

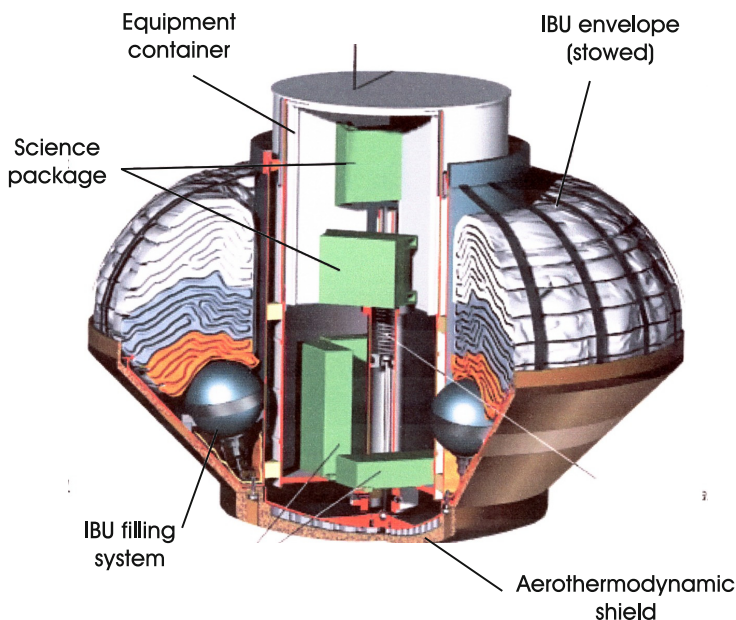


Fig. 5.39. IRDT: Orbital configuration with the equipment container and the stowed IBU envelope, [14]

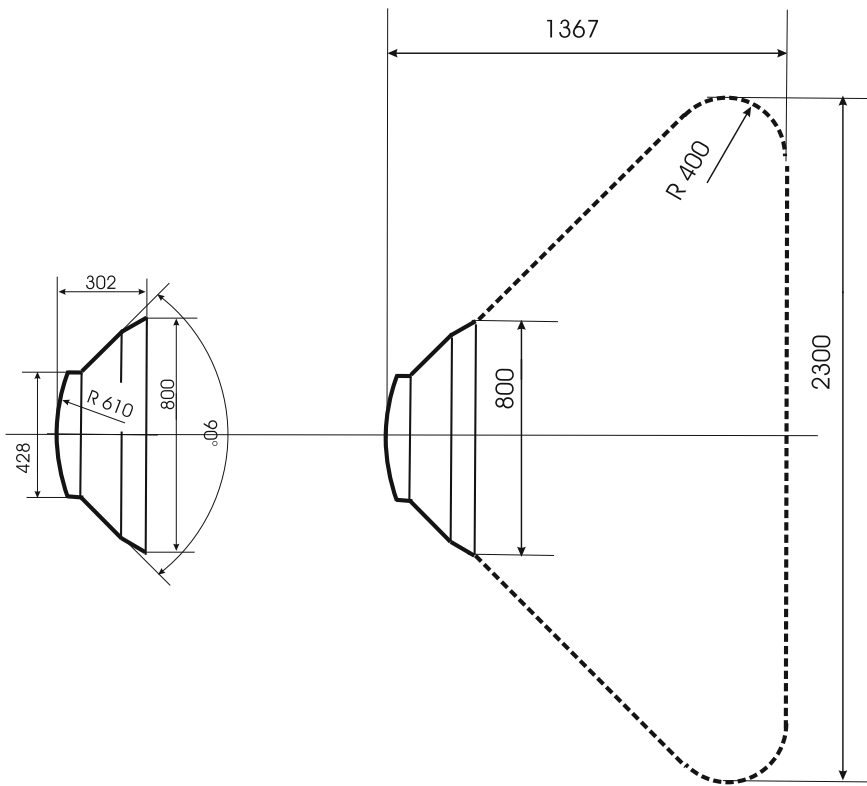


Fig. 5.40. Rigid part of the IRDT capsule (left), rigid part and deployed first stage of the inflatable braking unit (right); shape configurations with dimensions, [16]

Aerospace (Dasa, later EADS) in Germany had contributed to the completion of this aerodynamic data base through a series of numerical solutions (CFD) using the Euler equations, [18]. Fig. 5.41 shows for the Mach number $M_\infty = 5$ some results of the numerical simulations around the IRDT shape: rigid part and deployed first stage of the IBU. High Mach number flows ($M_\infty = 9$) were investigated in a wind tunnel for firstly the rigid part only and secondly the rigid part and the deployed first stage of the IBU. In Figs. 5.42 and 5.43 Schlieren photographs are presented illustrating the bow shock formation and its interaction with embedded shocks.

It is interesting to see that the embedded shock, generated behind the heat shield due to the cone, strengthens the bow shock and bends it against the oncoming flow. This behavior can be identified in both the numerical

solution on the windward side (Fig. 5.41, left) and the wind tunnel Schlieren photograph (Fig. 5.42). The aerodynamic data set presented below is valid for the rigid part and the deployed first stage of the IBU, Fig. 5.40 (right).

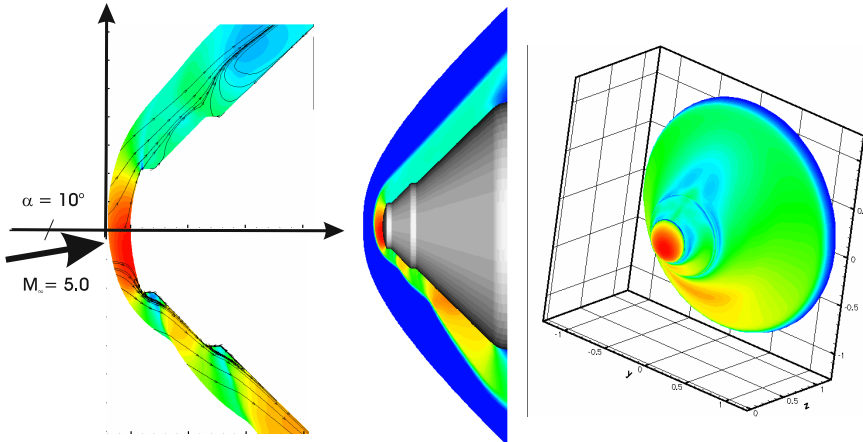


Fig. 5.41. IRDT: Numerical flow field simulation (Euler solution). Shown are the pressure coefficient distributions on the surface of the vehicle (right), in the plane of symmetry (middle), and in a zoomed front part, where also streamlines are plotted (left), [17]. $M_\infty = 5$, $\alpha = 10^\circ$.

Longitudinal Motion

The aerodynamic data set delivered by Lavoshkin in 1999 to Dasa had contained the two Mach numbers $M_\infty = 0$ and 100. The intention with these two Mach numbers was as follows:

- Mach number $M_\infty = 0$ should indicate that for the subsonic Mach numbers up to $M_\infty \approx 0.35$ truly incompressible flow can be expected and that the aerodynamic coefficients are in general constant between $M_\infty = 0$ and 0.35,
- Mach number $M_\infty = 100$ should indicate that the Mach number independence principle for hypersonic flows is valid, [1], which means that at least beyond $M_\infty \gtrsim 10$ no significant changes of the aerodynamic coefficients appear.

Firstly we mention, that due to the strong bluntness of the IRDT shape a positive lift is attained only for negative angles of attack, as it is typical for capsules, see Section 4.1. We have to accept this as true, despite the fact that the aft body of the IRDT shape consists of a truncated cone with a positive semi-apertural angle in contrast to the classical capsules, where the

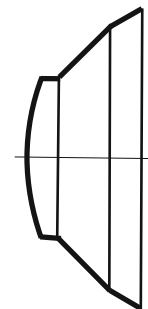
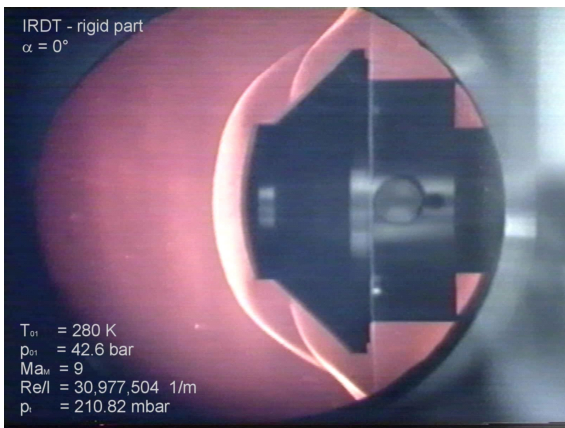


Fig. 5.42. Rigid part of the IRDT vehicle only. Test in a wind tunnel at Mach number $M_\infty = 9$, $\alpha = 0^\circ$ (left), shape configuration (right), [16, 17].

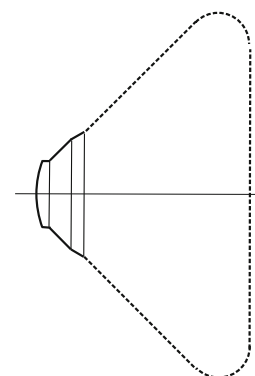
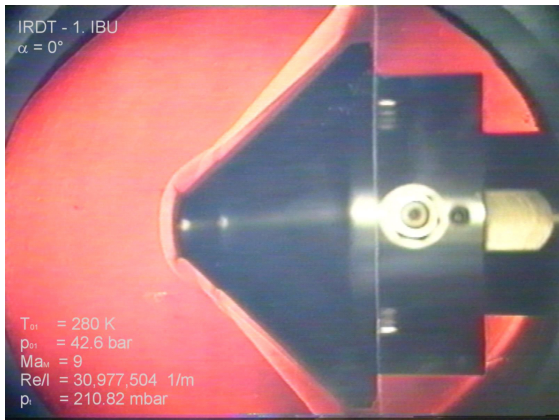


Fig. 5.43. Rigid part of the IRDT vehicle and deployed first stage of the inflatable braking unit (IBU). Test in a wind tunnel at Mach number $M_\infty = 9$, $\alpha = 0^\circ$ (left), shape configuration (right), [16, 17].

semi-apertural angle is negative, see for example the APOLLO or the SOYUZ shapes, Chapter 4.

A view at the diagram of the lift coefficient, Fig. 5.44, reveals that a large spread of C_L exists for the various Mach numbers. The lift coefficient behaves in general linear for angles of attack up to $\alpha \approx -30^\circ$. The values of the numerical simulation confirm on the whole the data of the aerodynamic data base, except for the trajectory point $M_\infty = 5$, $\alpha = -30^\circ$. There, it seems, that the convergence of the numerical solution was not completely achieved.

The drag is lowest in the low subsonic regime ($M_\infty = 0$) and highest for $M_\infty = 2$, Fig. 5.45. For hypersonic Mach numbers and the Mach number $M_\infty = 1$ we find very similar values of the drag coefficient, which is at least surprising. The expectation was that the drag is to be highest in the vicinity of $M_\infty \approx 1$, therefore we do not have an explanation for that.

The aerodynamic performance L/D is plotted in Fig. 5.46. The curve progressions (for angles of attack up to $\alpha \approx -60^\circ$) do not announce any maximum as it is the case for cone or bicone shapes as well as the winged shapes (see Chapter 6). Instead, this behavior supports the assessment that the IRDT shape acts more as a classical capsule than as a blunted cone. Note, that the lift and drag coefficients as well as the lift-to-drag ratio become Mach number independent above $M_\infty \approx 5$.

For all the Mach numbers investigated longitudinal static stability (pitch stability) is preserved, Fig. 5.47¹. Axisymmetric bodies, where the moment reference point lies on the line of symmetry (in this case here $x_{ref} = 0.325D$, $z_{ref} = 0$), are difficult to trim, see Section 4.1. The pitching moment for $\alpha = 0^\circ$ must be zero. As one can see, this condition is slightly violated by the numerical simulation results for $M_\infty = 7.5$. With a z-offset of the center-of-gravity the trim behavior of the vehicle is very much improved. Fig. 5.48 exhibits for the five Mach numbers $M_\infty = 0, 1, 2, 5, 100$ of the figure above the curve progression of the pitching moment, when the center-of-gravity is positioned slightly underneath of the symmetry line ($z_{ref} = -0.04D$). We then discern that the vehicle is trimmed in the whole Mach number range at angles of attack between $-23^\circ \lesssim \alpha_{trim} \lesssim -9^\circ$.

Lateral Motion

The vehicle is axisymmetric.

¹ Note, that the data base delivered by NPO Lavoshkin to Dasa in the year 2000 had for the pitching moment C_m identical values for $M_\infty = 0$ and 1 and also for $M_\infty = 5$ and 100. The identical data for $M_\infty = 5$ and 100 can be explained by the Mach number independence rule for hypersonic flows. But the C_m values for $M_\infty = 0$ and 1 should be different. Unfortunately we have no explanation for this fact.

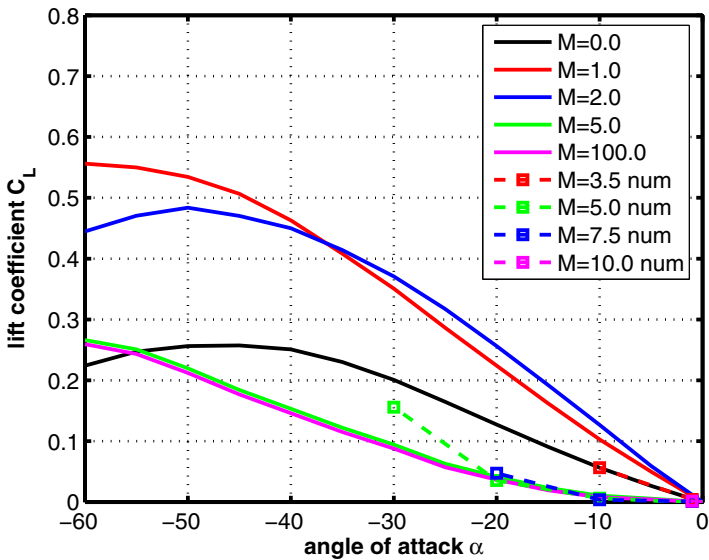


Fig. 5.44. Lift coefficient C_L as function of the angle of attack α , [17]

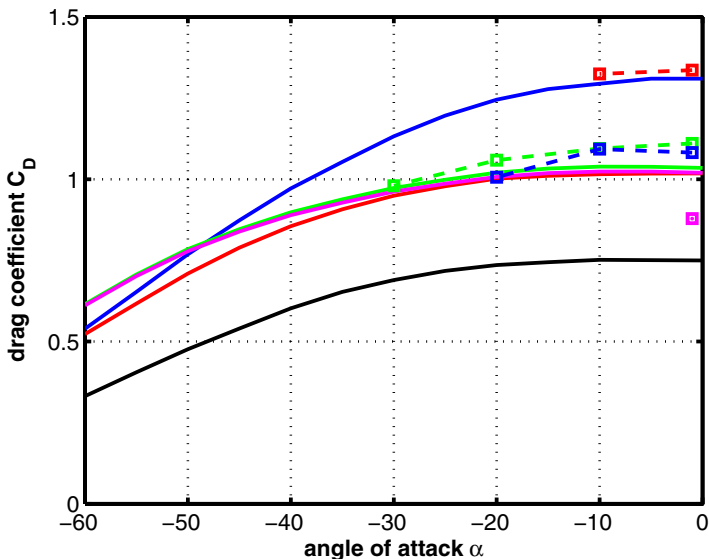


Fig. 5.45. Drag coefficient C_D as function of the angle of attack α , [17]

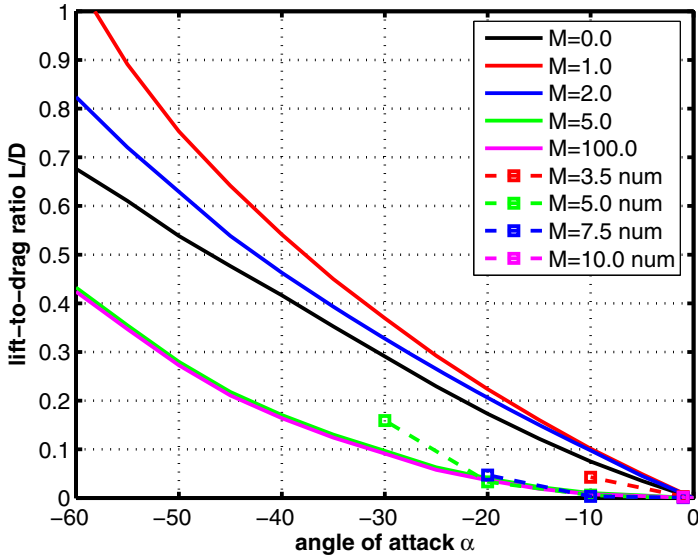


Fig. 5.46. Lift-to-drag ratio L/D as function of the angle of attack α , [17]

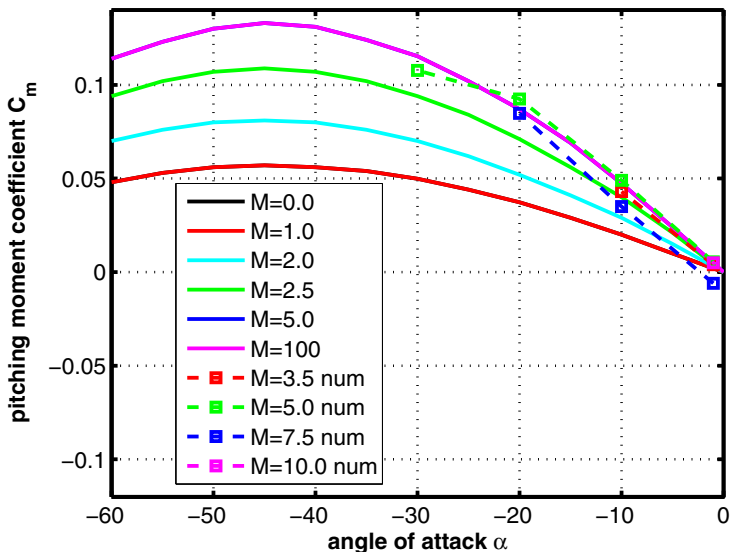


Fig. 5.47. Pitching moment coefficient C_m as function of the angle of attack α , [17]. Moment reference point, measured from nose tip, $x_{ref} = 0.325D$, $z_{ref} = 0$.

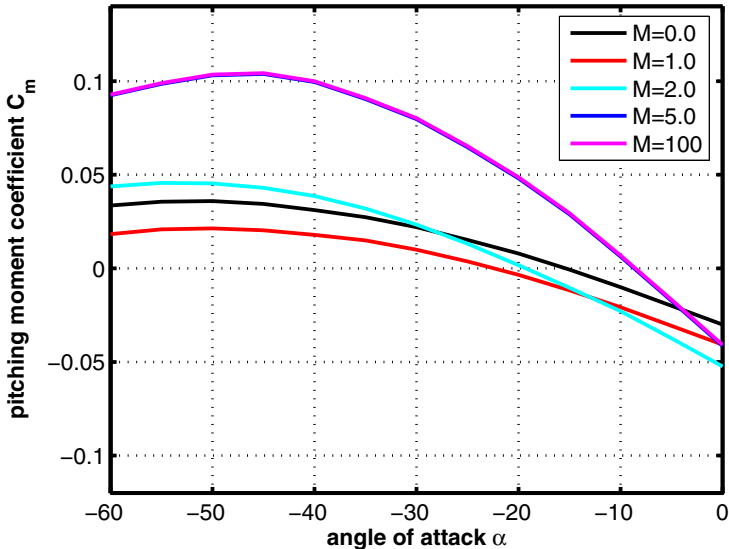


Fig. 5.48. Pitching moment coefficient C_m as function of angle of attack α . Moment reference point $x_{ref} = 0.325D$, $z_{ref} = -0.040D$.

5.6.3 Aerodynamic Data of Unsteady Motion

NPO Lavoshkin has delivered² also some data regarding the dynamic pitch stability (pitch damping coefficient) $C_{m\dot{\alpha}} + C_{mq}$, Fig. 5.49. It attracts attention that the values are often constant over larger angle of attack intervals. Further the data for $M_\infty = 0$ and 1 coincide completely! Since it is not known what the basis of these values is, we will not further discuss them.

² In the frame of the cooperation with the Deutsche Aerospace (Dasa).

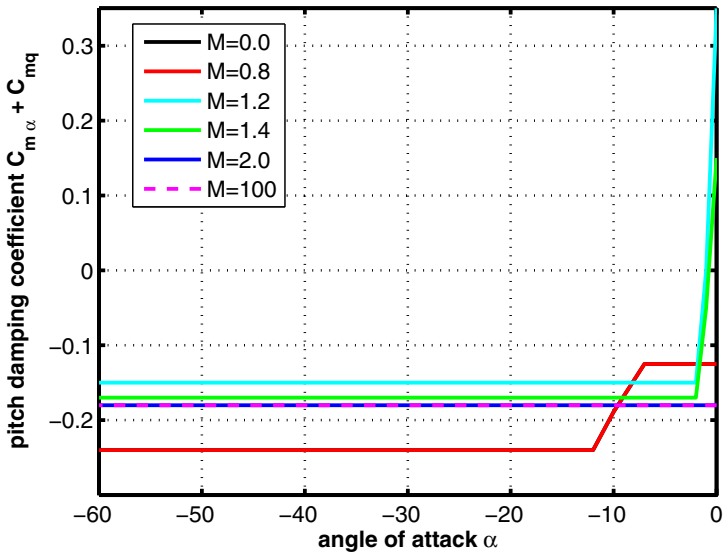


Fig. 5.49. Pitch damping coefficient $C_{m\alpha} + C_{mq}$ as function of the angle of attack α , [17]. Moment reference point, measured from nose tip, $x_{ref} = 0.325D$, $z_{ref} = 0$.

5.7 EXPERT (Europe)

During the European space programs HERMES, officially started in 1987, and later the MSTP program (Manned Space Transportation Program), started in 1994, the aerothermodynamic discipline did evolve to such an extent that with new hypersonic and/or high enthalpy wind tunnels, investigations in parameter ranges (Mach number, total temperature or enthalpy, Reynolds number, etc.) became possible, to which the researchers had no access in the earlier days. The same was true for the evolution of the numerical simulation methods. In the frame of the above mentioned programs the computational fluid dynamic (CFD) tools got the capability to handle three-dimensional flow fields past complex configurations, gas flows in thermodynamic equilibrium and non-equilibrium as well, complicated laminar and turbulent viscous flow structures and radiation cooled surfaces, just to mention some of the most challenging items. Since the results of all those investigation tools had to be validated, which could be conducted at best by a free flight experiment, the European Space Agency (ESA) with its technical branch ESTEC proposed to design and develop a flying testbed. This testbed got the name EXPERT (European eXPERimental Re-entry Testbed), [19, 20].

In the beginning of the EXPERT study two configurations were designed and their aerodynamic performance investigated. The first shape was the body of revolution REV (blunted cone with a flare), and the second one the blunted pyramid based model KHEOPS with genuine flaps, Fig. 5.50, [19]. Later in the project the KHEOPS shape was modified to some extent with open flaps to give the final EXPERT model configuration 4.2 (see Fig. 5.51), [19, 21, 22].

At this time (2013) it is planned to perform three ballistic re-entry flights with three expendable EXPERT vehicles. These vehicles are equipped with different types of instrumentation for measuring aerothermodynamic data. The launch system selected is the Russian VOLNA rocket.

5.7.1 Configurational Aspects

The KHEOPS configuration is a spherically blunted pyramidal shape featuring four flaps. It has been designed to meet the study of three-dimensional effects around the flaps, separation and reattachment heating, heating in corners with radiation effects, etc.. The configuration is described by the following quantities, Figs. 5.52 and 5.53 :

- nose radius 0.270 m,
- pyramidal dihedral angle 17°,
- base diameter 1.3 m,
- total length 1.08 m,
- reference length 1.08 m,
- reference area 1.2084 m²,

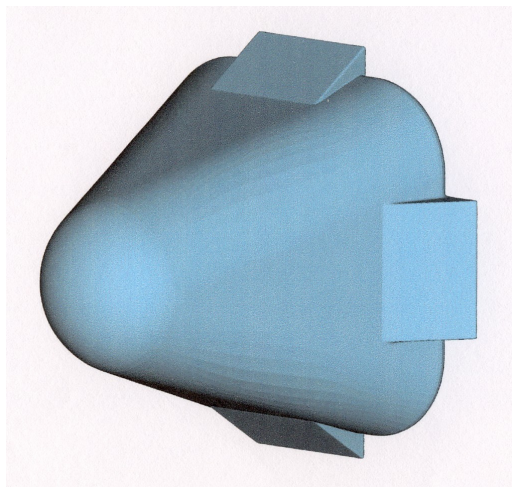


Fig. 5.50. 3D shape of the EXPERT project: KHEOPS, the pyramid based configuration with genuine flaps, [19]

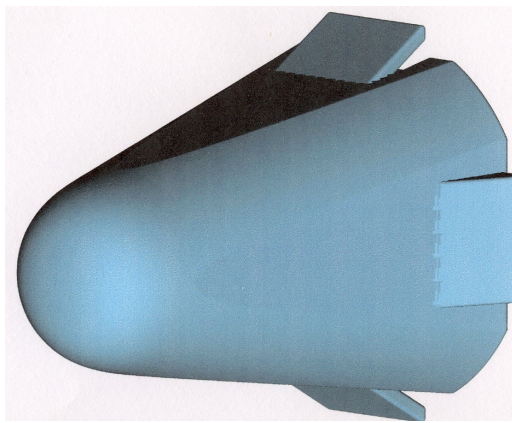


Fig. 5.51. 3D shape of the EXPERT project: model 4.2 with two open and two closed flaps, [19]

- deflection angles of flaps 15° and 20° ,
- hinge line of the flaps at $x_{bf} = 0.850$ m.

In order to optimize the EXPERT mission the KHEOPS configuration was varied by the following steps leading to the EXPERT model 4.2, Figs. 5.54, 5.55 and [19] :

- the spherical nose was replaced by an ellipsoid with an eccentricity of 2.5,
- the main shape consists now of a cone with a semi-apertural angle of 12.5° ,
- the cone is cut with four planes having a deflection angle of 9° ,
- four flaps are mounted with deflection angles of 20° , two of them in closed form and two of them in open form,
- the flap width was 0.4 m and the projected length 0.3 m,
- the total length was extended to 1.6 m,
- the reference area amounts to (wetted base area) 1.1877 m^2 .

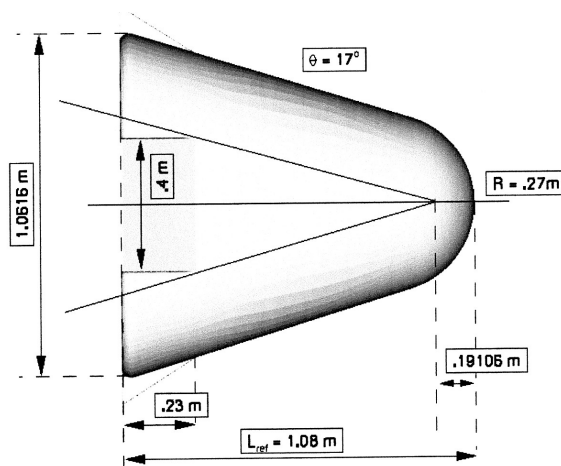


Fig. 5.52. 3D shape of the EXPERT project: Details of the KHEOPS model, side view, [19]

5.7.2 Aerodynamic Data of Steady Motion

Longitudinal Motion

KHEOPS configuration

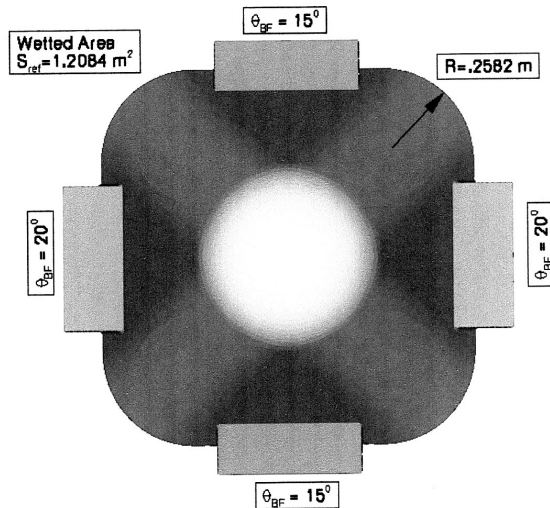


Fig. 5.53. 3D shape of the EXPERT project: Details of the KHEOPS model, front view, [19]

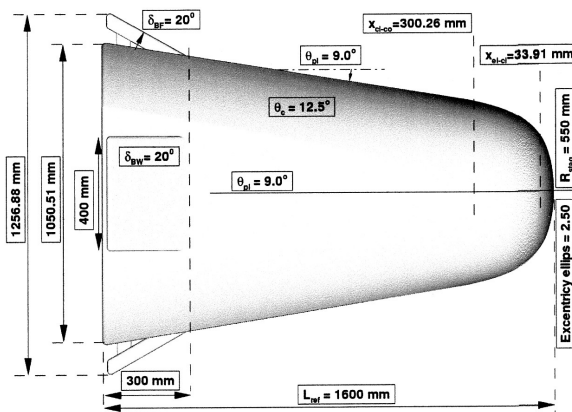


Fig. 5.54. 3D shape of the EXPERT project: Details of model 4.2 with two open and two closed flaps, side view, [19]

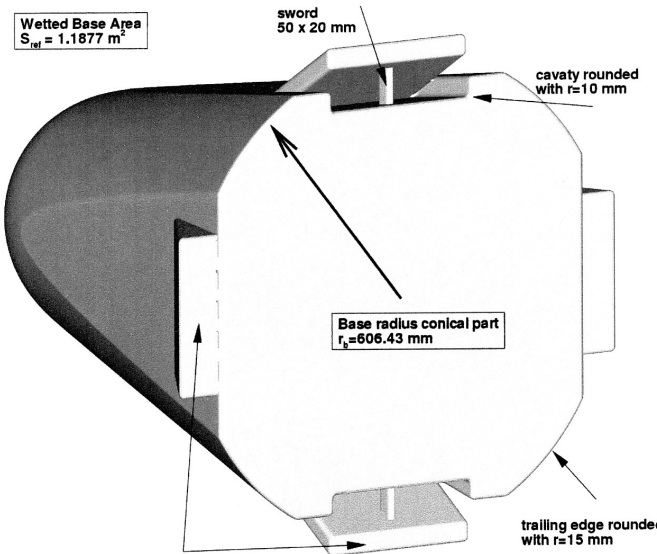


Fig. 5.55. 3D shape of the EXPERT project: Details of model 4.2 with two open and two closed flaps, view from behind, [19]

The aerodynamics of the KHEOPS model was exclusively investigated by numerical simulations using the Euler and Navier-Stokes equations, [19]. The following four figures (Figs. 5.56 - 5.59) show the lift, the drag and the pitching moment coefficients as well as the lift-to-drag ratio. The number of calculations³ was limited to 10, covering the Mach number range between $2 \leq M_\infty \leq 22.5$ and the angle of attack range between $0^\circ \leq \alpha \leq 10^\circ$. Indeed these are only a few points, but nevertheless these data are sufficient to reveal a tendency of the KHEOPS' aerodynamics.

Most of the aerodynamic data behave like expected, but there are two exceptions. First, the small increase of the lift slope with increasing Mach number is astonishing, Fig. 5.56. Normally, one would expect a decrease of the lift slope. Second, the non-monotonicity of the slope of the pitching moment coefficient C_m with respect to increasing Mach numbers cannot be explained, Fig. 5.59.

³ There were ten more computations, but with a turn of the model around the meridional angles $\phi = 45^\circ$ and 90° , in order to care for yaw effects. The yaw effects arise due to the unsymmetrical flow field generated by the different flap deflection angles $\eta_{bf} = 15^\circ$ and 20° .

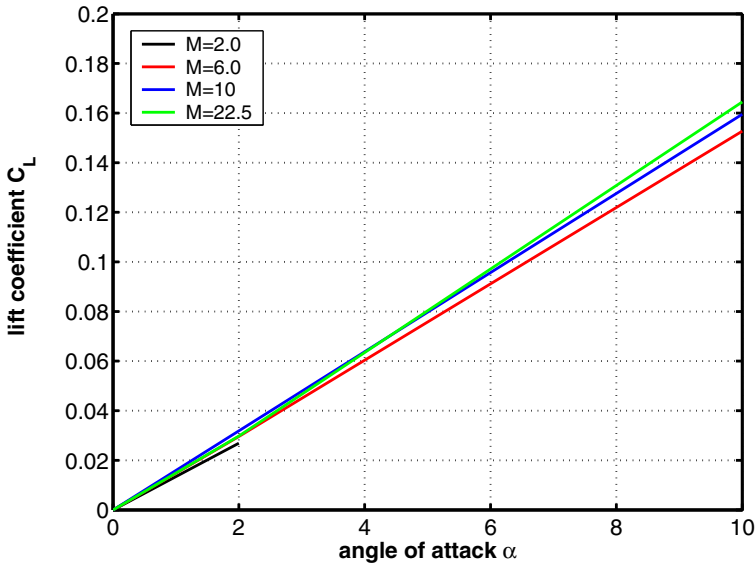


Fig. 5.56. EXPERT model KHEOPS: Lift coefficient C_L as function of the angle of attack α , [19]

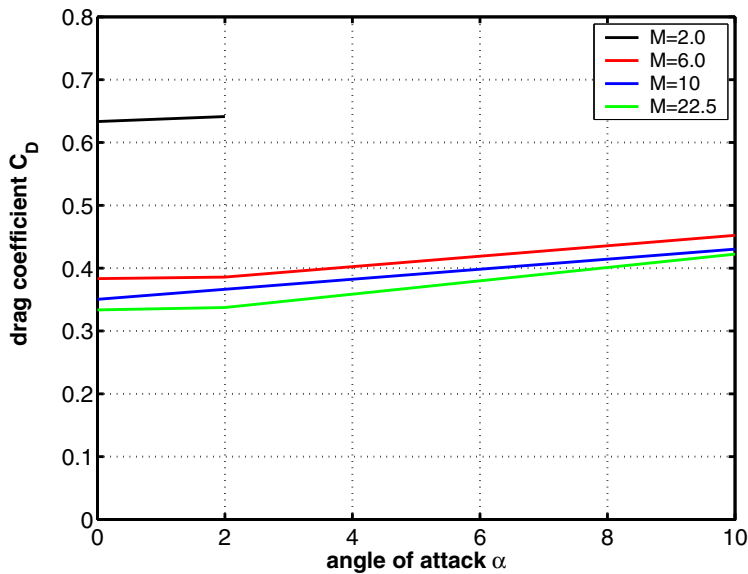


Fig. 5.57. EXPERT model KHEOPS: Drag coefficient C_D as function of the angle of attack α , [19]

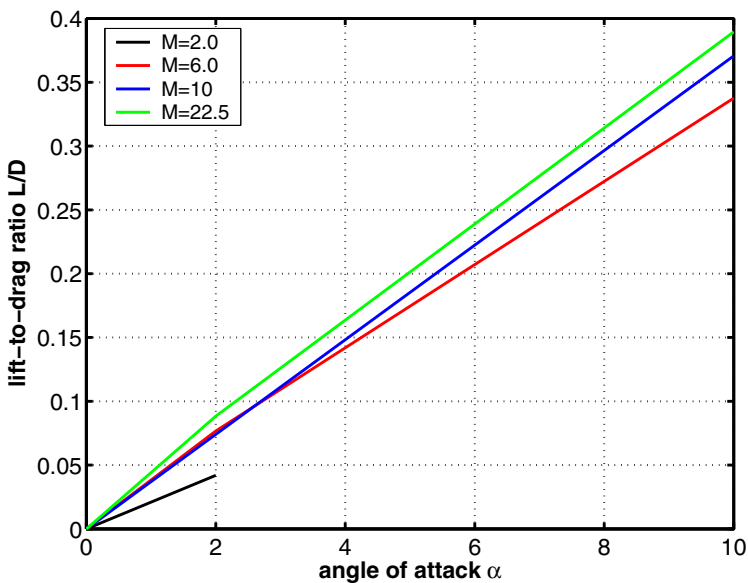


Fig. 5.58. EXPERT model KHEOPS: Lift-to-drag ratio L/D as function of the angle of attack α , [19]

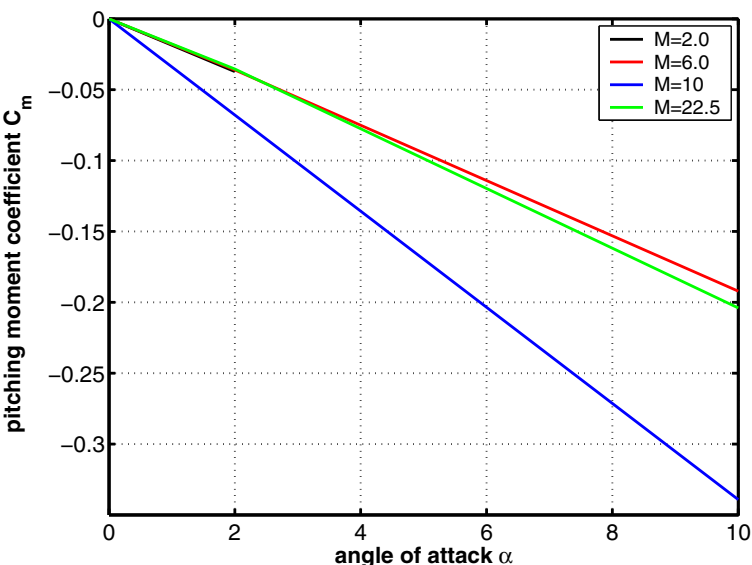


Fig. 5.59. EXPERT model KHEOPS: Pitching moment coefficient C_m as function of the angle of attack α , [19]. Moment reference point: nose tip ($x_{ref} = 0, z_{ref} = 0$).

EXPERT model 4.2 configuration

For the EXPERT model 4.2, the flight demonstration model, only the wind tunnel data of [21] are available⁴. These data were generated at the ITAM research institute in Novosibirsk, Russia. They performed in their supersonic wind tunnel T-313 measurements with $M_\infty = 4$ and in their shock tunnel AT-303 measurements with $M_\infty = 13.8$. The Figs. 5.60 to 5.63 show the lift, the drag and the pitching moment coefficients as well as the aerodynamic performance L/D . Comparing these data with the ones of the KHEOPS model (Fig. 5.50 and Figs. 5.56 to 5.59) indicates a good aerodynamic similarity of these two models. However the lift slope now decreases with increasing Mach number and C_m behaves like expected.

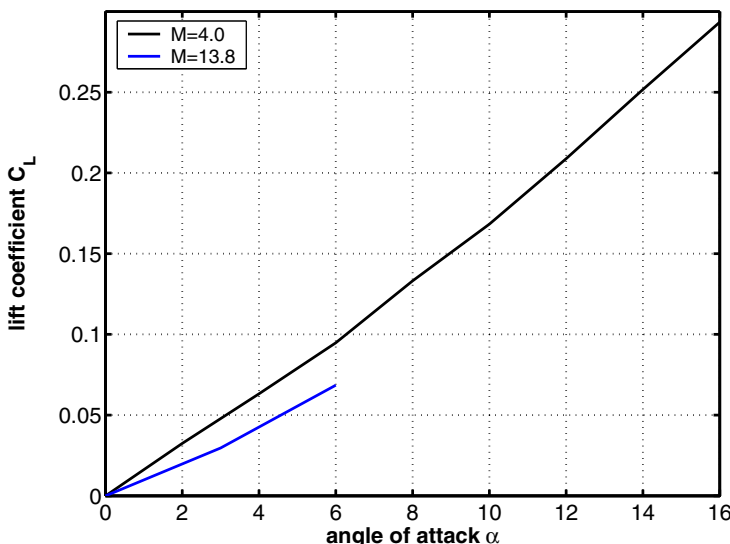


Fig. 5.60. EXPERT model 4.2: Lift coefficient C_L as function of the angle of attack α , [21]

Lateral Motion

Data of the lateral behavior as function of the yawing angle β are not available.

5.7.3 Aerodynamic Data of Unsteady Motion

Dynamic stability data are not available.

⁴ Obviously there exists a complete aerodynamic data base for the EXPERT model 4.2. Unfortunately, it was not possible for the author to obtain it from ESA/ESTEC.

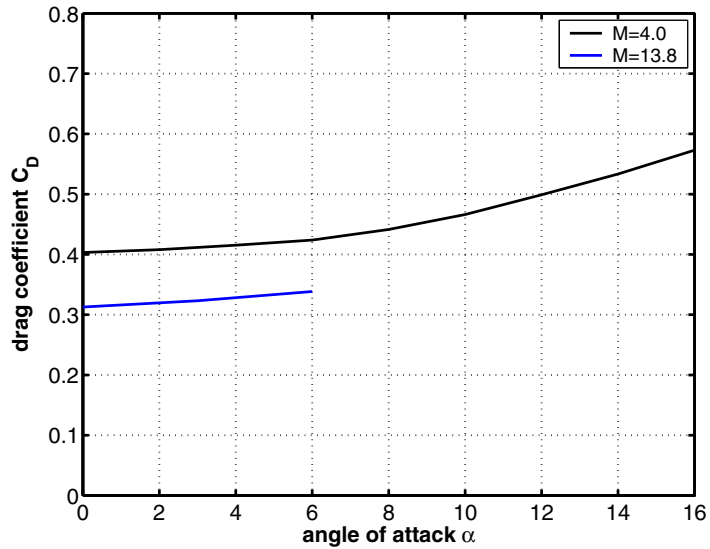


Fig. 5.61. EXPERT model 4.2: Drag coefficient C_D as function of the angle of attack α , [21]

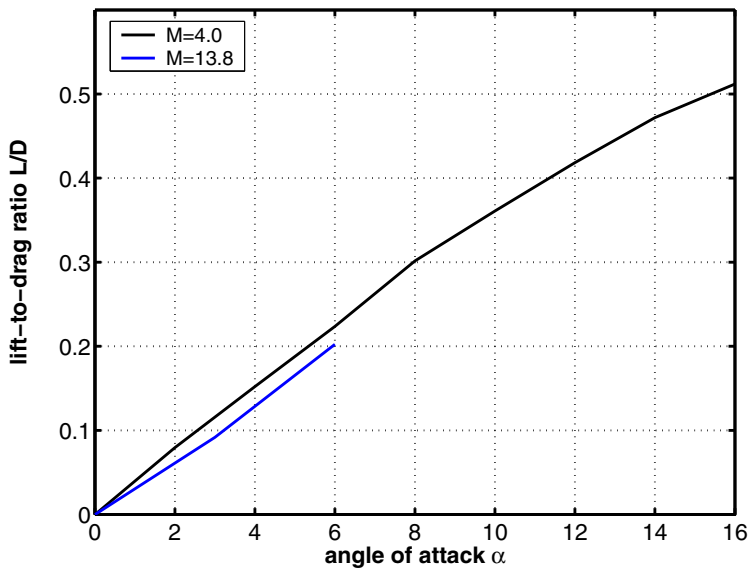


Fig. 5.62. EXPERT model 4.2: Lift-to-drag ratio L/D as function of the angle of attack α , [21]

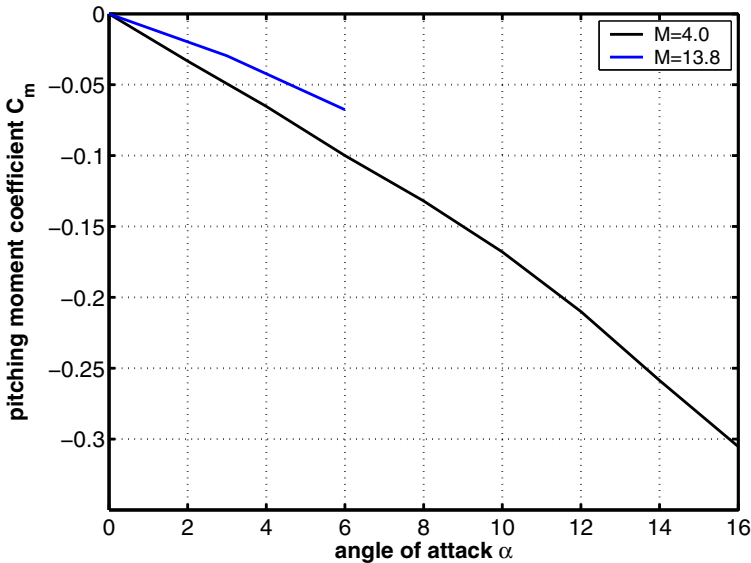


Fig. 5.63. EXPERT model 4.2: Pitching moment coefficient C_m as function of the angle of attack α , [21]. Moment reference point: nose tip ($x_{ref} = 0$, $z_{ref} = 0$).

References

1. Hirschel, E.H., Weiland, C.: Selected Aerothermodynamic Design Problems of Hypersonic Flight Vehicles, vol. 229. Springer, Heidelberg; Progress in Astronautics and Aeronautics. AIAA, Reston (2009)
2. Smith, A.J.: Entry and Vehicle Design Considerations. Capsule Aerothermodynamics, AGARD-R-808, Paper 4 (1997)
3. Weiland, C., Haidinger, F.A.: Entwurf von Kapseln und deren aerothermodynamische Verifikatio (Design of Capsules and Verification of their Aerothermodynamics. In: Proceedings DGLR-Fachsymposium Strömungen mit Ablösung (November 1996) (not published)
4. Davies, C.B., Park, C.: Aerodynamics of Generalized Bent Bicones for Aero-Assisted, Orbital-Transfer Vehicles. J. of Spacecraft 22(2), 104–111 (1985)
5. Miller, C.G., Blackstock, T.A., Helms, V.T., Midden, R.E.: An Experimental Investigation of Control Surface Effectiveness and Real-Gas Simulation for Bicones. AIAA-Paper 83-0213 (1983)
6. Ivanov, N.M.: Catalogue of Different Shapes for Unwinged Re-entry Vehicles. Final report, ESA Contract 10756/94/F/BM (1994)
7. N. N. INKA Study Results. Internal industrial communication, Deutsche Aerospace Dasa, Germany (1993)
8. N.N. CTV Dasa Data Base. Internal industrial communication, Deutsche Aerospace Dasa, Germany (1994)
9. Menne, S.: Computation of Non-Winged Vehicle Aerodynamics in the Low Supersonic Range. In: 2nd European Symposium on Aerothermodynamics for Space Vehicles, ESA-SP-367 (1994)
10. Weiland, C., Pfitzner, M.: 3D and 2D Solutions of the Quasi-Conservative Euler Equations. Lecture Notes in Physics, vol. 264, pp. 654–659. Springer (1986)
11. Pfitzner, M., Weiland, C.: 3D Euler Solutions for Hypersonic Free-Stream Mach Numbers. AGARD-CP-428, pp. 22-1–22-14 (1987)
12. Esch, H.: Kraftmessungen an einem Modell der semiballistischen Rückkehrkapsel Colibri (Force Measurements on a Model of the Semi-Ballistic Re-entry Vehicle Colibri). DLR Interlal Report, IB -39113-97A04 (1997)
13. Burkhardt, J.: Konzeptioneller Systementwurf und Missionsanalyse für den auftriebsgestützten Rückkehrkörper (Conceptional System Design and Mission Analysis of a Lifting Re-Entry Vehicle). Doctoral Thesis, University of Stuttgart, Germany (2001)
14. Marrappa, L., Kassing, D., Baglioni, P., Wilde, D., Walther, S., Pilchkhadze, K., Finchenko, V.: Inflatable Re-entry Technologies: Flight Demonstration and Future Prospects. ESA - Bulletin 103 (August 2000)
15. Jung, G.: Vorlesung Nutzlasten Inflatable Re-entry Technology (IRDT). University of Dresden, Germany (2001)
16. N. N. The System, Based on Inflatable Units and Intended for Delivery of Cargos from the International Space Station. Babakin Space Center Internal Report, ISSDLS-BSC-RP0001 (2000)

17. N. N. Industrial communication: EADS - Lavoshkin - ESA (2000)
18. N. N. Private communication (2005)
19. Walpot, L., Ottens, H.: FESART/EXPERT Aerodynamic and Aerothermodynamic Analysis of the REV and KHEOPS Configurations. Technical Report, TOS-MPA/2718/L.W., ESTEC, Noordwijk (2003)
20. Wong, H., Muylaert, J., Northey, D., Riley, D.: Assessment on EXPERT Descent and Landing System Aerodynamics. ESA-SP-659 (2009)
21. Kharitonov, A.M., Adamov, N.P., Mazhul, I.I., Vasenyov, L.G., Zvegintsev, V.I., Muylaert, J.: Aerodynamics of the EXPERT Re-Entry Ballistic Vehicle. ESA-SP-659 (2009)
22. Kharitonov, A.M., Zvegintsev, V.I., Brodetskay, M.D., Mazhul, I.I., Muylaert, J.M., Kordulla, W., Paulat, J.C.: Aerodynamic Investigation of Aerospace Vehicles in the New Hypersonic Wind Tunnel AT-303 in ITAM. In: 4th Int. Symp. on Atmosph. Re-entry Vehicle and Systems, Arcachon, France (2005)

Aerothermodynamic Data of Winged Re-entry Vehicles (RV-W)

The first period of space transportation was characterized by simple shapes like capsules and probes. The precision of the operations and the control capability of such vehicles was rather low. The natural step to improve this situation was to use in an advanced way the capacity of the atmosphere to support and control the flight of such space vehicles. Thus the winged space vehicles were born.

6.1 Introduction

The access to space is a difficult and very expensive task. From the beginning of the activities in the 1950s and 1960s when men entered for the first time Earth's orbits the costs had a tremendous magnitude. A race to space had begun. The main driver for this race was the competition of the two conflicting political and social systems in the world, the capitalism and the communism, represented by the United States of America¹ and the Soviet Union. This competition was called the cold war.

During that period the financial resources obviously had no bound. Nobody did put the question how reasonable and economically technical solutions of these activities were. The only impetus was, "we must be the first and we must have the better solution".

Therefore, the first manned transportation systems ascending to space orbits were very expensive rockets with capsules on top of these rockets.

The features of capsules (RV-NW) are (besides others):

- simple non-winged configurations,
- low aerodynamic performance $L/D \approx 0.35$ (APOLLO and SOYUZ), therefore low down-range and cross-range capabilities ,
- low aerodynamic controllability, since no aerodynamic controls are available, only the use of reaction control systems (RCS),
- expendable systems,
- laborious recovery systems after landing either in water or on ground (desert),
- low comfort for astronauts,

¹ And the states of Western Europe.

- high g-loads during entry,
- moderate payload capabilities.

After this period the governments in the United States and the Soviet Union have thought about advanced transportation systems, namely the SPACE SHUTTLE system and the BURAN system, which should avoid some of the drawbacks of the capsules.

The features of these systems (RV-W) are:

- winged configurations,
- advanced aerodynamic performance² L/D ($L/D_{max} \approx 2$ in the hypersonic regime),
- high aerodynamic controllability due to body flaps, elevons and rudders as well as speed-brakes,
- partly re-usability,
- landing on conventional runways,
- increased comfort for astronauts,
- reduced g-loads during entry,
- high payload capabilities.

At that time a discussion commenced about the costs per kg payload to be transported to space. The launch costs of the conventional rocket based systems were very high. It was the expectation to reduce these costs by using the partly reusable SPACE SHUTTLE system. But unfortunately this did not happen, as the following example for the SPACE SHUTTLE system shows:

Launch costs approximately 800 billion USD, maximal payload mass in the SHUTTLE bay approximately 26 to. Therefore costs per kg payload approximately 30 000 USD.

The main reason for that was the high effort to refurbish the SPACE SHUTTLE Orbiter for the next flight and in particular the refurbishment of the thermal protection system (TPS).

Europe as well as Japan had decided in the 1980s to work also on an autonomous access to space system and started with the HERMES project (Europe) and the HOPE project (later HOPE-X) (Japan) their own activities. Both projects were from the system point of view and technologically comparable to the SPACE SHUTTLE system, but were terminated in the 1990s.

The transportation of astronauts and payloads to and from the International Space Station ISS was conducted over a long time by the U.S. SPACE SHUTTLE Orbiter and the Russian SOYUZ capsule. Since 2011 when the SHUTTLE was put off duty, the only access to and from the ISS is by the SOYUZ capsule.

Because it could not completely be precluded that the scenario exists that the ISS has to be evacuated due to technical problems or accidents, or that

² All the presented performance data are untrimmed.

astronauts will be taken ill, the need for a Crew Rescue Vehicle (CRV) was becoming urgent. This CRV should be attached permanently to the ISS. Europe and the US had decided to develop on the basis of the X-24 lifting body a winged CRV, which got the name X-38. After a lot of development work in the late 1990s and the fabrication of two demonstrator vehicles, with which several successful flight demonstrations were performed, the project was cancelled in the early 2000s, too.

When the cold war ended the governments asked for really economical solutions!

This resulted in a lot of proposals and system studies carried for a next generation space transportation system, which should allow for payload transportation costs per kg mass of not more than 1000 USD.

Single-stage-to-orbit (SSTO) vehicles, like the NASP (National Aero-Space Plane) project of the United States or the HOTOL project of Great Britain, as well as two-stage-to-orbit systems (TSTO), like Germany's SAENGER concept, were considered. The European Space Agency ESA launched in the 1990s the Future European Space Transportation Investigation Programme (FESTIP) with the goal to investigate possible systems in this respect. But all these activities were scrapped or terminated.

In 1996 the United States started further activities with the X-33 vehicle, a single-stage-to-orbit (SSTO) demonstrator with a linear aerospike engine, and the X-34 vehicle, a flying laboratory for technologies and operations. Both projects were also scrapped in 2001 due to much too high technical risks and budgetary problems.

For the demonstration of reusable space technologies and orbital space-flight missions the X-37 project was launched, where in the first scenario the vehicle should be transported to a space orbit in the cargo bay of the SPACE SHUTTLE Orbiter. In 2004 the X-37 project was transferred from NASA to the Defense Advanced Research Projects Agency (DARPA) and a redesign took place for launch on an Atlas V rocket. First orbital flight happened in 2010 and two others one in 2011 and 2012.

Actually³, there is no real industrial project for replacing the SPACE SHUTTLE system, neither by conventional nor by advanced systems and technologies.

³ This is valid at least for the time-period 2010 - 2015.

6.2 SPACE SHUTTLE Orbiter (USA)

The SPACE SHUTTLE system represents a semi-reusable concept for the transportation of payloads and men into various (mostly circular) low Earth orbits. Orbit distances from the Earth surface between approximately 200 to 1500 km are called low Earth orbits. The SPACE SHUTTLE system consists of three elements (Fig. 6.1):

- the two solid rocket boosters,
- the external tank,
- the Orbiter vehicle.

During the ascent the boosters are separated from the tank at an altitude of approximately 50 km (after a burning time of ≈ 120 s). The burned-out boosters are recovered from the Atlantic Ocean, refurbished and refilled with solid propellant. The expendable tank is jettisoned at an altitude of roughly 110 km. A successful mission includes besides the ascent the descent phase, which consists of the de-orbiting boost of the Orbital Maneuvering System (OMS), the re-entry process into Earth's atmosphere and the proper touch down and landing on a runway. The whole re-entry process is unpowered.

When back on Earth's surface the Orbiter is reused after inspection and refurbishment. This space transportation concept was the only operational winged and manned system to reach the orbit and to land horizontally. The fleet has performed 135 flights⁴.

The missions of the SPACE SHUTTLE involved carrying large and heavy payloads to various low Earth orbits including elements of the International Space Station (ISS), performing service missions, also to satellites, e.g., upgrading the Hubble Space Telescope, and serving as crew transport system for the ISS.

The SPACE SHUTTLE program was officially started by the Nixon administration in January 1972. The first launch took place on April 12, 1981, followed by the first re-entry flight on April 14, 1981. Detailed accounts regarding flight experience, aerothermodynamic performance and problems of the first operational flights were published in, for instance, [1, 2].

Six Orbiter vehicles were built⁵:

- Enterprize⁶ (1977),
- Columbia (1981),
- Challenger (1983),
- Discovery (1984),
- Atlantis (1985),
- Endeavour (1992).

⁴ The last flight with the Orbiter Atlantis took place in July 2011.

⁵ Year of first flight in brackets.

⁶ This Orbiter had served as test vehicle regarding the atmospheric flight capability including terminal approach and landing. The vehicle had not the capability to perform a real re-entry flight.

Challenger (1986) and Columbia (2003) were lost by accidents⁷. The SPACE SHUTTLE systems were retired from service in July 2011.

Fig. 6.2 shows in the left picture the Orbiter Discovery during landing at Edwards Air Force Base on Sept. 11, 2009 (STS-128). In the right picture the touch down phase of the Orbiter Atlantis is captured, which returned from the mission of upgrading the Hubble Space Telescope. This landing took place on May 24, 2009 (STS-125).

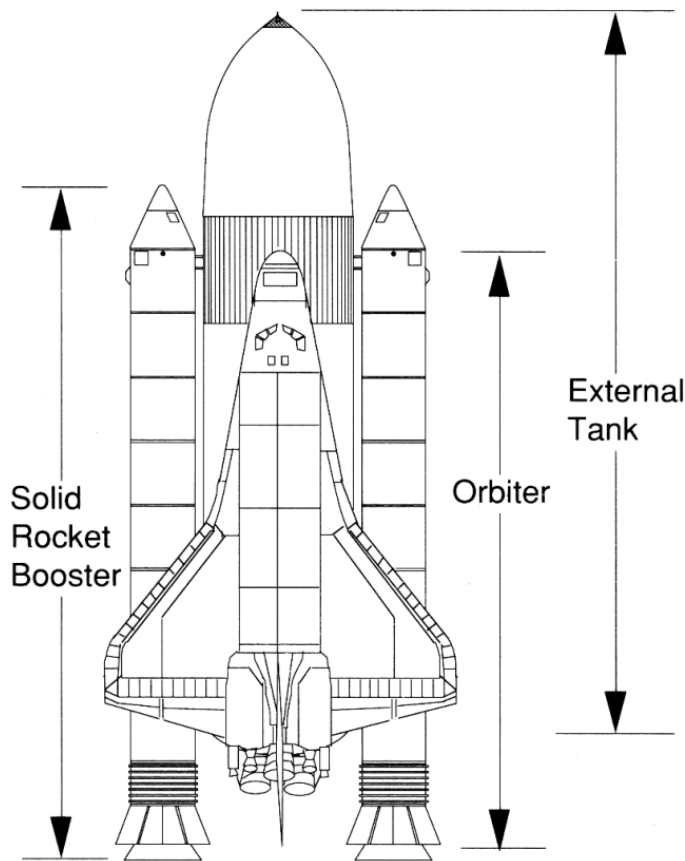


Fig. 6.1. The SPACE SHUTTLE system, [3]

⁷ Challenger in the ascent phase and Columbia in the re-entry phase.



Fig. 6.2. Left: Orbiter Discovery (flight STS-128) landing at Edwards Air Force Base on Sep. 11 2009. Right: Orbiter Atlantis (flight STS-125) landing at Edwards Air Force Base on May 24 2009 (Mission: Upgrade of the Hubble Space Telescope.). Pictures from NASA's gallery, [4].

6.2.1 Configurational Aspects

Figs. 6.3 and 6.4 show the side view and the top view of the SPACE SHUTTLE Orbiter. The SPACE SHUTTLE Orbiter is the largest space transportation vehicle ever built⁸, with a total length of 37.238 m and a span of 23.842 m. The nominal x -coordinate of the center-of-gravity is located at 21.303 m (0.65 L_{ref}) measured from the nose or 27.348 m measured in the configurational coordinate system (see Fig. 6.3). The z-coordinate of the center-of-gravity amounts to 9.525 m, measured also in the configurational coordinate system.

The SPACE SHUTTLE Orbiter has a double delta wing with sweep angles of 45 and 81 degrees. The three main engines are the most powerful rockets ever designed, each with a vacuum thrust of 2100 kN (\approx 214 tons) and a specific impulse of 455.2 s. The rockets of the Orbital Maneuvering System (OMS) are contained in the pods on the aft fuselage of the SHUTTLE Orbiter and generate a thrust of 27 kN (\approx 2.7 tons) each. These rockets are responsible for the generation of the thrust for the final orbit transfer and for the boost necessary for the initialization of the de-orbiting process. Further, a Reaction Control System (RCS) is installed, which consists of thrusters of the 500 N class. This RCS system conducts the pitch, yaw and roll control during the first part of the re-entry trajectory and is active as long as the aerodynamic control surfaces are not fully effective (approximately down to $M_\infty \approx 5$).

Design and equipment details of the SHUTTLE Orbiter can be found in Fig. 6.5, where also the payload bay is indicated, which measures 4.5 m (15

⁸ The size of the Russian BURAN is comparable to the U.S. SPACE SHUTTLE Orbiter, but this vehicle never became operational.

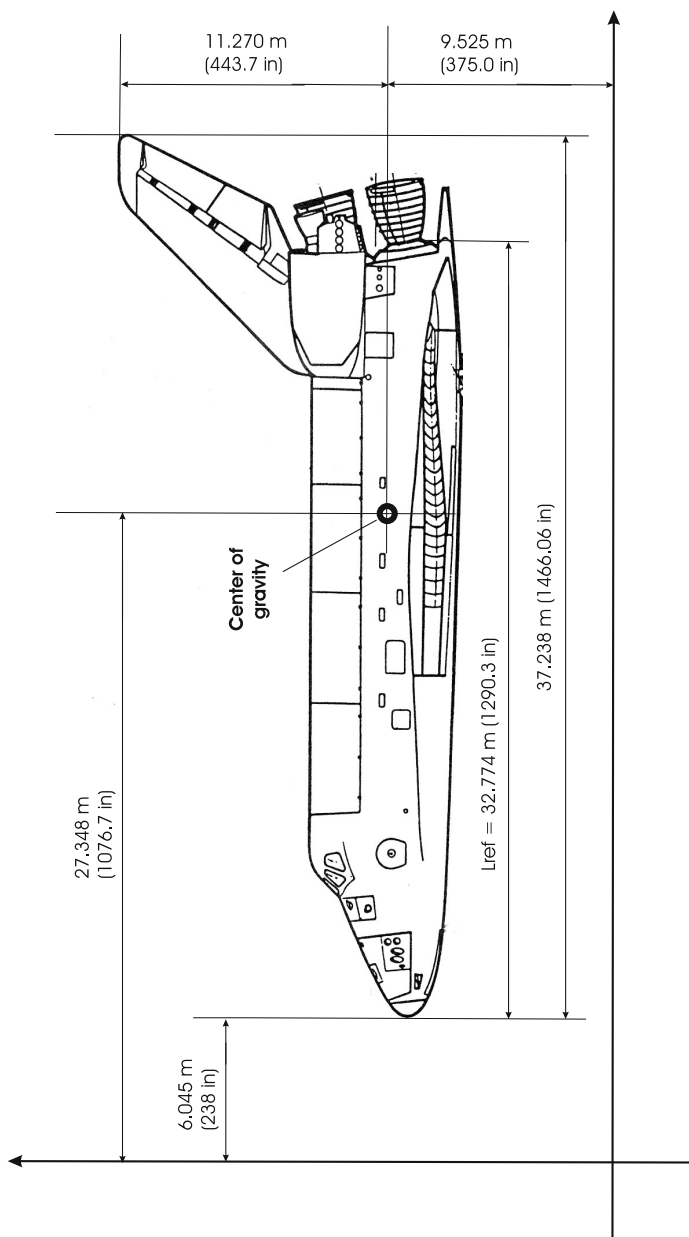


Fig. 6.3. Shape definition of the SPACE SHUTTLE Orbiter. Side view, [1, 5]

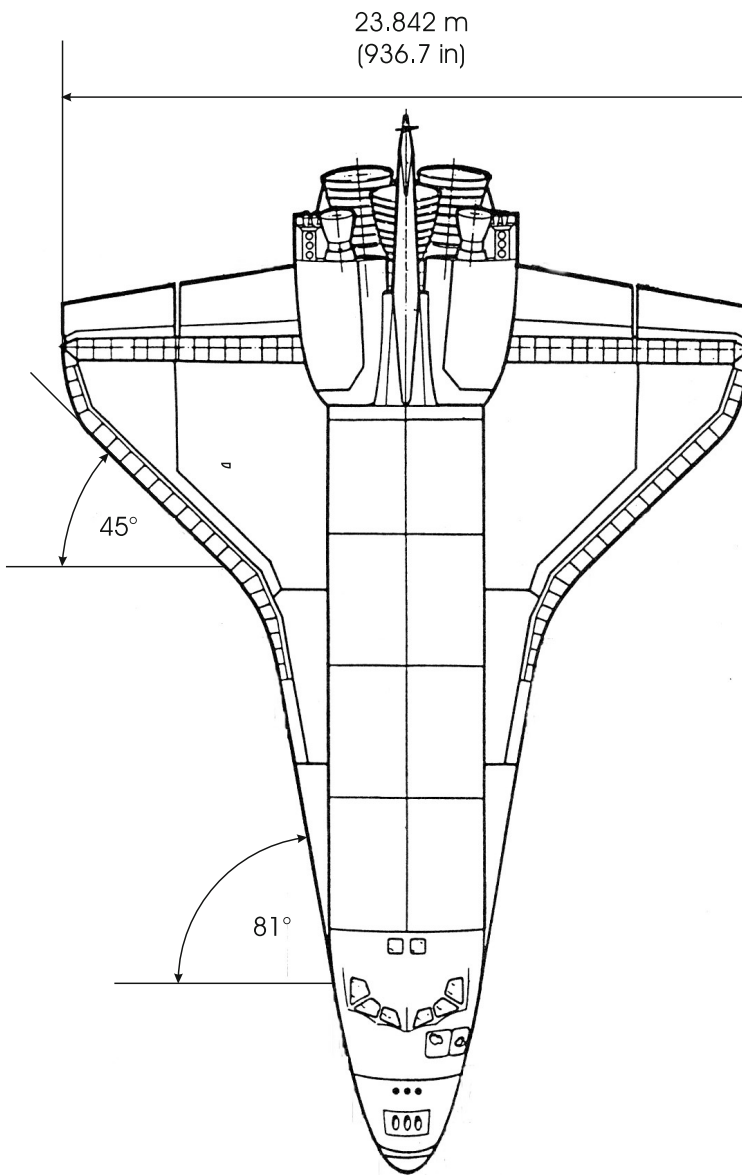


Fig. 6.4. Shape definition of the SPACE SHUTTLE Orbiter. Top view, [1, 5]

ft) by 18 m (60 ft). The mass capacity of the payload bay amounts to 24.4 tons for the low Earth orbit (LEO) and 3.81 tons for the geostationary orbit (GTO)⁹. The landing speed amounts to approximately 340 km/h (95 m/s). Some interesting measures, quantities and reference values are listed in Tab. 6.1.

During the European HERMES project, in the frame of research and development activities, some institutions had the task to investigate the SPACE SHUTTLE Orbiter aerodynamics. Besides numerical flow field computations some wind tunnel investigations were performed. In Fig. 6.6 a 1:90 SHUTTLE Orbiter model, mounted in the S4 tunnel of ONERA, Modane France, is presented (left). The right part of the figure gives a top view of this model, [6].

During this wind tunnel campaign oil flow pictures, representing the skin-friction-line patterns at the leeward side and the windward side were made, Fig. 6.7. Fig. 6.8 shows skin-friction lines at the windward side from non-equilibrium real gas Navier-Stokes solutions, [8, 9]. To ease the numerical computation the flow fields were calculated past the HALIS configuration, which has the same windward side as the SPACE SHUTTLE Orbiter, but a simplified leeward side. The HALIS configuration was introduced in [7].

6.2.2 Aerodynamic Data of Steady Motion

In the 1970s the numerical methods for solving the governing fluid-dynamical equations (Euler and Navier-Stokes equations) were not in a state to calculate three-dimensional flow fields past complex configurations for the determination (besides the flow field quantities) of the aerodynamic coefficients¹⁰. At that time the numerical tools did not contribute to the establishment of the aerodynamic data bases of airplanes and in particular not of space vehicles. That is the reason why the aerodynamic coefficients, which we present below, were mainly obtained from wind tunnel tests. Here lie also the roots of the so-called pitching moment anomaly, which was observed during the first re-entry flight of the SPACE SHUTTLE Orbiter. For a more recent explanation of this anomaly, see [10].

Longitudinal Motion

In the following figures the coefficients of lift C_L , drag C_D and pitching moment C_m as well as the aerodynamic performance L/D are plotted for the Mach number regime $0.25 \leq M_\infty \leq 20$. Due to the substantial spread of the data separate diagrams are presented for the subsonic-transonic ($0.25 \leq M_\infty \leq 0.98$), the transonic-supersonic ($1.1 \leq M_\infty \leq 4$) and the supersonic-hypersonic ($5 \leq M_\infty \leq 20$) Mach number regimes. All the data are taken

⁹ The geostationary transfer orbit GTO is an elliptical orbit, where the apogee distance is consistent with the radius of the circular geosynchronized orbit (GEO).

¹⁰ This had happened later in the century mainly during the European HERMES project at the beginning of the 1990s.

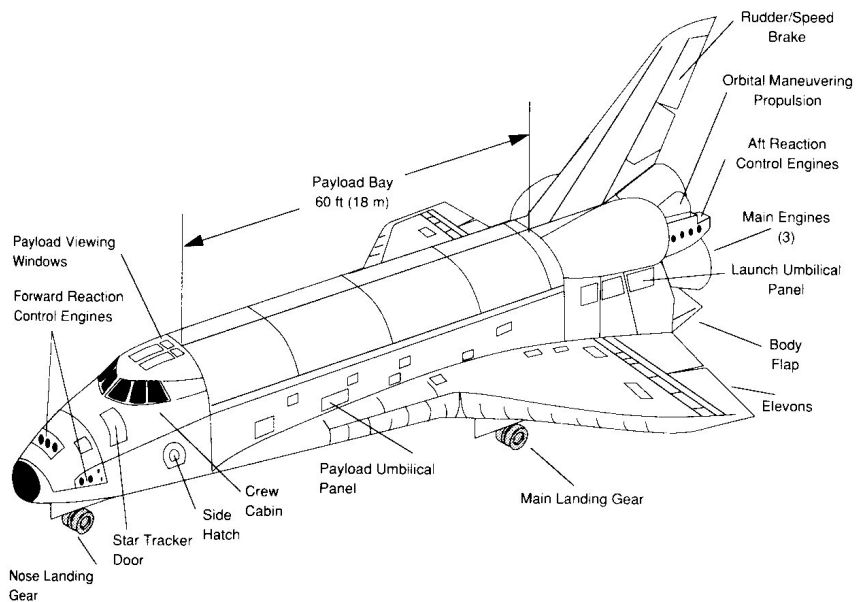


Fig. 6.5. SPACE SHUTTLE Orbiter: Design and equipment details, [3]

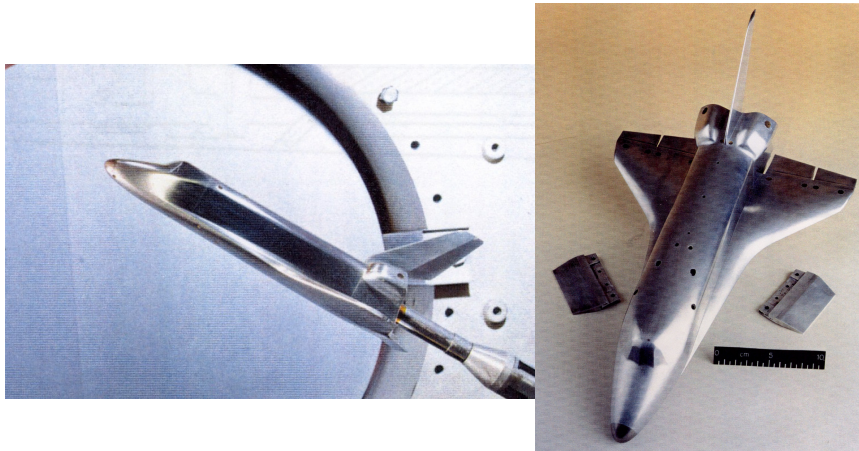


Fig. 6.6. SPACE SHUTTLE Orbiter: Photos from the S4 wind tunnel campaign. Model in the wind tunnel (left), top view of the model (right), model size 1:90, [6]

Table 6.1. SPACE SHUTTLE Orbiter shape: dimensions, quantities and reference values, [1, 5]. See also Figs. 6.3 and 6.4.

total length	L_{tot}	37.238 m
total width	W_{tot}	23.842 m
reference length	L_{ref}	32.774 m
reference area	S_{ref}	249.909 m ²
reference chord length (M.A.C.)	\bar{c}	12.060 m
x-coordinate of the center-of-gravity, nominal	x_{cog}	27.348 m $\Rightarrow 0.65 L_{ref}$ Fig. 6.3
z-coordinate of the center-of-gravity, nominal	z_{cog}	9.525 m Fig. 6.3
empty mass	m_e	78 000 kg
gross mass at launch	m_g	110 000 kg

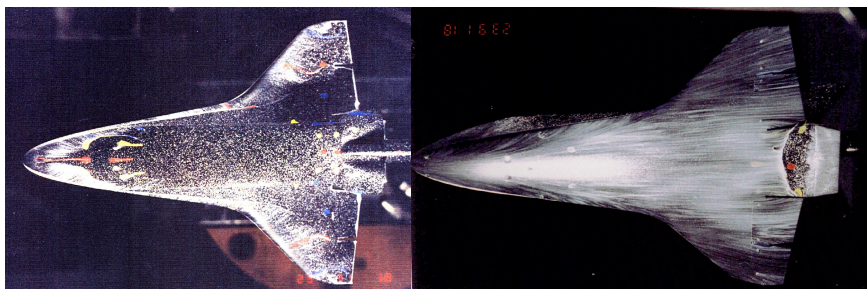


Fig. 6.7. SPACE SHUTTLE Orbiter: Photos from the S4 wind tunnel campaign. Oil flow picture at the leeward side (left) and at the windward side (right), $M_\infty = 9.77$, $\alpha = 30^\circ$, [6].

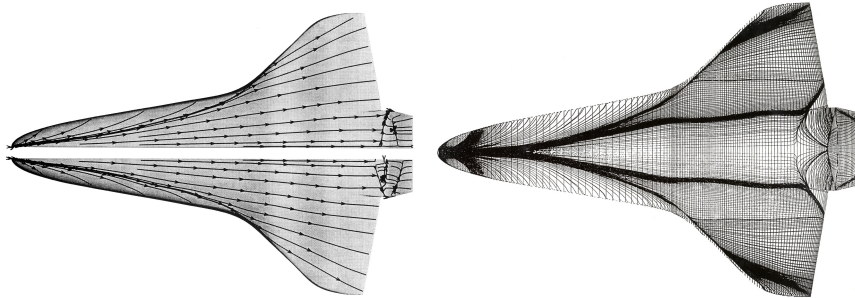


Fig. 6.8. HALIS configuration: Non-equilibrium real gas Navier-Stokes solutions. Skin-friction lines at the windward side. High enthalpy F4 wind tunnel conditions with $M_{\infty} = 8.86, \alpha = 40^\circ$. First solution (upper left) from Ref. [8], and second solution (right) from [9]. Solution for flight conditions with $M_{\infty} = 24, \alpha = 40^\circ, H = 72$ km (lower left) from [8].

from [5]. For Mach numbers up to $M_{\infty} = 4$ data are available for the angle of attack regime $-10^\circ \leq \alpha \leq 25^\circ$, whereas for higher Mach numbers the angle of attack regime is $-10^\circ \leq \alpha \leq 45^\circ$.

For subsonic-transonic Mach numbers the lift coefficient behaves linearly up to $\alpha \approx 20^\circ$ with only moderate changes of the gradient $\partial C_L / \partial \alpha$, Fig. 6.9. With rising Mach number the gradient $\partial C_L / \partial \alpha$ reduces substantially, Fig. 6.10. For hypersonic Mach numbers we observe on the one hand a positive lift curve break up to $\alpha \approx 35^\circ$ ($\partial C_L / \partial \alpha$ increases with increasing α) and on the other hand the validity of the Mach number independence rule [10], Fig. 6.11. The lift curve break for hypersonic Mach numbers is typical for this class of space vehicles.

The drag coefficient is largest for transonic Mach numbers, Figs. 6.12, 6.13, and becomes Mach number independent in the hypersonic flight regime, 6.14. Further the drag coefficient has its minimum for all Mach numbers at small angles of attack, as expected, and rises then fast (quadratically) to large values.

The maximum lift-to-drag ratio exists in the subsonic regime ($M_{\infty} = 0.25$) with $L/D|_{max} \approx 4.25$ for an angle of attack value of $\alpha \approx 12^\circ$. This reduces to $L/D|_{max} \approx 2.35$ for $M_{\infty} = 0.98$, Fig. 6.15. A further increase of the Mach number lowers additionally the maximum lift-to-drag value ($(L/D|_{max,M_{\infty}=20} \lesssim 2)$), whereby this maximum is shifted to larger angles of attack ($\alpha_{L/D_{max}} \Rightarrow 18^\circ$), Figs. 6.16 and 6.17.

The SPACE SHUTTLE Orbiter flies during the first part of the re-entry trajectory with an angle of attack of approximately 40° , for which from Fig. 6.17 an aerodynamic performance of $L/D \approx 1$ can be extracted.

When we turn towards the pitching moment we find for the low subsonic Mach number $M_{\infty} = 0.25$ only a marginal static stability ($\partial C_m / \partial \alpha \Rightarrow 0$) and

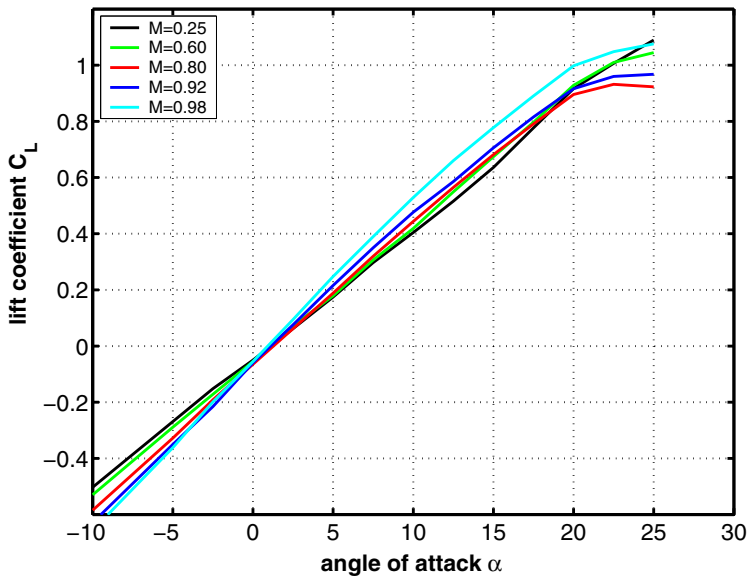


Fig. 6.9. Lift coefficient C_L as function of the angle of attack α for subsonic-transonic Mach numbers, [5]

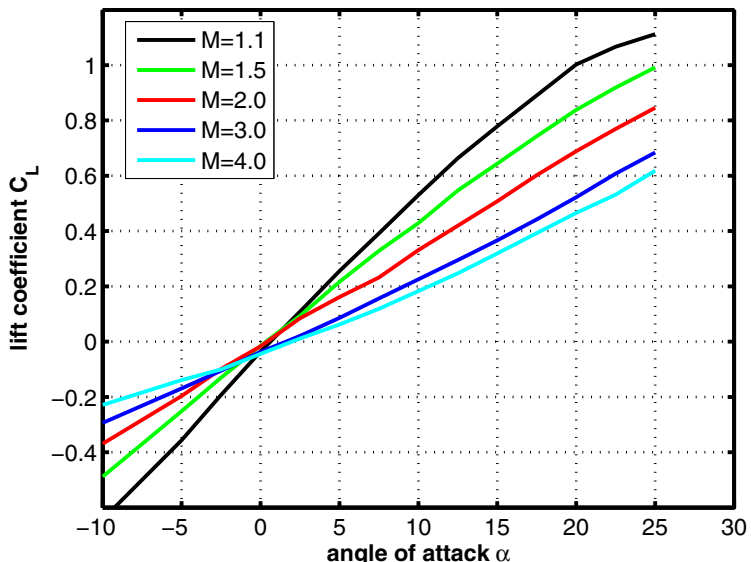


Fig. 6.10. Lift coefficient C_L as function of the angle of attack α for transonic-supersonic Mach numbers, [5]

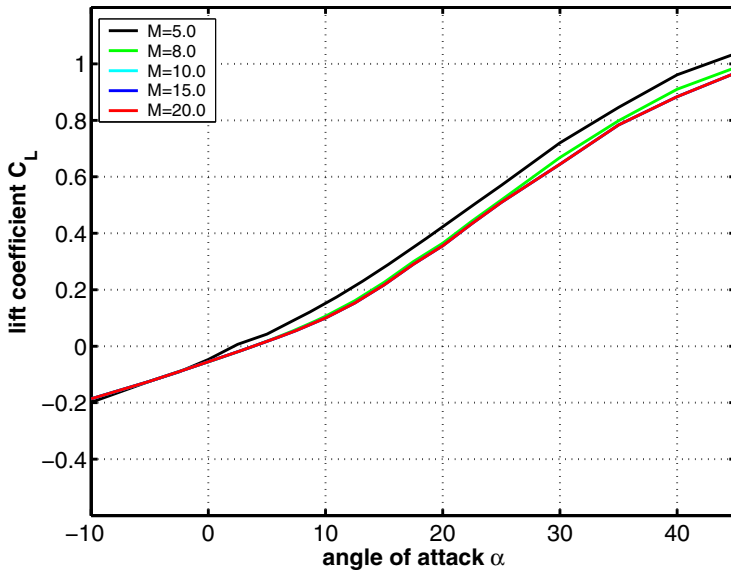


Fig. 6.11. Lift coefficient C_L as function of the angle of attack α for supersonic-hypersonic Mach numbers, [5]

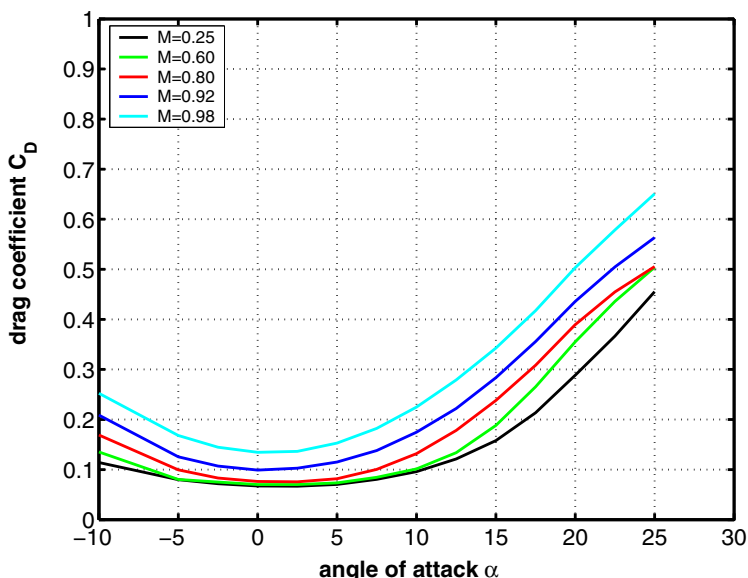


Fig. 6.12. Drag coefficient C_D as function of the angle of attack α for subsonic-transonic Mach numbers, [5]

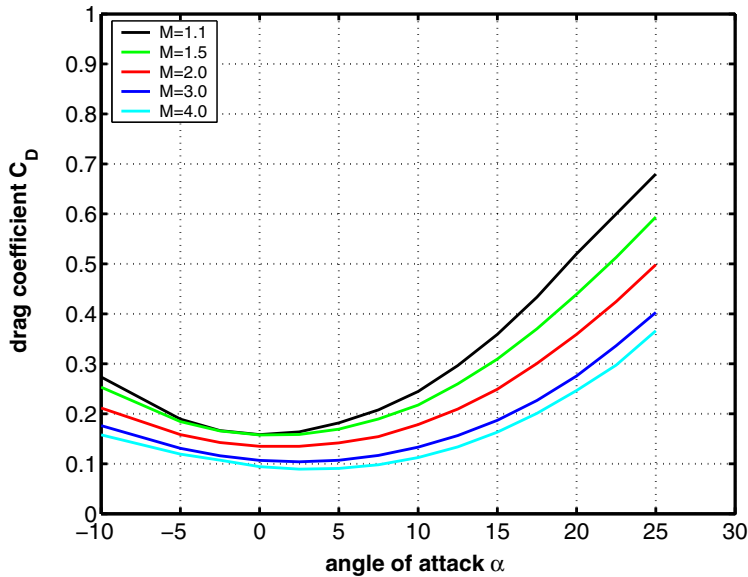


Fig. 6.13. Drag coefficient C_D as function of the angle of attack α for transonic-supersonic Mach numbers, [5]

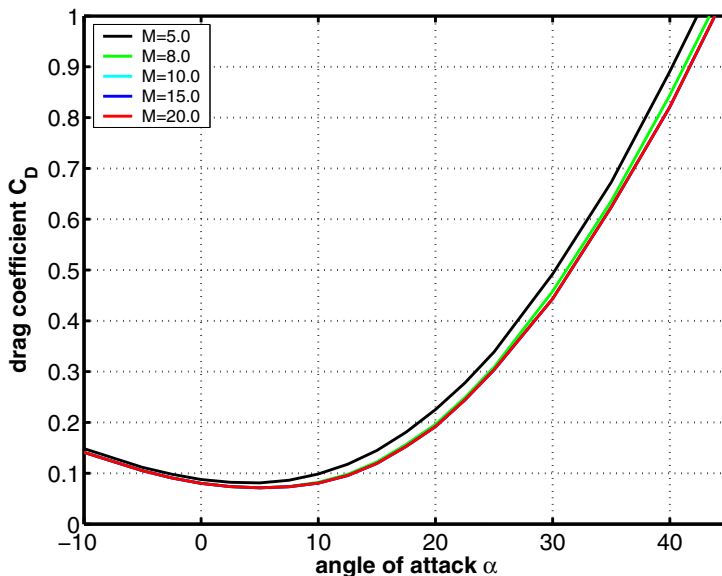


Fig. 6.14. Drag coefficient C_D as function of the angle of attack α for supersonic-hypersonic Mach numbers, [5]

no trim. This behavior is similar for $M_\infty = 0.6$, but when the Mach number approaches unity static stability is extensively growing and trim is achieved. Static stability reduces again, but is still available when the Mach number rises further up to $M_\infty = 2$. Then for $M_\infty = 3$ and 4 the stability becomes indifferent ($\partial C_m / \partial \alpha \Rightarrow 0$) and no trim is possible, see Figs. 6.18, 6.19. All that holds for the nominal center-of-gravity position $x_{cog}/L_{ref} = 0.65^{11}$.

In the Mach number regime $0.6 \leq M_\infty \leq 1.5$ one observes for $\alpha \approx 20^\circ$ a more or less sudden change of the pitching moment derivative $\partial C_m / \partial \alpha$ to positive values indicating static instability, whereby this trend can also be found for the HOPE-X shape (Section 6.8) and the PHOENIX shape (Section 6.7). For hypersonic Mach numbers static stability is only achieved for larger angles of attack ($\alpha > 20^\circ$), but the vehicle can not be trimmed there, Fig. 6.20.

In the case that a vehicle behaves unstable and/or can not be trimmed for a given set-up of center-of-gravity position and deflection angles of body flap and elevons (if available), trim and stability can be achieved in most cases by changing this set-up. A shift of the center-of-gravity rearwards decreases stability and the pitching moment grows (stronger pitch up behavior), in the opposite case, when the center-of-gravity is shifted forwards the stability increases and the pitching moment diminishes (stronger pitch down behavior).

Positive deflections of body flap and elevons have the effect to strengthen the pitch down part and to increase the stability, whereas negative deflection angles let in general the pitching moment rise and the stability decline.

To demonstrate the influence of a positive (downward) body flap deflection (say $\eta_{bf} = 10^\circ$) for the SPACE SHUTTLE Orbiter the pitching moment curves for the Mach numbers $M_\infty = 0.25, 0.6, 0.8$ are considered, which did show for $\eta_{bf} = 0^\circ$ only marginal stability and approximately no trim, Fig. 6.18. Despite that, when the body flap is deflected to $\eta_{bf} = 10^\circ$, the pitching moment is reduced, the stability is increased (this means that $\partial C_m / \partial \alpha$ is lowered) and trim exists for all the three Mach numbers, Fig. 6.21. Actually the descend flights of the SPACE SHUTTLE Orbiter in the hypersonic regime happened unstable, [10]. The body flap as main trim surface is deflected downwards.

Lateral Motion

Side force, yawing and rolling moment coefficients are presented in Figs. 6.22 to 6.33. For a better reading of the figures the Mach number regime is again separated into the three parts subsonic-transonic, transonic-supersonic and supersonic-hypersonic. The side force coefficients as function of the yaw angle β behave linearly for most of the plotted Mach numbers and the negative slope of the curves decreases with increasing Mach number, except for the very near transonic regime, Figs. 6.22 to 6.24. Fig. 6.25, where the side force

¹¹ The actual longitudinal center-of-gravity envelope of the SPACE SHUTTLE Orbiter at entry altitude (121.92 km) up to the year 1995 was $0.65 \leq x_{cog}/L_{ref} \leq 0.675$, [11].

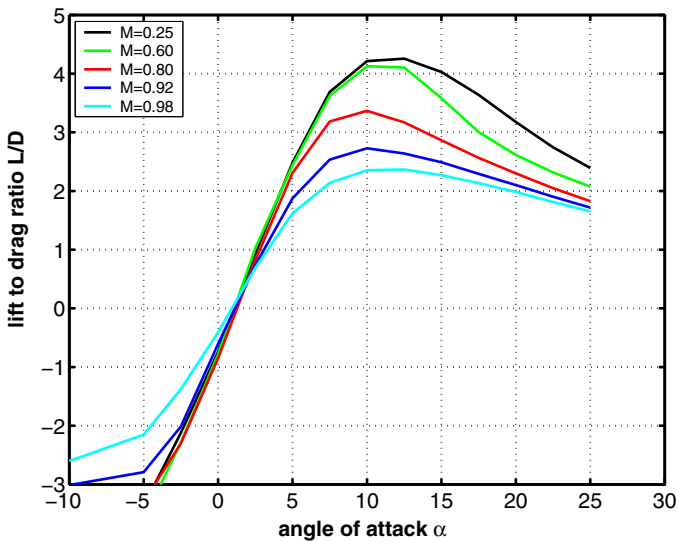


Fig. 6.15. Lift-to-drag ratio L/D as function of the angle of attack α for subsonic-transonic Mach numbers, [5]

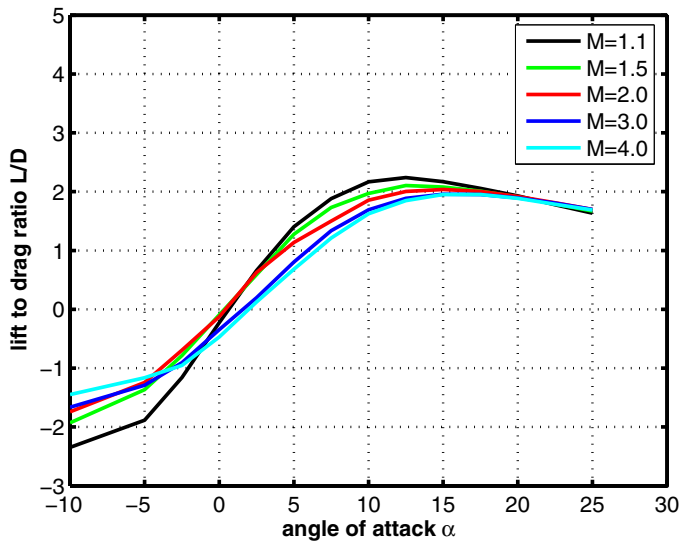


Fig. 6.16. Lift-to-drag ratio L/D as function of the angle of attack α for transonic-supersonic Mach numbers, [5]

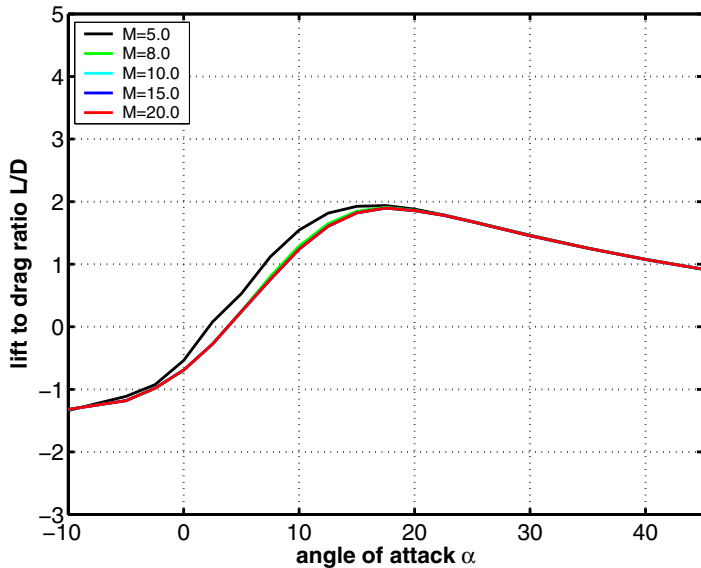


Fig. 6.17. Lift-to-drag ratio L/D as function of the angle of attack α for supersonic-hypersonic Mach numbers, [5]

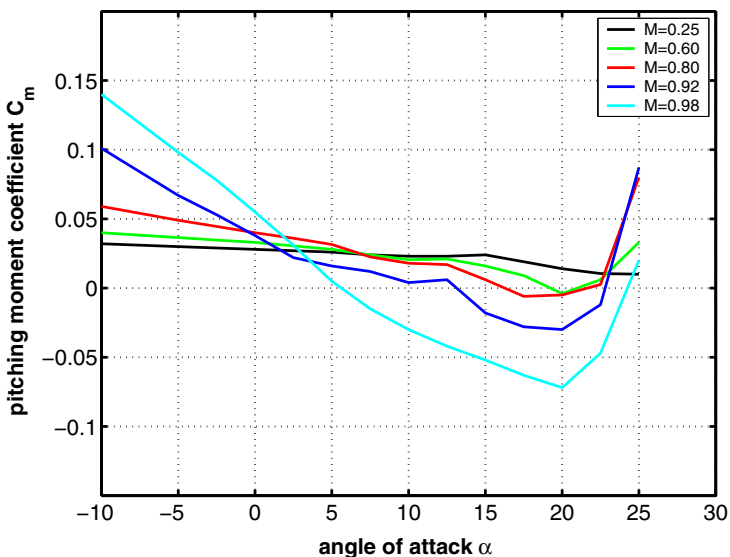


Fig. 6.18. Pitching moment coefficient C_m as function of the angle of attack α for subsonic-transonic Mach numbers, [5]. The x -position of the center-of-gravity is $x_{cog}/L_{ref} = 0.65$.

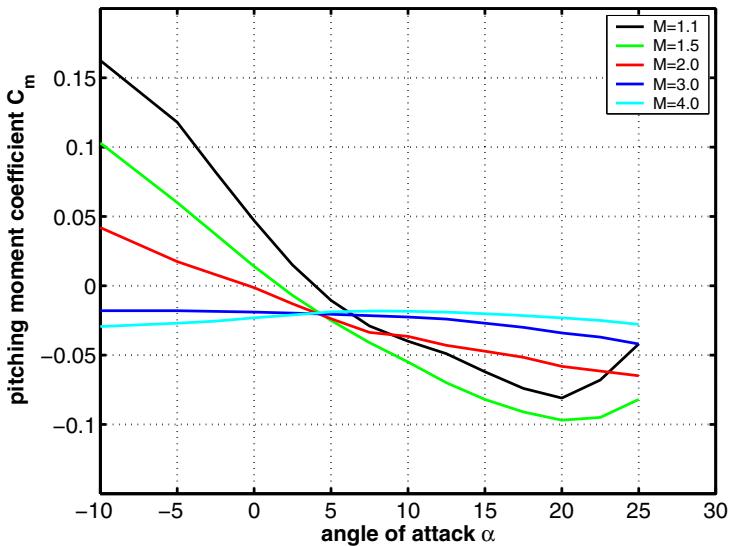


Fig. 6.19. Pitching moment coefficient C_m as function of the angle of attack α for transonic-supersonic Mach numbers, [5]. The x -position of the center-of-gravity is $x_{cog}/L_{ref} = 0.65$.

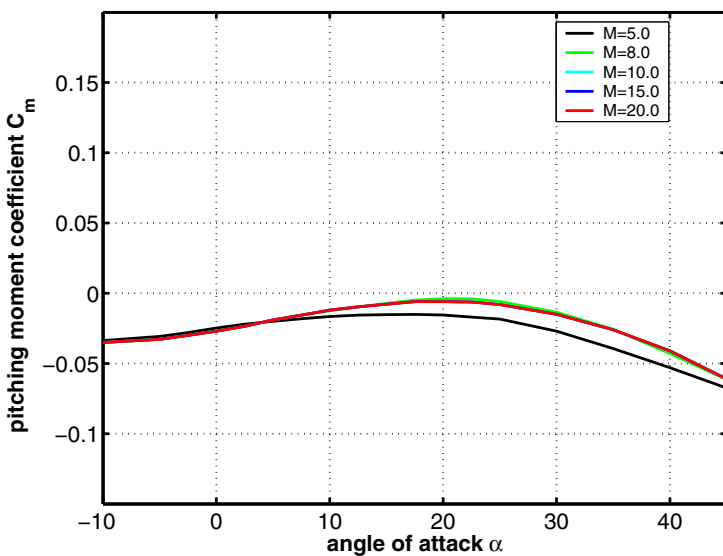


Fig. 6.20. Pitching moment coefficient C_m as function of the angle of attack α for supersonic-hypersonic Mach numbers, [5]. The x -position of the center-of-gravity is $x_{cog}/L_{ref} = 0.65$.

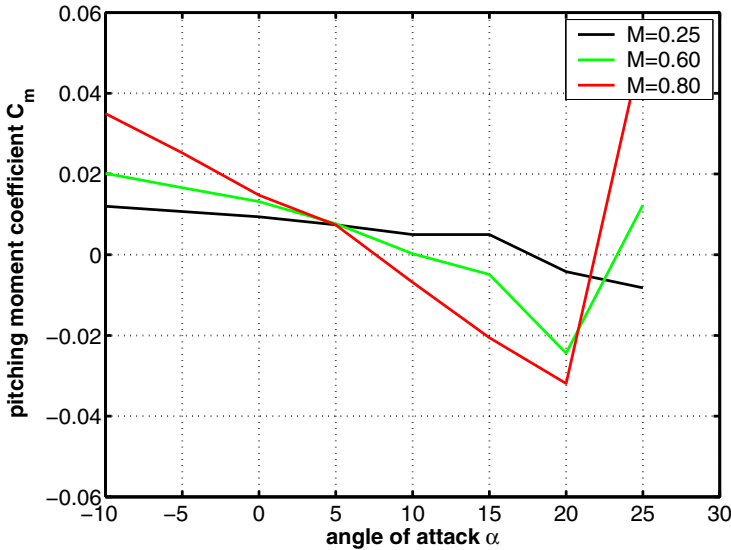


Fig. 6.21. Pitching moment coefficient C_m as function of the angle of attack α for the SPACE SHUTTLE Orbiter with body flap deflection $\eta_{bf} = 10^\circ$. Plotted are the data of three subsonic Mach numbers, [5]. The x -position of the center-of-gravity is $x_{cog}/L_{ref} = 0.65$.

coefficient as function of the Mach number (at $\beta = 6^\circ$) is plotted, emphasizes this transonic effect. Further it should be mentioned that from the Mach number $M_\infty \approx 8$ on the side force coefficient is Mach number independent, Fig. 6.24.

The yawing moment C_n for $\alpha = 0^\circ$ has a positive slope in the whole Mach number regime indicating directional stability, Figs. 6.26 - 6.28. The slope follows a monotonic trend, similar to that of the side force, namely to decrease with increasing Mach number but breaks this trend in the near transonic regime, where the slope has a maximum, Fig. 6.29. Mach number independency is given beyond $M_\infty \approx 8$, Fig. 6.28.

The rolling moment C_l for $\alpha = 0^\circ$ is presented in Figs. 6.30 to 6.32. The slope is always negative indicating a roll damping effect and decreases with growing Mach number with the same exception in the near transonic regime as for the other values mentioned above, Fig. 6.33.

The conclusion is that the SPACE SHUTTLE Orbiter flies laterally stable.

6.2.3 Aerodynamic Data of Unsteady Motion

The dynamic pitch motion is normally described by the coefficient $C_{m\dot{\alpha}} + C_{mq}$, with $C_{m\dot{\alpha}}$ being the change in the pitching moment coefficient due to the rate

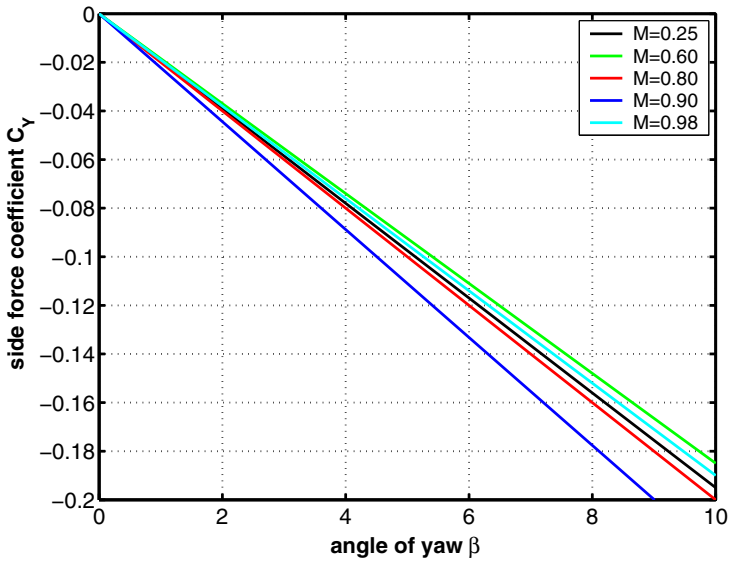


Fig. 6.22. Side force coefficient C_Y as function of the angle of yaw β at angle of attack $\alpha = 0^\circ$ for subsonic-transonic Mach numbers, [5].

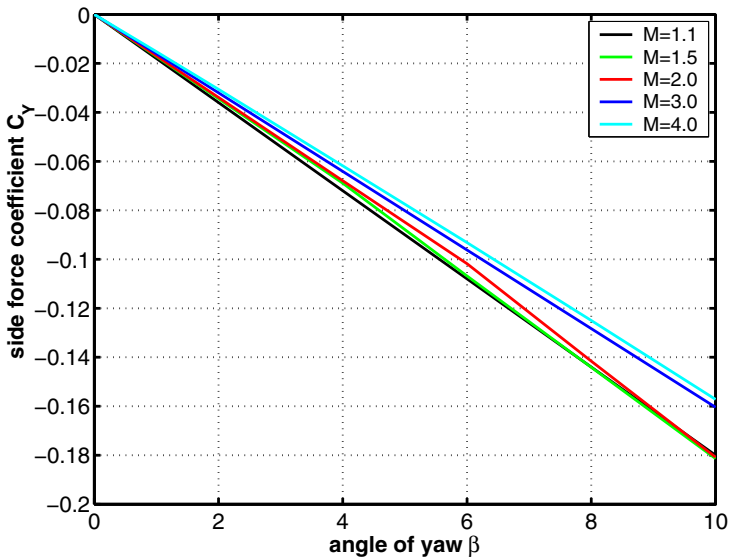


Fig. 6.23. Side force coefficient C_Y as function of the angle of yaw β at angle of attack $\alpha = 0^\circ$ for transonic-supersonic Mach numbers, [5]

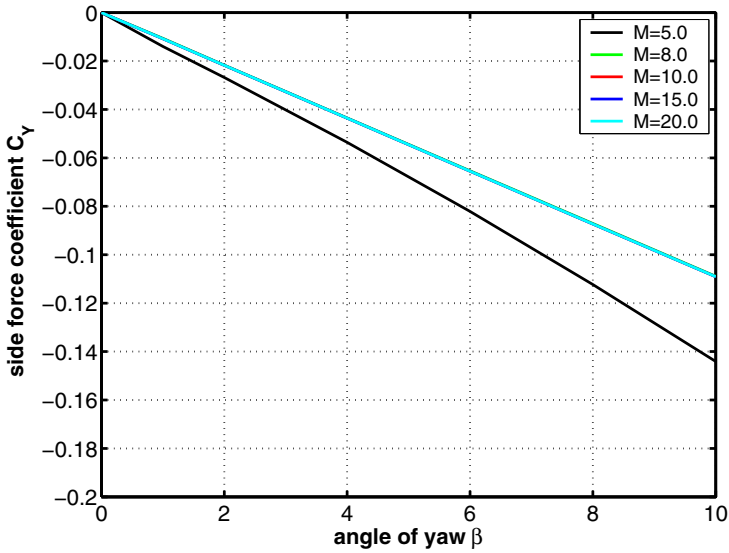


Fig. 6.24. Side force coefficient C_Y as function of the angle of yaw β at angle of attack $\alpha = 0^\circ$ for supersonic-hypersonic Mach numbers, [5]

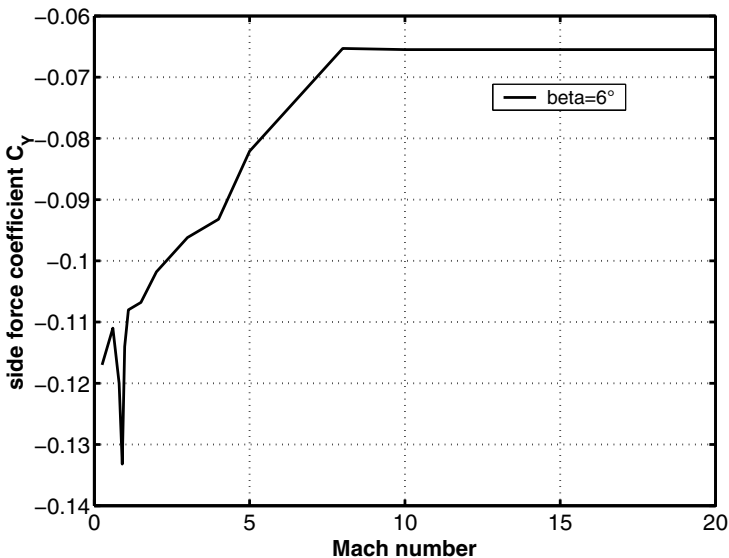


Fig. 6.25. Side force coefficient C_Y as function of the Mach number ($\alpha = 0^\circ$) at the angle of yaw $\beta = 6^\circ$, [5]

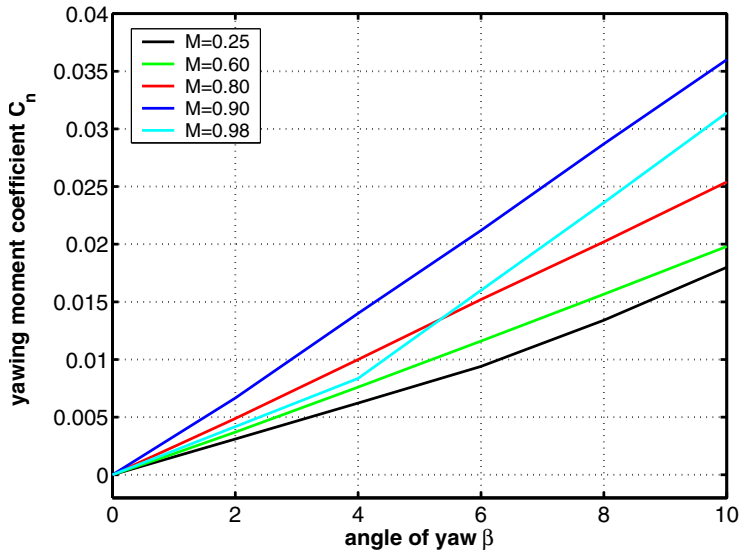


Fig. 6.26. Yawing moment coefficient C_n as function of the angle of yaw β at the angle of attack $\alpha = 0^\circ$ for subsonic-transonic Mach numbers, [5]

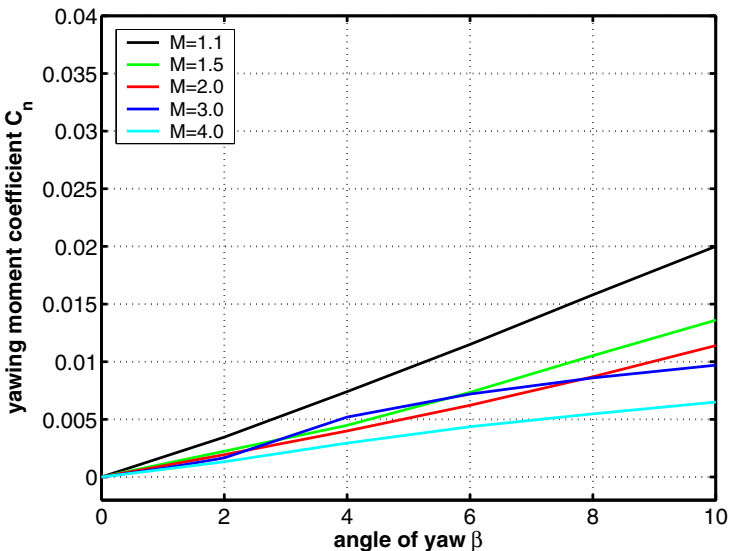


Fig. 6.27. Yawing moment coefficient C_n as function of the angle of yaw β at the angle of attack $\alpha = 0^\circ$ for transonic-supersonic Mach numbers, [5]

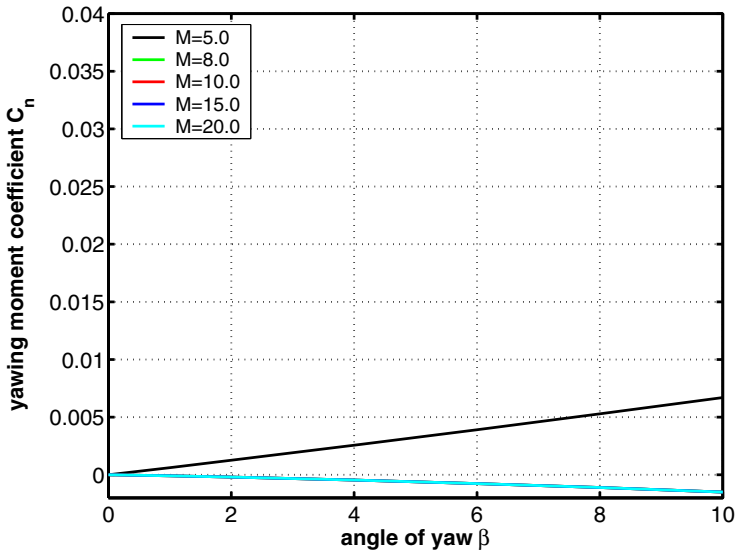


Fig. 6.28. Yawing moment coefficient C_n as function of the angle of yaw β at the angle of attack $\alpha = 0^\circ$ for supersonic-hypersonic Mach numbers, [5]

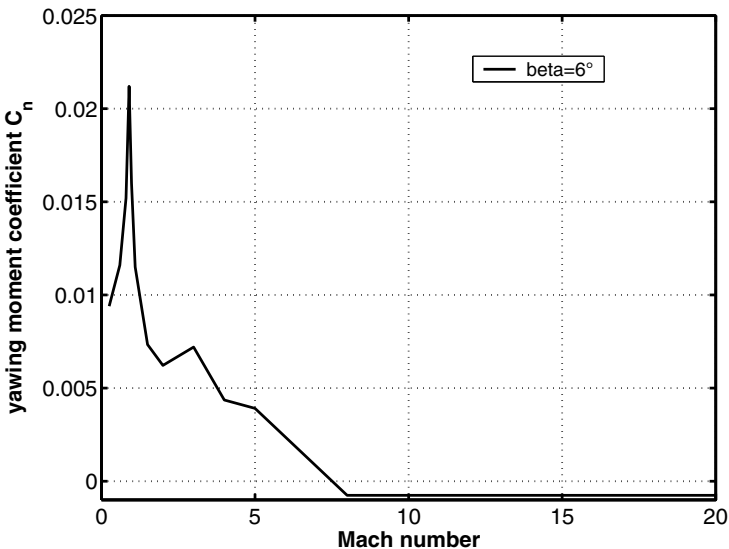


Fig. 6.29. Yawing moment coefficient C_n as function of the Mach number ($\alpha = 0^\circ$) at the angle of yaw $\beta = 6^\circ$, [5]

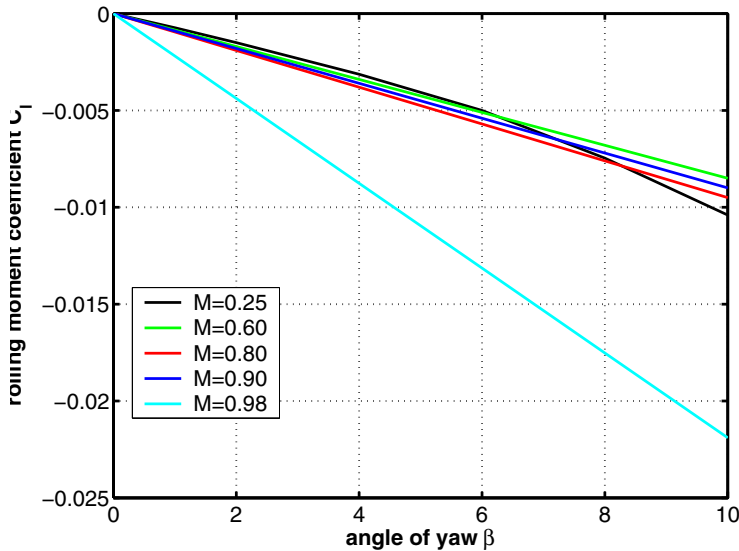


Fig. 6.30. Rolling moment coefficient C_l as function of angle of yaw β at the angle of attack $\alpha = 0^\circ$ for subsonic-transonic Mach numbers, [5]

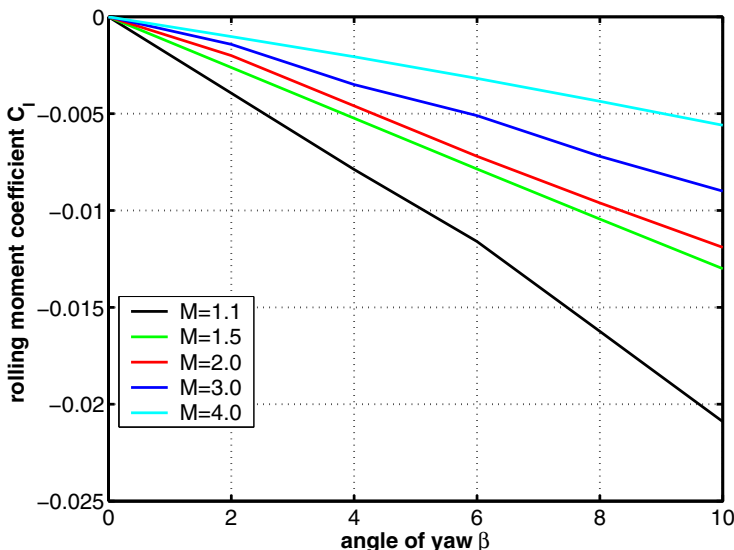


Fig. 6.31. Rolling moment coefficient C_l as function of the angle of yaw β at the angle of attack $\alpha = 0^\circ$ for transonic-supersonic Mach numbers, [5]

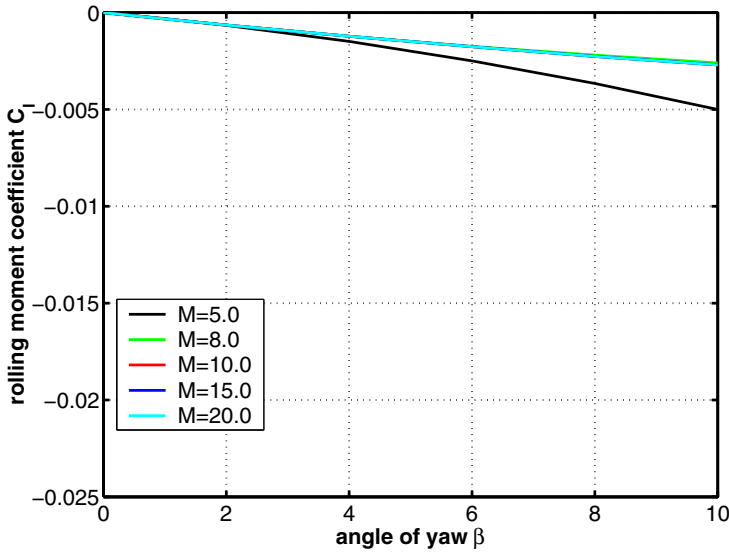


Fig. 6.32. Rolling moment coefficient C_l as function of the angle of yaw β at the angle of attack $\alpha = 0^\circ$ for supersonic-hypersonic Mach numbers, [5]

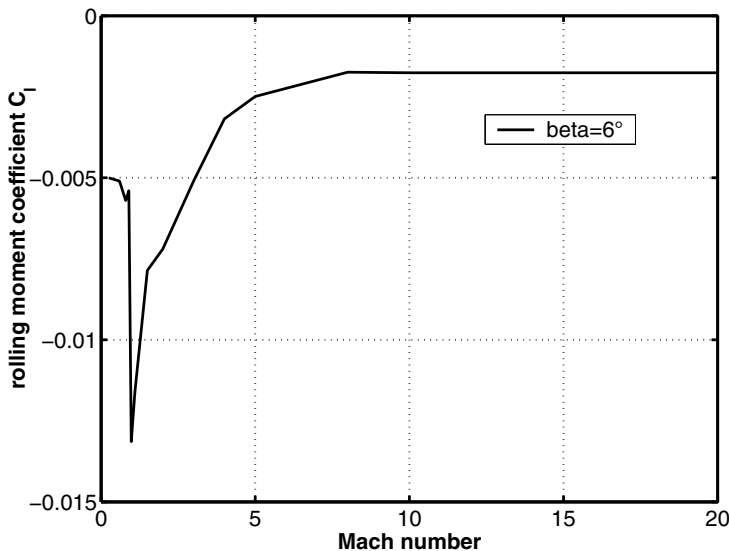


Fig. 6.33. Rolling moment coefficient C_l as function of the Mach number ($\alpha = 0^\circ$) at the angle of yaw $\beta = 6^\circ$, [5]

of change of the angle of attack $\dot{\alpha}$ (per radian) and C_{mq} the change in the pitching moment coefficient due to the pitch rate q (per radian). In [5] no distinction is made between these components and therefore only C_{mq} is considered ($C_{mq} \equiv C_{m\dot{\alpha}} + C_{mq!}$). Figs. 6.34, 6.35 show for all Mach numbers and all angles of attack negative C_{mq} values indicating that pitch damping is ensured throughout.

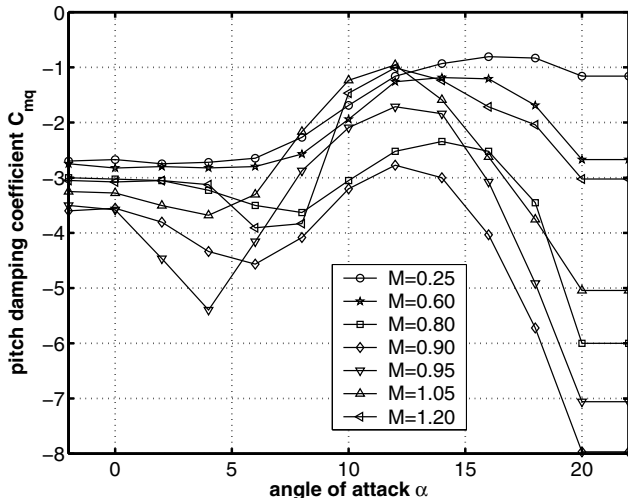


Fig. 6.34. Pitch damping coefficient C_{mq} as function of the angle of attack α for subsonic-transonic Mach numbers, [5]

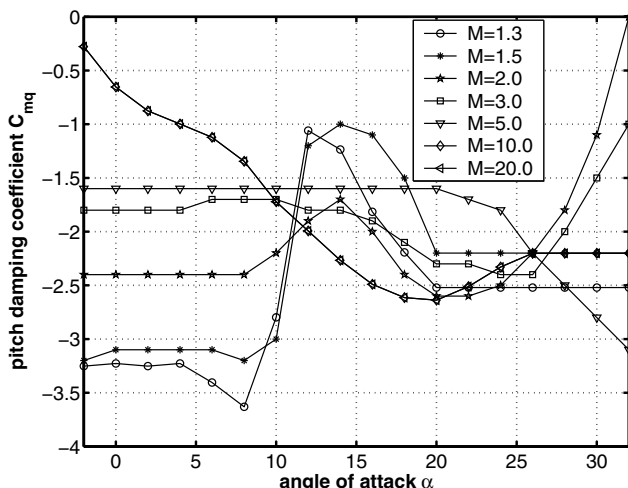


Fig. 6.35. Pitch damping coefficient C_{mq} as function of the angle of attack α for transonic-hypersonic Mach numbers, [5]

6.3 X-33 Vehicle (USA)

The development and fabrication of the U.S. SPACE SHUTTLE system had allowed for a first time to bring humans and payload to space and back by a winged space vehicle. The SPACE SHUTTLE program was started in 1972 and the first flight took place in April 1981, see Chapter 6.2. Prior to that time humans and payloads were transported into space only by capsules (non-winged re-entry vehicles), whereby the costs per transported payload mass are very high. The expectation was that these costs could be considerably reduced by the SPACE SHUTTLE system, but this never happened due to, besides others, the very high refurbishment costs of the SPACE SHUTTLE Orbiter. To overcome this problem the NASA had thought about a fully reusable single-stage-to-orbit (SSTO) space vehicle having a combined ram/scram/rocket propulsion system, which is able to start and land horizontally (NASA's National Aerospace Plane Program NASP), [12]. But it turned out that the technological challenges were so exceptional, that a realization was not possible at that time. Therefore the NASP program was cancelled in 1993.

Instead, NASA launched a research program¹² in 1996 in order to develop and then to test key technologies with specific experimental vehicles. One of these vehicles was the X-33 demonstrator¹³. The X-33 demonstrator was a single-stage-to-orbit (SSTO) reusable launch vehicle (RLV) with the capability to launch vertically and to land horizontally on a conventional runway, Fig. 6.36. The propulsion system was given by two linear aerospike engines, which are special kinds of rocket motors, [13]. The intention was to prove the feasibility of the SSTO-RLV concept through demonstration of the key technologies and operational aspects of the vehicle. However, technical and costs concerns led to the cancellation of the project in 2001.

6.3.1 Configurational Aspects

The shape of the X-33 vehicle consists of a delta formed lifting body with two 20° dihedral canted fins, two windward side body flaps and two vertical tails, Fig. 6.37. The size of the lifting body is constructed such that it can accommodate the tanks for the liquid oxygen and the liquid hydrogen, which are the propellants of the linear aerospike rocket motors.

¹² The "Reusable Launch Vehicle (RLV) Technology Program", as partnership of NASA, the U.S. Air Force and private industry.

¹³ The prime contractor of the X-33 demonstrator program was Lockheed Martin. Lockheed Martin had also planned to build on the basis of the X-33 an operable hypersonic vehicle twice as large as the X-33, called the Venture Star.



Fig. 6.36. Three synthetic images of the X-33 demonstrator: view from rear (left), vehicle in launch position (middle), front view (right), [4]

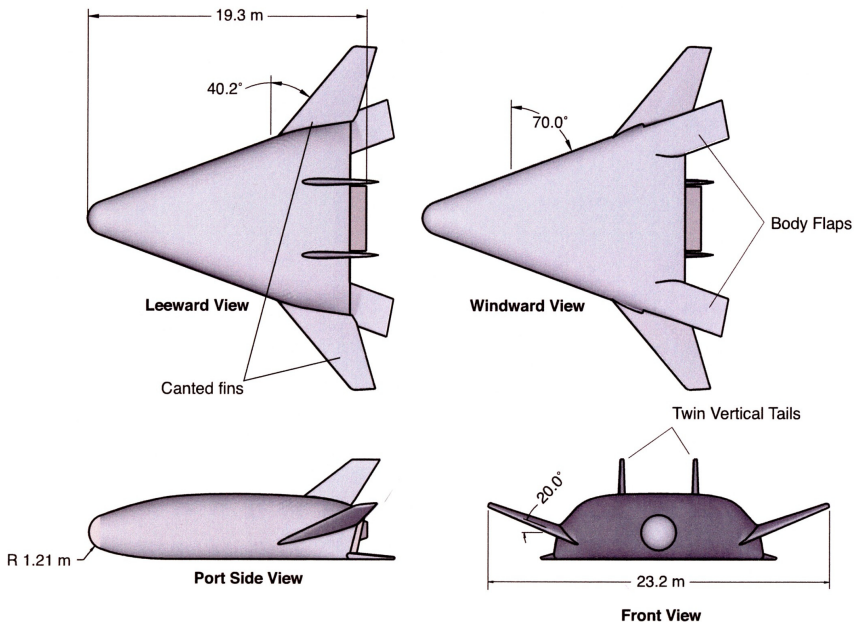


Fig. 6.37. Shape definition of the X-33 configuration, engineering drawings with dimensions, [14, 15]

Table 6.2. Reference values for the X-33 vehicle, [15]

reference length	$L_{ref} = 19.3 \text{ m (63.2 ft)}$
reference area	$S_{ref} = 149.4 \text{ m}^2 (1608 \text{ ft}^2)$
pitching moment reference point	$x_{ref} = 12.71 \text{ m (41.7 ft)}$ $\Rightarrow 0.66 L_{ref}$

6.3.2 Aerodynamic Data of Steady Motion

Aerodynamic data exist for the Mach number regime $4 \leq M_\infty \leq 10$ and angles of attack $0^\circ \leq \alpha \leq 50^\circ$. Both, wind tunnel tests and numerical flow field simulations have contributed to the establishment of the aerodynamic data set. Two air wind tunnels¹⁴ for $M_\infty = 6$ and 10 of NASA's Langley Research Center were applied for the generation of the basic data comprising longitudinal and lateral forces and moments.

Tests in Langley's CF₄ tunnel¹⁵ for $M_\infty = 6$ were performed in order to investigate the magnitude of the shock density ratio on the aerodynamic coefficients. Despite the fact that the CF₄ gas behaves perfect, a hint on the influence of real gas effects on the aerodynamics is given by these data, since the ratio of specific heats of CF₄ amounts to $\gamma_{CF_4} = 1.22$, which is considerably lower than that for perfect gas air with $\gamma_{air} = 1.4$.

Longitudinal Motion

The aerodynamic coefficients presented in Figs. 6.40 to 6.43 are taken from the references [14] and [15]. The curves for the Mach numbers $M_\infty = 6$ and 10 stem from tests in the before mentioned NASA wind tunnels, [15], whereas for $M_\infty = 4, 5$ and 8 numerical solutions of the Navier-Stokes equations are the origin of the data, [14].

The lift coefficient data exhibit almost linear behavior for all Mach numbers between $\alpha \approx 10^\circ$ and 40° . For larger α values C_L becomes non-linear due to the enforced generation of leeside vortices, which is common for all delta wing like configurations. A further general trend is the decrease of C_L with increasing Mach number, Fig. 6.40. This is true also for the drag coefficient C_D . The differences of the drag data for the plotted Mach number values ($4 \leq M_\infty \leq 10$) are small, Fig. 6.41. The aerodynamic performance for $M_\infty = 4$ is highest with $L/D_{max} = 1.25$ at $\alpha = 20^\circ$, while L/D_{max} at Mach 10 is 1.2 at a shifted angle of attack value $\alpha \approx 24^\circ$, Fig. 6.42.

The pitching moment characteristics are shown in Fig. 6.43. All the Mach numbers possess an angle of attack range, where the vehicle is statically

¹⁴ LaRC 20-Inch Mach 6 Air Tunnel and LaRC 31-Inch Mach 10 Air Tunnel .

¹⁵ LaRC 20-Inch Mach 6 CF₄ Tunnel .

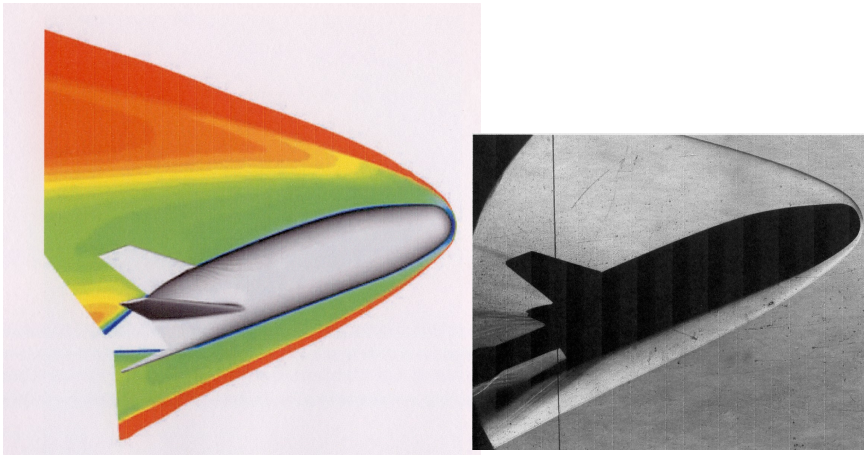


Fig. 6.38. X-33 flow field; wind tunnel conditions are $M_\infty = 6$ and $\alpha = 20^\circ$. Mach number isolines of numerical solution (left), wind tunnel Schlieren image (right), [14].

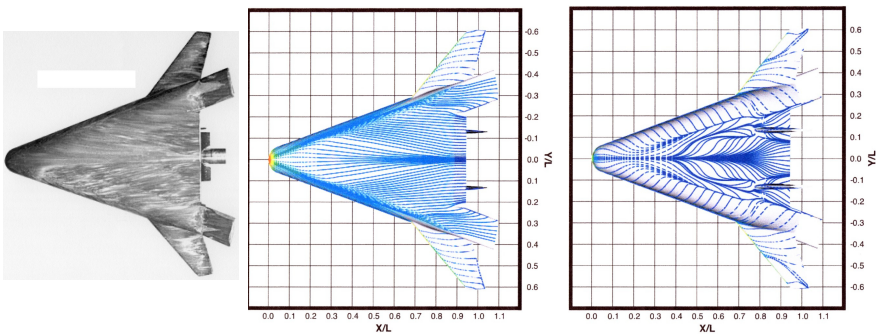


Fig. 6.39. X-33 flow field; wind tunnel conditions are $M_\infty = 6$ and $\alpha = 20^\circ$. Windward side oil flow image (left), skin-friction lines at the windward side (middle) and at the leeward side (right), both evaluated from a numerical solution, [14].

stable. The general C_m behavior for the given reference point $x_{ref} = 0.66 L_{ref}$ is slightly different for the data coming from the numerical simulations ($M_\infty = 4, 5$ and 8 , [14]) compared to the wind tunnel data ($M_\infty = 6$ and 10 , [15]). The reason for that is unexplained. C_m indicates longitudinal stability for $M_\infty = 4$ at $10^\circ \leq \alpha \leq 40^\circ$, for $M_\infty = 5$ at $10^\circ \leq \alpha \leq 50^\circ$, for $M_\infty = 6$ at $15^\circ \leq \alpha \leq 50^\circ$, for $M_\infty = 8$ at $20^\circ \leq \alpha \leq 50^\circ$ and for $M_\infty = 10$ at

$22^\circ \leq \alpha \leq 45^\circ$. It should be mentioned that there is obviously a slight trend to lower C_m values (decreased pitch-up moment) in the numerical solutions.

Further, we point out that there exists an unexplained crossover of the C_m curves for $M_\infty = 6$ and 10, which was observed both in experiments and numerical simulations, [15, 16].

A concluding observation was that real gas effects have only little influence on the aerodynamic coefficients of the X-33 vehicle in the considered Mach number regime as tests in NASA's CF_4 Mach 6 tunnel [15], and numerical solutions [17], have shown.

The data of the pitching moment in Fig. 6.43 indicate a possible vehicle trim around $\alpha \approx 40^\circ$ for $M_\infty = 4, 5$ and 8, but no trim for $M_\infty = 6$ and 10. There is indeed, as already mentioned, an ambiguity with respect to the uniqueness of the data. Nevertheless, an inspection of the influence of body flap deflections on the pitching moment is useful. We do that for the $M_\infty = 6$ case with body flap deflections of $\eta_{bf} = 0^\circ, 10^\circ, 20^\circ$ in Fig. 6.44. It can be seen that already a deflection angle of $\eta_{bf} = 10^\circ$ leads to such a strong pitch-down effect that vehicle trim is possible at $\alpha_{trim} \approx 20^\circ$. This shows that the effectiveness of the body flaps is definitely strong enough to control the vehicle, particularly since the maximum body flap deflection is $\eta_{bf} = 30^\circ$.

But we will advert to another flow effect in connection with the body flap, namely that the pitching moment curve for $\eta_{bf} = 20^\circ$ has an inflection point around $\alpha \approx 37^\circ$, Fig. 6.44. When the bow shock interacts with the embedded body flap shock an expansion zone is generated, which impinges around $\alpha \approx 37^\circ$ on the lower side of the body flap. Correspondingly the pressure on the body flap lower surface is decreased and a pitch-up effect arises.

Lateral Motion

Directional stability is given when the yawing moment C_n has a positive slope with respect to the yawing angle β . This is not the case for the X-33 vehicle for $M_\infty = 6$ and 10 as Fig. 6.45 shows. There, $\partial C_n / \partial \beta$ is negative in the whole angle of attack regime, indicating directional instability, which is common for this type of aerospace configurations. The small twin vertical tails in the aft part of the upper side of the vehicle contribute only little to the yaw stability, in particular when at higher angles of attack the tails lie in the hypersonic shadow of the flow field.

The rolling moment derivative $\partial C_l / \partial \beta$ is negative for all angles of attack $\alpha > 4^\circ$. The two 20° dihedral canted fins generate mainly this negative $C_{l\beta}$ demonstrating the damping of roll motion, which increases nearly linearly with increasing angle of attack, Fig. 6.46. Wing dihedral (positive and negative) is long since a well known measure to ensure roll damping.

6.3.3 Aerodynamic Data of Unsteady Motion

Results of investigations of the dynamic stability are not available.

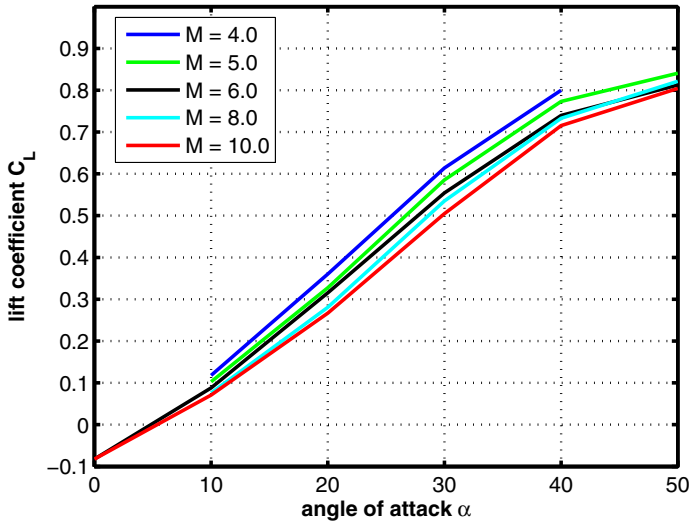


Fig. 6.40. Lift coefficient C_L as function of the angle of attack α for supersonic-hypersonic Mach numbers, [14, 15]

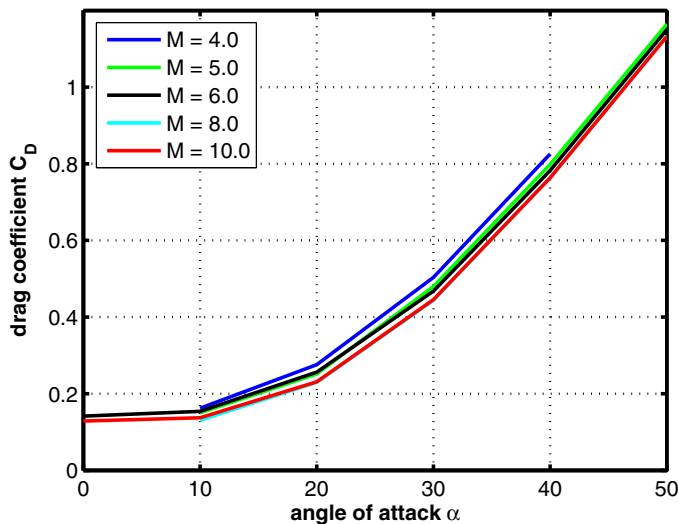


Fig. 6.41. Drag coefficient C_D as function of the angle of attack α for supersonic-hypersonic Mach numbers, [14, 15]

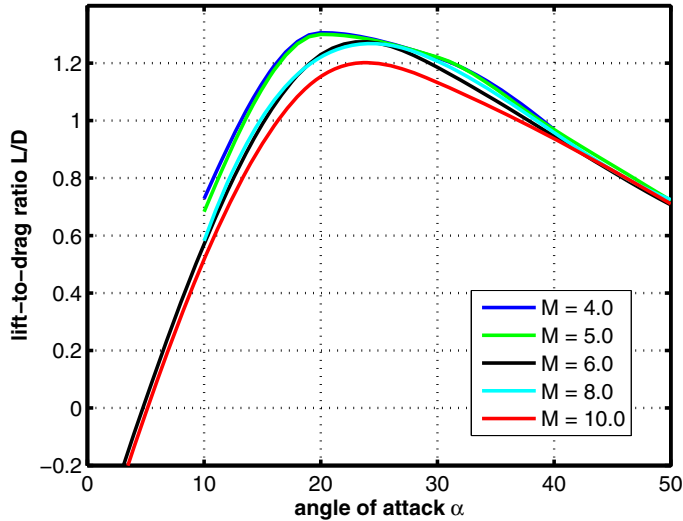


Fig. 6.42. Lift-to-drag ratio L/D as function of the angle of attack α for supersonic-hypersonic Mach numbers, [14, 15]

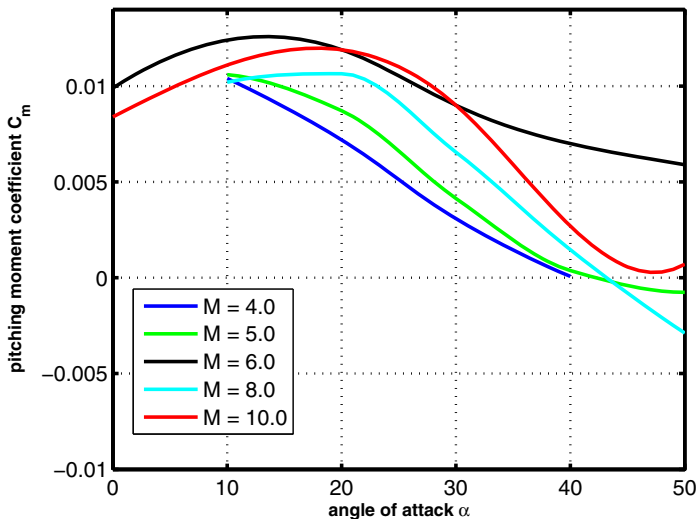


Fig. 6.43. Pitching moment coefficient C_m as function of the angle of attack α for supersonic-hypersonic Mach numbers, [14, 15]. The moment reference point is $x_{ref} = 0.66 L_{ref}$.

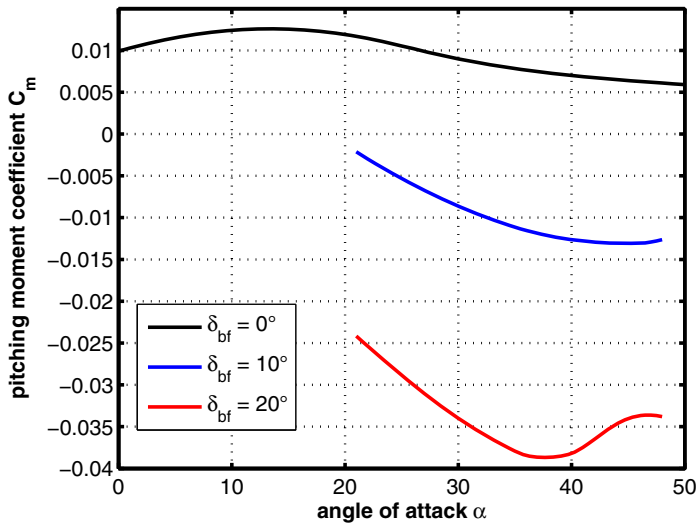


Fig. 6.44. Influence of the body flap deflection on the pitching moment coefficient C_m as function of the angle of attack α for the free-stream Mach number $M_\infty = 6$, [15]. The moment reference point is $x_{ref} = 0.66 L_{ref}$.

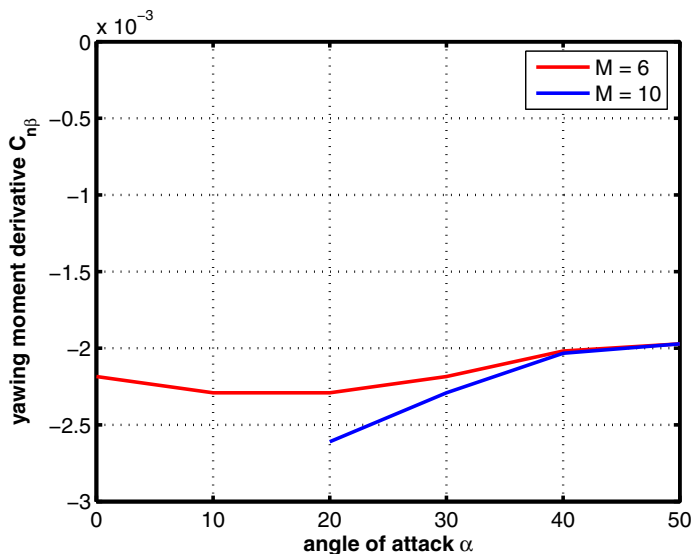


Fig. 6.45. The yawing moment derivative $C_{n\beta}$ (criterion of directional stability) as function of angle of the attack α for the free-stream Mach numbers $M_\infty = 6$ and 10, [15]

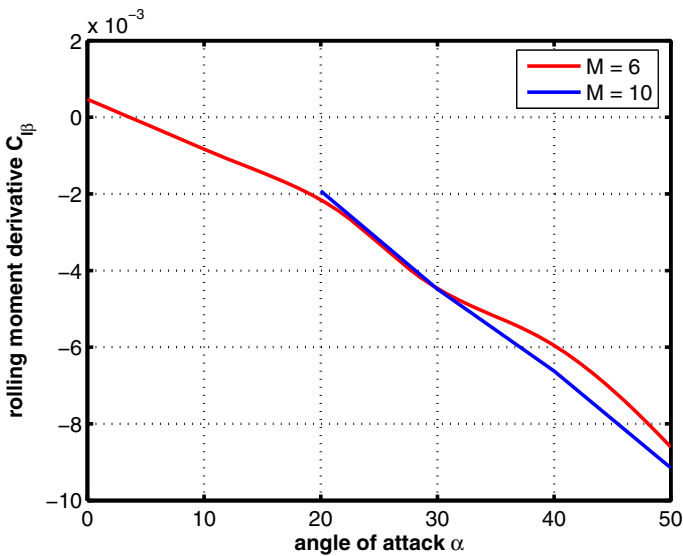


Fig. 6.46. The rolling moment derivative $C_{l\beta}$ (dihedral effect due to the canted wings) as function of the angle of attack α for the free-stream Mach numbers $M_\infty = 6$ and 10 , [15]

6.4 X-34 Vehicle (USA)

As mentioned already in Section 6.3 NASA had cancelled its National Aerospace Plane (NASP) program in 1993, and launched in 1996 a new activity called Reusable Launch Vehicle (RLV) Technology Program, a partnership among NASA, the U.S. Air Force and private industry. This program had encompassed three demonstrator vehicles, with the primary goal to develop and investigate key technologies, which should significantly lower the cost of access to space, necessary for the design and operation of a future reusable launch vehicle.

The first flight demonstrator was the Delta Clipper Experimental Advanced (DC-XA)¹⁶ vehicle initialized, designed and tested by McDonnell Douglas, Fig. 6.47.



Fig. 6.47. Delta Clipper Experimental Advanced vehicle, [4]

This vehicle should mainly demonstrate, [12, 18]

- the flight control system,
- the aircraft-like operability through a low turnaround time,
- the vertical ascent and landing capability.

After an accident—the oxygen tank exploded—the program was terminated at the end of 1996.

The second vehicle was the X-33 demonstrator, already described in Section 6.3, with Lockheed Martin as prime contractor.

¹⁶ This initiative was already started in the beginning of the 1990s by McDonnell Douglas as the "Delta Clipper Experimental (DC-X)" project.

The third demonstrator vehicle, called X-34, was developed by the Orbital Sciences Corporation and was to serve as test bed for new technologies and progressive operations, [18] - [20]. These were:

- lightweight primary and secondary composite structures,
- reusable composite propellant tanks,
- advanced thermal protection system (TPS),
- flush air data system,
- integrated low cost avionics using differential Global Positioning System (GPS),
- rapid turn-around times,
- airplane-like operations at all weather conditions,
- autonomous flight including automatic landing.

Three vehicles were built in order to perform the ambitious flight test program, which had the goal to reach finally a maximum speed of $M_{\infty} = 8$ at an altitude of 76 km. The X-34 was to be air-launched from an L-1011 carrier aircraft at $M_{\infty} = 0.7$ and an altitude of approximately 11500 m, Fig. 6.48. It was to be powered by a new low-cost rocket engine called "Fastrac". Fig. 6.49 shows two photographs of the X-34 vehicle on the ground.

In March 2001 NASA decided to scrap the X-34 vehicle program, since the projected cost of completing the vehicle had hit an unacceptable level and the program too many technical risks.



Fig. 6.48. The X-34 vehicle underneath of the L-1011 carrier (left), free flight test including automatic terminal approach and landing (right), [4, 21]

6.4.1 Configurational Aspects

The X-34 planform is remotely similar to that of the SPACE SHUTTLE Orbiter. The vehicle has a double delta wing with a 45° sweep of the main wing and a 80° leading edge strake. A wing dihedral of 6° was chosen to

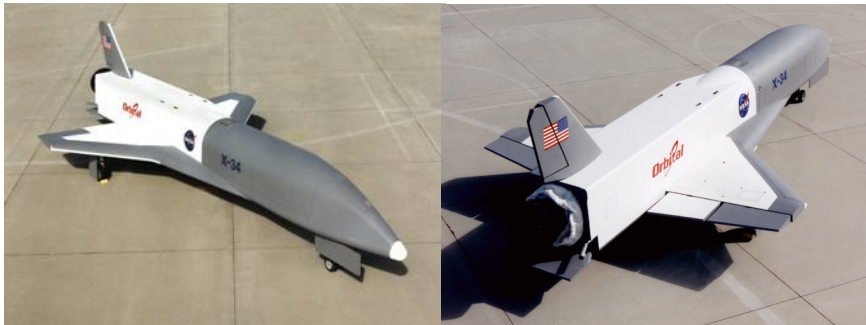


Fig. 6.49. The X-34 vehicle on the test range: lateral front view (left), lateral view from behind (right), [4, 21]

control roll motion. The reference values are listed in Table 6.3. Full span elevons serve as part of the pitch control when symmetrically deflected and roll control when asymmetrically deflected. Another element to control the pitch movement is given by the body flap mounted at the back part of the fuselage underneath the engine nozzle. Directional stability is secured by a vertical tail as long as angle of attack and Mach number are in a range that the tail does not lie in the flow shadow. Fig. 6.50 shows the vehicle's configuration including the main dimensions.

Table 6.3. Reference dimensions of the X-34 vehicle, [18, 19]

reference length	$L_{ref} = 646.9 \text{ in. (16.43 m)}$
reference width	$B_{ref} = 332.9 \text{ in. (8.45 m)}$
reference height	$L_{ref} = 142.2 \text{ in. (3.61 m)}$
reference area	$S_{ref} = 357.5 \text{ ft}^2 (33.21 \text{ m}^2)$
moment reference point	$x_{ref} = 420 \text{ in. (10.67 m)}$ $\implies 0.65 L_{ref}$

6.4.2 Aerodynamic Data of Steady Motion

Aerodynamic data exist for steady longitudinal and lateral motions. The main part of the investigations had been performed in the wind tunnels of NASA

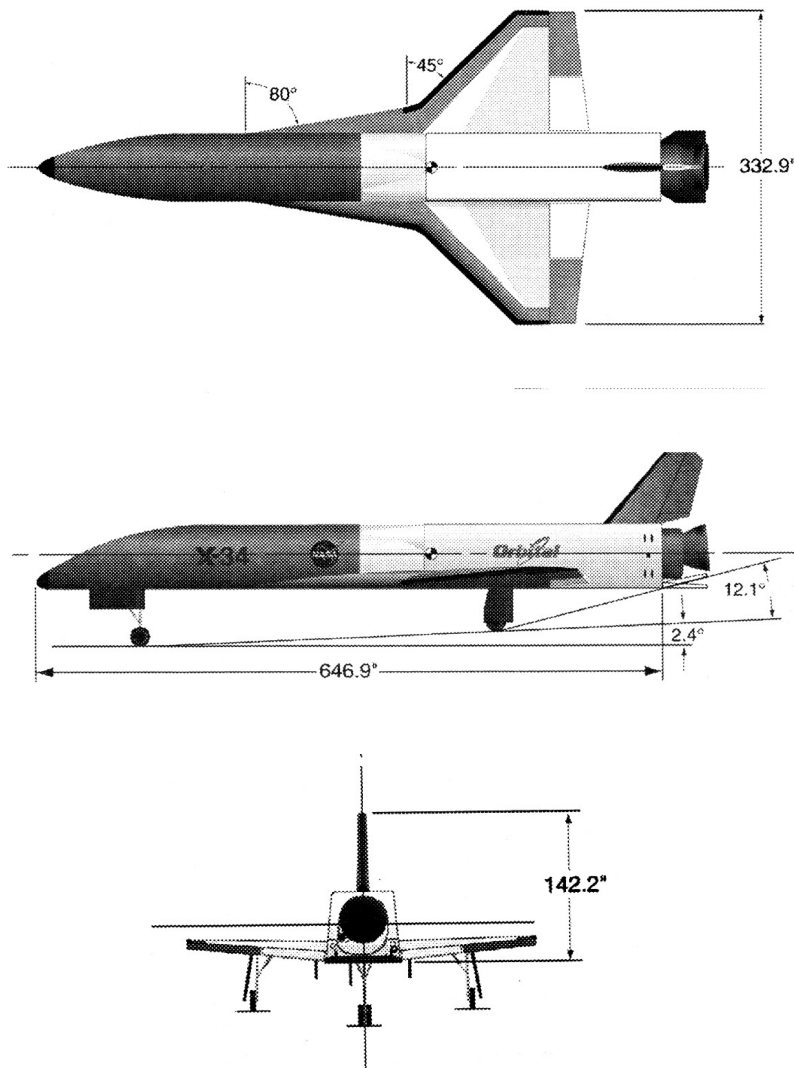


Fig. 6.50. Shape definition of the X-34 configuration, synthetic images with measures, [18, 19]

Langley's Research Center¹⁷. The Mach number covered the range from 0.25 to 10, and the angle of attack that from -5° to 40° , [18] - [20]. In another campaign numerical simulations solving the Euler equations were conducted for Mach numbers $1.25 \leq M_\infty \leq 6$ and angles of attack $-4^\circ \leq \alpha \leq 32^\circ$, [22].

Longitudinal Motion

The lift coefficient C_L , Fig. 6.51, for $M_\infty = 0.4$ is linear up to $\alpha \approx 12^\circ$ where an increase of the curve shape can be observed which is due to the generation of vortices over the wing (vortex lift). It seems that the vortex lift breaks down when the Mach number increases ($M_\infty = 0.8, 0.9, 1.05$). For the Mach number $M_\infty = 2$ C_L is linear in the angle of attack regime plotted. Increasing the Mach number to $M_\infty \geq 4$ exhibits the typical non-linear C_L curves known for such kinds of vehicles.

The drag at given angle of attack α has a maximum for transonic speed ($M_\infty = 1.05$). Around zero angle of attack the subsonic drag ($M_\infty = 0.4$) and the hypersonic drag (($M_\infty = 6$)) have similar values. For higher angles of attack the drag is lowest for hypersonic Mach numbers, Fig. 6.52.

The aerodynamic performance L/D has its maximum value for the subsonic Mach number $M_\infty = 0.4$ with $L/D_{max} \approx 7$ at $\alpha_{max} \approx 7^\circ$. With increasing Mach number the maximum value decreases, while α_{max} decreases for $M_\infty < 1$. In supersonic-hypersonic flow the L/D curves are flattened with a maximum of L/D of approximately 2.5, Fig. 6.53.

A view onto the pitching moment diagram (Fig. 6.54) reveals that C_m is negative for all Mach numbers and angles of attack (nose-down moment). This is an indication that negative deflections (upwards) of the control surfaces would be needed to trim the vehicle. The vehicle is unstable or neutrally stable in the subsonic regime ($M_\infty \leq 0.8$) for lower angles of attack ($\alpha \lesssim 12^\circ$). In the transonic-supersonic regime ($M_\infty = 0.9, 1.05, 2$) the vehicle becomes stable ($\partial C_m / \partial \alpha < 0$) due to the aft movement of the center-of-pressure up to angles of attack $\alpha \lesssim 13^\circ$. For the given pitching moment references point ($x_{ref} = 0.65 L_{ref}$) static instability can be observed in the hypersonic regime for angles of attack $\alpha \lesssim 25^\circ$, where for higher α values a slight tendency to static stability can be identified, Fig. 6.54. Generally, the pitching moment is less nose-down when the Mach number reaches hypersonic values.

¹⁷ the following five wind tunnels were used:

- LaRC 14-by 22-Foot Subsonic Tunnel (LTPT) for $M_\infty = 0.25$,
- LaRC 16-Foot Transonic Tunnel (16-ft TT) for $0.3 \leq M_\infty \leq 1.3$, $-4^\circ \leq \alpha \leq 25^\circ$,
- LaRC Unitary Plan Wind Tunnel (UPWT-1, UPWT-2) for $1.45 \leq M_\infty \leq 2.86$ (UPTW-1) and $2.3 \leq M_\infty \leq 4.6$ (UPWT-2), $-12^\circ \leq \alpha \leq 22^\circ$,
- LaRC 20-Inch Mach 6 Air Tunnel for $M_\infty = 6$, $-4^\circ \leq \alpha \leq 40^\circ$,
- LaRC 31-Inch Mach 10 Air Tunnel for $M_\infty = 10$, $-4^\circ \leq \alpha \leq 40^\circ$.

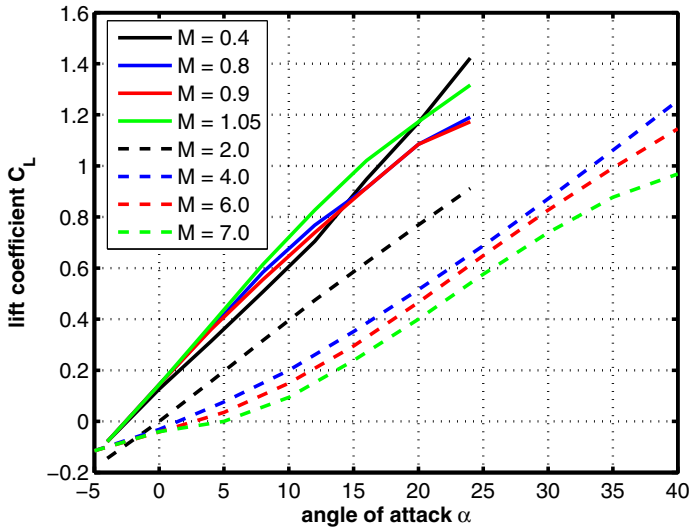


Fig. 6.51. Lift coefficient C_L as function of the angle of attack α for subsonic to hypersonic Mach numbers, [18, 19]

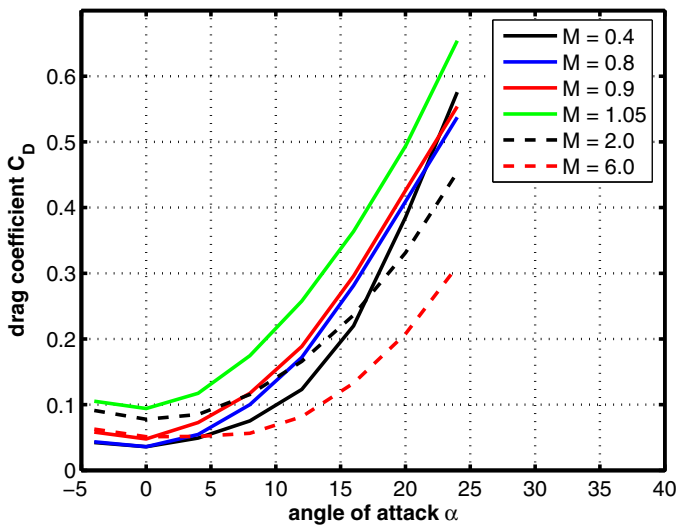


Fig. 6.52. Drag coefficient C_D as function of the angle of attack α for subsonic to hypersonic Mach numbers, [18, 19]

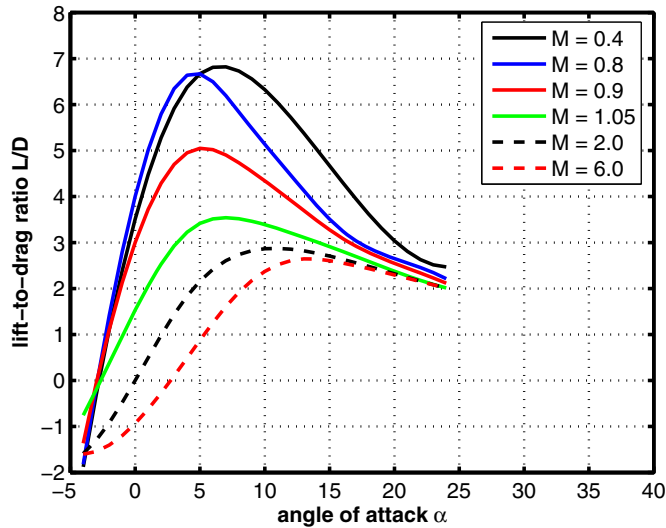


Fig. 6.53. Lift-to-drag ratio L/D as function of the angle of attack α for subsonic to hypersonic Mach numbers, [18, 19]

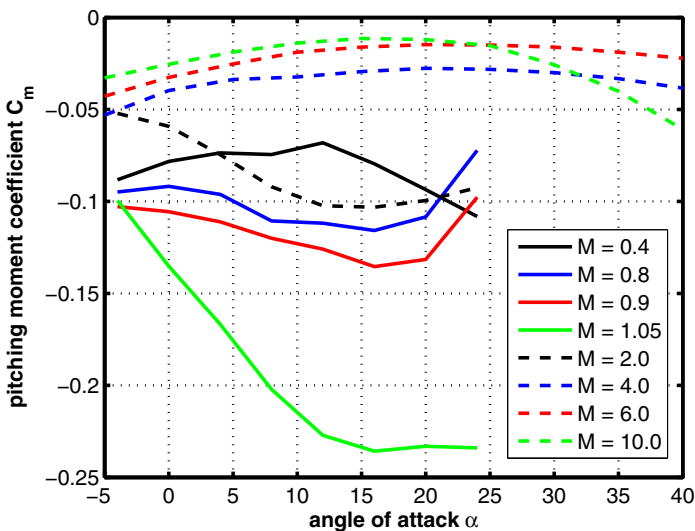


Fig. 6.54. Pitching moment coefficient C_m as function of the angle of attack α for subsonic to hypersonic Mach numbers, [18, 19]. The moment reference point is at $x_{ref} = 0.65 L_{ref}$.

Lateral Motion

Figs. 6.55 and 6.56 are ambiguous in view of the directional stability (yawing moment) of the vehicle. As is well known, directional stability requires a positive gradient of the yawing moment coefficient C_n with respect to the yaw angle β ($\partial C_n / \partial \beta > 0$). At an angle of attack of $\alpha = 18^\circ$ $\partial C_n / \partial \beta$ is negative for the plotted Mach numbers ($M_\infty = 1.25, 2, 6$) indicating directional instability, Fig. 6.55. On the other hand Fig. 6.56 exhibits that for lower angles of attack ($\alpha \lesssim 12^\circ$) the vehicle is directionally stable for $M_\infty = 1.25$, which is also true for $M_\infty = 0.9$. At increasing Mach numbers ($M_\infty = 2, 6$) the vehicle is definitely directionally unstable.

Roll attenuation or damping of roll motion is shown in Figs. 6.57 and 6.58. If the derivative of the rolling moment coefficient with respect to the yawing angle β is negative roll motion is abated, the vehicle is stable in roll. At $\alpha = 18^\circ$ this is the case for all Mach numbers, Fig. 6.57, where with increasing Mach number the vehicle is less stable in roll. For transonic Mach numbers ($M_\infty = 0.9, 1.25$) $\partial C_l / \partial \beta$ is negative for nearly all angles of attack, whereas for higher Mach numbers ($M_\infty = 2, 6$) roll instability occurs for angles of attack $\alpha \lesssim 10^\circ$, Fig. 6.58. Generally, $\partial C_l / \partial \beta$ becomes more negative when the angle of attack grows, which is due to the increase of the effectiveness of the wing dihedral.

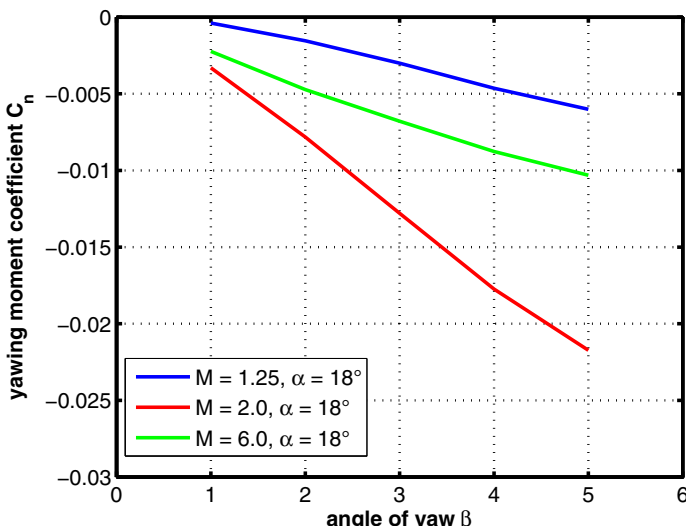


Fig. 6.55. Yawing moment coefficient C_n as function of the yaw angle β , [18, 19]. The moment reference point is $x_{ref} = 0.65 L_{ref}$.

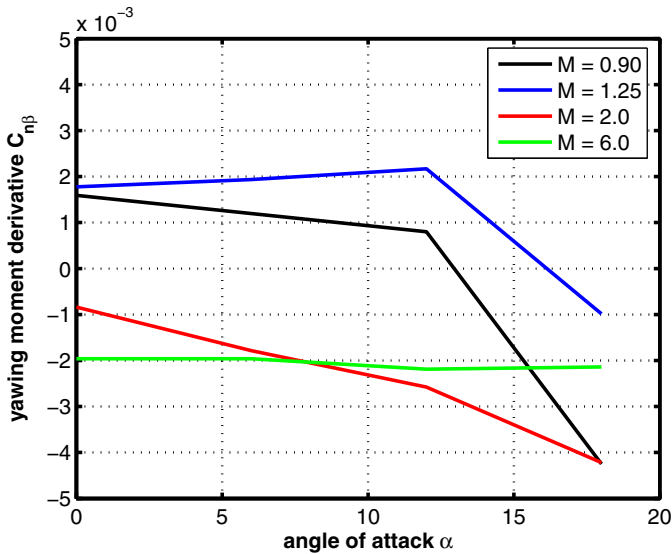


Fig. 6.56. Yawing moment derivative $C_{n\beta}$ as function of the angle of attack α , [18, 19]. The moment reference point is $x_{ref} = 0.65 L_{ref}$.

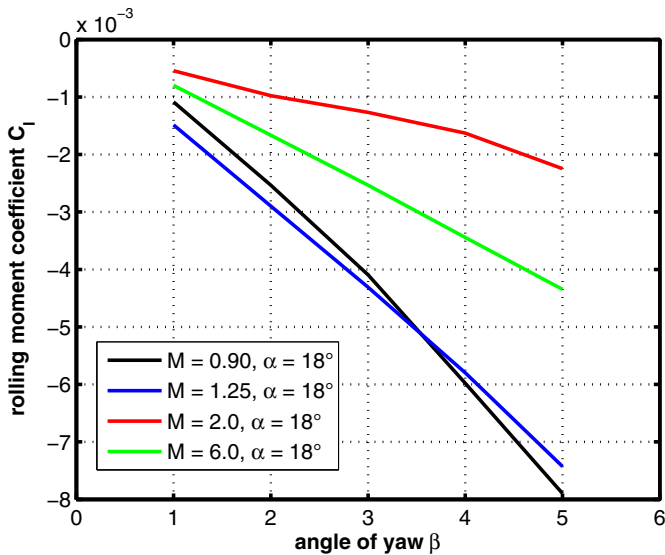


Fig. 6.57. Rolling moment coefficient C_l as function of the yaw angle β , [18, 19]

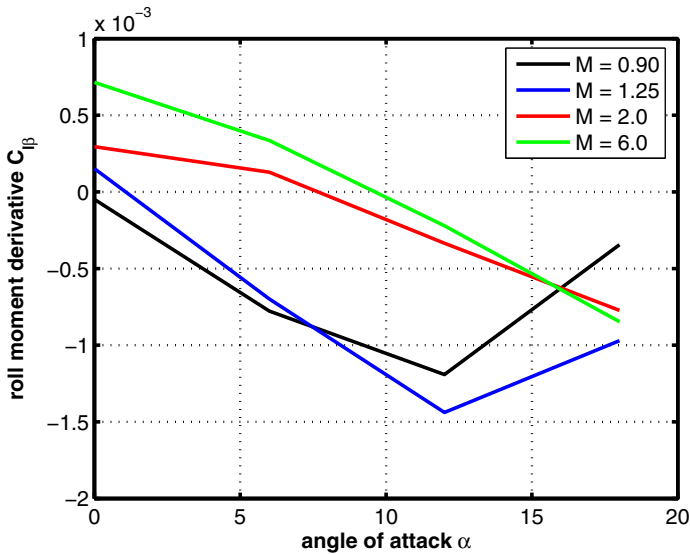


Fig. 6.58. Rolling moment derivative $C_{l\beta}$ as function of the angle of attack α , [18, 19]

6.4.3 Aerodynamic Data of Unsteady Motion

Results of investigations of dynamic stability are not available.

6.5 X-37 Vehicle (USA)

The X-37 was the third in the series of advanced reusable technology demonstrators following the X-33 and X-34 vehicles. Whereas those demonstrators were designed to flight test technologies at lower altitudes and speeds, the X-37 would be the first to explore the orbital and re-entry phases of flight. Fig. 6.59 exhibits the test envelopes of the three space vehicles, [23].

In 1996 the United States started the activities with the X-33 vehicle, a single-stage-to-orbit (SSTO) demonstrator with a linear aerospike engine, and the X-34 vehicle, being a flying laboratory for technologies and operations. Both projects were scrapped in 2001, due to much too high technical risks and budgetary problems.

For the demonstration of reusable space technologies and orbital space-flight missions the X-37 project was launched in 1999, where in the first scenario the vehicle should be transported into an Earth orbit inside the cargo bay of the SPACE SHUTTLE Orbiter. In 2004 the X-37 project was transferred from NASA to the Defense Advanced Research Projects Agency (DARPA) and a redesign took place for launch on an Atlas V rocket.

The Boeing company was the prime contractor of the X-37 vehicle. The project included the development and manufacturing of two demonstrator vehicles. One for the approach and landing part of the flight trajectory and one for the deorbiting and re-entry part.

The first orbital flight happened in 2010 and two others in 2011 and 2012. Among the technologies, which are demonstrated, are improved thermal protection systems (hot structures, conformal reusable insulation, high temperature seals, etc.), avionics and an autonomous guidance, navigation and control system. All flights were classified.

Some synthetic images of the X-37 vehicle, taken from [21] and [23], are shown in Figs. 6.60 and 6.61.

6.5.1 Configurational Aspects

The X-37 is 8.382 m (27.5 feet) long, has a wingspan of about 4.572 m (15 feet) and weighs about 6 tons. The shape of the X-37 vehicle is a 120 percent scaled up version of the X-40 configuration, [23], which was also developed and built by the Boeing company.

6.5.2 Aerodynamic Data of Steady and Unsteady Motions

There was no access for the author to the aerodynamic data.

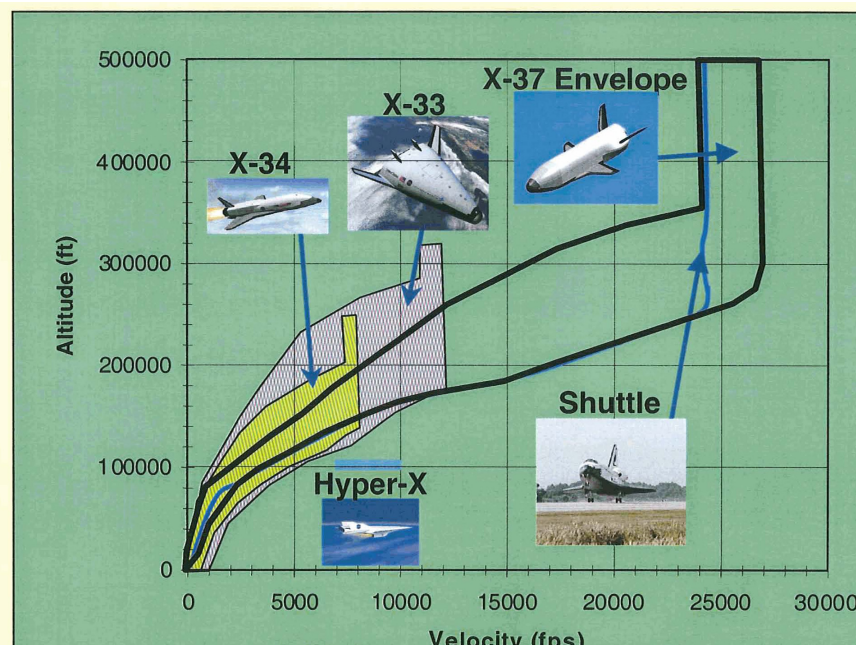


Fig. 6.59. Test envelopes of X-33, X-34 and X-37, [23]



Fig. 6.60. Synthetic views of the X-37 vehicle. Flight in orbit (left), atmospheric flight during re-entry (right), [21].

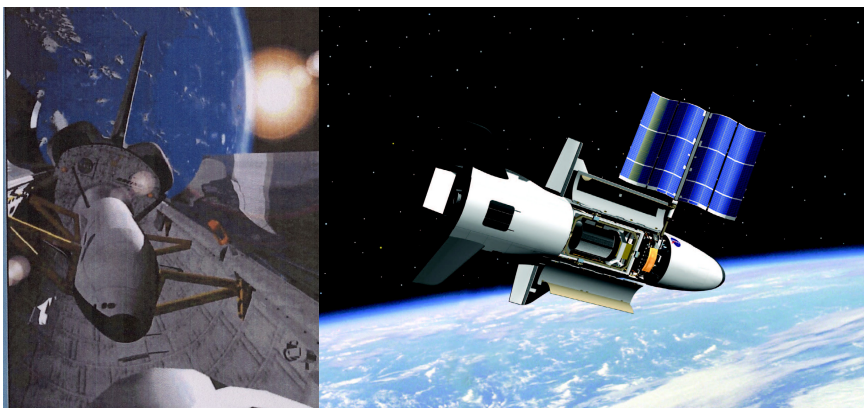


Fig. 6.61. Synthetic views of the X-37 vehicle. X-37 in the cargo bay of the SPACE SHUTTLE Orbiter (left), flight in orbit with deployed solar generator (right), [21, 23].

6.6 X-38 Vehicle (USA-Europe)

The United States' National Aeronautics and Space Administration (NASA) had envisaged in the 1990s to develop for operational missions in connection with the International Space Station (ISS) a Crew Rescue Vehicle (CRV), replacing the Russian SOYUZ capsule and also, if necessary, the SPACE SHUTTLE Orbiter. In the case of illness of crew members or any other emergency, the CRV should be able to bring back to Earth the complete crew of the ISS (at maximum seven astronauts). The essential point was that the crew return could be carried out un-piloted, which means that the vehicle was to operate automatically. For this mission a configuration on the basis of a lifting body, viz. the X-24A shape [24], was selected and got the name X-38.

The vehicle had to have the following features:

- accurate and soft landing to allow for the transportation of injured crew members,
- load factor minimization,
- sufficient cross-range capability for reaching the selected landing site also at adverse weather conditions.

The X-38 vehicle is not a RV-W in the strict sense. As a lifting body, it glides after the de-orbit boost like a winged re-entry vehicle, unpowered along a given trajectory down to a specified altitude and conducts then the final descent and landing by a steerable heavy load parafoil system, Fig. 6.62. The parafoil is a must because the aerodynamic performance L/D of such a lifting body in the subsonic flight regime is too low for an aero-assisted (winged) terminal approach and landing .

To provide enough space for seven crew members, the X-24A shape was scaled-up by a factor of 1.2 and the fuselage was redesigned at the leeward side to increase the volume. The resulting shape, named X-38 Rev. 8.3, served as a technology demonstrator for the prototype CRV.

A close cooperation between NASA, European industries, agencies and research organizations (Dassault, EADS-Space, MAN, ESA, DLR, ONERA, etc.) was arranged in particular for the establishment of the aerodynamic data base. Various pictures of the wind tunnel campaign are shown in Fig. 6.63. Further some evaluations of numerical solutions of the Navier-Stokes equations are plotted in Fig. 6.64.

Unfortunately, in 2002 NASA changed its strategy and aimed for a multipurpose vehicle, which could provide both the crew transport and crew return capabilities, instead of the single purpose vehicle X-38¹⁸. In June 2002

¹⁸ Single purpose vehicle means: the X-38 vehicle is transported in the SPACE SHUTTLE Orbiter bay into the Earth orbit and then docked at the ISS.

Multi purpose vehicle means: the X-38 is able to transport crew members to and from the ISS, performing an autonomous ascent (independent of the SPACE SHUTTLE Orbiter).

the X-38 project was cancelled. Up to now (2013) no follow-on project was launched.

Nevertheless, the work on the aerodynamic data base was brought to a reasonable end. Therefore, we are able to present in the following section detailed aerodynamic data for the longitudinal and lateral motion as well as some investigations of dynamic stability. All these data were received from wind tunnel experiments and numerical solutions of either the Euler or the Navier-Stokes equations.



Fig. 6.62. Drop test including parafoil landing of the X-38 vehicle, Rev. 8.3 with docking port, [4]



Fig. 6.63. X-38 vehicle: Pictures from various wind tunnel campaigns. Wind tunnel flow field, [25] (left), model in the TMK tunnel of the DLR, Cologne (middle), [26, 27], model in the S4 tunnel of ONERA, Modane, [28] (right).

6.6.1 Configurational Aspects

In Fig. 6.65 we present three-dimensional views of the X-38 vehicle, Rev. 8.3 including the device for docking on the International Space Station (docking

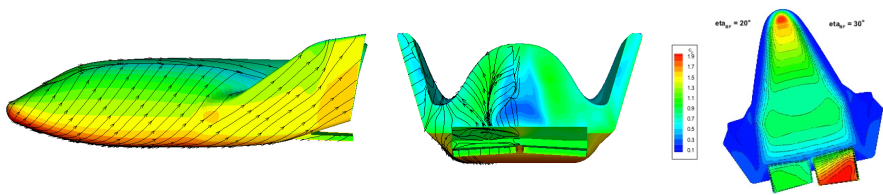


Fig. 6.64. X-38 vehicle: Navier-Stokes solutions. Pressure distribution and skin-friction lines ($M_\infty = 15, \alpha = 40^\circ, \eta_{bf} = 20^\circ$), side view (left), rear view including body flap cavity (middle), [29]. Pressure distribution at the lower side with two different body flap deflections ($\eta_{bf} = 20^\circ$ and $\eta_{bf} = 30^\circ$) (right), [30].

port). The shape presented has a body flap deflection of $\eta_{bf} = 20^\circ$, which is made visible in the rear view plot of the vehicle (right part of the figure). For most of the experimental and numerical investigations for the preparation of the aerodynamic data base the nominal body flap deflection angle was $\eta_{bf} = 20^\circ$ (see the following sections). Fig. 6.66 contains a side and a top view with some measures and the definition of the nominal moment reference point.

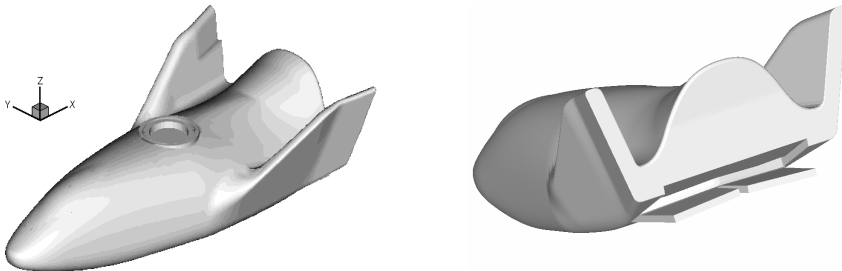


Fig. 6.65. 3D shape presentation of the X-38 vehicle, Rev.8.3 with the docking port

6.6.2 Aerodynamic Data of Steady Motion

Longitudinal Motion

As mentioned above, the X-38 vehicle is a lifting body, which does not strictly belong to the class of winged re-entry vehicles. Classical winged re-entry

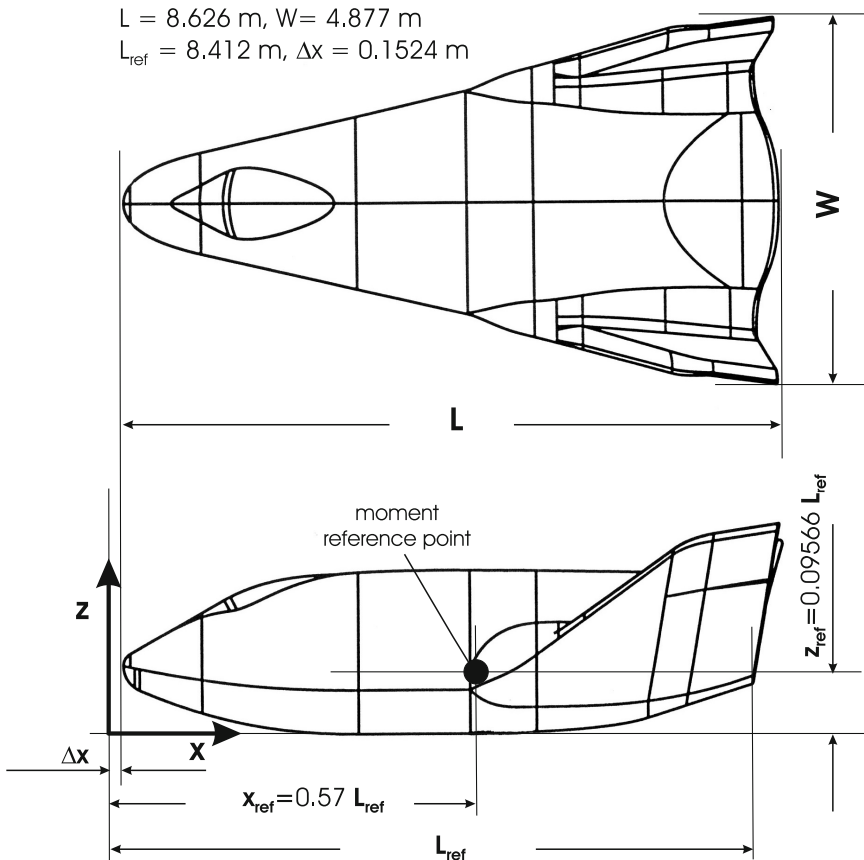


Fig. 6.66. Shape definition of the X-38 vehicle, Rev. 8.3, [31]

vehicles are able to conduct the landing by its own shape, which means that their shape produces in the subsonic flight regime at the minimum a L/D value of 4.5 to 5. When we look upon the subsonic aerodynamic performance of the X-38 vehicle in Fig. 6.69, we find a L/D of order 2, which is far below the required value. This is the reason, why the final descent and landing of the X-38 vehicle is carried out with a steerable parafoil system, [32, 33]. Figs. 6.67 - 6.70 exhibit for subsonic, transonic and supersonic Mach numbers lift, drag and pitching moment coefficients as well as the lift-to-drag ratio L/D . Most of the data are taken from the Aerodynamic Data Base (ADB) assembled by Dassault Aviation, [34] and some come from numerical Euler solutions performed by [35]. The large pitching moment coefficients at small angles of attack, Fig. 6.70, are due to the strong boat-tailing of the lower side of the

X-38 vehicle, see Fig. 6.66. Another observation of the aerodynamics of the X-38 shape is that the drag coefficient is substantially larger compared to other RV-W's, Fig. 6.68. The results of the Euler computations are consistent with the ADB data except for the pitching moment coefficients for $M_\infty = 1.72$, where some deviations occur.

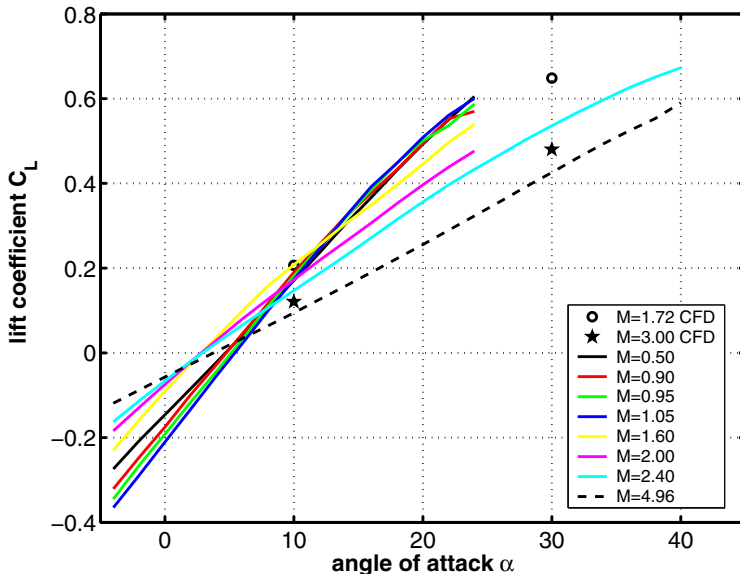


Fig. 6.67. Lift coefficient C_L as function of the angle of attack α for subsonic-transonic-supersonic Mach numbers, [34, 35]. Body flap deflection $\eta_{bf} = 20^\circ$.

Supersonic and hypersonic Mach numbers are considered in Figs. 6.71 to 6.74. These data were obtained mainly from wind tunnel investigations¹⁹, [28, 36, 37], and verified by some Navier-Stokes computations, [30]. For supersonic Mach numbers the aerodynamic performance L/D is of order 1.4, which diminishes to 1.3 for hypersonic Mach numbers. Further one can observe that the aerodynamic coefficients become asymptotically independent of the Mach number above $M_\infty \approx 5$. The data from the Navier-Stokes computations with $M_\infty = 10, 15, 17.5$ at $\alpha = 40^\circ$ show excellent agreement with the wind tunnel data.

In Fig. 6.75 the trim angle of attack extracted from the Figs. 6.70 and 6.74 is plotted. Three observations can be stated by a critical view at this diagram:

¹⁹ The following wind tunnels were used: TMK of DLR Cologne, Germany, S3 and S4 of ONERA Modane, France.

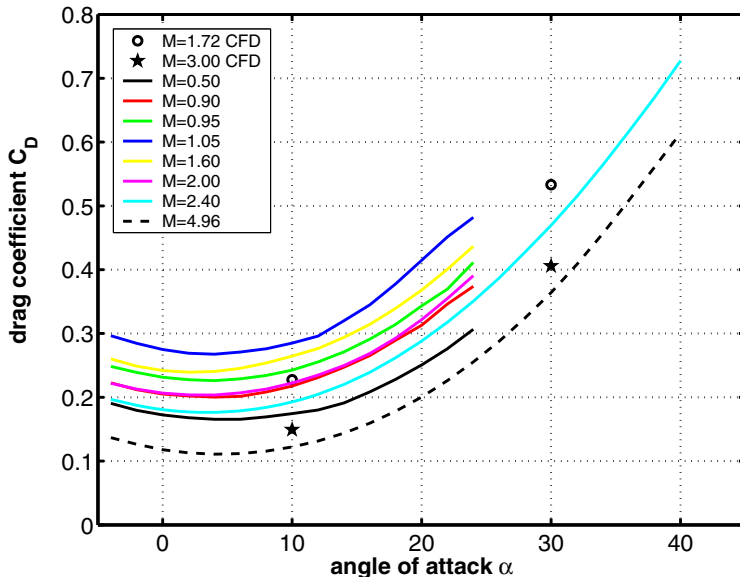


Fig. 6.68. Drag coefficient C_D as function of the angle of attack α for subsonic-transonic-supersonic Mach numbers, [34, 35]. Body flap deflection $\eta_{bf} = 20^\circ$.

- firstly, there are obviously no trim angles of attack present for $M_\infty = 0.9$ and 0.95 for the conditions $\eta_{bf} = 20^\circ$ and $x_{ref} = 0.57L_{ref}$, see Fig. 6.70,
- secondly, the trim angles of attack in the Mach number range $1.6 \lesssim M_\infty \lesssim 5.5$, taken from Figs. 6.70 and 6.74, differ somewhat from each other, but the slope of the curves are very similar,
- thirdly, the trim angle in the hypersonic flight regime approaches approximately 30° . Since the re-entry flight trajectory of the X-38 vehicle requires an angle of attack of $\approx 40^\circ$ (in hypersonic flight) an adjustment of the body flap deflection η_{bf} and/or the center-of-gravity x_{ref} is necessary (see Figs. 6.76, 6.77).

The influence of the moment reference point on the pitching moment coefficient for $M_\infty = 9.92$ (S4 wind tunnel data) is shown in Fig. 6.76. As expected the pitching moment grows with increasing x_{ref} (for the definition of a positive pitching moment see Fig. 8.2.). This results in a trim angle increase from $\alpha_{trim} \approx 30^\circ$ for $x_{ref} = 57\%$ to $\alpha_{trim} \approx 37^\circ$ for $x_{ref} = 59\%$. Another effective possibility for increasing the trim angle of attack consists in the reduction of the body flap deflection. Reducing the body flap deflection η_{bf} from 20° to 10° changes the trim angle from $\alpha_{trim} \approx 30^\circ$ to $\approx 45^\circ$, Fig. 6.77. The physics behind that is the reduction of the pressure at the windward side of the body flap surface when η_{bf} is decreased. That leads to a front shift of the

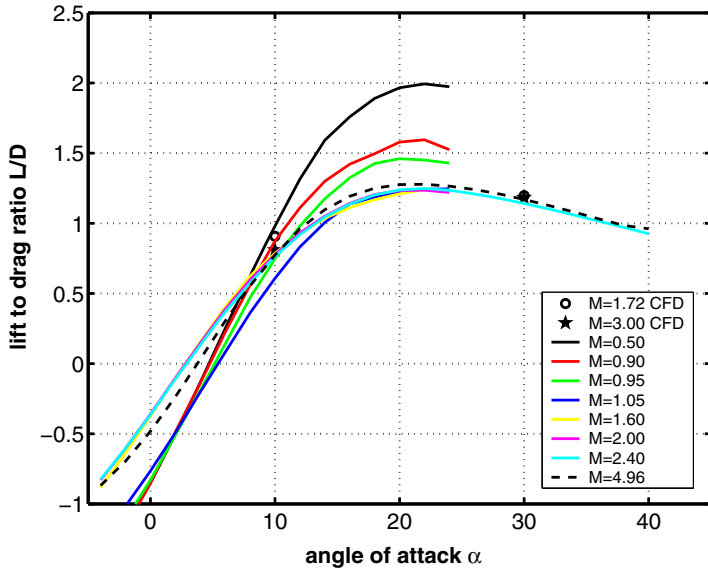


Fig. 6.69. Lift-to-drag L/D as function of the angle of attack α for subsonic-transonic-supersonic Mach numbers, [34, 35]. Body flap deflection $\eta_{bf} = 20^\circ$.

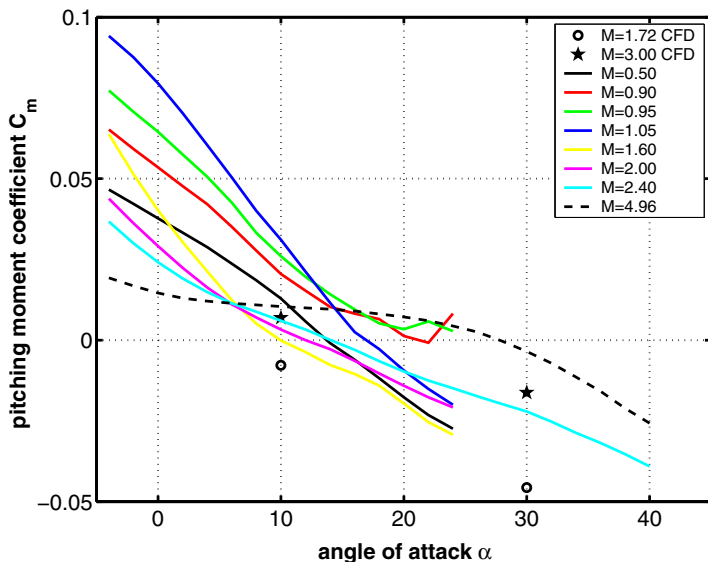


Fig. 6.70. Pitching moment coefficient C_m as function of the angle of attack α for subsonic-transonic-supersonic Mach numbers, [34, 35]. Body flap deflection $\eta_{bf} = 20^\circ$. Moment reference point $x_{ref} = 0.57 L_{ref}$, $z_{ref} = 0.09566 L_{ref}$.

center-of-pressure (or the line of the resultant aerodynamic force, see [10]) generating an increase of the pitching moment.

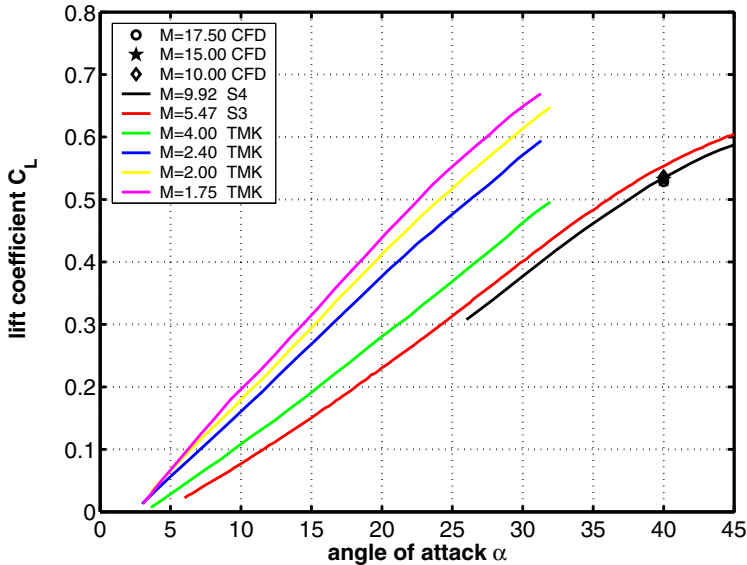


Fig. 6.71. Lift coefficient C_L as function of the angle of attack α for supersonic and hypersonic Mach numbers, [28, 30, 36, 37]. Body flap deflection $\eta_{bf} = 20^\circ$.

Lateral Motion

The side force coefficients as well as the rolling and yawing moment coefficients as function of the side slip angle β are presented in Figs. 6.78 to 6.80. The data were taken from the wind tunnel investigations in the S4, S3 and TMK wind tunnel facilities. The slope of the side force coefficient grows with decreasing Mach numbers. The rolling and yawing moment coefficients are plotted in Figs. 6.79 and 6.80 for $M_\infty = 9.92$, with $\alpha = 40^\circ$, $M_\infty = 5.47$, with $\alpha = 40.5^\circ$ and $M_\infty = 4, 2.4, 2, 1.75$ with $\alpha = 20^\circ$.

Generally the rolling moment coefficient has a negative slope indicating roll motion damping, which increases for lower Mach numbers and growing angles of attack at least above $\alpha \gtrsim 10^\circ$, Fig. 6.81. The yawing moment has always a positive slope, which indicates directional stability. This stability increases for higher angles of attack and diminishes when the Mach number goes up as Fig. 6.82 shows.

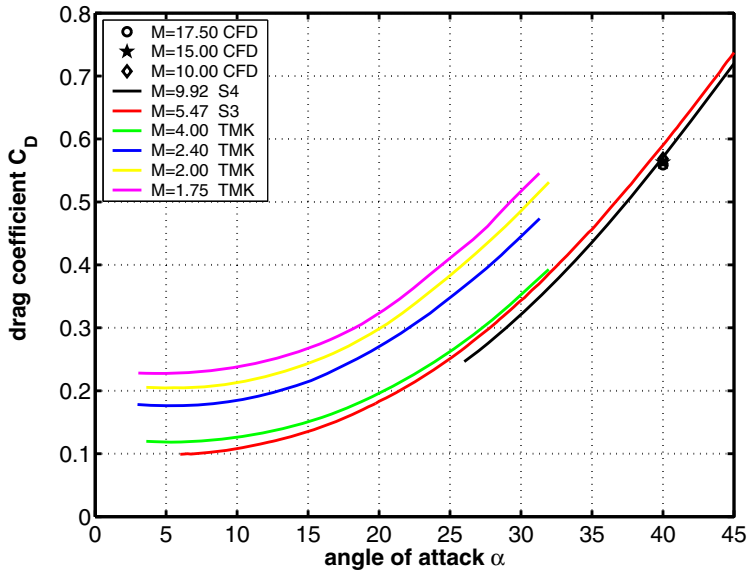


Fig. 6.72. Drag coefficient C_D as function of the angle of attack α for supersonic and hypersonic Mach numbers, [28, 30, 36, 37]. Body flap deflection $\eta_{bf} = 20^\circ$.

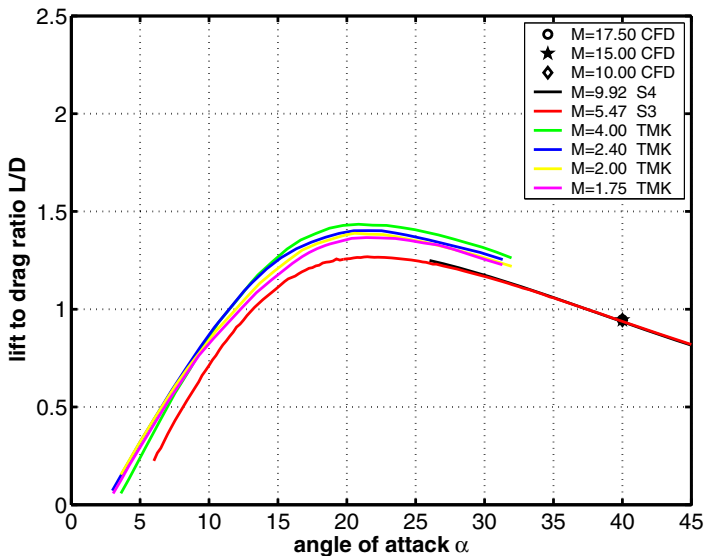


Fig. 6.73. Aerodynamic performance L/D as function of the angle of attack α for supersonic and hypersonic Mach numbers, [28, 30, 36, 37]. Body flap deflection $\eta_{bf} = 20^\circ$.

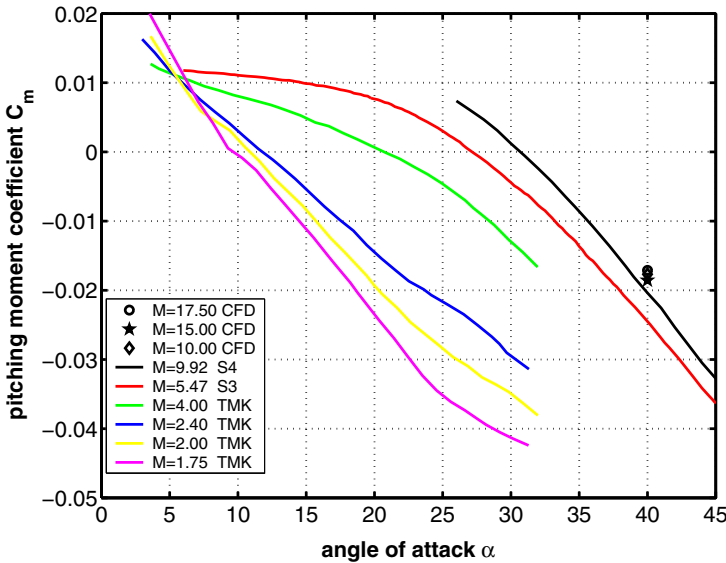


Fig. 6.74. Pitching moment coefficient C_m as function of the angle of attack α for supersonic and hypersonic Mach numbers, [28, 30, 36, 37]. Body flap deflection $\eta_{bf} = 20^\circ$. Moment reference point $x_{ref} = 0.57 L_{ref}$, $z_{ref} = 0.09566 L_{ref}$.

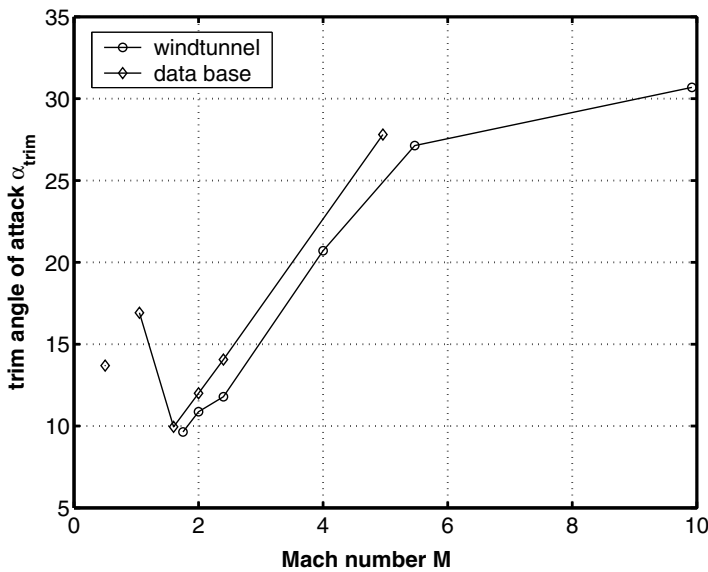


Fig. 6.75. Trim angle of attack. Evaluations of the data base values from Fig. 6.74 and wind tunnel values from Fig. 6.74. Moment reference point $x_{ref} = 0.57 L_{ref}$, $z_{ref} = 0.09566 L_{ref}$.

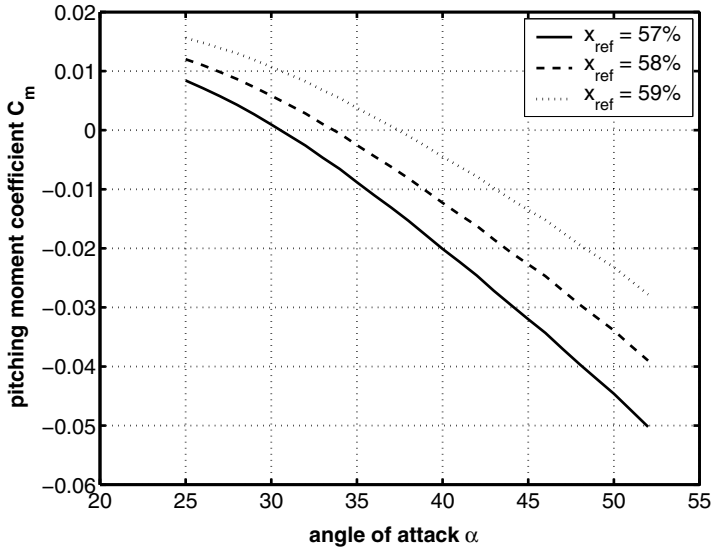


Fig. 6.76. Influence of the moment reference point variations (with $z_{ref} = 0.09566 L_{ref} = \text{const}$) on the pitching moment coefficient. Evaluation of S4 wind tunnel data with $M_\infty = 9.92$, [28].

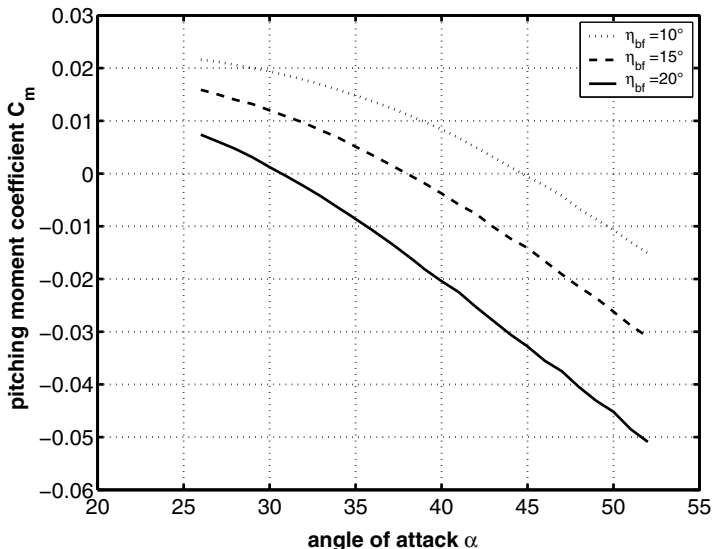


Fig. 6.77. Influence of the body flap deflection on the pitching moment coefficient. Moment reference point $x_{ref} = 0.57 L_{ref}$, $z_{ref} = 0.09566 L_{ref}$. S4 wind tunnel data with $M_\infty = 9.92$, [28].

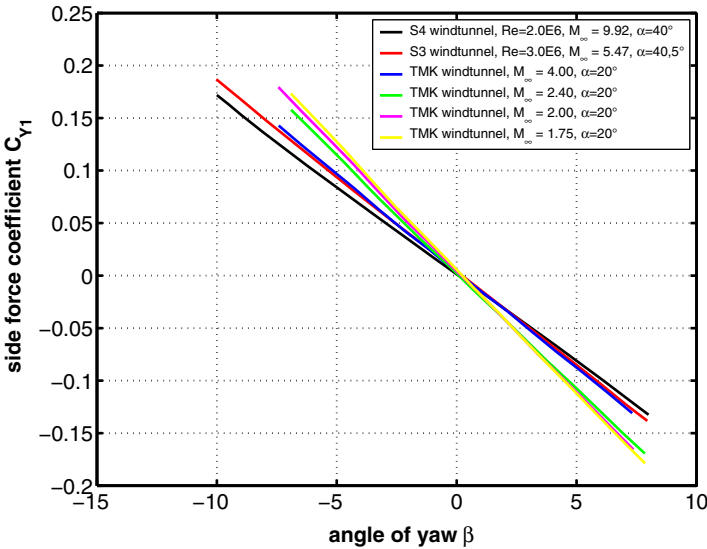


Fig. 6.78. Side force coefficient C_{Y1} as function of the angle of yaw β for supersonic and hypersonic Mach numbers, [28, 36, 37]. Body flap deflection $\eta_{bf} = 20^\circ$.

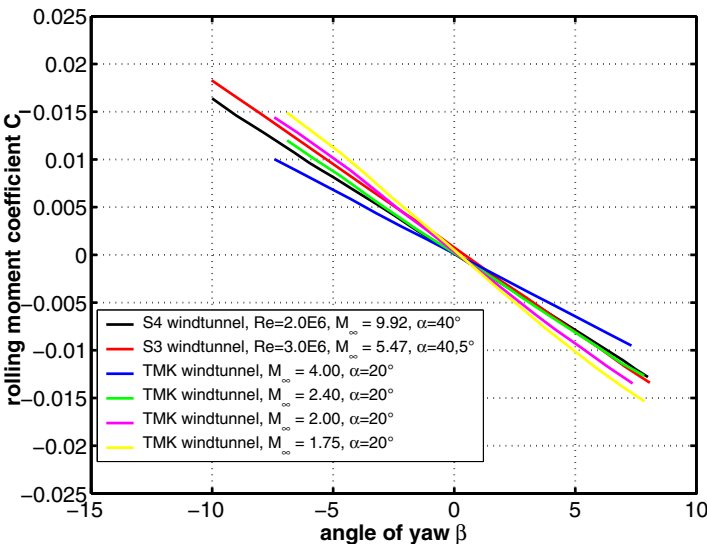


Fig. 6.79. Rolling moment coefficient C_l as function of the angle of yaw β for supersonic and hypersonic Mach numbers, [28, 36, 37]. Body flap deflection $\eta_{bf} = 20^\circ$.

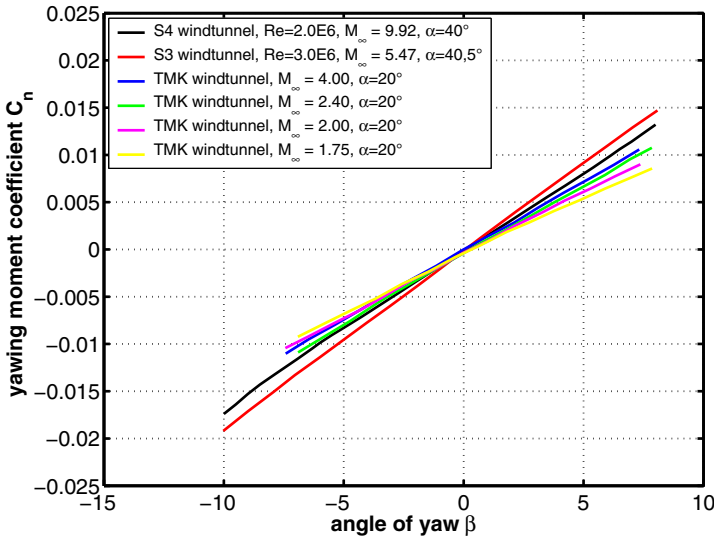


Fig. 6.80. Yawing moment coefficient C_n as function of the angle of yaw β for supersonic and hypersonic Mach numbers, [28, 36, 37]. Moment reference point $x_{ref} = 0.57 L_{ref}$, $z_{ref} = 0.09566 L_{ref}$. Body flap deflection $\eta_{bf} = 20^\circ$.

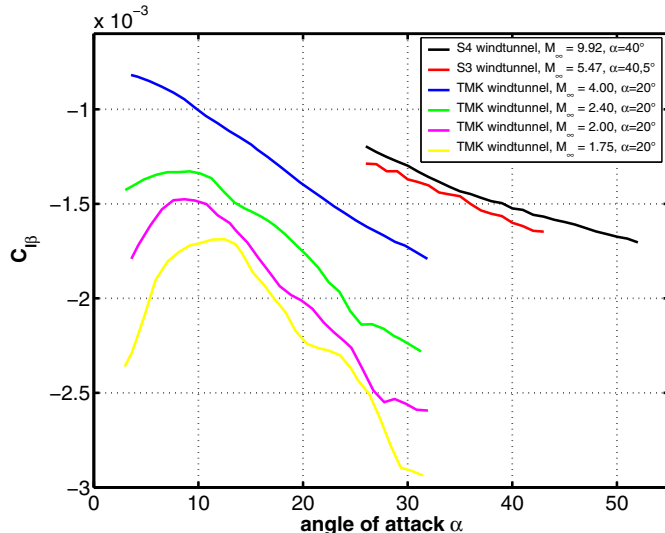


Fig. 6.81. Rolling moment coefficient per degree $C_{l\beta}$ as function of the angle of attack α for supersonic and hypersonic Mach numbers, [28, 36, 37]. Body flap deflection $\eta_{bf} = 20^\circ$.

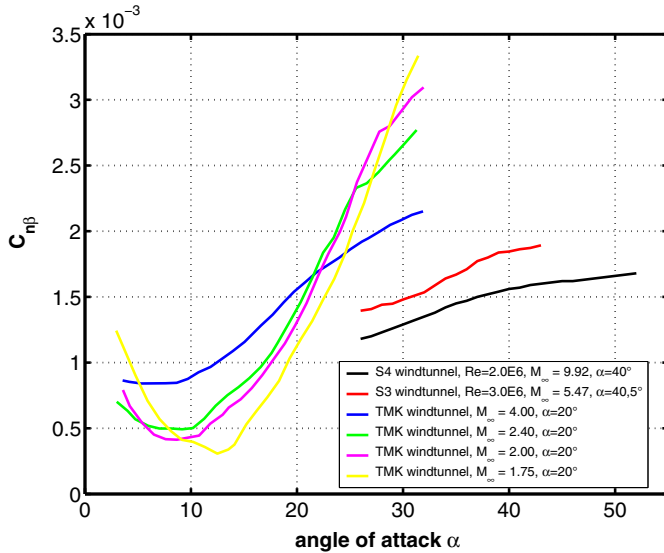


Fig. 6.82. Yawing moment coefficient per degree $C_{n\beta}$ as function of the angle of attack α for supersonic and hypersonic Mach numbers, [28, 36, 37]. Moment reference point $x_{ref} = 0.57 L_{ref}$, $z_{ref} = 0.09566 L_{ref}$. Body flap deflection $\eta_{bf} = 20^\circ$.

6.6.3 Aerodynamic Data of Unsteady Motion

Experience shows that the dynamic behavior of re-entry vehicles can be critical in the vicinity of the transonic Mach number, which means the regime between $0.8 \lesssim M_\infty \lesssim 1.2$. For higher Mach numbers the dynamic derivatives play only a minor role. Therefore we present for longitudinal motion in the transonic flight regime the pitch damping derivative $C_{mq} + C_{m\dot{\alpha}}$, Fig. 6.83. The dotted curve was established by five points, each generated by unsteady, three-dimensional Navier-Stokes computations, [38, 39]. Since $C_{mq} + C_{m\dot{\alpha}}$ is negative in the Mach number regime considered, dynamic motions of the X-38 vehicle (e.g., pitch oscillations) will be damped.

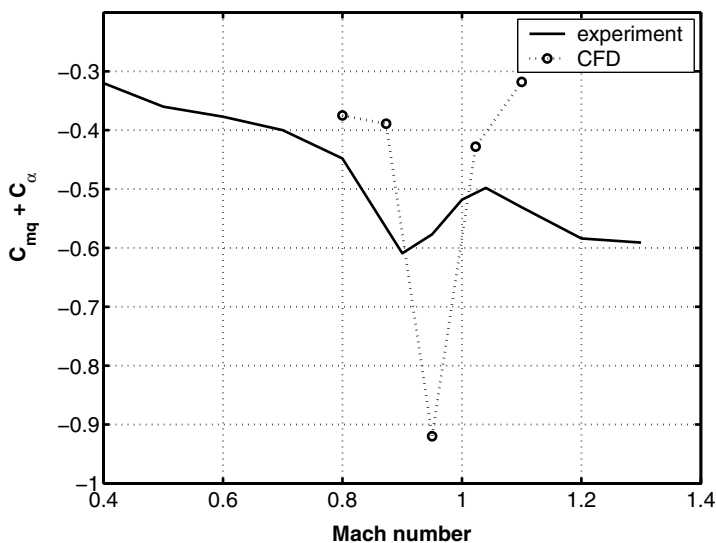


Fig. 6.83. Damping derivative of the longitudinal pitch motion $C_{mq} + C_{m\dot{\alpha}}$. Data source: [38, 39].

6.7 PHOENIX Demonstrator (Germany)

In the frame of the "Future European Space Transportation Investigation Programme (FESTIP)", several Reusable Launch Vehicle (RLV) concepts were designed and investigated with the goal of making access to space more reliable and cost effective. The major objective of FESTIP was firstly to compare launcher concepts on an equal basis, and secondly to determine which of these concepts become technically feasible with respect to the technologies already available and the ones which would have to be developed in the near term in Europe. Eight promising candidate concepts were selected representing the most significant design philosophies as they are: the number of stages, the types of propulsion system, the mode of take-off and landing, the vehicle configuration and the flight mission, [12].

One of these concepts is the HOPPER vehicle, Fig. 6.84 (left), which was foreseen to fly along a suborbital trajectory, [40]. This means that this vehicle does not reach the velocity necessary for moving into an Earth target orbit²⁰. This also means, that the vehicle is not able to return to the launch base, but has to fly to another landing ground.

The main features of the system are the horizontal take-off (sled launch) and landing capability and the reusability of most of the vehicle parts. After release from the sled the HOPPER vehicle is powered by three Vulcain 2 engines²¹.

To demonstrate the low speed and landing properties of the vehicle shape a 1:7 down-scaled flight demonstrator, called PHOENIX, was developed and manufactured within the framework of the German ASTRA²² program, Fig. 6.84 (right). In order to guarantee that the PHOENIX demonstrator flights are representative of the full scale HOPPER flights, the aerodynamic performance, the center-of-gravity position, the flight quality and the landing speed (71 m/s) are the same for both vehicles, [41, 42].

The aerodynamic data base of the PHOENIX vehicle was compiled from the experimental data coming from six wind tunnels²³ and from numerical simulations (Euler- and Navier-Stokes computations).

Fig. 6.85 presents pictures of a flow field and of models in two of these wind tunnels. Solutions of numerical simulations, in particular when viscous effects come into play (Navier-Stokes solutions), offer the potential to reveal specific flow phenomena from the computed three-dimensional flow fields. Some ex-

²⁰ For example, a circular Earth target orbit of an altitude of $H = 400$ km requires a velocity of the space vehicle of 7671.74 m/s, [33]

²¹ The Vulcain 2 rocket motor is the main engine of the advanced version of the European ARIANE V rocket.

²² ASTRA \Rightarrow Ausgewählte Systeme und Technologien für zukünftige Raumtransportsystem-Anwendungen (Selected Systems and Technologies for Future Space Transportation Applications).

²³ DLR's NWB wind tunnel (subsonic), DLR's TWG wind tunnel (subsonic-transonic-low supersonic), NLR's HST wind tunnel (subsonic-transonic-low supersonic), NLR's SST wind tunnel (supersonic), DNW's LLF wind tunnel (low subsonic), Technical University of Aachen's TH2 shock tunnel (hypersonic).

amples are shown in Fig. 6.86, where wing tip and trailing vortices (left figure), the radiation-adiabatic wall temperature distribution, [43], (middle figure) and skin-friction lines (right figure) are plotted.

The demonstration of the landing capacity of the PHOENIX vehicle was conducted at the North European Aerospace Test Range (NEAT) in Vidsel (North Sweden). For the test flight the vehicle was dropped from a helicopter at an altitude of 2.4 km and a distance to the runway of approximately 6 km. The subsequent free flight had included an accelerating dive to merge with a steep final approach path representative for an RLV, followed by a long flare manoeuvre and a touch down on the runway, Fig.6.87, [42].

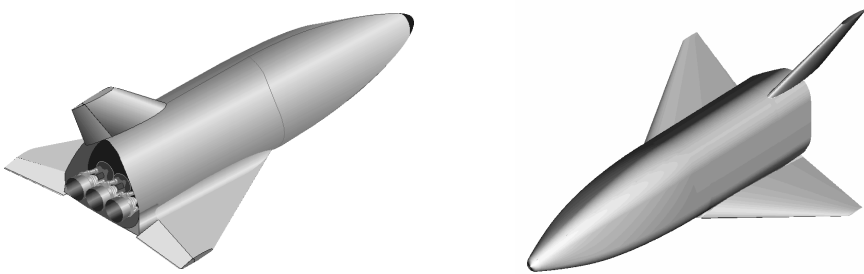


Fig. 6.84. 3-D model of the HOPPER shape including three rockets of Vulcain 2 type (left), 3-D model of the PHOENIX demonstrator (right), [44, 45]



Fig. 6.85. Test of the PHOENIX model in the shock tunnel TH2 of the Technical University of Aachen. Test conditions: $M_\infty = 6.6$, $\alpha = 35^\circ$, $T_0 = 7400$ K, $\eta_{bf} = 20^\circ$ (left), [46]. PHOENIX model in the HST wind tunnel of NLR, The Netherlands, (middle). PHOENIX in 1:1 scale in the Large Low Speed Facility (LLF) of DNW, Germany/The Netherlands (right), [41, 42].

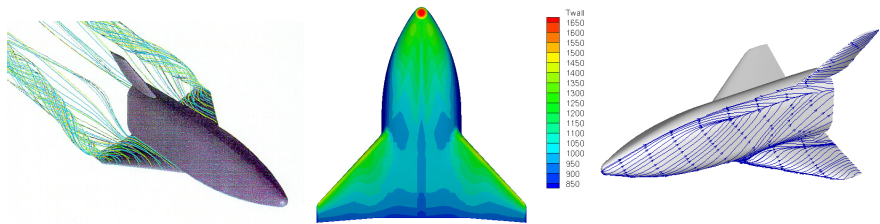


Fig. 6.86. Navier-Stokes solutions for the PHOENIX configuration, turbulent flow. Wing tip and trailing vortices $M_\infty = 0.6$, $\alpha = 12^\circ$ (left), radiation-adiabatic wall temperature distribution at the windward side $M_\infty = 11.1$, $\alpha = 19.6^\circ$, $H = 55.4$ km (middle), skin-friction lines, solution with real gas assumption $M_\infty = 15$, $\alpha = 25^\circ$, $H = 54.5$ km (right), [44, 47].



Fig. 6.87. PHOENIX demonstrator: Test of subsonic free flight (helicopter drop test) and automatic landing capability in Vidsel, Sweden in May 2004, [41, 42]

6.7.1 Configurational Aspects

Reusable launch vehicles have to meet contradicting demands during their space missions. Their missions comprise all the operation phases consisting of launch, ascent and final boost for arriving the target orbit as well as de-orbiting, re-entry, hypersonic flight and terminal approach and landing. Therefore such vehicles are characterized by compact shapes with small-span wings and aerodynamic controls.

The shape of the PHOENIX demonstrator, as a 1:7 down-scaled HOPPER configuration, has an overall length of 6.90 m, a span of 3.84 m and an overall height of 2.56 m, Figs. 6.88 - 6.90.

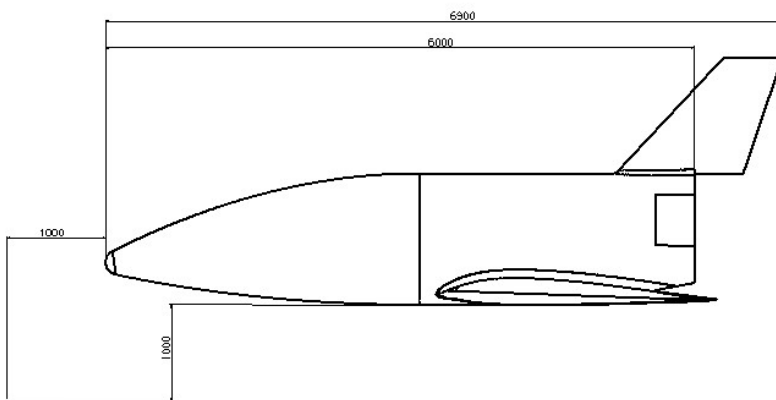


Fig. 6.88. Engineering drawing of the PHOENIX shape: side view [44]

6.7.2 Aerodynamic Data of Steady Motion

As already mentioned the aerodynamic data base was established via experiments in several wind tunnels as well as numerical simulations (3D Euler and Navier-Stokes computations). The numerical simulations included modern turbulence models²⁴ and real gas effects, where necessary, [44, 47].

Longitudinal Motion

The lift coefficient C_L as function of the angle of attack α for subsonic-transonic and transonic-supersonic Mach numbers is presented in Figs. 6.91 and 6.92. In the subsonic-transonic regime the slope of the lift coefficient with respect to the angle of attack $\partial C_L / \partial \alpha$ is slightly increasing with increasing

²⁴ Either fully turbulent flow or flow with fixed laminar-turbulent transition can be handled.

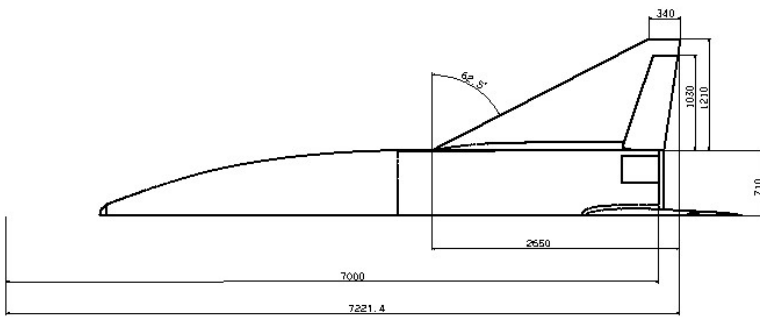


Fig. 6.89. Engineering drawing of the PHOENIX shape (half model): top view [44]

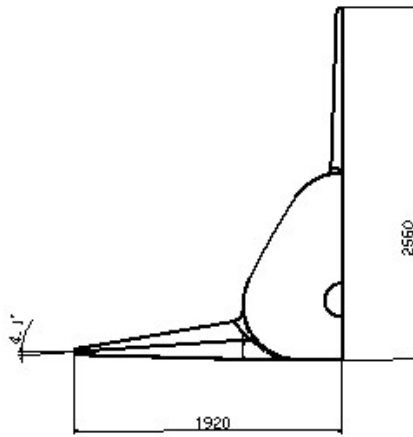


Fig. 6.90. Engineering drawing of the PHOENIX shape (half model): front view [44]

Mach number, whereas the linear behavior breaks down for lower angles of attack when the Mach number rises. The highest $\partial C_L / \partial \alpha$ value is given for $M_\infty = 1.1$ which is then lowered continuously with rising Mach number. Further, in the transonic-supersonic regime, the break down of the linear behavior of C_L is shifted to higher angles of attack, Fig. 6.92.

The drag coefficient C_D for two Mach number regimes (subsonic-transonic, transonic-supersonic) is presented in Figs. 6.93 and 6.94. As expected, C_D increases with increasing Mach number from the subsonic regime to a

maximum value around $M_\infty \approx 1$. Then it decreases again in the supersonic domain. Notable is the strong jump of the C_D values – the drag divergence – for the Mach number passage $M_\infty = 0.95 \Rightarrow M_\infty = 1.1$ for moderate angles of attack.

For a save landing of unpowered space vehicles at minimum an aerodynamic performance L/D , according to experience, of approximately 5 is necessary. As Fig. 6.95 exhibits PHOENIX possess a value of $L/D_{M_\infty=0.2} \approx 5.5$, which is sufficient for an autonomous landing. Beyond $M_\infty \approx 1$ the maximum lift-to-drag value reduces to $L/D_{max} \lesssim 2$ for all Mach numbers considered, Fig. 6.96.

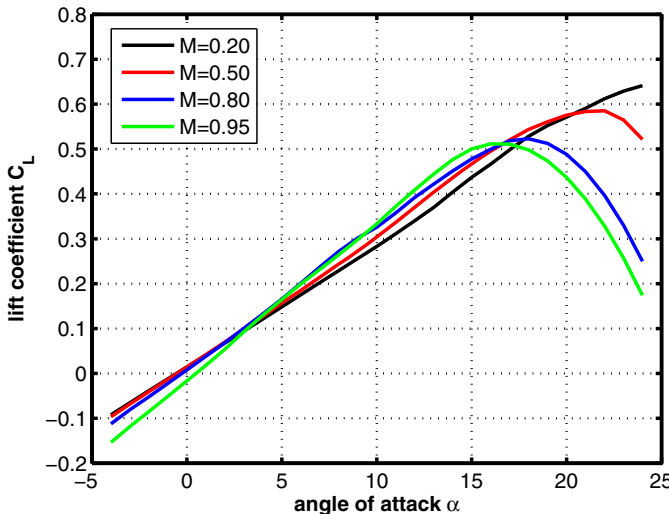


Fig. 6.91. Lift coefficient C_L as function of the angle of attack α for subsonic-transonic Mach numbers, [48]

The pitching moment plots reveal static stability, – for the selected center-of-gravity position $x_{ref} = 0.68 L_{ref}$ ²⁵ –, for all the subsonic-transonic Mach numbers of Fig. 6.97, and for the Mach numbers $M_\infty = 1.1, 1.33, 1.72$ of the transonic-supersonic regime, Fig. 6.98. In the true transonic regime ($0.8 \lesssim M_\infty \lesssim 1.33$) the slope $\partial C_m / \partial \alpha$ is highest, indicating a distinct static stability, which breaks down for angles of attack $\alpha \gtrsim 15^\circ$. Low subsonic Mach numbers hold marginal stability, while for increasing supersonic Mach numbers the

²⁵ The lay-out of the PHOENIX demonstrator was strongly influenced by the hardware of the flight test instrumentations and the other experimental equipment. Thereby the center-of-gravity position of the real flight vehicle was shifted to $x_{ref} = 0.70 L_{ref}$ with the consequence that the vehicle became statically unstable in the subsonic regime, [42].

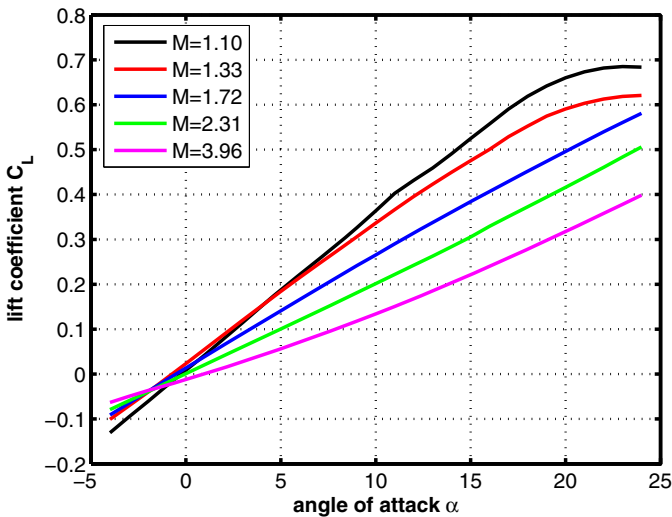


Fig. 6.92. Lift coefficient C_L as function of the angle of attack α for transonic-supersonic Mach numbers, [48]

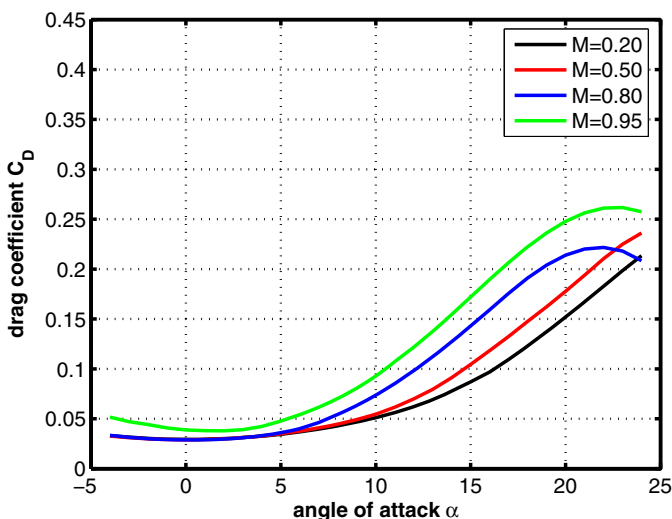


Fig. 6.93. Drag coefficient C_D as function of the angle of attack α for subsonic-transonic Mach numbers, [48]

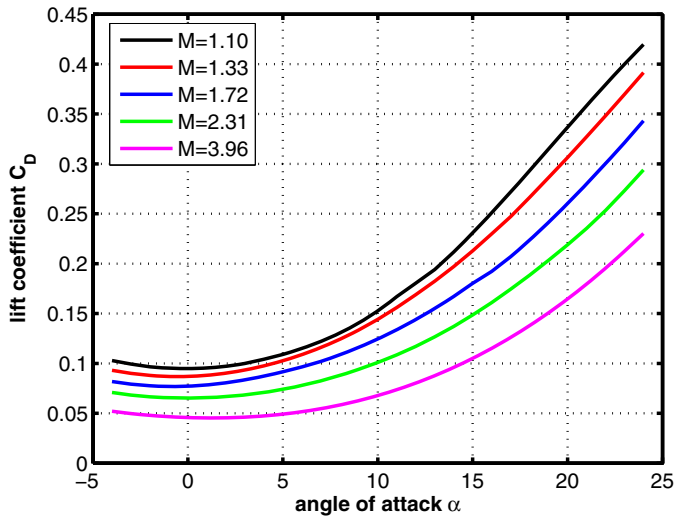


Fig. 6.94. Drag coefficient C_D as function of the angle of attack α for transonic-supersonic Mach numbers, [48]

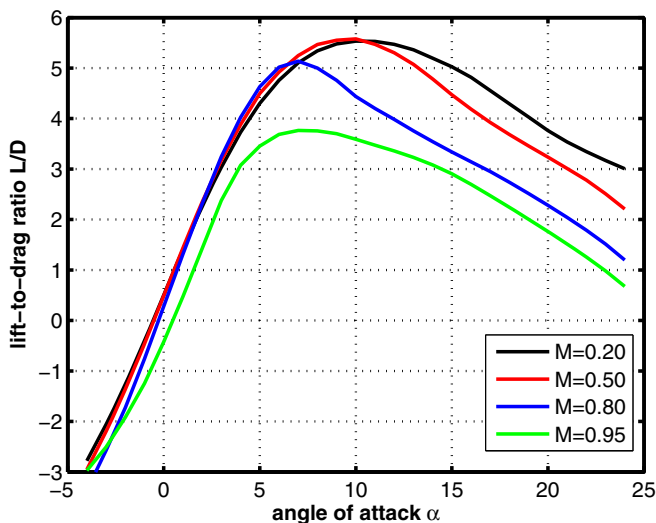


Fig. 6.95. Lift-to-drag ratio L/D as function of the angle of attack α for subsonic-transonic Mach numbers, [48]

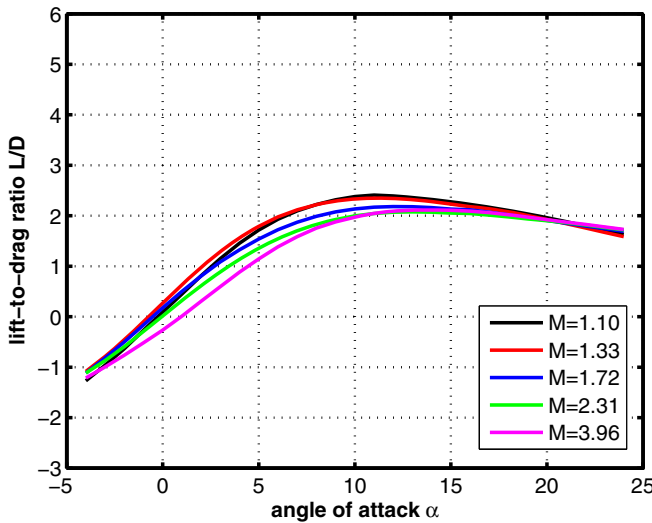


Fig. 6.96. Lift-to-drag ratio L/D as function of the angle of attack α for transonic-supersonic Mach numbers, [48]

vehicle becomes statically unstable. The vehicle can be trimmed (when all aerodynamic control surfaces are in neutral positions) only for $M_\infty = 0.95$ and 1.1 for small angles of attack.

The investigation of the higher Mach number (supersonic-hypersonic) regime was exclusively performed by numerical simulation tools (CFD), Figs. 6.99 - 6.102. Lift and drag coefficients seem to decrease with increasing Mach number and exhibit approximately the well known Mach number independency in the hypersonic regime, Figs. 6.99 and 6.100.

The lift-to-drag ratio L/D does not show a strict hypersonic Mach number independency, but reveals a continuous reduction of L/D with rising Mach number, so that for example for $M_\infty = 10$ a $L/D_{max} \approx 2$. and for $M_\infty = 15$ a $L/D_{max} \approx 1.75$ is given, Fig. 6.101.

Finally, the pitching moment coefficient C_m behaves in the supersonic-hypersonic regime as expected. The trend of Fig. 6.98 is carried forward, namely that the vehicle with increasing Mach number becomes more and more statically unstable, Fig. 6.102. This is true despite the fact that the numerical simulations for the single trajectory points of $M_\infty = 11.1$, $\alpha = 19.6^\circ$ and $M_\infty = 14.4$, $\alpha = 31.3^\circ$ do not confirm this picture.

We describe now by which measures longitudinal static stability and trim of a space vehicle can be achieved if, for example, the pitching moment coefficient behaves like that of the PHOENIX shape at $M_\infty = 3.96$, Fig. 6.98. For this reason we demonstrate the effects of body flap deflection and forward shift of the center-of-gravity on static stability and trim. In general a

positive (downwards) deflected body flap ($\eta_{bf} > 0$) provokes a nose-down effect, which results in a diminishment of the pitching moment coefficient. On the other hand a negative body flap deflection ($\eta_{bf} < 0$) produces an additional nose-up moment as can be seen in Fig. 6.103. Usually for re-entry vehicles flying classical entry trajectories the angle of attack regime for $M_\infty \approx 4$ is given by $20^\circ \lesssim \alpha \lesssim 30^\circ$, [10]. By considering Fig. 6.103 it seems that only for $\alpha \approx 30^\circ$ and a body flap deflection of $\eta_{bf} = +10^\circ$ a trimmed and statically stable flight situation exists.

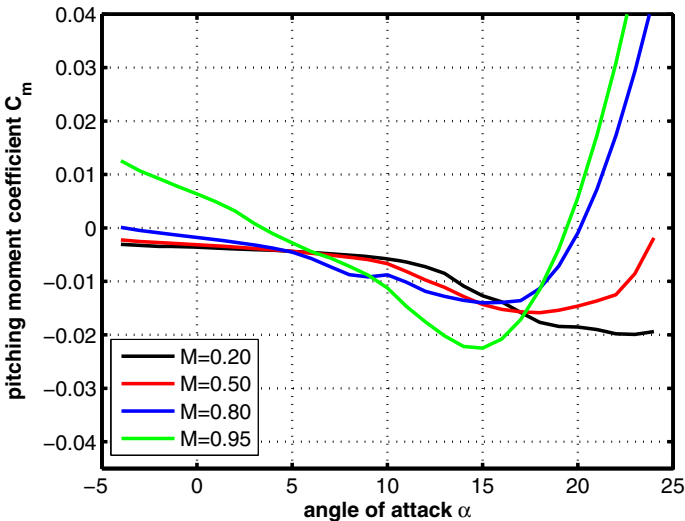


Fig. 6.97. Pitching moment coefficient C_m as function of the angle of attack α for subsonic-transonic Mach numbers; moment reference point $x_{ref} = 0.68 L_{ref}$, [48]

The other possibility for attaining static stability consists in a forward shift of the center-of-gravity, Fig. 6.104. As a basic principle static stability is enforced by moving the center-of-gravity forward. In the case considered here, the additional nose-down moment prevents trim for $\eta_{bf} = +10^\circ$, but allows statically stable and trimmed flight for a body flap deflection of $\eta_{bf} = -10^\circ$ and $\alpha \approx 28^\circ$. This, however, is possible only at vehicle attitudes and Mach numbers, where the upward deflected trim surface does not lie in the hypersonic shadow.

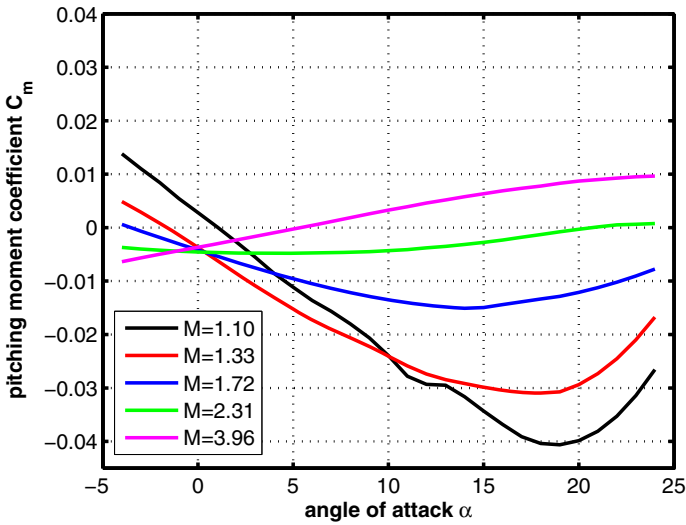


Fig. 6.98. Pitching moment coefficient C_m as function of the angle of attack α for transonic-supersonic Mach numbers; moment reference point $x_{ref} = 0.68 L_{ref}$, [48]

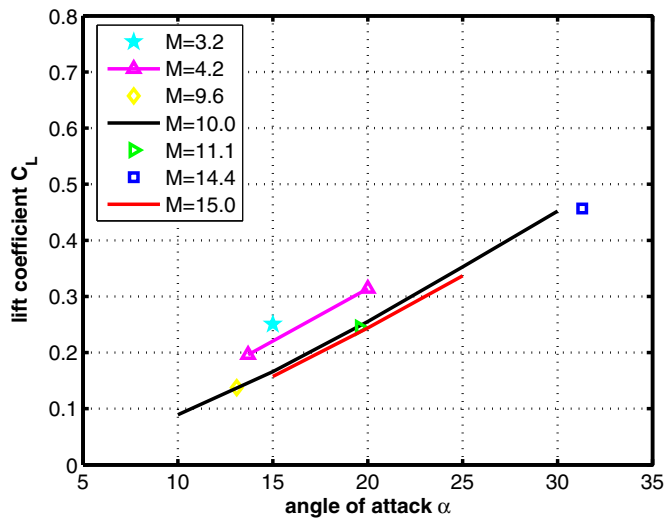


Fig. 6.99. Lift coefficient C_L as function of the angle of attack α for supersonic-hypersonic Mach numbers. Data taken from Navier-Stokes solutions, [44, 47].

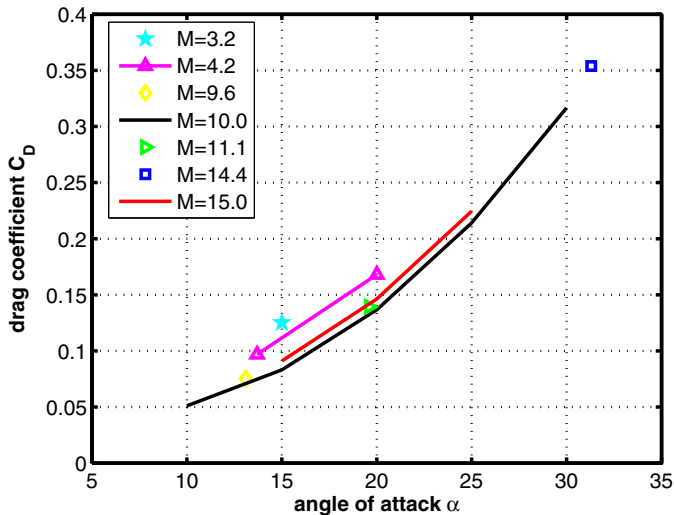


Fig. 6.100. Drag coefficient C_D as function of the angle of attack α for supersonic-hypersonic Mach numbers. Data taken from Navier-Stokes solutions, [44, 47].

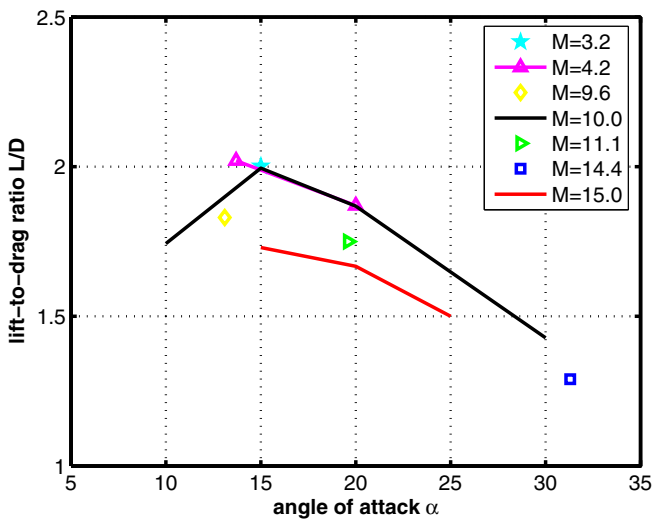


Fig. 6.101. Lift-to-drag ratio L/D as function of the angle of attack α for supersonic-hypersonic Mach numbers. Data taken from Navier-Stokes solutions, [44, 47].

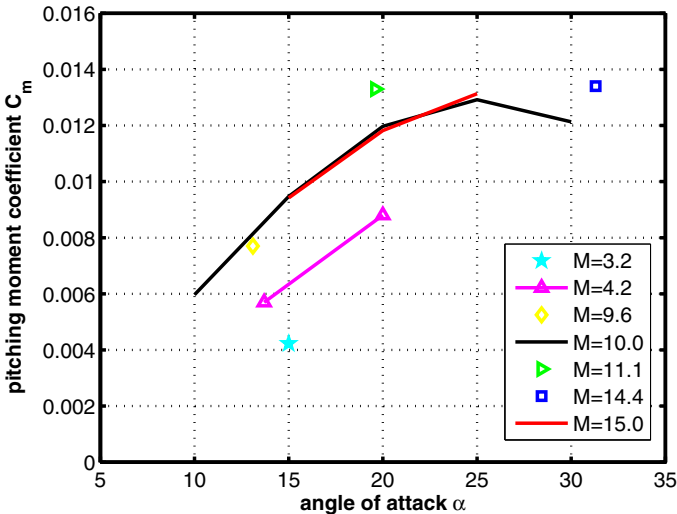


Fig. 6.102. Pitching moment coefficient C_m as function of the angle of attack α for supersonic-hypersonic Mach numbers. Moment reference point $x_{ref} = 0.68 L_{ref}$. Data taken from Navier-Stokes solutions, [44, 47].

Lateral Motion

The lateral motion of a flight vehicle is defined by the side force coefficient C_Y ²⁶, the rolling moment coefficient C_l and the yawing moment coefficient C_n . All these coefficients as function of the yaw angle β are presented in the Figs. 6.105 to 6.110. Generally, the side slip derivative of the side force $\partial C_Y / \partial \beta$ is small and therefore can often be neglected in contrast to the yawing and rolling moment derivatives $\partial C_n / \partial \beta$ and $\partial C_l / \partial \beta$.

The side force coefficients plotted in Figs. 6.105 and 6.106 for the subsonic-transonic and transonic-supersonic regimes exhibit a linear behavior with a more or less constant slope with regard to the slide slip angle β , except for $M_\infty = 3.96$ where the slope decreases somewhat.

Directional stability requires a positive $\partial C_n / \partial \beta$, which means that with increasing side slip angle β the capability to restore the space vehicle into the neutral position (wind position, $\beta \rightarrow 0^\circ$) has to grow. A view on Fig. 6.107 shows that in the subsonic-transonic regime this is only marginally the case. Further, for the transonic-supersonic regime (Fig. 6.108), we see that with increasing Mach number the vehicle becomes more and more directionally unstable.

²⁶ The side force coefficient C_Y is usually defined in body fixed coordinates, see eq. (8.2), but can be transformed to aerodynamic coordinates by $C_Y = -C_D \sin \beta + C_{Y_a} \cos \beta$, see also Fig. 8.1.

Since the character of the rolling moment is quite distinct to that of the yawing moment (– for the rolling moment no restoring effect exists –), we can assert that the rolling moment derivative $\partial C_l / \partial \beta$ is primarily negative in the whole Mach number regime considered here, Figs. 6.109 and 6.110. This provokes a damping of the roll motion. The principal contributions to the rolling moment derivative $\partial C_l / \partial \beta$ in flight with side slip angle $\beta > 0^\circ$ come from the dihedral angle of the wing, the sweep angle of the wing and the vertical fin²⁷. All these effects produce negative (damping) contributions to the rolling moment of the PHOENIX demonstrator. Therefore we are not surprised that PHOENIX shows the above described behavior for the rolling moment derivative, Figs. 6.109 and 6.110.

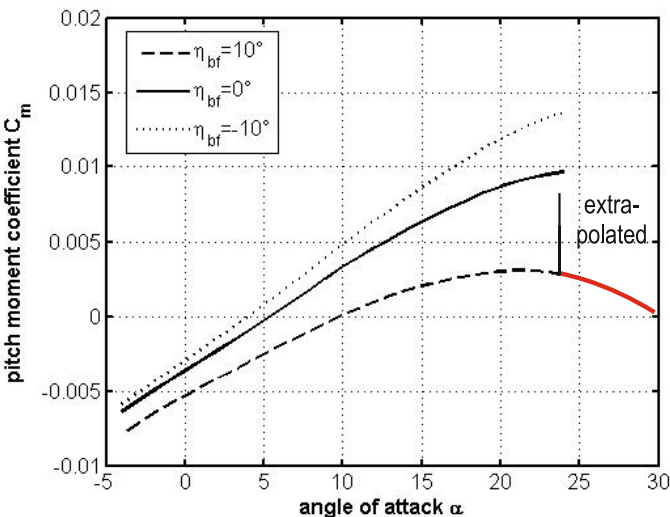


Fig. 6.103. Pitching moment behavior of the PHOENIX shape. Variation of the body flap angle η_{bf} . Moment reference point $x_{ref} = 0.680 L_{ref}$, $M_\infty = 3.96$. Data taken from [48].

6.7.3 Aerodynamic Data of Unsteady Motion

Results of investigations of dynamic stability are not available.

²⁷ Of course, there are other effects present influencing the rolling moment, like the ones of the fuselage and the aspect ratio of the wing, but they are in general of minor importance, [49, 50].

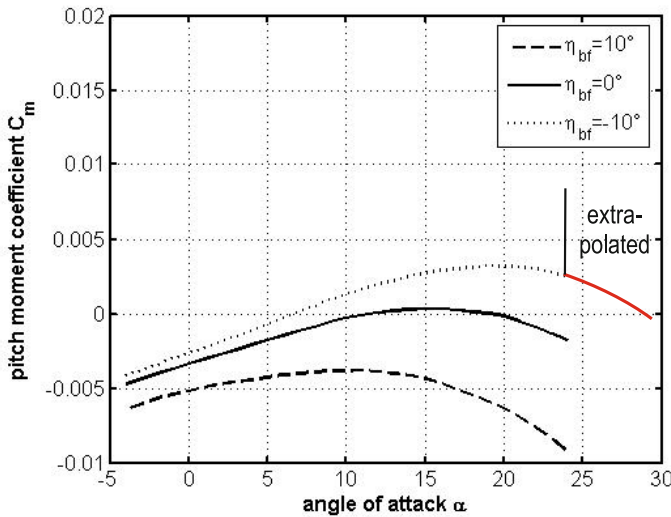


Fig. 6.104. Pitching moment behavior of the PHOENIX shape. Variation of the body flap angle η_{bf} and change of the moment reference point to $x_{ref} = 0.655 L_{ref}$, $M_\infty = 3.96$. Data taken from [48].

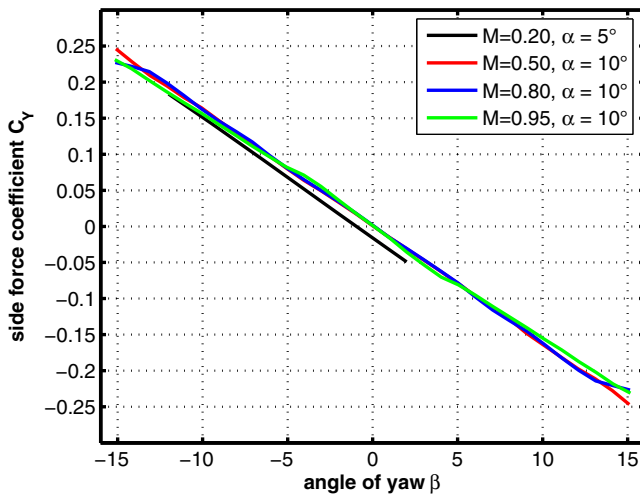


Fig. 6.105. Side force coefficient C_Y defined in body fixed coordinates as function of the yaw angle β for subsonic-transonic Mach numbers, [48]

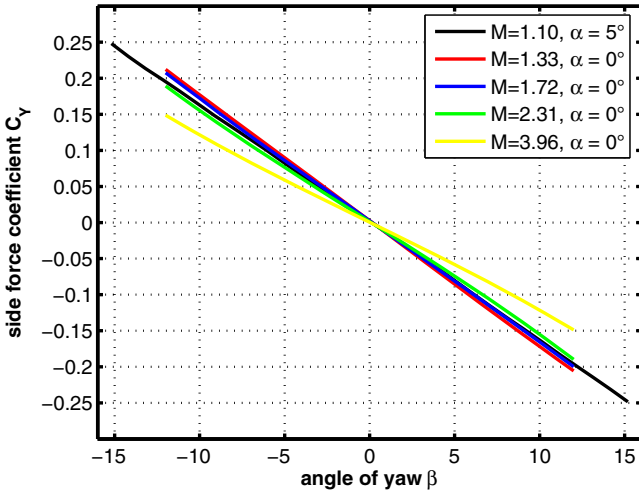


Fig. 6.106. Side force coefficient C_Y defined in body fixed coordinates as function of the yaw angle β for transonic-supersonic Mach numbers, [48]

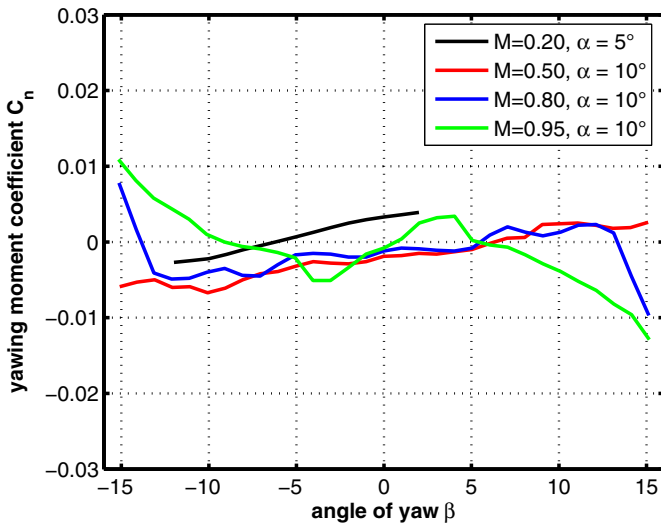


Fig. 6.107. Yawing moment coefficient C_n as function of the yaw angle β for subsonic-transonic Mach numbers. Moment reference point $x_{ref} = 0.680 L_{ref}$, [48].

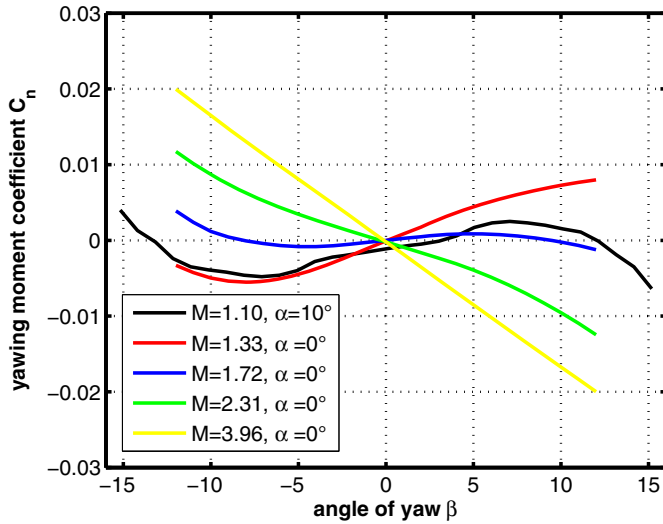


Fig. 6.108. Yawing moment coefficient C_n as function of the yaw angle β for transonic-supersonic Mach numbers. Moment reference point $x_{ref} = 0.680 L_{ref}$, [48].

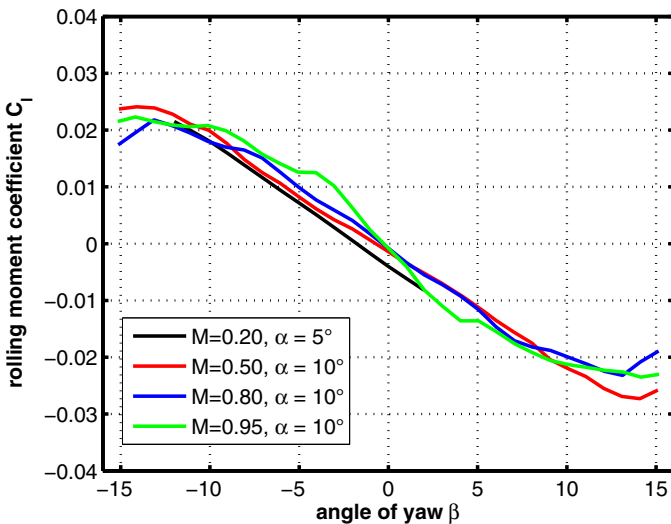


Fig. 6.109. Rolling moment coefficient C_l as function of the yaw angle β for subsonic-transonic Mach numbers, [48].

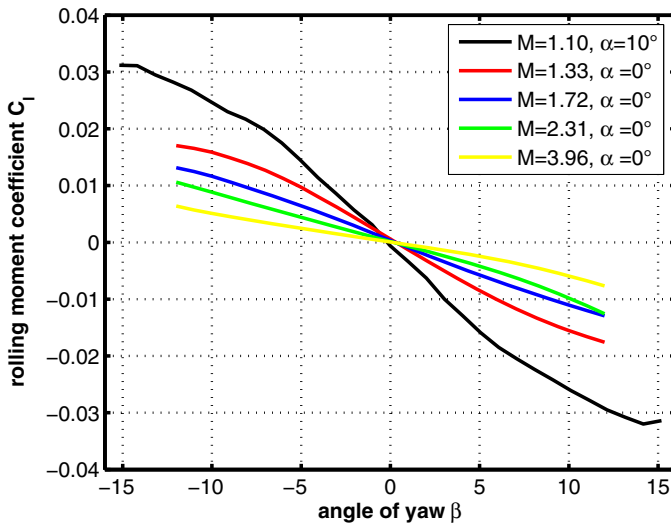


Fig. 6.110. Rolling moment coefficient C_l as function of the yaw angle β for transonic-supersonic Mach numbers, [48].

6.8 HOPE-X (Japan)

In the 1980s, Japan joined the community of nations, like the USA and the Soviet Union, or the group of nations, like the European Community, striving for an autonomous access to space. Besides rocket activities, Japan developed a conceptual re-entry vehicle called HOPE, which was planned for the payload transportation to and from the International Space Station ISS. Due to budget constraints in the 1990s and the run-down and cancellation of the development of most of the manned space transportation systems at that time in the countries mentioned above, for example HERMES in Europe, BURAN in the Soviet Union and X33, X34 and X38 in the USA, this program was re-oriented in the sense to develop a smaller, lighter and cheaper vehicle called HOPE-X. That was then cancelled in 2003. The planned mission of HOPE-X was to transport payloads to and from the ISS in an unmanned mode, Fig. 6.111.

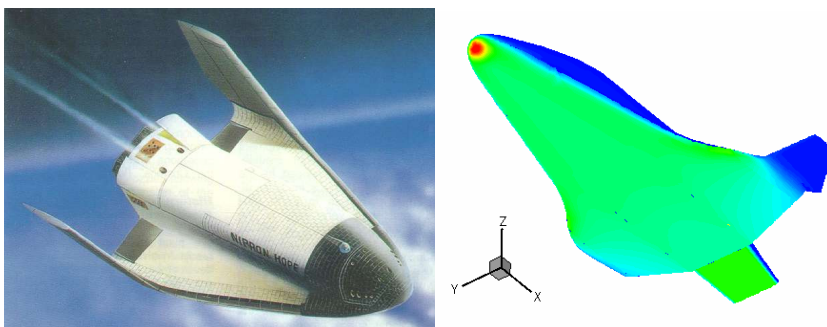


Fig. 6.111. HOPE-X shape: synthetic image (left), surface pressure distribution for $M_{\infty} = 3$ and $\alpha = 35^\circ$ (right), [51] to [53]. Note that the shape of the synthetic image differs somewhat from that of the nominal shape.

6.8.1 Configurational Aspects

The HOPE-X shape has a double delta type wing, similar to that of the SPACE SHUTTLE Orbiter. For the control of the lateral motion the designers installed winglets at the wing tips comparable to the ones of the HERMES and the X-38 vehicle. A three-views presentation of the HOPE-X shape is given in the Figs. 6.112 to 6.114. These figures, showing a panelisation of the shape, were produced in the frame of a cooperation between Germany's aerospace company Dasa (later EADS) and Japan's space agency NASDA (later JAXA). Four positions of the body flap were aerodynamically investigated. These positions can be seen best in Fig. 6.113.

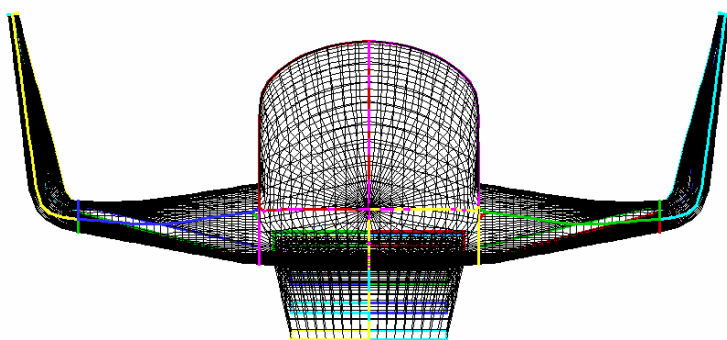


Fig. 6.112. HOPE-X shape: front view generated by quadrilateral panels, [53]

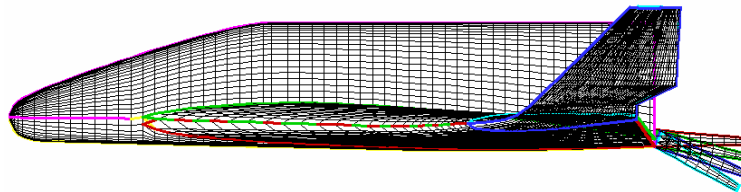


Fig. 6.113. HOPE-X shape: side view including four body flap positions generated by quadrilateral panels, [53]

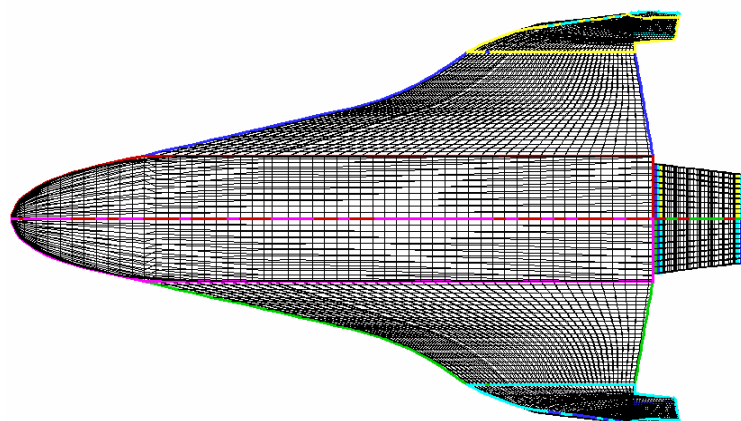


Fig. 6.114. HOPE-X shape: top view generated by quadrilateral panels, [53]

6.8.2 Aerodynamic Data of Steady Motion

Longitudinal Motion

All the data for the longitudinal motion, taken from [53], are given for the Mach number range $0.2 \leq M_\infty \leq 3.5$ and the angle of attack range $-5^\circ \leq \alpha \leq 30^\circ$.²⁸

The behavior of the lift coefficient C_L in the subsonic-transonic regime shows only minor variations in slope, but deviates for the Mach numbers $M_\infty = 0.8$ and 0.9 somewhat from linearity, Fig. 6.115. This picture changes in the transonic-supersonic regime, where cumulatively a linear behavior can be observed, and where the slope decreases monotonically with increasing Mach number, Fig. 6.116.

The drag coefficient C_D in the subsonic-transonic regime increases in general with increasing Mach number, but shows for low angles of attack ($-2^\circ \lesssim \alpha \lesssim 5^\circ$) a regime where C_D seems to be approximately constant with respect to the Mach number, Fig. 6.117. Beyond Mach number one, where one expects to have the highest drag, the C_D values continuously decrease with growing Mach number, Fig. 6.118.

The aerodynamic performance L/D is highest for the lowest Mach number ($M_\infty = 0.2$) and has a value there of approximately 5.8 at an angle of attack $\alpha \approx 11^\circ$. With increasing Mach number the peak values (L/D_{max}) shift towards lower α values, while the magnitude of L/D_{max} decreases only slightly, Fig. 6.119. When the Mach number crosses one, the L/D_{max} values diminish strongly to ≈ 3 ($M_\infty = 1.1$) and further to ≈ 2 ($M_\infty = 3.5$), Fig. 6.120.

The pitching moment coefficient indicates in the subsonic-transonic regime for $M_\infty = 0.2, 0.4$ and 0.6 a slight instability, which becomes stronger for $M_\infty = 0.8$ and 0.9 , in particular for $\alpha \gtrsim 12^\circ$, Fig. 6.121. The vehicle seems to be trimmable in this Mach number range, except for $M_\infty = 0.2$. On the other hand in the transonic-supersonic regime static stability is in particular preserved for $M_\infty = 1.1$ and 1.2 , whereby with increasing Mach number the vehicle loses its static stability. Further, trim is given for $M_\infty = 1.1$ and 1.2 , but only for slightly negative angles of attack, at which the vehicle does not operate, Fig. 6.122.

Lateral Motion

The Figs. 6.123 - 6.128 show the coefficients per degree of yaw angle for the side force as well as the rolling and yawing moments. The slope of the rolling moment ($\partial C_l / \partial \beta$) is negative for most of the Mach numbers in the subsonic-transonic regime in the whole angle of attack range indicating damping of roll motion with the only exception that $\partial C_l / \partial \beta$ becomes positive for $M_\infty =$

²⁸ Note: For some of the curves the data are only given for $\alpha \leq 25^\circ$ and in two Mach number cases the data start with $\alpha = 0^\circ$, and not with $\alpha = -5^\circ$.

Data for higher Mach numbers were not made available to the author.

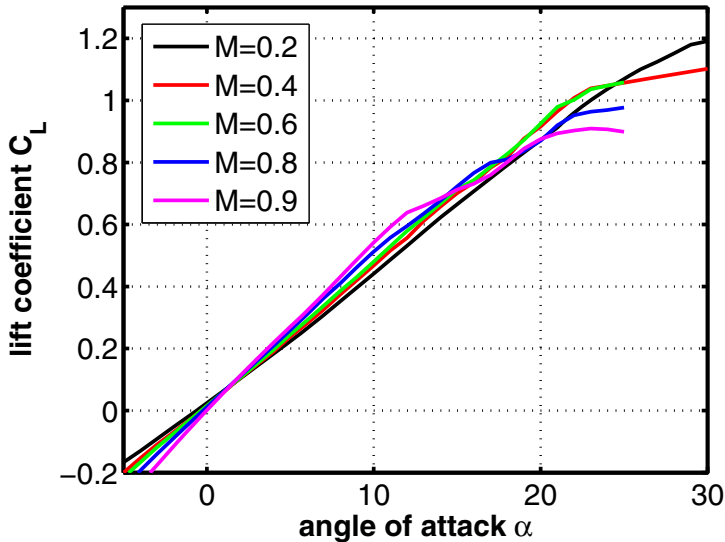


Fig. 6.115. Lift coefficient C_L as function of the angle of attack α for subsonic-transonic Mach numbers, [51]

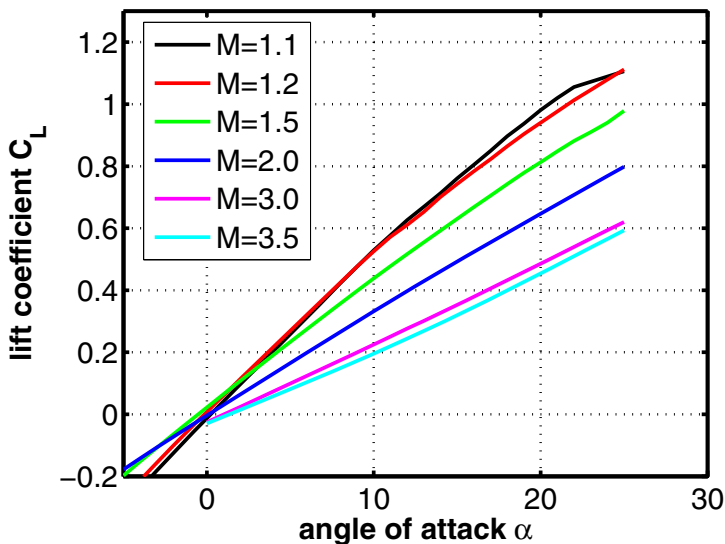


Fig. 6.116. Lift coefficient C_L as function of the angle of attack α for transonic-supersonic Mach numbers, [51]

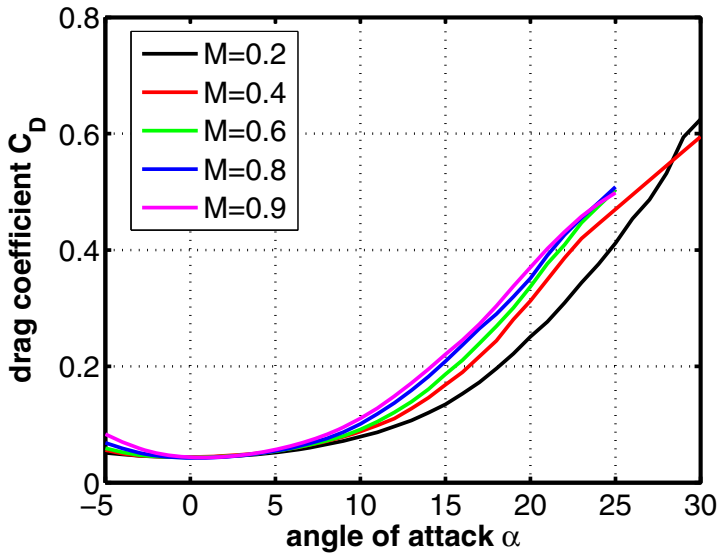


Fig. 6.117. Drag coefficient C_D as function of the angle of attack α for subsonic-transonic Mach numbers, [51]

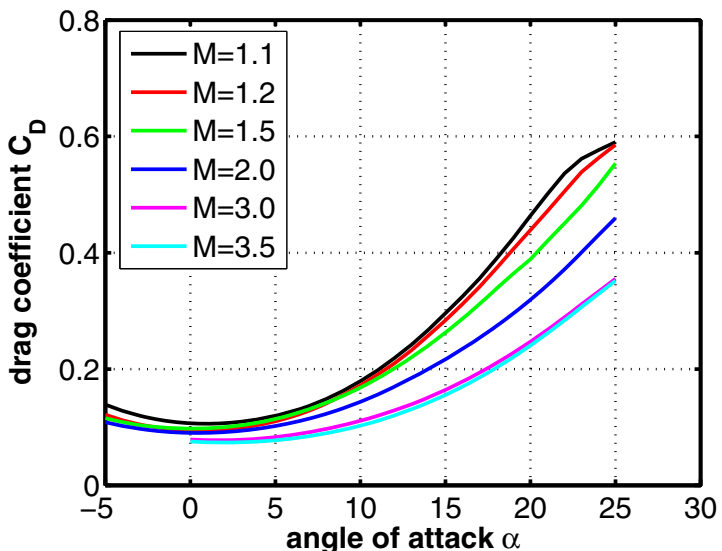


Fig. 6.118. Drag coefficient C_D as function of the angle of attack α for transonic-supersonic Mach numbers, [51]

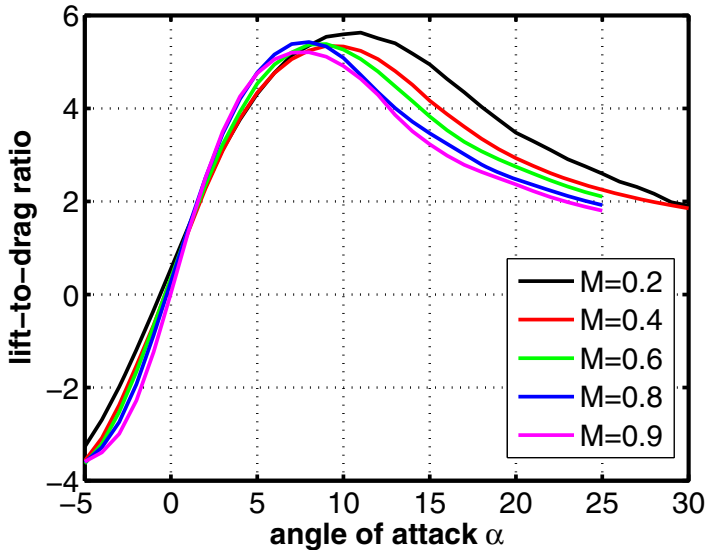


Fig. 6.119. Lift-to-drag ratio L/D as function of the angle of attack α for subsonic-transonic Mach numbers, [51]

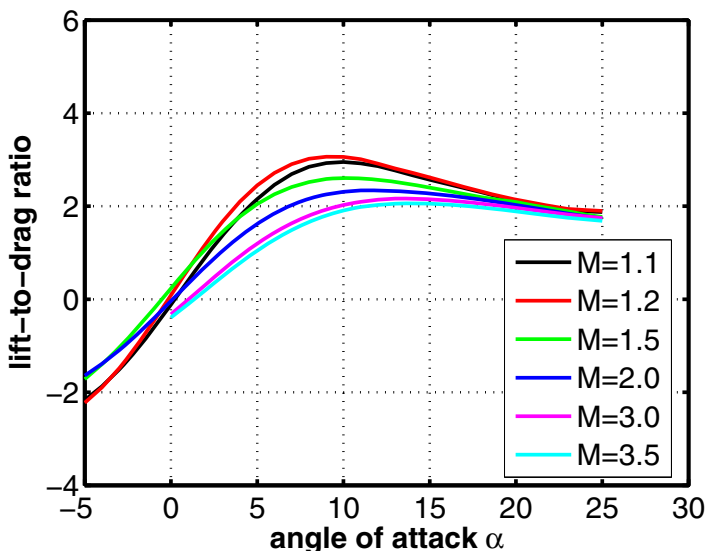


Fig. 6.120. Lift-to-drag ratio L/D as function of the angle of attack α for transonic-supersonic Mach numbers, [51]

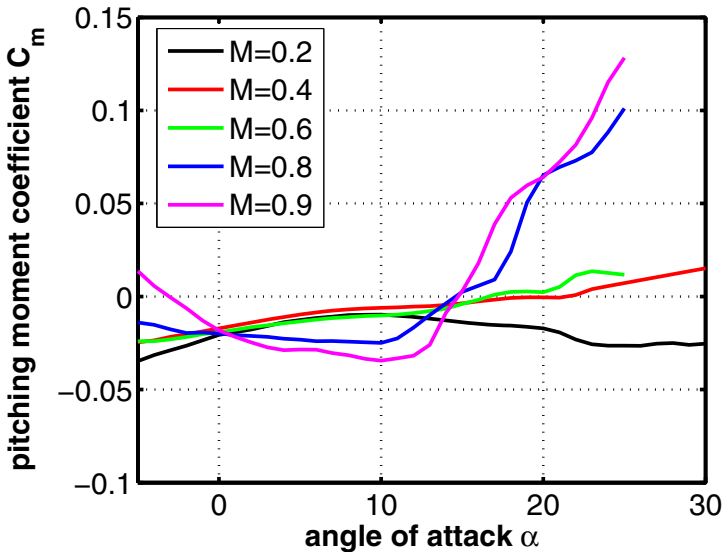


Fig. 6.121. Pitching moment coefficient C_m as function of the angle of attack α for subsonic-transonic Mach numbers, [51]

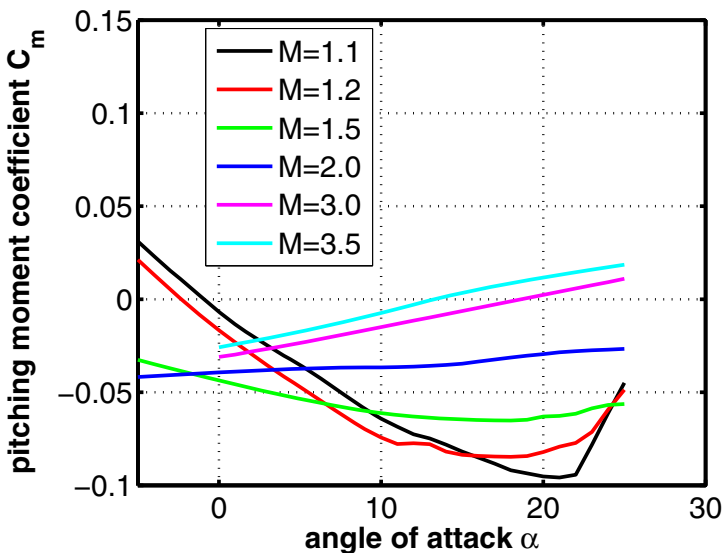


Fig. 6.122. Pitching moment coefficient C_m as function of the angle of attack α for transonic-supersonic Mach numbers, [51]

0.9 and $\alpha \gtrsim 20^\circ$, Fig. 6.125. In the transonic-supersonic regime the general trend is that with increasing Mach number the $\partial C_l / \partial \beta$ values changes from negative to positive over the whole angle of attack range, which means that with increasing Mach number the roll motion is less damped or will even be amplified, Fig. 6.126.

As is well known, directional stability requires yawing moments with positive slopes ($\partial C_n / \partial \beta > 0$). In most of the Mach number and angle of attack regimes the HOPE-X vehicle has negative $\partial C_n / \partial \beta$ values indicating directional instability. A possible reason for that could be the ineffective winglets. Only for the Mach numbers $M_\infty = 1.1$ and 1.2 a small angle of attack band exists with positive $\partial C_n / \partial \beta$ values, Figs. 6.127 - 6.128.

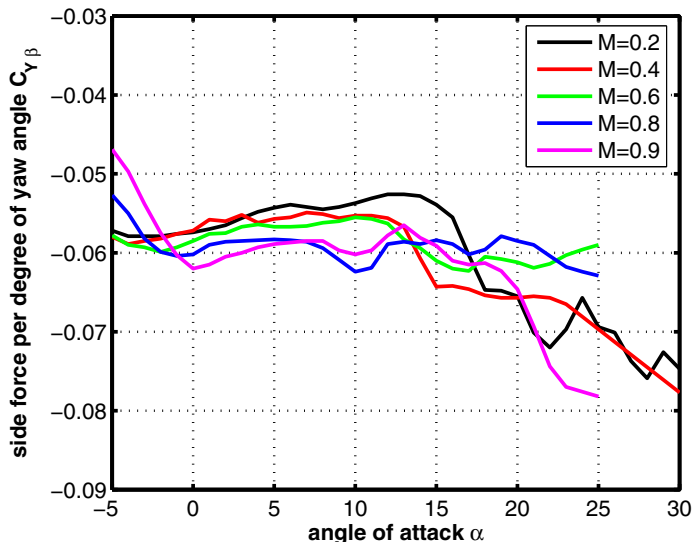


Fig. 6.123. Side force coefficient per degree of the yaw angle β ($\partial C_Y / \partial \beta$) as function of the angle of attack α for subsonic-transonic Mach numbers, [51]

6.8.3 Aerodynamic Data of Unsteady Motion

Data of investigations of dynamic stability are not available.

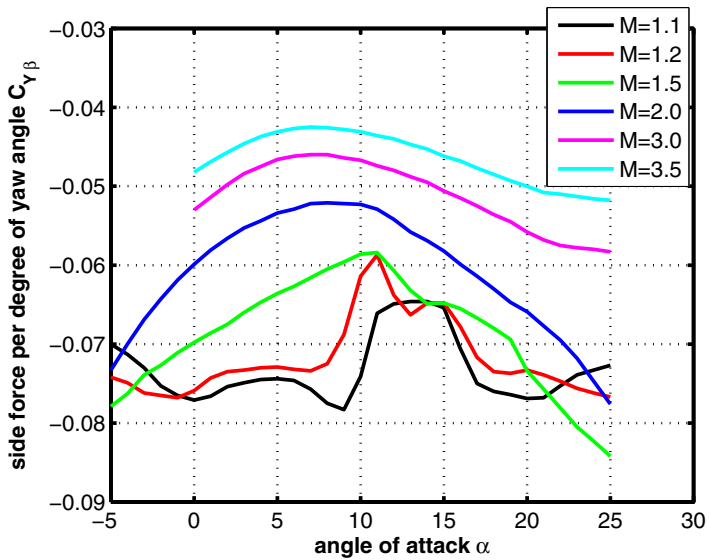


Fig. 6.124. Side force coefficient per degree of the yaw angle β ($\partial C_Y / \partial \beta$) as function of the angle of attack α for transonic-supersonic Mach numbers, [51]

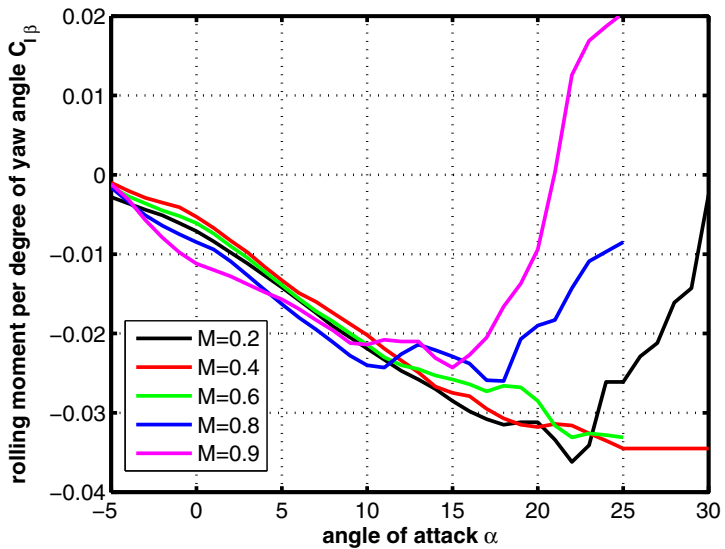


Fig. 6.125. Rolling moment coefficient per degree of the yaw angle β ($\partial C_l / \partial \beta$) as function of the angle of attack α for subsonic-transonic Mach numbers, [51]

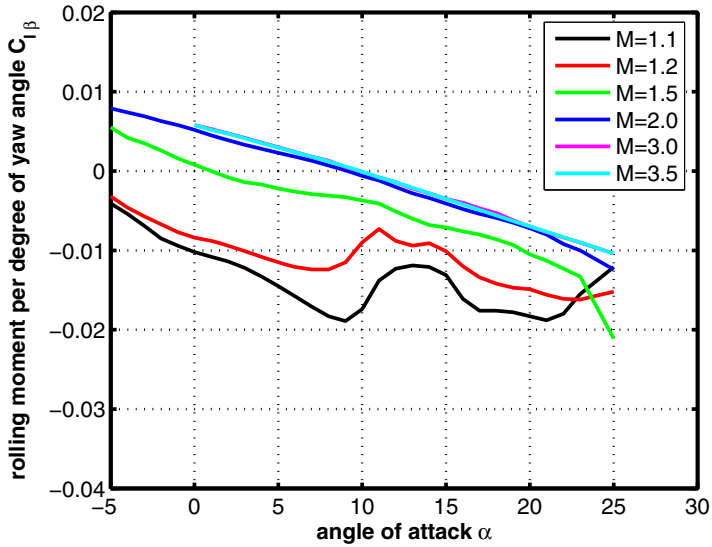


Fig. 6.126. Rolling moment coefficient per degree of yaw angle β ($\partial C_l / \partial \beta$) as function of the angle of attack α for transonic-supersonic Mach numbers, [51]

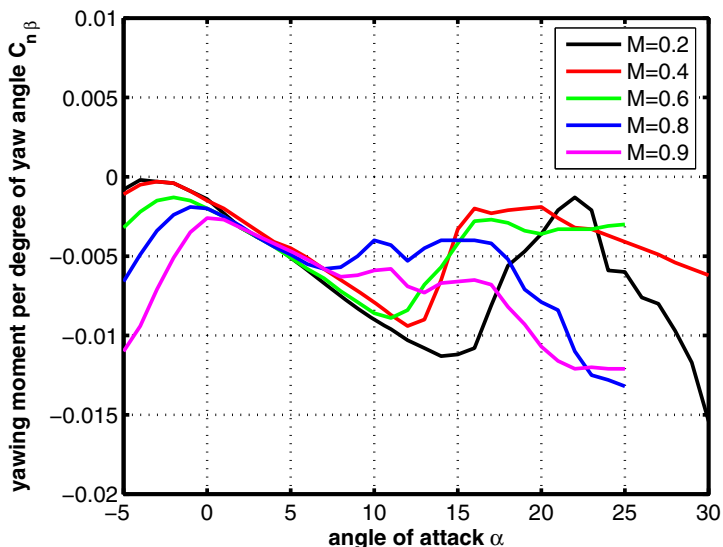


Fig. 6.127. Yawing moment coefficient per degree of the yaw angle β ($\partial C_n / \partial \beta$) as function of the angle of attack α for subsonic-transonic Mach numbers, [51]

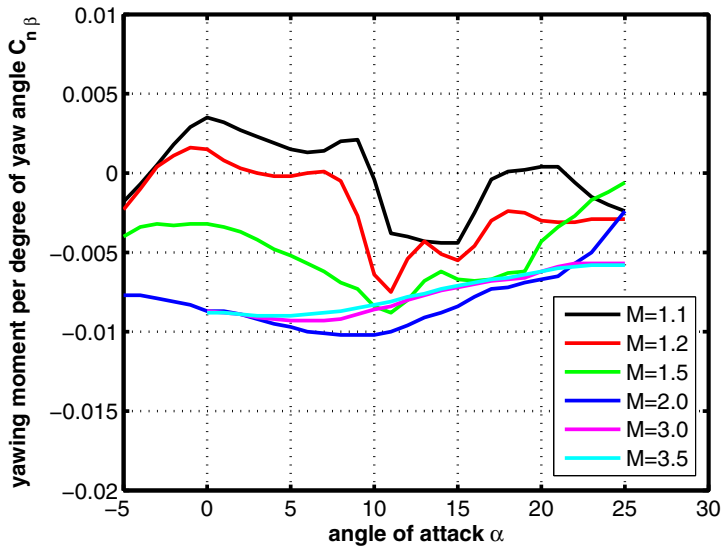


Fig. 6.128. Yawing moment coefficient per degree of the yaw angle β ($\partial C_n / \partial \beta$) as function of the angle of attack α for transonic-supersonic Mach numbers, [51]

6.9 Facetted DS6 Configuration (Germany)

Today we have the situation, that there is no real industrial project, by which the SPACE SHUTTLE system could be replaced²⁹, neither by conventional nor by advanced systems and technologies.

Therefore some research institutes for aeronautics and space applications use the time to reflect about approaches for new shape designs of space vehicles, in particular with respect to reduce the costs for payload transportation.

One of these ideas is to define vehicle shapes with facetted surfaces, generating sharp edged contours, by the German Aerospace Center DLR. In this way the thermal protection system would become much simpler and cheaper, than for example for the SPACE SHUTTLE Orbiter, where almost all the TPS tiles were individual items.

Of course, during re-entry, where flight Mach numbers up to 30 occurs, thermal loads are exceptional high. The surface radiation cooling, [43], is effective only at configuration parts with large curvature radii. That is one of the reasons that conventional re-entry vehicles have blunt noses, like capsules, orbiters, etc.. With the advent of modern Ceramic Matrix Composite (CMC) materials, like C/C-SiC, which can be applied as hot structures, keeping their mechanical properties also at very high temperatures, large bluntness in the former sense may not be longer a necessary feature of re-entry vehicles.

6.9.1 Configurational Aspects

The DLR launched a program named SHEFEX (SSharp Edge Flight EXperiment), where first a non-winged configuration (Fig. 6.129), and second a winged configuration (Fig. 6.130), both with facetted surfaces and sharp edges were investigated with numerical simulation methods, by wind tunnel tests and in free-flight experiments. The main goal was to analyze the thermal loads (heat transfer rates and surface temperatures) in particular along the sharp edges, the aerodynamic performance L/D (longitudinal and lateral flight capacity), and to obtain data from the free-flight experiments for the validation of the numerical prediction methods. The first free-flight, where the non-winged shape was transported sub-orbital on top of a sounding rocket, named SHEFEX I, took place in Oct. 2005, [54] - [56]. Fig. 6.131 shows the re-entry configuration of SHEFEX I. The second free-flight, SHEFEX II, transporting the winged shape to space, took place on June 2012, Fig. 6.132.

With the experience gained with the facetted configurations (SHEFEX I and SHEFEX II) and the waverider concept the DLR has designed a space vehicle shape with high aerodynamic performance L/D in the hypersonic flight regime. The reason for this is to improve the operational capacity, which means lower g-loads, higher longitudinal and lateral flight capability, lower

²⁹ This is valid at least for the time-period 2010 - 2015.



Fig. 6.129. Facetted configurations: SHEFEX I, non-winged shape without aerodynamic control surfaces; design by the DLR. Various views at the shape, [54, 55]

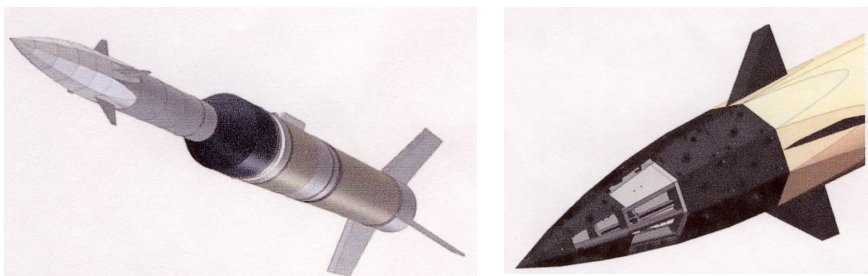


Fig. 6.130. Facetted configurations: SHEFEX II, winged shape with aerodynamic control surfaces; design by the DLR, [56]. Space vehicle on top of the booster rocket, the launch configuration (left), space vehicle (right).

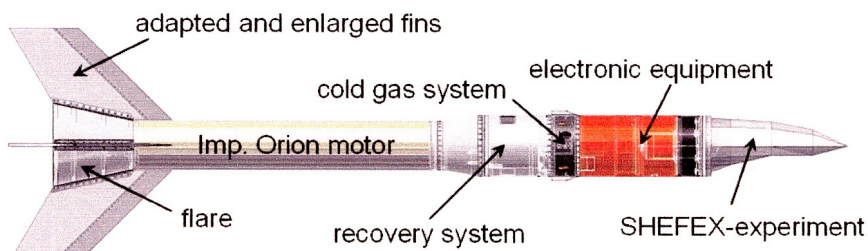


Fig. 6.131. SHEFEX I: Re-entry configuration of the non-winged SHEFEX I experiment, [55]



Fig. 6.132. SHEFEX II: Launch configuration with the winged SHEFEX II shape, [56]

peak heat transfer rates, etc., as well as the comfort for the crew members if the vehicle is manned [57] - [59].

The outcome is the DS6 shape, Fig. 6.133, with a L/D higher than 3 in the hypersonic flight regime for a body flap deflection $\eta_{bf} = 0^\circ$. For this shape in the following section aerodynamic data are presented and discussed.

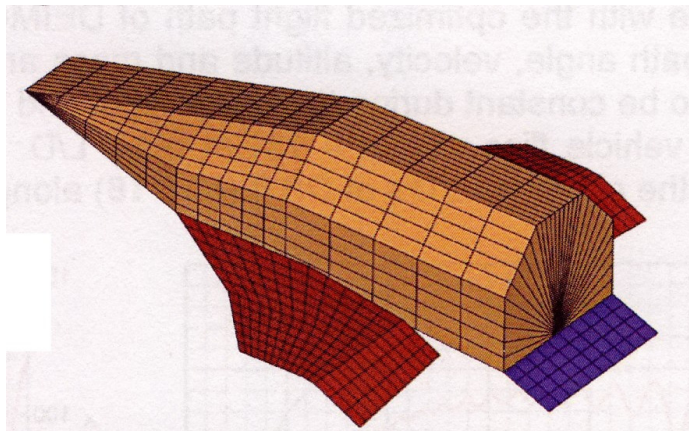


Fig. 6.133. Facetted DS6 configuration: winged shape with aerodynamic trim and control surfaces; design by German Aerospace Center DLR, [57, 58]

6.9.2 Aerodynamic Data of Steady Motion

Longitudinal Motion

The aerodynamic performance L/D as function of angle of attack α for $M_\infty = 8$ is shown in Fig. 6.134. For the neutral body flap deflection ($\eta_{bf} = 0^\circ$) L/D is highest (around $\alpha \approx 12^\circ$). The positive body flap deflection $\eta_{bf} = 20^\circ$ (downward) reduces strongly the aerodynamic performance L/D obviously due to the drag increase, whereas the moderate L/D reduction for the negative body flap deflection $\eta_{bf} = -20^\circ$ is due to the degradation in lift. A draw back of this configuration is apparently the longitudinal static instability which cannot be repaired. On the other hand the vehicle is trimmable for reasonable body flap deflections and angles of attack, Fig. 6.135.

Fig. 6.136 exhibits L/D values for the Mach number range $4 \leq M_\infty \leq 25$. Since the body flap deflection was $\eta_{bf} = 10^\circ$, the maximum L/D value does not exceed the value of 3, [57, 59].

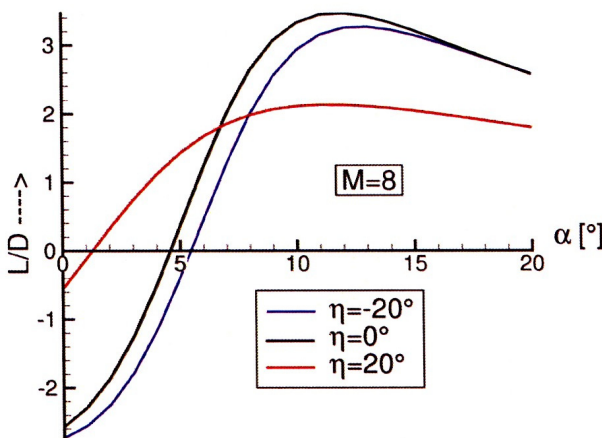


Fig. 6.134. Facetted DS6 configuration: the lift-to-drag ratio as function of the angle of attack α for $M_\infty = 8$ and various body flap deflection angles, [57].

Lateral Motion

Investigations regarding the lateral motion were not reported.

6.9.3 Aerodynamic Data of Unsteady Motion

Data of investigations of dynamic stability are not available.

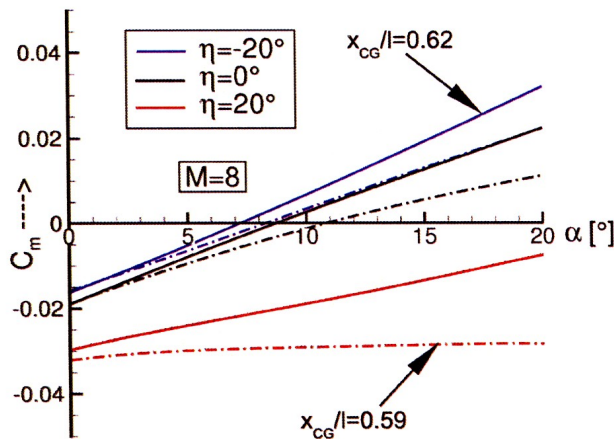


Fig. 6.135. Facetted DS6 configuration: pitching moment coefficient C_m as function of the angle of attack α for $M_\infty = 8$ and various body flap deflection angles, [57].

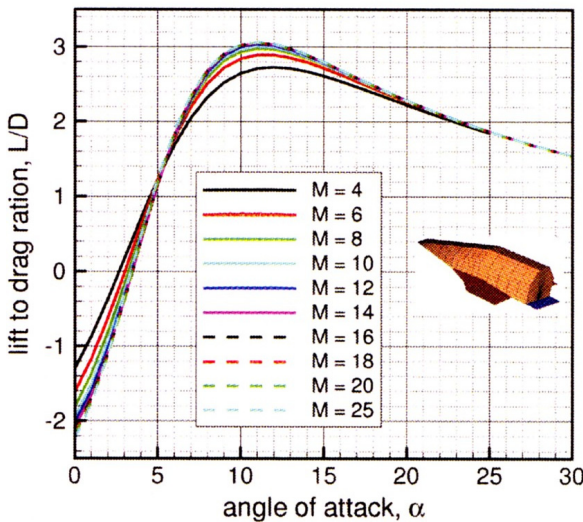


Fig. 6.136. Facetted DS6 configuration: lift-to-drag ratio as function of the angle of attack α in the hypersonic flight regime. Body flap deflection $\eta_{bf} = 10^\circ$, [57, 59].

6.10 PRORA (Italy)

Italy has launched in 2000 the Aerospace Research Program PRORA with the goal to improve the technology basis and the system cognitions about the transportation of space vehicles into Earth's orbits. This was done due to the fact that Italy's space agency CIRA had the impression that their experience in space applications were not evident enough for taking part in advanced European and international space programs.

In the frame of this program the development of a flight demonstrator called "Unmanned Space Vehicle (USV)" was planned. With this flight vehicle the following tasks were to be performed:

- atmospheric re-entry,
- sustained hypersonic flight,
- reusability.

Therefore the planned USV flight modes were:

- a dropped transonic flight,
- a suborbital re-entry flight,
- a sustained hypersonic flight,
- an orbital re-entry flight.

For all these flights the USV was to be brought to an appropriate altitude by a balloon, then released or dropped from this balloon and powered for the re-entry and hypersonic flight cases by a solid rocket booster, [60]. The final landing was to be conducted by a parachute system either at sea or on ground. Fig. 6.137 shows the USV vehicle ready for the transonic demonstrator flight.

Besides the demonstration of the system aspects of the above listed flights, technologies, like materials for advanced thermal protection systems, flight control system, air data system, aerodynamic shape design, etc., were also aspects of investigations.



Fig. 6.137. CIRA's PRORA-USV vehicle fabricated for the transonic flight demonstration, [61]

6.10.1 Configurational Aspects

In order to minimize the configurational risks a conventional shape was selected for the USV³⁰. It consists of a fuselage with a compact cross section, which has a blunted nose, and a double delta wing positioned rearward, with sweep angles of 45 and 76 degrees. The wing trailing edge has a forward sweep angle of 6 degrees. Further for roll stability reasons the wing has a dihedral angle of 5 degrees. The overall length is $L = 8$ m and the wingspan $b = 3.56$ m, [62]. As Fig. 6.138 exhibits, the USV shape has some volitional similarities to NASA's X-34 vehicle, which for its part was similar to the SHUTTLE Orbiter. This configuration was used for the transonic flight test, which has taken place in Feb. 2007. After an extended evaluation phase of the first transonic flight, the planning of the next demonstration flight began in 2013, [63].

For an earlier version of the USV shape, defined in [64, 65], we also present for comparison reasons some aerodynamic coefficients. The configurational characteristics of this shape were: overall length $L = 7$ m, wingspan $B = 3.8$ m, sweep angles of the double delta wing 45 and 80 degrees.

6.10.2 Aerodynamic Data of Steady Motion

The aerodynamic data for the nominal shape covered the Mach number range, which was to be reached during the transonic flight demonstration tests, namely $0.7 \leq M_\infty \leq 2$. The first of these flight tests took place in Feb. 2007, [61]. The aerodynamic data stem mainly from wind tunnel tests. Numerical simulations were also conducted in particular for validation reasons and extrapolation to flight conditions. It should be noted that the drag coefficient, presented below, does not include the base drag, since this drag was difficult to determine from wind tunnel tests due to the strong influence of the model sting on the base flow, [62].

The aerodynamic data for the earlier shape are taken from [65]. This data come from 3-D Euler solutions, where the fins, the base flow and the viscous part of the flow were not included. Thus the data have a preliminary status. The effects of the base flow and the viscosity on the aerodynamic coefficients were taken into account by simple semi-empirical formulas often.

The aerodynamic coefficients for the nominal shape and the earlier shape were normalized with different values, [62, 65], see Tab. 6.4.

In Fig. 6.139 a Schlieren photograph of the USV model during a wind tunnel test with $M_\infty = 1.2$, $\alpha = 10^\circ$ (left) and the wind tunnel model itself (right) are shown, [62, 66]. Surface pressure distributions evaluated from an Euler solution for the transonic flow condition $M_\infty = 1.035$, $\alpha = 6.405^\circ$, with a negative elevon deflection of $\delta_E = -9.87^\circ$ (upward) are shown in

³⁰ We call the shape, which was used for the transonic demonstrator test, the nominal shape.

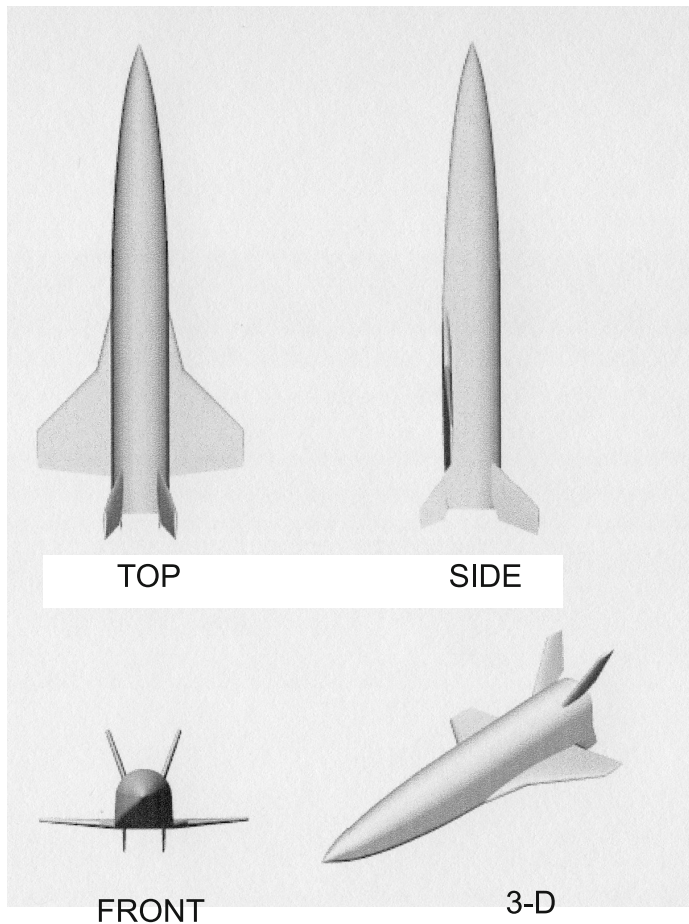


Fig. 6.138. Sketch of the PRORA-USV vehicle (earlier shape) with top, side, front and 3-D view, [62]. The vehicle has an overall reference length of 8 m, and a wingspan of 3.8 m.

Fig. 6.140 (left), [61, 62]. The right part of this figure exhibits the vortex formations along the wing leading edge, the wing tip and the fuselage as they were predicted by a Navier-Stokes simulation of the flow field with $M_\infty = 0.70$, $\alpha = 10^\circ$, $Re = 6.5 \cdot 10^6$, [67, 68]

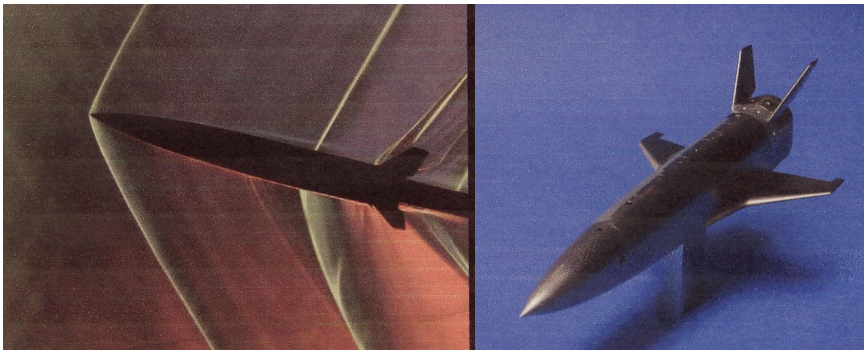


Fig. 6.139. PRORA-USV vehicle: Schlieren photograph in the windtunnel for $M_\infty = 1.2$, $\alpha = 10^\circ$ (left), wind tunnel model (right), [62, 66].

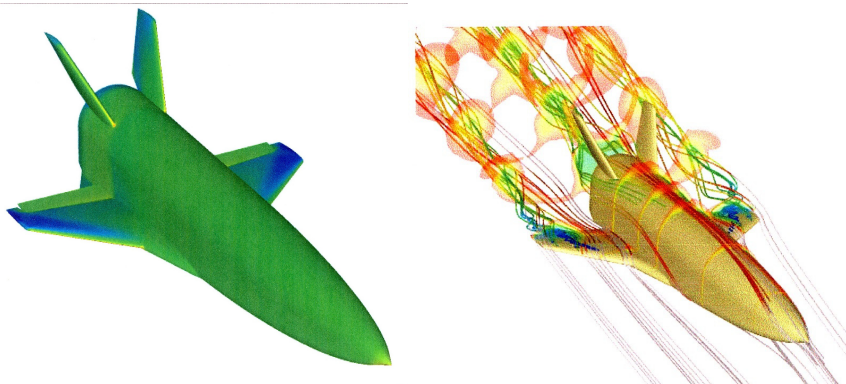


Fig. 6.140. PRORA-USV vehicle: Surface pressure distribution of an Euler solution with $M_\infty = 1.035$, $\alpha = 6.405^\circ$, $\delta_E = -9.87^\circ$ (left), Navier-Stokes solution with $M_\infty = 0.70$, $\alpha = 10^\circ$, $Re = 6.5 \cdot 10^6$ showing the vortex formation by streamlines (right), [61, 62, 67, 68].

Table 6.4. Reference values for the nominal shape, [62] and the earlier shape, [65]

	nominal shape	earlier shape
reference length	1.05 m	8 m
reference area	3.60 m ²	11.5 m ²
reference span	3.56 m	3.8 m

Longitudinal Motion

The lift coefficient, presented in Fig. 6.141, exhibits the well known behavior for RV-W's of USV-type, namely an increasing lift slope $\partial C_L / \partial \alpha$ with growing Mach number until the transonic Mach number $M_\infty = 1.05$ is reached, followed by a decreasing lift slope for increasing supersonic Mach numbers. For the transonic Mach numbers ($M_\infty = 0.7, 0.94, 1.05, 1.2$) the linearity of C_L breaks around $\alpha \gtrsim 12^\circ$, obviously due to the decay of the wing vortex. For supersonic Mach numbers ($M_\infty = 1.52, 2$) C_L linearity is retained.

We note again that the drag coefficient C_D does not contain the base drag, which is explained in more detail below. The usual behavior of the drag can be observed with an overall maximum near $M_\infty \approx 1$, Fig. 6.142.

In order to show the general characteristics of the aerodynamic performance of the nominal USV vehicle we have drawn exemplarily for $M_\infty = 0.7, 1.05, 2$ the lift-to-drag ratio L/D , despite the fact, that the drag coefficient has not been included the base drag, Fig. 6.143.

The base drag is mainly driven by the pressure coefficient $c_{p, base}$ with

$$c_{p, base} = \frac{(p_{base} - p_\infty)}{0.5 \rho_\infty v_\infty^2} = \frac{2}{\gamma M_\infty^2} \left(\frac{p_{base}}{p_\infty} - 1 \right). \quad (6.1)$$

$c_{p, base}$ is zero for $p_{base} = p_\infty$ and also for $M_\infty \Rightarrow \infty$, which is the Newton limit for hypersonic flows. When $c_{p, base} \Rightarrow 0$, no contribution to the total drag is present. For $c_{p, base} > 0$ the total drag is reduced and in the case that $c_{p, base} < 0$ the total drag increases. Since the flow expands around the base of the USV vehicle, $c_{p, base}$ will probably be negative, which means that the total drag increases and L/D decreases. Therefore the L/D values of Fig. 6.143 are certainly too high. The realistic L/D magnitudes are without doubt closer to the ones of Fig. 6.145 for the earlier USV shape.

The pitching moment diagram, Fig. 6.144, shows that the vehicle behaves statically stable throughout the considered Mach number range for angles of attack $\alpha \lesssim 15^\circ$, except for $M_\infty = 2$. The general trend that the longitudinal static stability is largest around $M_\infty \approx 1$ for such kind of vehicles is

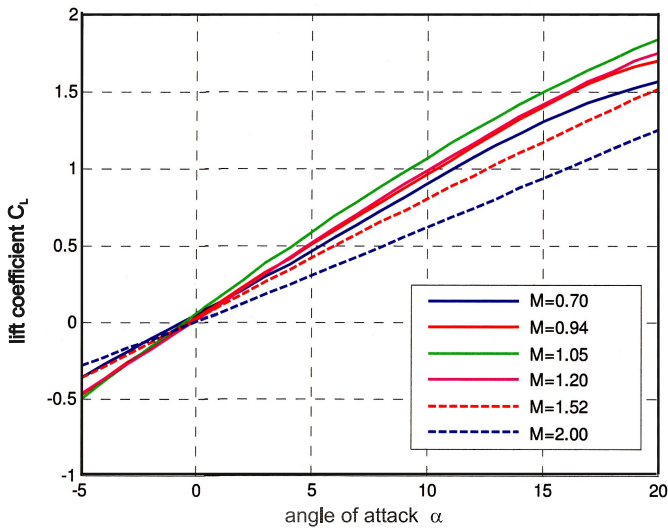


Fig. 6.141. Lift coefficient C_L as function of the angle of attack α for transonic-supersonic Mach numbers, [62]

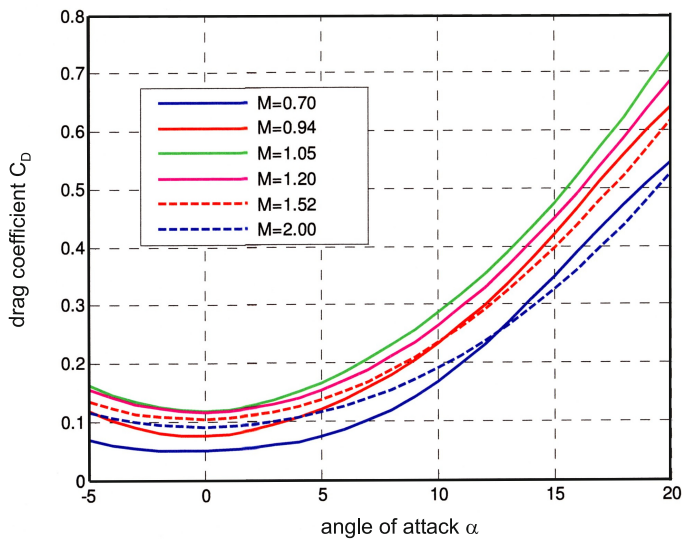


Fig. 6.142. Drag coefficient C_D as function of the angle of attack α for transonic-supersonic Mach numbers, [62]

confirmed. Trim seems to be achievable for angles of attack around 0° for the Mach numbers $M_\infty = 0.94, 1.05, 1.2, 1.52$. On the other hand owing to the flight trajectory trim should be feasible in this Mach number regime for angles of attack around 10° . Therefore the pitching moment curves have to be lifted up. An increasing of the pitching moment coefficient, which means to aim for a positive increment (pitch-up), can be achieved either by a negative elevon deflection ($\delta_E < 0$) and/or by a rearward shift of the center-of-gravity.

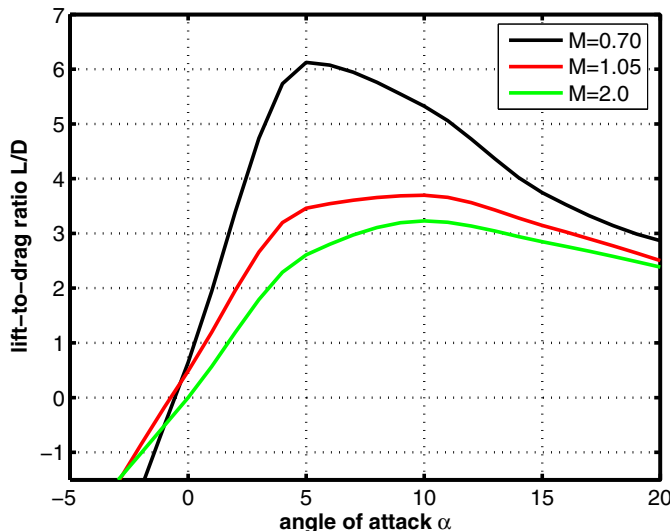


Fig. 6.143. Lift-to-drag ratio L/D as function of the angle of attack α for three sample Mach numbers, [62]. The drag coefficient does not contain the base drag.

Fig. 6.145 shows the aerodynamic coefficients in short for the earlier USV vehicle. Note the different normalization quantities (see Table 6.4). As expected the aerodynamic characteristics are very similar for the nominal and the earlier shape.

Lateral Motion

The side force coefficient C_Y plotted against the side slip angle β , Fig. 6.146, behaves primarily linear ($\partial C_Y / \partial \beta \approx \text{const.}$) and has its maximum slope for $M_\infty = 1.05$. Of course, there exists a strong α - dependency of the lateral aerodynamic coefficients at high angles of attack, when the fins get into the shadow of the fuselage.

The rolling moment coefficient has a negative slope ($\partial C_l / \partial \beta < 0$), which indicates a damping of the rolling motion, hence roll stability, Fig. 6.147. From

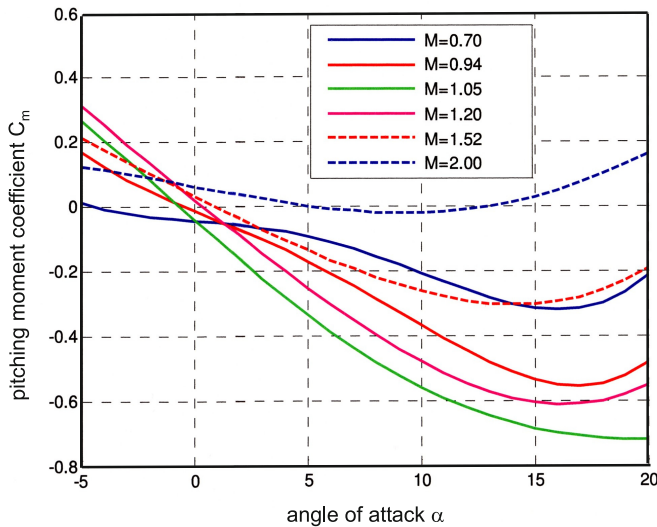


Fig. 6.144. Pitching moment coefficient C_m as function of the angle of attack α for transonic-supersonic Mach numbers, [62]. Moment reference point is located at 68.5% of the body length $L = 8$ m.

the six Mach numbers plotted in the diagram the three transonic ones exhibits some deviations from linearity, whereas the other three ($M_\infty = 0.7, 1.52, 2$) are strictly linear. The largest slope can be observed for $M_\infty = 1.05$.

First measurements of the yawing moment have shown that there exists only a marginal directional stability. To improve this ventral fins were added to the configuration and mounted at the lower side (windward side) of the shape (see in Fig. 6.138 the lower left front view picture). Indeed, these aerodynamic stabilization surfaces have caused directional stability ($\partial C_n / \partial \beta > 0$) for Mach numbers up to $M_\infty = 1.2$, Fig. 6.148. For higher supersonic Mach numbers the vehicle tends to become directionally unstable.

6.10.3 Aerodynamic Data of Unsteady Motion

Data from investigations of dynamic stability are not available.

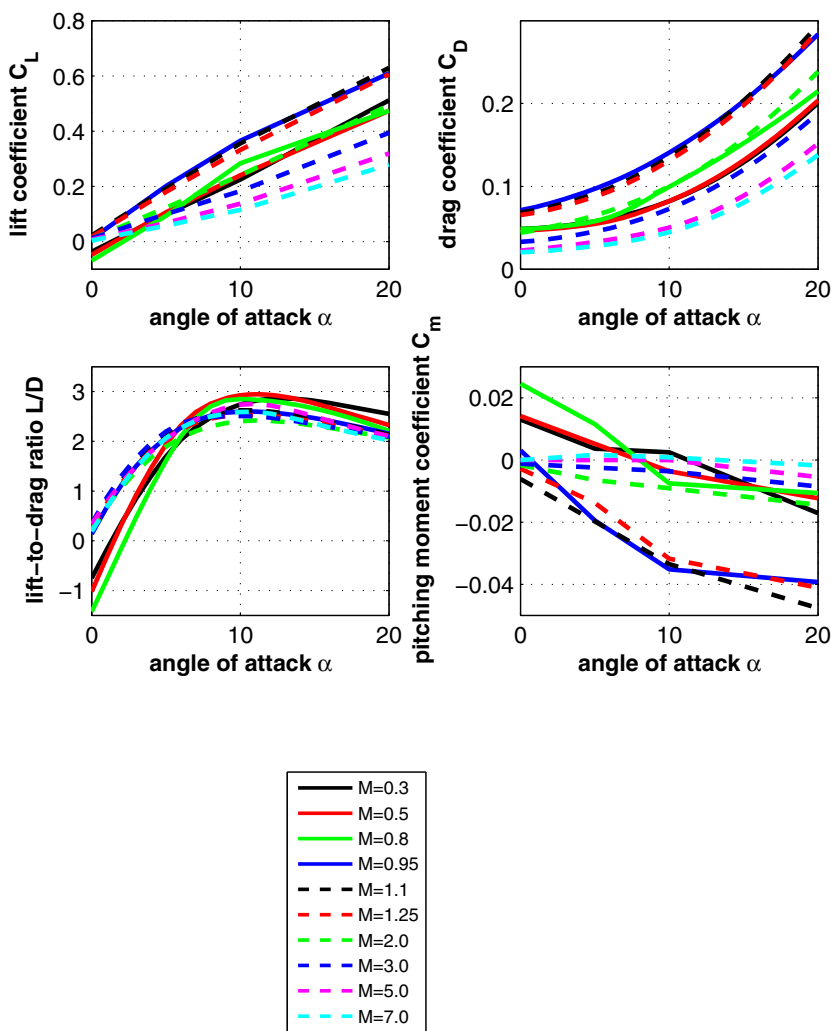


Fig. 6.145. Longitudinal aerodynamic database as function of the angle of attack α for the earlier version of the USV shape, [65]

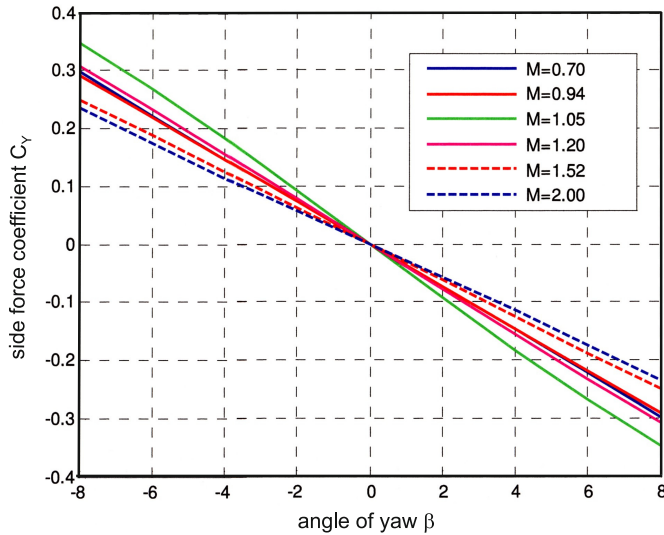


Fig. 6.146. Side force coefficient C_Y as function of the angle of side slip β for transonic-supersonic Mach numbers and $\alpha = 5^\circ$, [62]

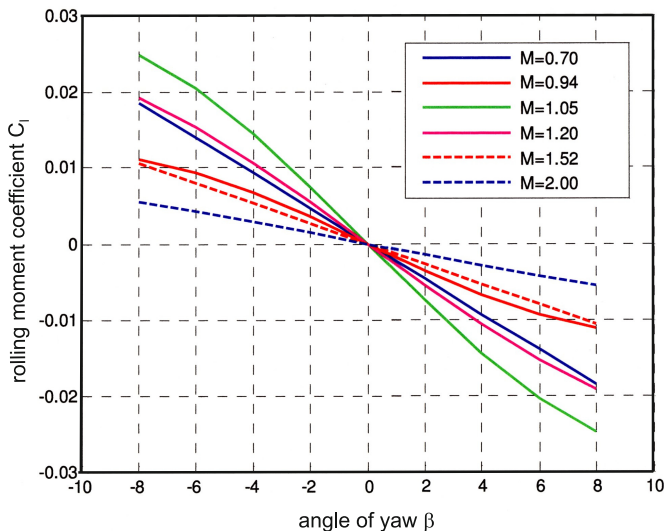


Fig. 6.147. Rolling moment coefficient C_l as function of the angle of side slip β for transonic-supersonic Mach numbers and $\alpha = 5^\circ$, [62]

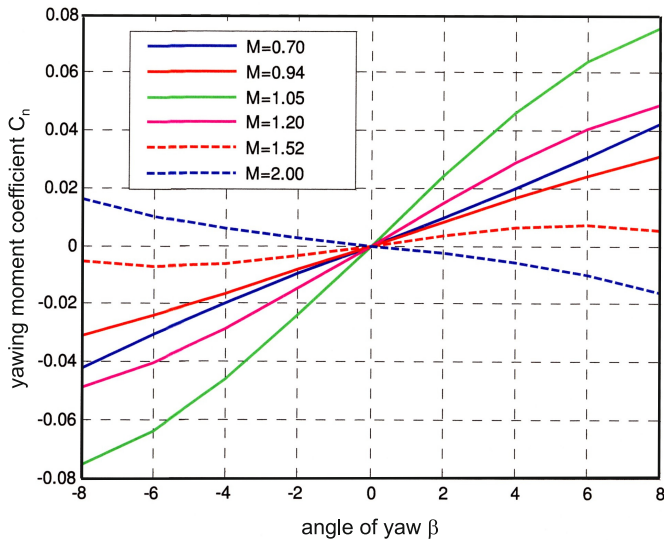


Fig. 6.148. Yawing moment coefficient C_n as function of the angle of side slip β for transonic-supersonic Mach numbers and $\alpha = 5^\circ$, [62]. The moment reference point is located at 68.5% of the body length $L = 8$ m.

6.11 HERMES (Europe)

In 1984, the French government launched a proposal for the development of a space transportation system in order to guarantee Europe an autonomous and manned access to space. Key parts of this system were the RV-W space plane HERMES, Fig. 6.149, intended for a gliding re-entry from space to an Earth landing site, and the launch system ARIANE V, which at that time was a completely new rocket system. The original French project officially became an European project under the supervision of the European Space Agency (ESA) in November 1987. HERMES was conceived to have the following features:

- ascent to low Earth orbit (up to 800 km) on top of the ARIANE V rocket,
- 30-90 days mission duration in orbit,
- total launch mass 21000 kg,
- fully reusability,
- initially, the transportation of six astronauts and 4 500 kg payload into low Earth orbit, and after a reorientation a reduction to three astronauts and a transportation payload of 3000 kg.

In 1993 the HERMES project was cancelled due to the new political environment (end of the cold war) and budget constraints. At that time a total of approximately \$ 2 billion had already been invested in the HERMES project. The pitching moment anomaly, [10], observed during the first re-entry flight of the SPACE SHUTTLE Orbiter, had not found a profound explanation when the HERMES development begun. Because it was suspected that it was due to wind tunnel shortcomings, emphasis was put on the use of the at that time emerging methods of numerical aerothermodynamics. The related need of validation data as well as systems tests had led to the proposal of the sub-scale experimental vehicle MAIA, [69].

No HERMES vehicle, nor the proposed sub-scale experimental vehicle MAIA [69], was ever built.



Fig. 6.149. HERMES mock-up with propulsion and service module (left), HERMES shape with propulsion and service module docked at the Columbus module (Manned Tended Free Flyer MTFF), synthetic image (middle), HERMES orbiter during re-entry flight, synthetic image (right), [70].

Initially the numerical methods had not the capability to contribute essentially to the establishment of the aerothermodynamic data base of HERMES. The computational fluid dynamic (CFD) codes did not yet meet the following requirements³¹:

- three-dimensional grid generation around complex configurations including flaps, rudders and gaps,
- fast and robust solver of the convective part of the governing equations (Euler equations),
- description of real gas effects in thermodynamic equilibrium,
- description of real gas effects in thermodynamic non-equilibrium,
- full set of equations for viscous flows (Navier-Stokes equations),
- turbulence models for industrial purposes, which are calibrated by selected wind tunnel experiments,
- consideration of catalytic walls,
- accurate and reliable prediction of the laminar-turbulent transition zone,
- proper resolution of turbulent boundary layers for the determination of wall heat transfer,
- wall radiation cooling including a view factor approach for non-convex configuration parts,
- general validation with flight test data.

With the passage of time, due to a research and development program in the frame of the HERMES project, the requirements mentioned above were developed and implemented piece by piece in the various CFD codes. In 1990 a first three-dimensional Euler solution with a non-equilibrium real gas approach was obtained, Fig. 6.150 (right), [72]. This Euler solution was then coupled with a three-dimensional second-order boundary layer solution, formulated also for a non-equilibrium real gas, [73].

A great challenge for every CFD code consists in the computation of flow fields which contain the base flow area. In base flow areas of space vehicles often body flaps, wing elevons and rudders are positioned, which in general are deflected during operational flight, and which therefore generate very complex flow structures. Fig. 6.150 (left) shows an example of such a flow field, [75].

In the middle of Fig. 6.150 the plotted skin-friction lines at the leeward side of the HERMES vehicle give an impression of the complex flow structure with several separation and reattachment lines.

6.11.1 Configurational Aspects

The Figs. 6.151 to 6.153 show the side view, the front view and the top view of the HERMES shape 1.0, [78]. The total length of the vehicle was 14.574 m

³¹ This was true not only for Europe but also for the other countries involved in space vehicle projects like the United States of America, the Soviet Union and Japan.

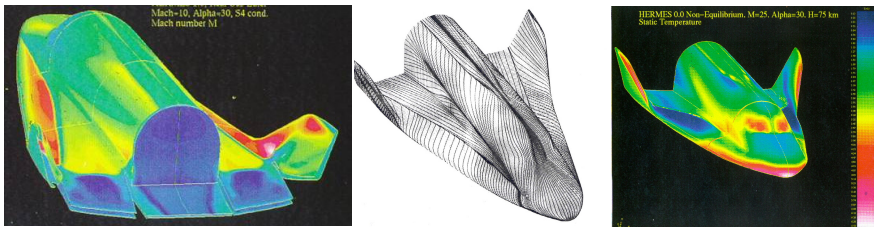


Fig. 6.150. HERMES shape 1.0: Euler solution including flaps and rudders for wind tunnel conditions (left), skin-friction lines of a Navier-Stokes solution at the leeward side (middle), Euler solution using a non-equilibrium real gas approach (right), [71] - [75]

and the total width 9.379 m. At that time the center-of-gravity location was not yet fixed. In our moment diagrams we therefore have used a preliminary value of $0.6 L_{ref}$.

The HERMES shape 1.0 has a delta wing with a sweep angle of 74 degrees. Some interesting dimensions, quantities and reference values are listed in Tab. 6.5.

Table 6.5. HERMES shape 1.0: dimensions, quantities and reference values, [78]. See Figs. 6.151 to 6.153.

total length	L_{tot}	14.574 m
total width	W_{tot}	9.379 m
reference length	L_{ref}	15.500 m
reference area	S_{ref}	84.67 m^2
x-coordinate of center-of-gravity	x_{cog}	8.722 m Fig. 6.153
empty mass	m_e	15 000 kg
gross mass at launch	m_g	21 000 kg

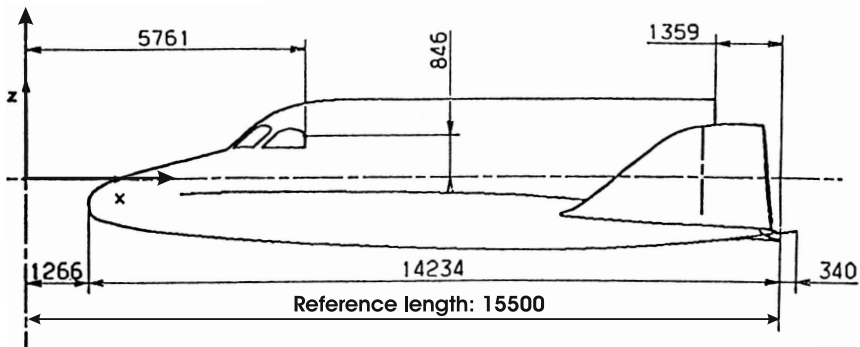


Fig. 6.151. Definition of HERMES shape 1.0. Side view, [78].

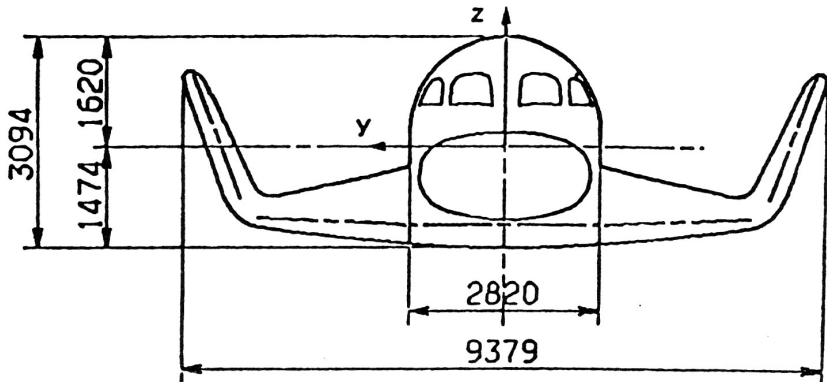


Fig. 6.152. Definition of HERMES shape 1.0. Front view, [78].

The design philosophy of the HERMES configuration was different from that of, for example, the SPACE SHUTTLE Orbiter. Its lateral stability is caused by winglets and controlled by rudders mounted at the rear part of these winglets. The SPACE SHUTTLE Orbiter uses for this function a central fin. The advantage of the winglet design consists in the fact, that during re-entry the winglets become aerodynamically effective earlier (at an altitude of ≈ 70 km) compared to the central fin solution (effective at an altitude of ≈ 30 km). This is because the central fin lies mostly in the hypersonic shadow due to the high angles of attack on the re-entry path. The consequence for the SPACE SHUTTLE Orbiter is, that the lateral stability has to be controlled by a reaction control system (RCS) (down to an altitude of ≈ 30 km). This is

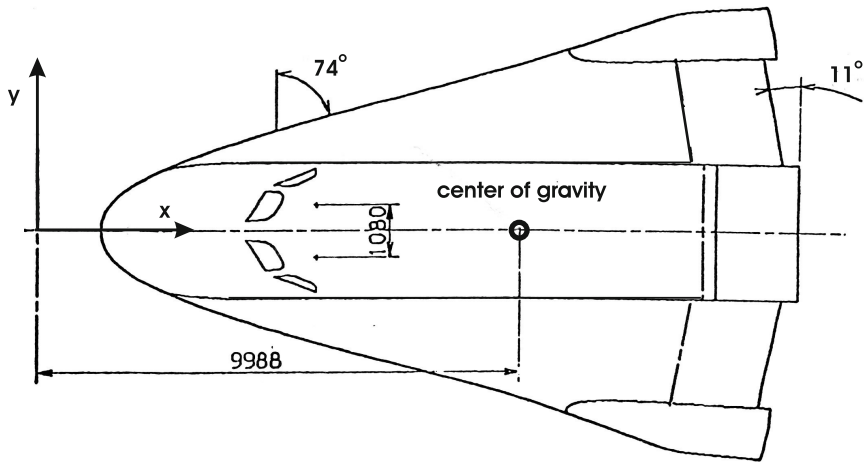


Fig. 6.153. Definition of HERMES shape 1.0. Top view [78].

not necessary to this extent in the case of the winglet design of the HERMES configuration.

6.11.2 Aerodynamic Data of Steady Motion

The presented aerodynamic data are split into the Mach number groups subsonic-supersonic and supersonic-hypersonic. Data for the longitudinal stability with regard to the subsonic-supersonic regime are presented in Figs. 6.154 to 6.157 and with respect to the supersonic-hypersonic regime in Figs. 6.158 to 6.161.

Data for the lateral stability regarding the subsonic-supersonic regime can be found in Figs. 6.165 to 6.167 and regarding the supersonic-hypersonic regime in Figs. 6.168 to 6.170.

The data base is composed with results from wind tunnel tests, approximate design methods and numerical simulations, [76, 77].

Longitudinal Motion

subsonic-supersonic regime

The lift coefficient C_L shows a nearly linear behavior over the whole angle of attack range ($-5^\circ \leq \alpha \leq 30^\circ$), Fig. 6.154. The drag coefficient C_D around $\alpha \approx 0^\circ$ is small for all Mach numbers, rising with increasing angle of attack as expected. For transonic Mach numbers C_D is largest, Fig. 6.155. The maximum lift-to-drag ratio $L/D_{max} \approx 5$ occurs at $\alpha \approx 10^\circ$ in the subsonic

flight regime and reduces for the low supersonic Mach numbers ($1.5 \leq M_{\infty} \leq 2.5$) to $L/D \approx 2$ at $\alpha \approx 15^\circ$, Fig. 6.156. The pitching moment data shown in Fig. 6.157 indicate static stability ($\partial C_m / \partial \alpha < 0$) only for $M_{\infty} = 1.1$ and 1.5 up to $\alpha \approx 10^\circ$ but with no trim point. In all other situations the HERMES shape 1.0 behaves statically unstable ($\partial C_m / \partial \alpha > 0$). Of course, it should be mentioned that this is valid for a moment reference point of 0.6 L_{ref} , and when flaps and rudders are in neutral position.

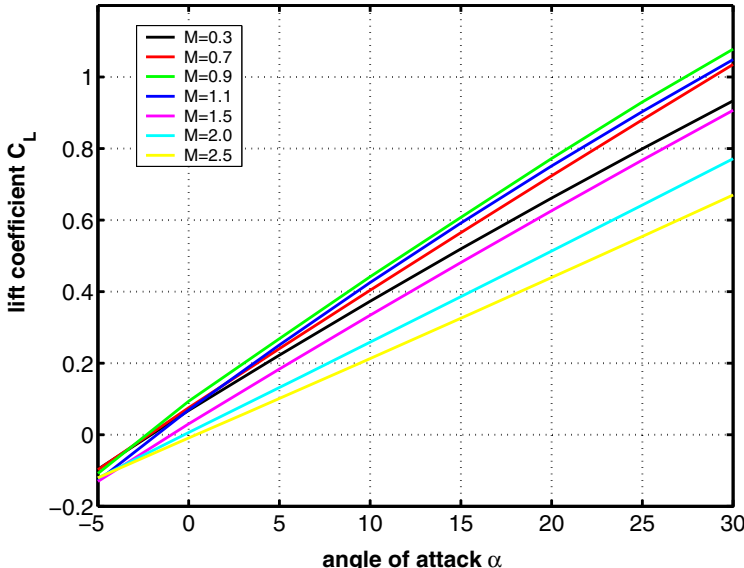


Fig. 6.154. Lift coefficient C_L as function of the angle of attack α for subsonic-supersonic Mach numbers, [76].

supersonic-hypersonic regime

The lift coefficient C_L becomes non-linear for angles of attack $\alpha > 30^\circ$. For hypersonic Mach numbers ($M_{\infty} \geq 10$) we can observe the well known slight increase of the C_L slope³² ($\partial C_L / \partial \alpha$) around $\alpha \approx 20^\circ$, Fig. 6.158. The drag behaves like expected, Fig. 6.159. The maximum lift-to-drag ratio L/D_{max} reduces to values smaller than 2 for angles of attack $\alpha \approx 15^\circ$, Fig. 6.160.

In this Mach number regime longitudinal stability is given for angles of attack $\alpha \gtrsim 30^\circ$, and the vehicle can be trimmed without any deflection of the aerodynamic control surfaces (see the pitching moment diagram Fig. 6.161).

³² The reason for this probably is the lee-side vortex development.

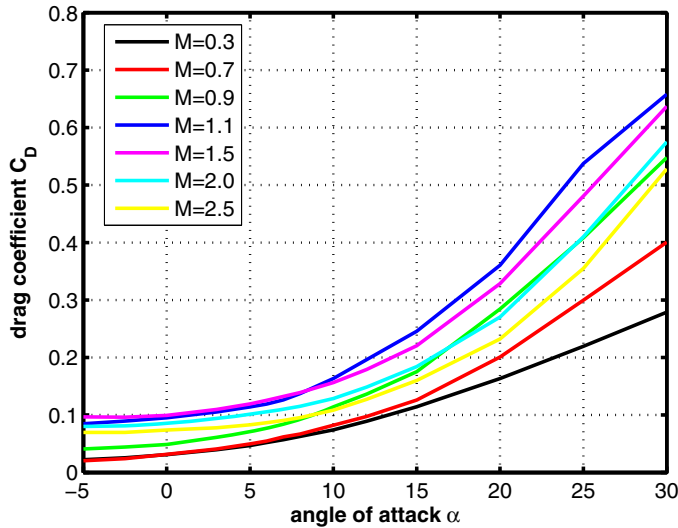


Fig. 6.155. Drag coefficient C_D as function of the angle of attack α for subsonic-supersonic Mach numbers, [76]

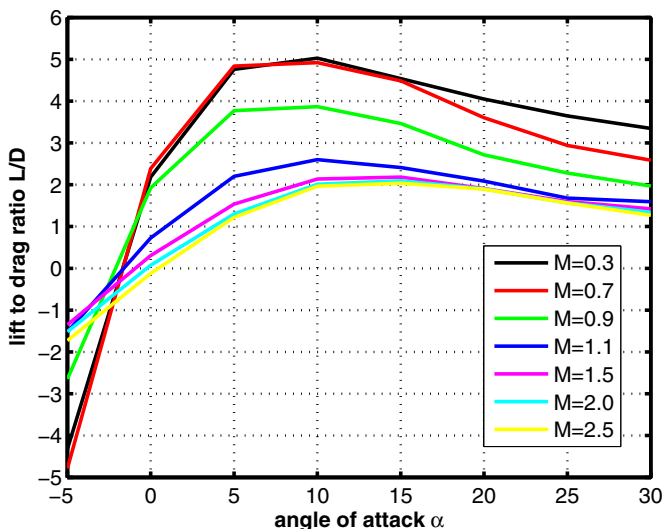


Fig. 6.156. Lift-to-drag ratio L/D as function of the angle of attack α for subsonic-supersonic Mach numbers, [76]

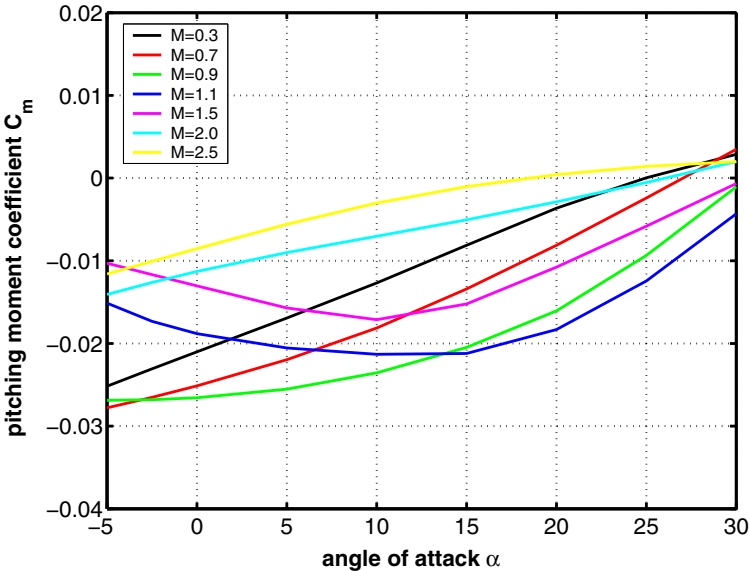


Fig. 6.157. Pitching moment coefficient C_m as function of the angle of attack α for subsonic-supersonic Mach numbers, moment reference point $x_{ref} = 0.6 L_{ref}$, [76]

Finally, we point out the Mach number independence of C_L , C_D and L/D , [10].

pitching moment considerations

We consider now the influence of body flap and elevon deflections on the pitching moment. As an example we look at the case $M_\infty = 10$. When the body flap is deflected downwards to $\eta_{bf} = 10^\circ$ or 20° , the pressure force at the aft part of the configuration increases, which leads to a pitch down effect, with the consequence that the static stability grows slightly and the trim point is shifted to lower angle of attack values, Fig. 6.162 (red and blue curves). In contrast to that, when the body flap and the elevon are deflected upwards ($\eta_{bf} = -15^\circ$, $\eta_{el} = -10^\circ$), the pressure force at the aft part is reduced which subsequently leads to a pitch up effect. Static stability is lost and the trim point is no longer inside the considered angle of attack range α ($\alpha_{max} = 50^\circ$), Fig. 6.162 (green curve).

As we have experienced from Fig. 6.157, the pitching moment for the subsonic Mach numbers $M_\infty = 0.3$, 0.7 and 0.9 indicates strong static instability. By a forward shift of the center-of-gravity from $x_{ref} = 0.6 L_{ref}$ to $x_{ref} = 0.565 L_{ref}$ a pitch down effect is generated and the instability is decreased, but no trim is ensured, Fig. 6.163. In order to ensure trim the body flap and the elevons are deflected upwards ($\eta_{bf} = -10^\circ$, $\eta_{el} = -10^\circ$),

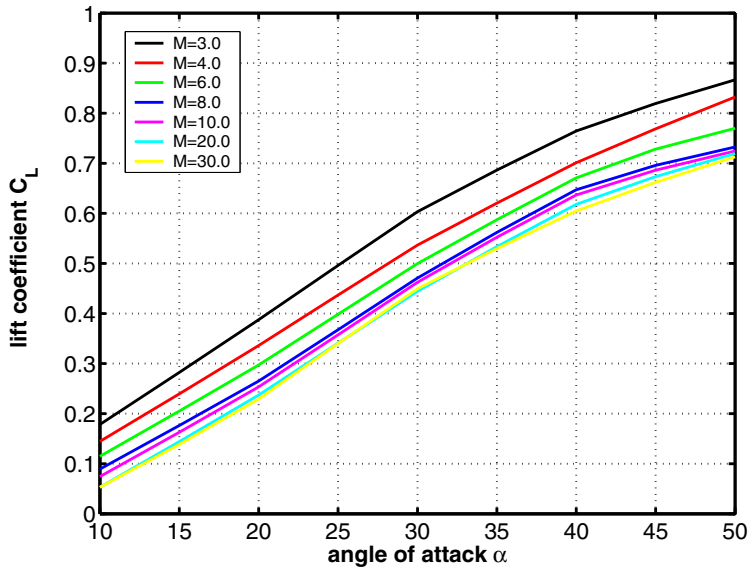


Fig. 6.158. Lift coefficient C_L as function of the angle of attack α for supersonic-hypersonic Mach numbers, [76]

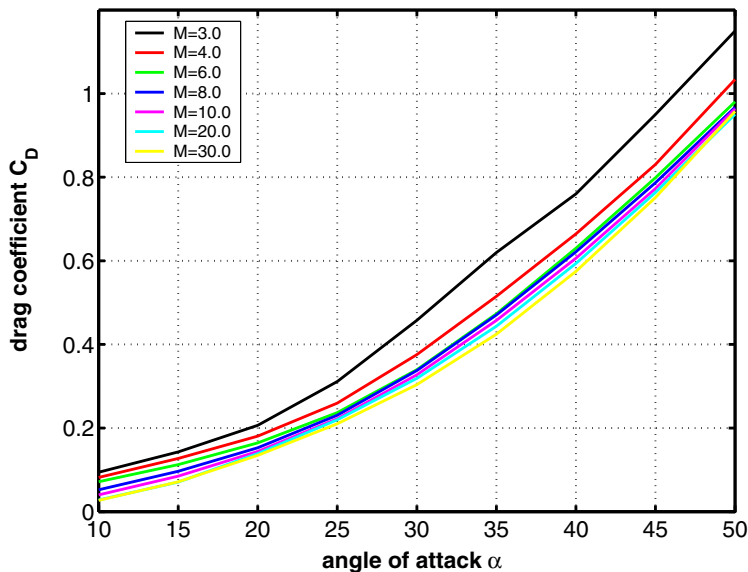


Fig. 6.159. Drag coefficient C_D as function of the angle of attack α for supersonic-hypersonic Mach numbers, [76]

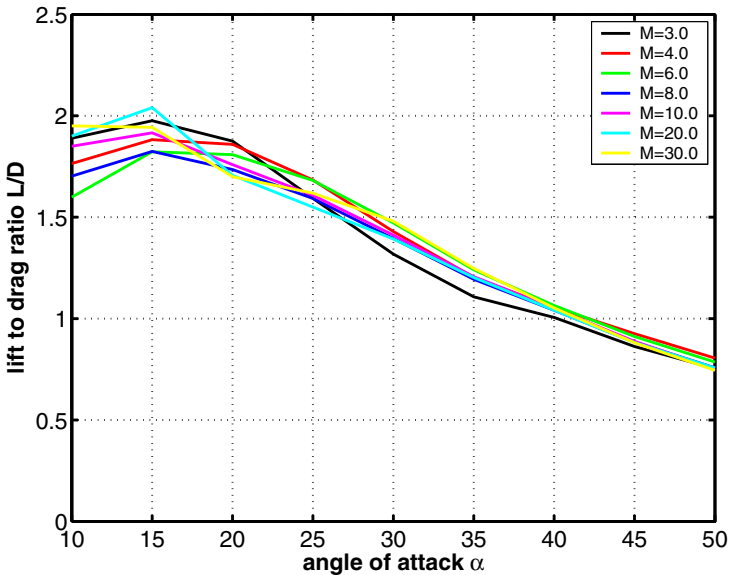


Fig. 6.160. Lift-to-drag ratio L/D as function of the angle of attack α for supersonic-hypersonic Mach numbers, [76]

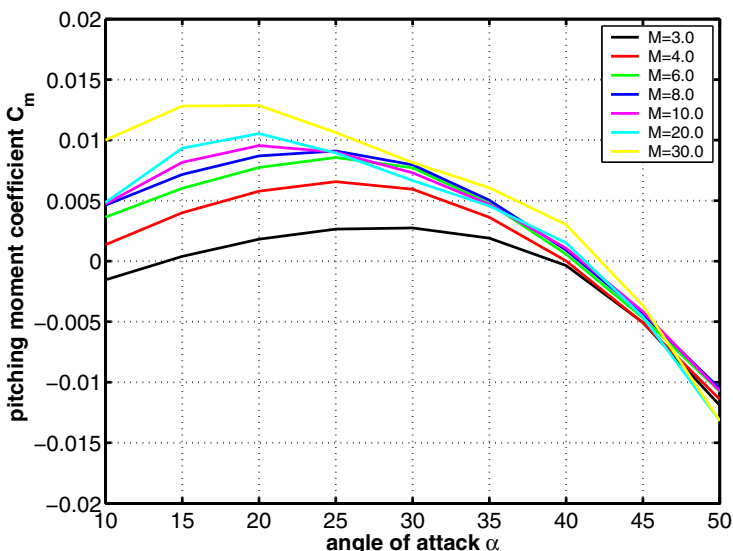


Fig. 6.161. Pitching moment coefficient C_m as function of the angle of attack α for supersonic-hypersonic Mach numbers, moment reference point $x_{ref} = 0.6 L_{ref}$, [76]

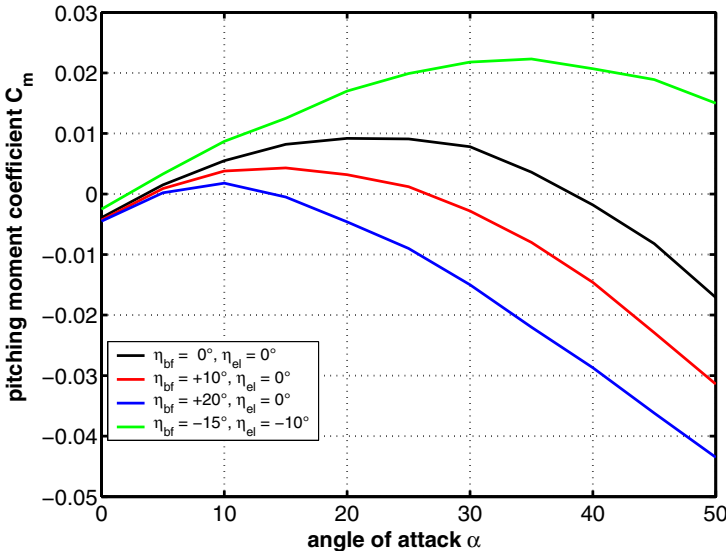


Fig. 6.162. Pitching moment coefficient C_m as function of the angle of attack α . Body flap and elevon efficiency for $M_\infty = 10$. Moment reference point $x_{ref} = 0.6 L_{ref}$, [76].

whereby, as mentioned above, the pressure force in the aft part of the configuration is reduced which causes a pitch up effect. For these Mach numbers in this way a trimmed flight of the HERMES configuration is possible, Fig. 6.164.

Lateral Motion

subsonic-supersonic regime

The rolling moment and the yawing moment per degree of the sideslip angle β are shown in Figs. 6.165 and 6.166. The roll motion is damped throughout almost the whole subsonic-supersonic Mach number and angle of attack range and that all the more if α increases. The yawing moment indicates static stability only beyond angle of attack values $\alpha \gtrsim 15^\circ$. Fig. 6.167 displays the side force as function of the sideslip angle β .

supersonic-hypersonic regime

Also in the supersonic-hypersonic regime roll motion is damped ($\partial C_l / \partial \beta < 0$), where the diagram shows also the begin of the Mach number independency (or very weak dependency) with increasing hypersonic Mach number, Fig. 6.168. The yaw stability is somewhat more critical for high Mach numbers and is obviously only attained at high angles of attack, e.g., $M_\infty = 30 \Rightarrow \alpha \gtrsim 48^\circ$,

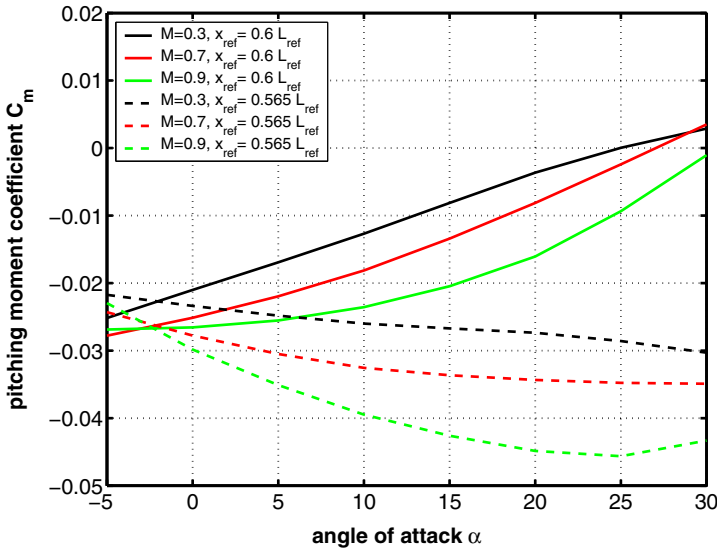


Fig. 6.163. Pitching moment coefficient C_m as function of the angle of attack α for three subsonic Mach numbers. Comparison of the nominal moment reference point $x_{ref} = 0.6 L_{ref}$ with the forward shifted moment reference point $x_{ref} = 0.565 L_{ref}$, [76].

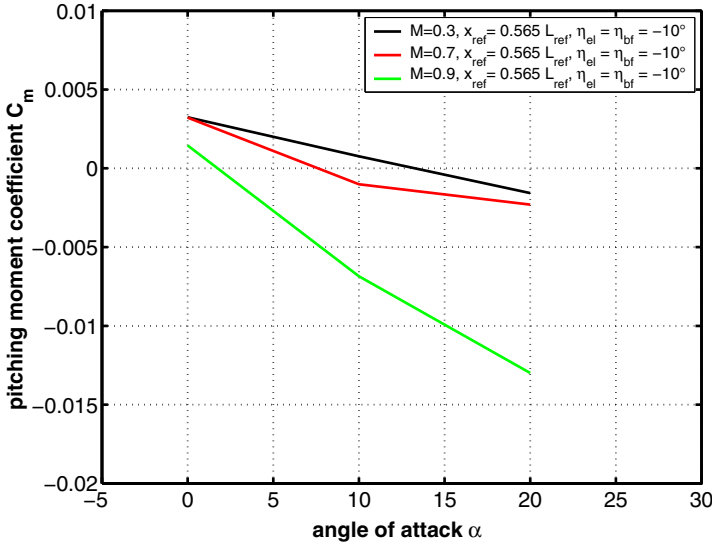


Fig. 6.164. Pitching moment coefficient C_m as function of the angle of attack α for three subsonic Mach numbers. Body flap deflection $\eta_{bf} = -10^\circ$, elevon deflection $\eta_{el} = -10^\circ$. Moment reference point $x_{ref} = 0.565 L_{ref}$, [76].

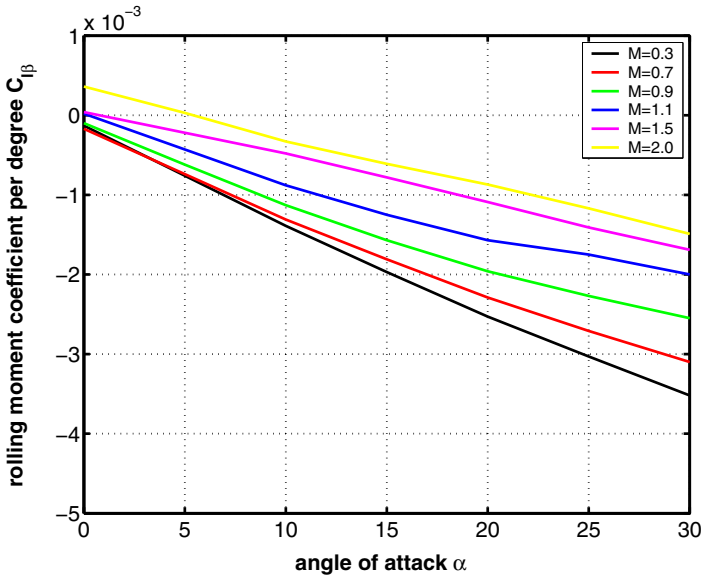


Fig. 6.165. Rolling moment coefficient per degree $C_{l\beta}$ as function of the angle of attack α . Subsonic-supersonic Mach numbers, [76].

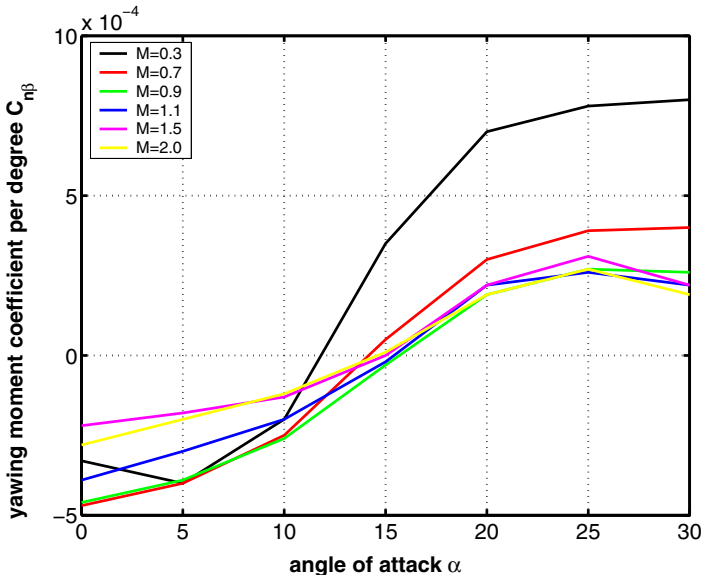


Fig. 6.166. Yawing moment coefficient per degree $C_{n\beta}$ as function of the angle of attack α . Moment reference point $x_{ref} = 0.6 L_{ref}$. Subsonic-supersonic Mach numbers, [76].

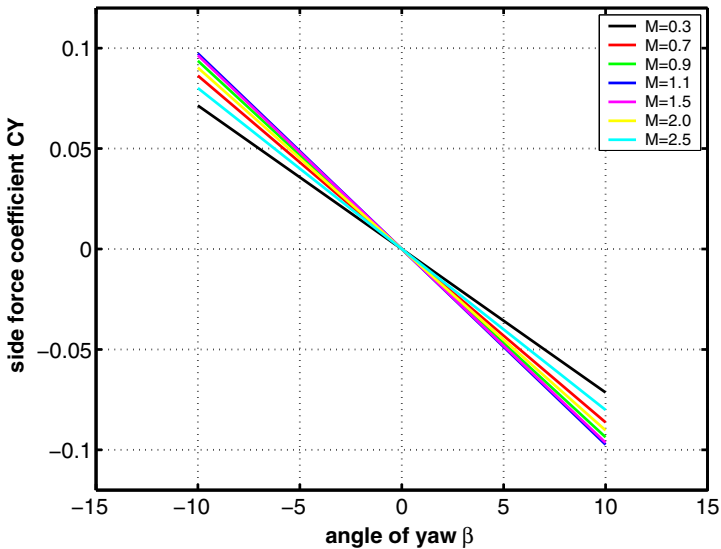


Fig. 6.167. Side force coefficient C_Y as function of the angle of the yaw β for an angle of attack $\alpha = 30^\circ$. Subsonic-supersonic Mach numbers, [76].

Fig. 6.169. Again, the side force gives a nice impression of the Mach number independency of the aerodynamic coefficients, Fig. 6.170.

6.11.3 Aerodynamic Data of Unsteady Motion

Data from the investigations of the dynamic stability are not available.

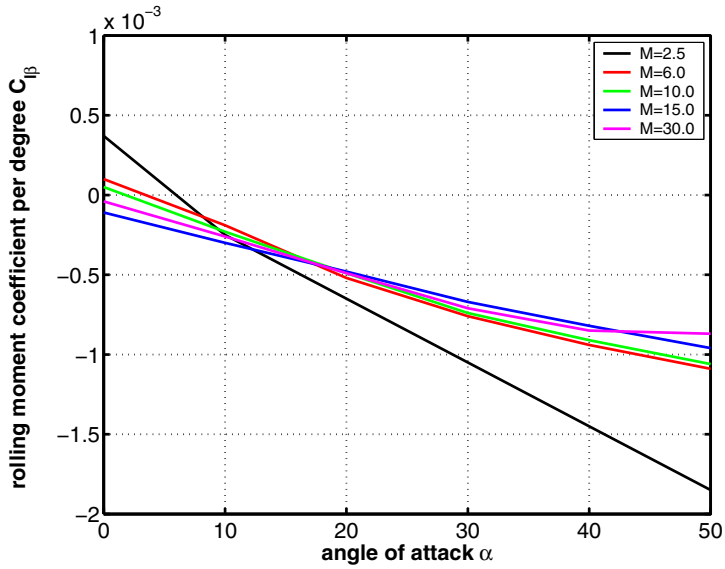


Fig. 6.168. Rolling moment coefficient per degree $C_{l\beta}$ as function of the angle of attack α . Supersonic-hypersonic Mach numbers, [76].

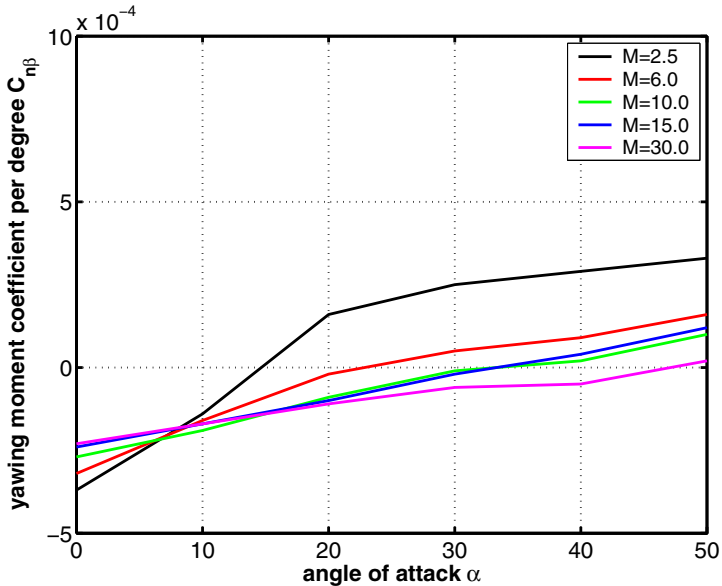


Fig. 6.169. Yawing moment coefficient per degree $C_{n\beta}$ as function of the angle of attack α . Moment reference point $x_{ref} = 0.6 L_{ref}$. Supersonic-hypersonic Mach numbers, [76].

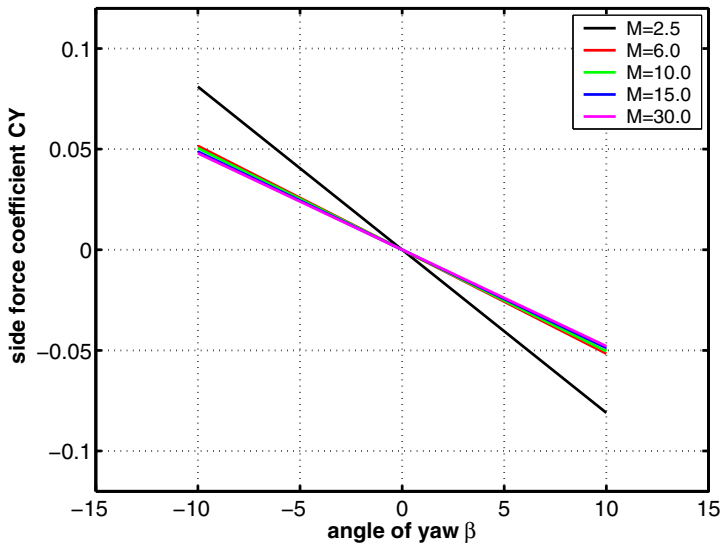


Fig. 6.170. Side force coefficient C_Y as function of the angle of yaw β for an angle of attack $\alpha = 40^\circ$. Supersonic-hypersonic Mach numbers, [76].

References

1. Arrington, J.P., Jones, J.J.: Shuttle Performance: Lessons Learned. NASA Conference Publication 2283, Part 1 (1983)
2. Throckmorton, D.A. (ed.): Orbiter Experiments (OEX) Aerothermodynamics Symposium. NASA CP-3248 (1995)
3. Isakowitz, S.J.: International Reference Guide to SPACE LAUNCH SYSTEMS. AIAA 1991 Edition (1991)
4. <http://www.dfrc.nasa.gov/gallery>
5. N.N. Aerodynamic Design Data Book - Orbiter Vehicle STS-1. Rockwell International, USA (1980)
6. Martin, L.: Aerodynamic Coefficient Measurements, Body Flap Efficiency and Oil Flow Visualization on an Orbiter Model at Mach 10 in the ONERA S4 Wind Tunnel. ONERA Report No. 8907 GY 400G (1995)
7. Griffith, B.F., Maus, J.R., Best, J.T.: Explanation of the Hypersonic Longitudinal Stability Problem - Lessons Learned. In: Arrington, J.P., Jones, J.J. (eds.) Shuttle Performance: Lessons Learned. NASA CP-2283, Part 1, pp. 347–380 (1983)
8. Brück, S., Radespiel, R.: Navier-Stokes Solutions for the Flow Around the HALIS Configuration – F4 Wind Tunnel Conditions –. DLR Internal Report, IB 129 - 96/2 (1996)
9. Hartmann, G., Menne, S.: Winged Aerothermodynamic Activities. MSTP Report, H-TN-E33.3-004-DASA, Dasa, München/Ottobrunn, Germany (1996)
10. Hirschel, E.H., Weiland, C.: Selected Aerothermodynamic Design Problems of Hypersonic Flight Vehicles, vol. 229. Springer, Heidelberg; Progress in Astronautics and Aeronautics. AIAA, Reston (2009)
11. Iliff, K.W., Shafer, M.F.: Extraction of Stability and Control Derivatives from Orbiter Flight Data. In: Throckmorton, D. A. (ed.) Orbiter Experiments (OEX) Aerothermodynamics Symposium. NASA CP-3248, Part 1, pp. 299–344 (1995)
12. Kuczera, H., Sacher, P.: Reusable Space Transportation Systems. Springer, Heidelberg (2011)
13. N. N. Rocket Propulsion Systems. The Boeing Company - Rocketdyne Propulsion & Power, Pub. 573-A-100 New 9/99 (1999)
14. Hollis, B.R., Thompson, R.A., Berry, S.A., Horvath, T.J., Murphy, K.J., Nowak, R.J., Alter, S.J.: X-33 Computational Aeroheating/Aerodynamic Predictions and Comparisons with Experimental Data. NASA / TP-2003-212160 (2003)
15. Murphy, K.J., Nowak, R.J., Thompson, R.A., Hollis, B.R., Prabhu, R.K.: X-33 Hypersonic Aerodynamic Characteristics. AIAA-Paper 99-4162 (1999)
16. Hollis, B.R., Thompson, R.A., Murphy, K.J., Nowak, R.J., Riley, C.J., Wood, W.A., Alter, S.J., Prabhu, R.K.: X-33 Aerodynamic and Aeroheating Computations for Wind Tunnel and Flight Conditions. AIAA-Paper 99-4163 (1999)

17. Prabhu, R.K.: An Inviscid Computational Study of an X-33 Configuration at Hypersonic Speeds. NASA/CR-1999-209366 (1999)
18. Pamadi, B.N., Brauckmann, G.J., Ruth, M.J., Fuhrmann, H.D.: Aerodynamic Characteristics, Database Development and Flight Simulation of the X-34 Vehicle. AIAA-Paper 2000-0900 (2000)
19. Brauckmann, G.J.: X-34 Vehicle Aerodynamic Characteristics. J. of Spacecraft and Rockets 36(2) (March-April 1999)
20. Pamadi, B.N., Brauckmann, G.J.: Aerodynamic Characteristics and Development of the Aerodynamic Database of the X-34 Reusable Launch Vehicle. In: Proceedings 1st Int. Symp. on Atmospheric Re-entry Vehicles and Systems, Arcachon, France (1999)
21. http://www.nasa.gov/centers_marshall/news
22. Prabhu, R.K.: Inviscid Flow Computations of the Orbital Sciences X-34 Over a Mach Number Range of 1.25 to 6.0. NASA / CR-2001-210849 (2001)
23. Manley, D.J., Cervisi, R.T., Staszak, P.R.: Nasa powerpoint presentation (2001),
http://www.nasa.gov/centers_marshall/news/background/facts
24. Campbell, C.H., Caram, J.M., Li, C.P., Madden, C.B.: Aerothermodynamic environment definition for an X-23/X-24A derived assured crew return vehicle. AIAA-Paper 96-1862 (1996)
25. Tarfeld, F.: Measurement of Direct Dynamic Derivatives with the Forced-Oscillation Technique on the Reentry Vehicle X-38 in Supersonic Flow. DLR, TETRA Programme, TET-DLR-21-TN-3104 (2001)
26. Weiland, C., Longo, J.M.A., Gülhan, A., Decker, K.: Aerothermodynamics for Reusable Launch Systems. Aerospace Science and Technology 8, 101–110 (2004)
27. Longo, J.: Aerothermodynamik Endbericht. Deutsches Zentrum für Luft- und Raumfahrt DLR, TETRA Programme, TET-DLR-21-PR-3018 (2003)
28. Weiland, C.: X-38 CRV S4MA Windtunnel Test Results. Dasa, X-CRV Report, HT-TN-001/99-DASA, Dasa, München/Ottobrunn, Germany (1999)
29. Behr, R.: Hot, Radiation Cooled Surfaces. TETRA Programme, TET-DASA-21-TN-2410, Dasa München/Ottobrunn, Germany (2002)
30. Goergen, J.: CFD Analysis of X-38 Free Flight. TETRA Programme, TET-DASA-21-TN-2401, Dasa München/Ottobrunn, Germany (1999)
31. N. N. X-38 Aerodynamic Design Data Book. NASA/ESA/DLR/Dassault, Internal Meeting Report EG3-X38-ADB 0001 (October 1999)
32. Labbe, S.G., Perez, L.F., Fitzgerald, S., Longo, J.M.A., Molina, R., Rapuc, M.: X-38 Integrated Aero- and Aerothermodynamic Activities. Aerospace Science and Technology 3, 485–493 (1999)
33. Weiland, C.: Computational Space Flight Mechanics. Springer, Heidelberg (2010)
34. N.N. X-38 Data Base. Industrial communication, Dassault Aviation - NASA - European Aeronautic Defence and Space Company, EADS (1999)
35. Behr, R., Weber, C.: Aerothermodynamics - Euler Computations. X-CRV Rep., HT-TN-002/2000-DASA, Dasa, München/Ottobrunn, Germany (2000)

36. Aiello, M., Stojanowski, M.: X-38 CRV, S3MA Windtunnel Test Results. X-CRV Rep., DGT No. 73442, Aviation M. Dassault, St. Cloud, France (1998)
37. Esch, H., Tarfeld, F.: Force Measurements on a 3.3% Model of X-38, Rev.8.3 Space Vehicle in Supersonic Flow. DLR IB - 39113-99C12 (1999)
38. Giese, P., Heinrich, R., Radespiel, R.: Numerical Prediction of Dynamic Derivatives for Lifting Bodies with a Navier-Stokes Solver. In: Notes on Numerical Fluid Mechanics, vol. 72, pp. 186–193. Vieweg Verlag (1999)
39. Giese, P.: Numerical Prediction of First Order Dynamic Derivatives with Help of the Flower Code. DLR TETRA Programme, TET-DLR-21-TN-3201 (2000)
40. Daimler-Benz Aerospace Space Infrastructure, FESTIP System Study Proceedings. FFSC-15 Suborbital HTO-HL System Concept Family. EADS, München/Ottobrunn, Germany (1999)
41. Jategaonkar, R., Behr, R., Gockel, W., Zorn, C.: Data Analysis of Phoenix RLV Demonstrator Flight Test. AIAA-AFM Conference, San Francisco, AIAA-Paper 2005-6129 (2005)
42. Janovsky, R., Behr, R.: Flight Testing and Test Instrumentation of Phoenix. In: 5th European Symposium on Aerothermodynamics for Space Vehicles, ESA-SP-563 (2004)
43. Hirschel, E.H.: Basics of Aerothermodynamics, vol. 204. Springer, Heidelberg; Progress in Astronautics and Aeronautics. AIAA, Reston (2004)
44. Häberle, J.: Einfluss heißer Oberflächen auf aerothermodynamische Flugeigenschaften von HOPPER/PHOENIX (Influence of Hot Surfaces on Aerothermodynamic Flight Properties of HOPPER/PHOENIX). Diploma Thesis, Institut für Aerodynamik und Gasdynamik, Universität Stuttgart, Germany (2004)
45. N.N. PHOENIX Data Base. Internal industrial communication, EADS, München/Ottobrunn, Germany (2004)
46. N.N. PHOENIX Tests in Shock Tunnel. Private Communication between TH2 shock tunnel of University of Aachen and Dasa Munich (2002)
47. Behr, R.: CFD Computations. Private communications, EADS München / Ottobrunn, Germany (2007)
48. Behr, R.: Phoenix: Aerodynamic Data Base, Version 3.1. EADS-ST Report PHX-DP-01, EADS-ST Munich Germany (2004)
49. Etkin, B.: Dynamics of Atmospheric Flight. John Wiley & Sons, New York (1972)
50. Brockhaus, R.: Flugregelung. Springer, Heidelberg (2001)
51. N.N. HOPE-X Data Base. Industrial communication, European Aeronautic Defence and Space Company, EADS/Japanese Space Agency, NASDA (1998)
52. Tsujimoto, T., Sakamoto, Y., Akimoto, T., Kouchiyama, J., Ishimoto, S., Aoki, T.: Aerodynamic Characteristics of HOPE-X Configuration with Twin Tails. AIAA-Paper 2001-1827 (2001)
53. Behr, R., Wagner, A., Buhl, W.H.-X.: Feasibility Study. Deutsche Aerospace Dasa, DASA-TN-HOPE 001 (1999) (unpublished)

54. Barth, T.: Aerothermodynamische Untersuchungen Facettierter Raumfahrzeuge unter Wiedereintrittsbedingungen (Aerothermodynamic Investigations of Facetted Space Vehicles under Re-entry Conditions). Doctoral Thesis, Institut für Thermodynamik der Luft- und Raumfahrt, Universität Stuttgart (2010)
55. Eggers, T., Longo, J.M.A., Turner, J., Jung, W., Horschgen, M., Stamminger, A., Gülan, A., Siebe, F., Requart, G., Laux, T., Reimer, T., Weihs, H.: The SHEFEX Flight Experiment -Pathfinder Experiment for a Sky Based Test Facility-. AIAA-Paper 2006-7921 (2006)
56. Weihs, H., Turner, J., Longo, J.M.A., Gülan, A.: Key Experiments within the Shefex II Mission. In: 60th International Aeronautical Congress, IAC-08-D2.6.4 (2008)
57. Eggers, T.: Project HILIFT. High Hypersonic L/D Preliminary Reference Configurations. DLR-IB 124-2009/901 (2009)
58. Ramos, R.H., Bonetti, D., De Zaiacomo, G., Eggers, T., Fossati, F., Serpico, M., Molina, R., Caporicci, M.: High Lift-to-Drag Re-entry Concepts for Space Transportation Missions. AIAA-Paper 2009-7412 (2009)
59. Hirschel, E.H., Weiland, C.: Design of hypersonic flight vehicles: some lessons from the past and future challenges. CEAS Space Journal 1(1), 3–22 (2011)
60. Russo, G., Capuano, A.: The PRORA-USV Program. ESA-SP-487, pp. 37–48 (2002)
61. Rufolo, G.C., Roncioni, P., Marini, M., Borrelli, S.: Post Flight Aerodynamic Analysis of the Experimental Vehicle PRORA USV 1. AIAA-Paper 2008-2661 (2008)
62. Rufolo, G.C., Roncioni, P., Marini, M., Votta, R., Palazzo, S.: Experimental and Numerical Aerodynamic Data Integration and Aerodatabase Development for the PRORA-USV-FTB-1 Reusable Vehicle. AIAA-Paper 2006-8031 (2006)
63. Borrelli, S.: Private communication (2013)
64. Borrelli, S., Marini, M.: The Technology Program in Aerothermodynamics for PRORA-USV. ESA-SP-487, pp. 49 - 57 (2002)
65. Serpico, M., Schettino, A.: Preliminary Aerodynamic Performance of the PRORA-USV Experimental Vehicle. ESA-SP-487, pp.183–1900 (2002)
66. Russo, G.: The USV Advanced Re-entry Experimental Flying Laboratories. In: Proceedings: 4th Int. Symp. of Atmospheric Re-entry Vehicles and Systems (Powerpoint presentation), Arcachon (March 2005)
67. Rufolo, G.C., Marini, M., Roncioni, P., Borrelli, S.: In Flight Aerodynamic Experiment for the Unmanned Space Vehicle FTB-1. In: 1st CEAS European Air and Space Conference, Berlin, Germany (2007)
68. Roncioni, P., Rufolo, G.C., Marini, M., Borrelli, S.: CFD Rebuilding of USVDTFT1 Vehicle In-Flight Experiment. In: 59th Int. Astron. Cong., Glasgow, U.K. (2008)
69. Hirschel, E.H., Grallert, H., Lafon, J., Rapuc, M.: Acquisition of an Aerodynamic Data Base by Means of a Winged Experimental Reentry Vehicle. Zeitschrift für Flugwissenschaften und Weltraumforschung (ZFW) 16(1), 15–27 (1992)

70. <http://www.esa.int>
71. Hartmann, G., Weiland, C.: Strömungsfeldberechnungen um den HERMES Raumgleiter während der Wiedereintrittsphase. DGLR-Paper 91-223, Jahrestagung Berlin (1991)
72. Menne, S., Weiland, C., Pfitzner, M.: Computation of 3-D Hypersonic Flows in Chemical Non-Equilibrium Including Transport Phenomena. AIAA-Paper 92-2876, 1992. J. of Aircraft 31(3) (1994)
73. Monnoyer, F., Mundt, C., Pfitzner, M.: Calculation of the Hypersonic Viscous Flow Past Re-entry Vehicles with an Euler/Boundary Layer Coupling Method. AIAA-Paper 90-0417 (1990)
74. Weiland, C., Schröder, W., Menne, S.: An Extended Insight into Hypersonic Flow Phenomena Using Numerical Methods. Computer and Fluids 22 (1993)
75. Weiland, C.: Numerical Aerothermodynamics. In: Proceedings: 2nd International Symposium on Atmospheric Re-entry Vehicles and Systems, Arcachon France (2001)
76. Courty, J.C., Rapuc, M., Vancamberg, P.: Aerodynamic and Thermal Data Bases. HERMES Report, H-NT-1-1206-AMD, Aviation M. Dassault, St. Cloud, France (1991)
77. Hartmann, G., Menne, S., Schröder, W.: Uncertainties Analysis/Critical Points. HERMES Report, H-NT-1-0329-DASA, Dasa, München/Ottobrunn, Germany (1994)
78. Courty, J.C., Vancamberg, P.: Justification of the Choice of Shape 1.0. HERMES Report, H-BT-1-1003-AMD, Aviation M. Dassault, St. Cloud, France (1990)

Aerothermodynamic Data of Cruise and Acceleration Vehicles (CAV)

Most of the space vehicles which became operational or had carried out at least one demonstrator flight stem from the RV-NW vehicle class (capsules, probes, cones), Sections 4 and 5. For the more complex RV-W vehicles we know that just one object became operational, the SPACE SHUTTLE Orbiter, and some objects had undertaken demonstrator flights, Section 6. For the most complex space transportation systems, which will operate on the basis of the CAV vehicle class, either Single-Stage-To-Orbit (SSTO) or Two-Stage-To-Orbit (TSTO) systems, up to now, only system and technology studies have been and are performed. Nevertheless the future will be among the CAV based systems.

7.1 Introduction

The access to space has taken place from the beginning essentially by rocket systems. These systems have carried, – and this is true until these days –, the unmanned and manned capsules, probes and satellites. The destinations were and are various Earth's orbits, the Moon and the planets of our planetary system and their moons. Most of the parts of the rockets are expendable, which is true also for the early re-entry vehicles, viz. the capsules.

After this period of space transport the space agencies began to think about advancements regarding the philosophy and structure of space transportation.

The disadvantages of the carriage of men into space by a rocket/capsule system are as follows:

1. Take-off from a vertical launch pad requires a very long preparation.
2. The expendability of the whole system leads to very high recurring costs (refurbishment and mission operations) with the consequence that the costs for carrying payloads into space are severe.
3. The landing procedure of the capsules with their impact either on water surfaces or on rigid grounds is always critical.
4. The small cross-range capability.

The first step to overcome some of these disadvantages was taken by the development of the SPACE SHUTTLE system. However the SPACE SHUT-

TLE system maintains the disadvantage item 1. But the degree of expendability (item 2) is strongly reduced, since the Orbiter is fully reusable and the boosters are at least partly reusable. Only the tank remains expendable. Item 3 does not hold, because the Orbiter is a winged re-entry vehicle with sufficient aerodynamic performance (lift-to-drag ratio) in subsonic flight, and therefore is able to land horizontally on a suitable run way. The generation of an adequate amount of cross-range capacity is necessary for the compensation of vehicle drifts away from the destined landing ground due to critical or bad weather conditions¹ as well as due to inaccuracies or failures in the flight mechanical system. The relatively high lift-to-drag ratio of the SHUTTLE Orbiter guarantees a sufficient cross-range margin, whereby item 4 essentially is eliminated.

Since the access to space after the drop of the iron curtain more or less is only a commercial market driven business, the cost efficiency of future launch systems has highest priority. The system with the lowest costs for carrying reliably payloads into space will have the best chances to be competitive in the globalized world. Therefore space transportation systems have to be considered which eliminate the drawbacks of the systems described above.

There is no doubt about the agreement that such systems must be fully reusable and must have a horizontal landing capability, [2, 3]. Two classes of systems, viz. the Single-Stage-to-Orbit (SSTO) and the Two-Stage-to-Orbit (TSTO) vehicles, come into consideration. Both systems land horizontally, but the launch can either be vertically or horizontally. A further agreement is that the requirements on the transportation framework and on the technologies are much more challenging for the realization of a SSTO system than for a TSTO system. Therefore the next step for designing an advanced space plane, was to deal with the TSTO approach.

We discuss in the following sections² the aerodynamic data of two of such systems.

¹ Or the inaccurate knowledge of the atmospheric density at high altitude, see, e.g., [1].

² Regrettably it was only possible to present data from German TSTO studies. Data from, for instance, STAR-H, PREPHA, MIGAKS, etc., were not available.

7.2 SAENGER (Germany)

In 1986 the German ministry of research and technology decided to start a national technology activity dealing exclusively with hypersonic flight. The reason for that was to find new solutions for the access to space by using advanced space vehicles beyond the expendable rocket based concepts of capsules or the partly reusable SPACE SHUTTLE system. Therefore in 1988 the German Hypersonic Technology Program was initiated. The objectives of this program were

- the definition of a reference concept,
- the identification of technological needs,
- the establishment of a development and verification strategy,

all that for hypersonic flight, [2, 4].

Forerunner of the technology program was a study in which different possible supersonic and hypersonic flight vehicles were investigated. The reference concept of the hypersonic technology program was a Two-Stage-To-Orbit system (TSTO). Actually it was the lower stage, which was derived from the "Leitkonzept" (reference concept) of the forerunner study, [5].

One of the main attributes of a TSTO system is its horizontal take off and landing capability, which would make an operating base in Europe possible. Since the German aerospace engineer Eugen Sänger had already suggested in 1963 to develop a TSTO system as an advanced future space transportation vehicle, the reference concept of the program got the name SAENGER II (in the following referred to simply as SAENGER).

SAENGER consists of a lower and an upper stage. In the frame of the initial study phase it was planned to analyze if the lower stage could meet two different mission scenarios. On the one hand it was to serve as a transporter of the upper stage to an altitude of approximately 33 km, where the upper stage was then separated for the subsequent climb to an Earth orbit. On the other hand it was asked whether a hypersonic passenger aircraft could be derived from it. This $M_\infty = 4$ aircraft was called European Hypersonic Transport Vehicle (EHTV).

The lower stage has a trough on the upper side, where the upper stage is positioned (piggy-back situation), if the lower stage serves as upper stage transporter to space. The upper stage got the name HORUS.

Fig. 7.1 shows two synthetic images of the SAENGER system. The stage separation is illustrated with two synthetic images in Fig. 7.2. The lower stage with the through for the upper stage is seen in Fig. 7.3 left (the trough is visible also in Fig. 7.2), whereas the right part of this figure shows the configuration including HORUS. The following sections deal only with the lower stage of the SAENGER system.



Fig. 7.1. Two-Stage-to-Orbit configuration SAENGER/HORUS, synthetic images, [2, 6]



Fig. 7.2. Two-Stage-to-Orbit configuration SAENGER/HORUS, synthetic images of stage separation, [6]

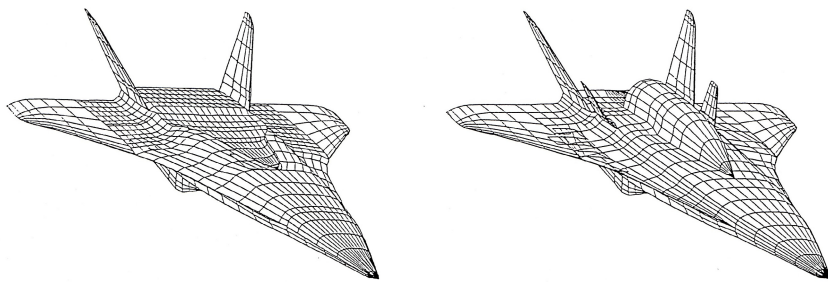


Fig. 7.3. Panel grids: SAENGER lower stage without the HORUS Orbiter (left), with the HORUS Orbiter (right), [11]

7.2.1 Configurational Aspects

A first configuration of the SAENGER lower stage was established in Aug. 1988 (configuration 8/88). The aerodynamic data set of the lower stage was generated from a large amount of wind tunnel tests, [7] - [10], solutions of approximate design methods and numerical flow field calculations for some selected trajectory points. As a result of these activities some drawbacks of the aerodynamic design of the lower stage were identified³, which led to a redesign of the shape. The engineering drawings of this enhanced shape, denoted by configuration 4/92, are displayed in Fig. 7.4. The total length of the vehicle amounts to 82.4 m, its span width is 45.2 m. The characteristics of the shape are determined by a nearly double delta wing structure with a small negative dihedral in the aft part of the wing and the distinct fuselage with a width of 14.4 m. The aerodynamic data base presented in the section below corresponds to this advanced shape. This data base was established essentially by the application of approximate design methods together with calibration procedures based on the aerodynamic data set of the 8/88 shape.

7.2.2 Aerodynamic Data of Steady Motion

The focus of our discussion regarding the aerodynamic data base is placed on the lower stage (without HORUS) of the SAENGER system. For completeness we will also present an overview about the aerodynamics of the SAENGER lower stage with HORUS.

In the frame of the European HERMES project (see Section 6.11) intensive activities were conducted in Europe, and therefore also in Germany, to bring the numerical methods for solving the Euler and Navier-Stokes) equations for flow fields past complex space vehicles to such a maturity that besides the flow details also the integral values of the forces and moments acting on the vehicles (aerodynamic coefficients) are ascertainable with high accuracy.

In Fig. 7.5 we present an example of a Navier-Stokes solution around the SAENGER lower stage. The free-stream conditions constituting a free flight situation are: $M_\infty = 4.5$, $\alpha = 6^\circ$, $Re_L = 2.6 \times 10^8$, $T_\infty = 222$ K, $H = 26$ km. The wing flaps (elevator) are deflected by $\delta = 5^\circ$ (downward). The flow was treated to be fully turbulent and the surface was to be considered as a radiation adiabatic wall with an emissivity coefficient $\varepsilon = 0.85$.

In the left part of the figure the skin-friction lines on the leeward side including the trough area are shown, the middle part presents the numerical grid and the right part exhibits the radiation adiabatic wall temperatures and again the skin friction lines. The skin-friction lines indicate over the wings an incipient flow separation forming the well known lee-side vortices of delta wing shapes. Further at the lateral boundaries of the trough the

³ These drawbacks did not come exclusively from the original shape, but also from the need to better integrate the propulsion system, see [1].

flow separates and again vortices are formed. High temperatures exists at the leading edges of the double delta wing and the tails as well as at the end of the trough, where the vortices coming from the trough edges impinge on the surface.

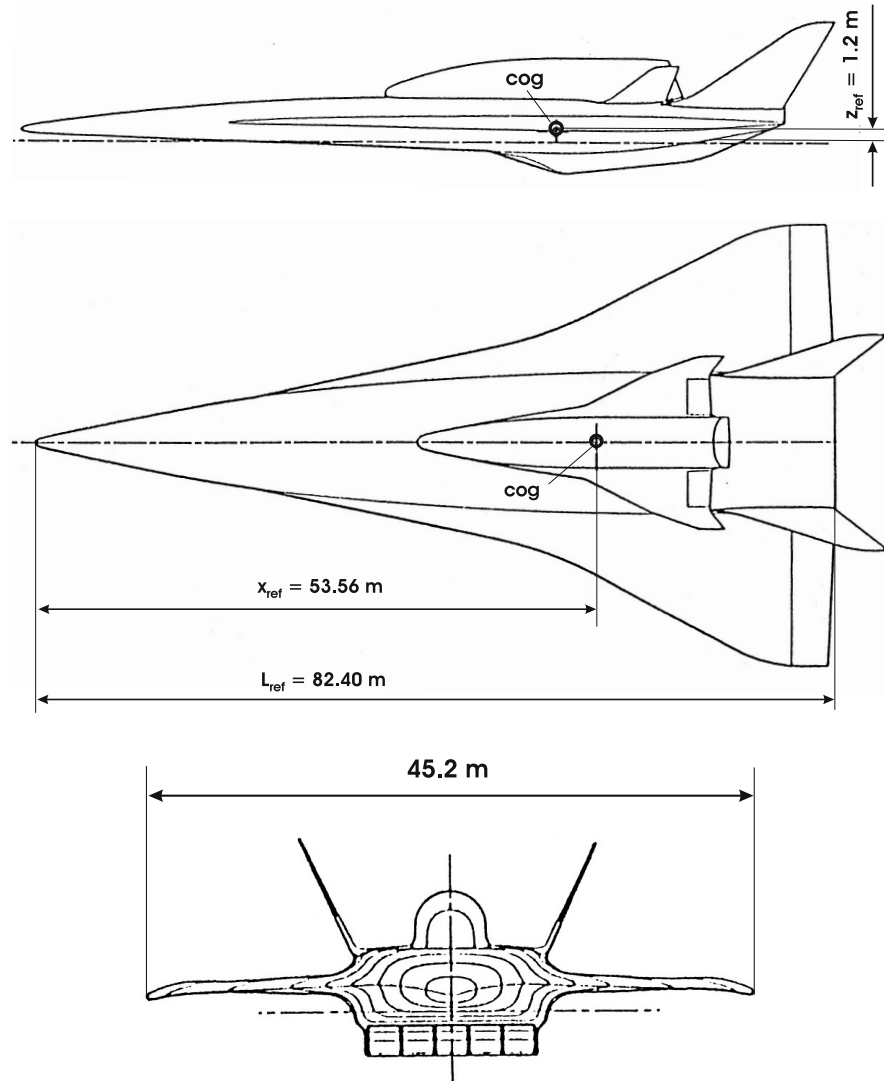


Fig. 7.4. Shape definition of the SAENGER 4/92 configuration, engineering drawings of side view (above), top view (middle) and front view (below), [11]

One of the advantages of the numerical flow field computations is that in principle every flight situation can be simulated, for example free flight conditions with various atmospheric specifications or wind tunnel conditions with similarity parameters like the Reynolds number, the Mach number or the total enthalpy, which do not meet always the free flight reality. By integration of the pressure and the shear-stress fields at the wall, as part of numerically simulated three-dimensional flow fields, for example given in Fig. 7.5, every static aerodynamic coefficient, either longitudinal or lateral, can be calculated. In our example we have listed in Table 7.1 the coefficients of longitudinal motion for one free flight trajectory point and one wind tunnel condition. The results fit very good in the aerodynamic data base discussed further below.

Table 7.1. Results of Navier-Stokes solutions past the SAENGER lower stage configuration (4/92). Flight condition 1, free-flight, fully turbulent flow: $M_\infty = 4.5$, $\alpha = 6^\circ$, $Re_L = 2.6 \times 10^8$, $T_\infty = 222$ K, $H = 26$ km, $\delta = 5^\circ$, [12]. Flight condition 2, wind tunnel, laminar flow: $M_\infty = 6.83$, $\alpha = 6^\circ$, $Re_L = 0.403 \times 10^6$, [10].

	C_L	C_D	L/D	C_m
$M_\infty = 4.5$, $Re_L = 2.6 \times 10^8$ Flight condition 1	0.06490	0.01200	5.425	- 0.00147
$M_\infty = 6.83$, $Re_L = 0.403 \times 10^6$ Flight condition 2	0.04668	0.01362	3.426	- 0.00157

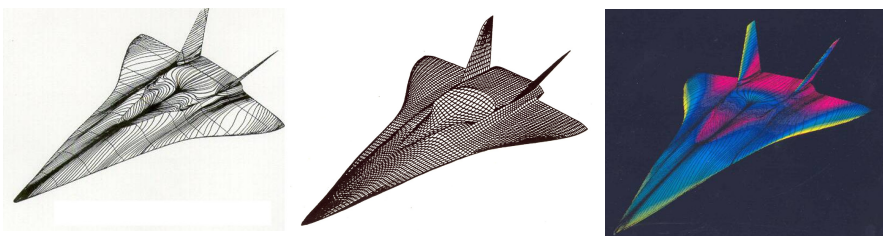


Fig. 7.5. Flow field investigations of the SAENGER lower stage. Numerical flow field simulation (Navier-Stokes solution) with free-stream conditions $M_\infty = 4.5$, $\alpha = 6^\circ$, $Re = 2.6 \times 10^8$, $T_\infty = 222$ K, $H = 26$ km, fully turbulent. Skin-friction lines at the leeward side including the trough area (left), numerical surface grid (middle), skin-friction lines and surface temperatures at the leeward side (right), [12] - [14].

The space mission of a TSTO system requires the separation of the upper stage from the lower stage at a prescribed trajectory point. This procedure is shown in a more illustrating way in [2]. Fig. 7.6 exhibits the stage separation model mounted in the hypersonic wind tunnel H2K of the DLR, Cologne Germany, [16].

The prediction of the aerodynamic behavior of the two stages of the SAENGER system during stage separation is a very challenging task, since strong interactions occur between the flow fields of the two stages. The main interactions come from the shock waves and the vortices. Fig. 7.7 shows left a wind tunnel test, [16], and right the corresponding three-dimensional numerical solution, [17]. The agreement of the flow field structures is evident.

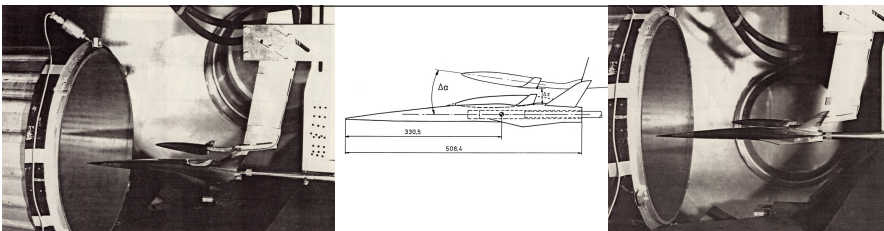


Fig. 7.6. Model for the stage separation test in the hypersonic wind tunnel H2K (left, right), sketch of the stage separation procedure (middle) [15, 16]

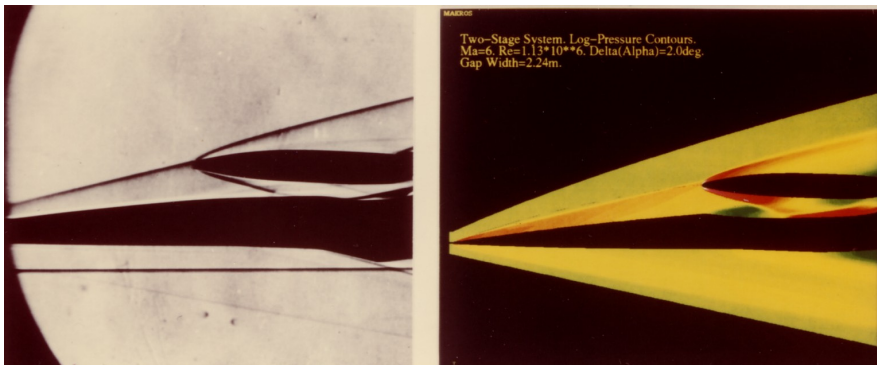


Fig. 7.7. Stage separation test in the wind tunnel (left), [15, 16], numerical simulation of the stage separation flow field (right), [17]

Longitudinal Motion

The aerodynamic coefficients of the longitudinal motion of the lower stage of the SAENGER system are depicted in Figs. 7.8 - 7.18. Note that the aerodynamic data base was established with a configuration without the propulsion system. For a discussion of the book-keeping procedure of aerodynamic and propulsion forces see [1].

The lift coefficients for the subsonic-transonic regime, plotted in Fig. 7.8, reveal a non-linear behavior, which is typical for delta wings, and is due to the formation of the lee-side vortices which reduces the magnitude of the lee-side surface pressure. For higher Mach numbers this effect vanishes and a strictly linear behavior can be observed, Fig. 7.9. Further the lift slope ($\partial C_L / \partial \alpha$) decreases beyond the transonic regime continuously with growing Mach number. The drag coefficient C_D is lowest around $\alpha \approx 0^\circ$: we have $C_{D,M_\infty=0.2,\alpha\approx0^\circ} = 0.00750$. The drag increases in the transonic regime to a local maximum with $C_{D,M_\infty=1.1,\alpha\approx0^\circ} = 0.0156$ and diminishes again in the hypersonic regime to $C_{D,M_\infty=7,\alpha\approx0^\circ} = 0.00742$. Generally, the lowest drag coefficient as function of α ensues for $M_\infty = 7$, Figs. 7.10, 7.11. It seems that Mach number independency is reached around $M_\infty \gtrsim 7$ which is somewhat later than for capsules or pure re-entry vehicles where this happens at $M_\infty \approx 5.5$.

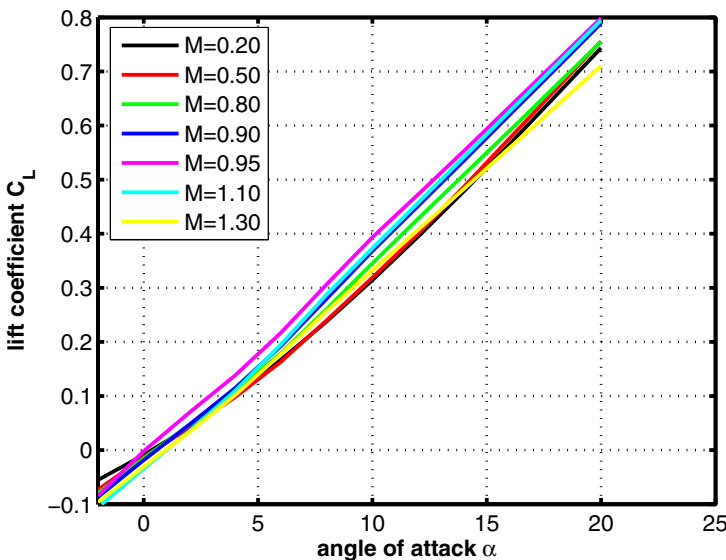


Fig. 7.8. Lift coefficient C_L as function of the angle of attack α for the subsonic-transonic Mach number regime, [11]

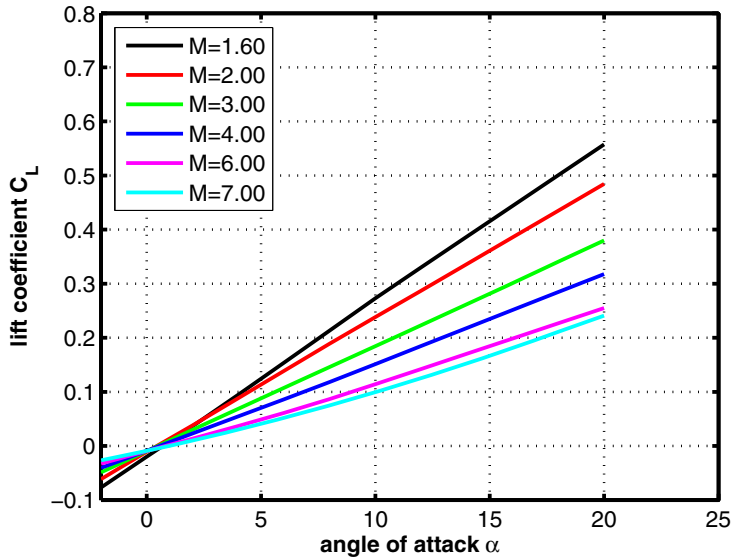


Fig. 7.9. Lift coefficient C_L as function of the angle of attack α for the supersonic-hypersonic Mach number regime, [11]

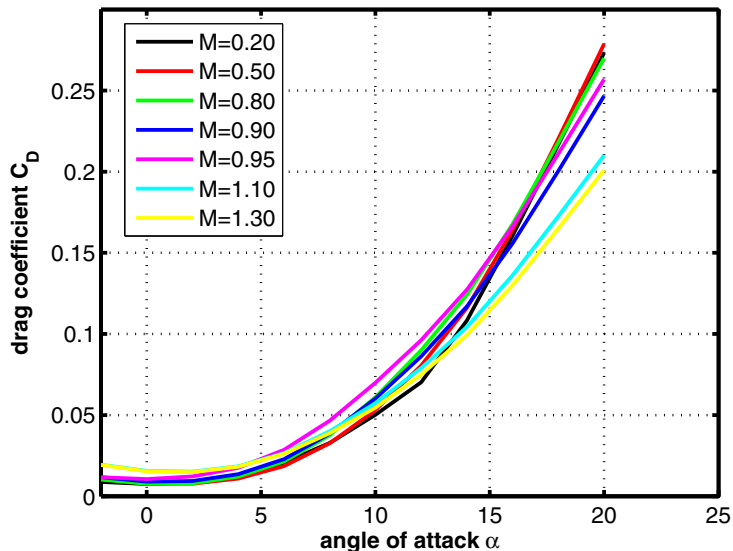


Fig. 7.10. Drag coefficient C_D as function of the angle of attack α for the subsonic-transonic Mach number regime, [11]

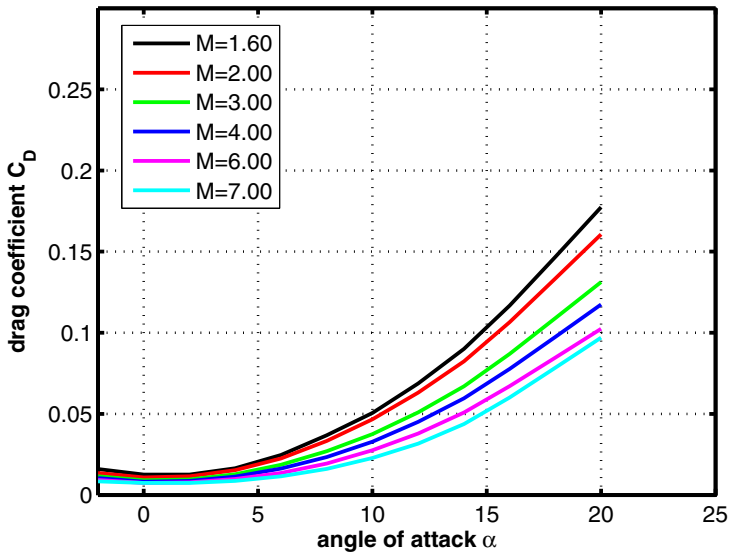


Fig. 7.11. Drag coefficient C_D as function of the angle of attack α for the supersonic-hypersonic Mach number regime, [11]

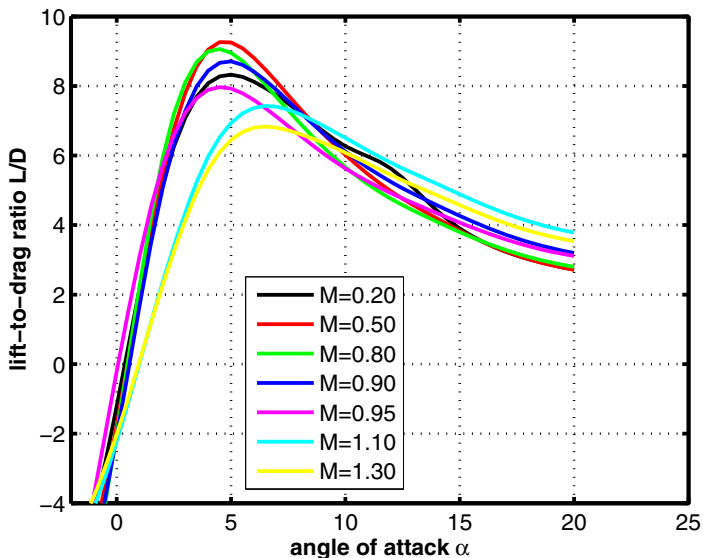


Fig. 7.12. Lift-to-drag ratio L/D as function of the angle of attack α for the subsonic-transonic Mach number regime, [11]

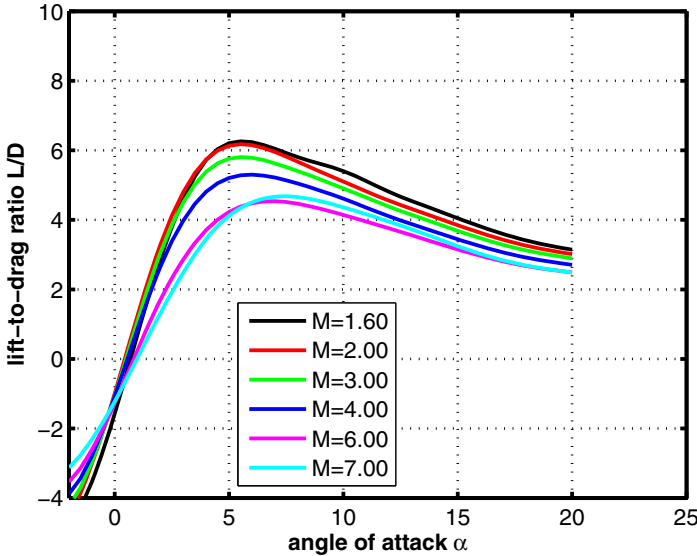


Fig. 7.13. Lift-to-drag ratio L/D as function of the angle of attack α for the supersonic-hypersonic Mach number regime, [11]

The maximum aerodynamic performance is obtained for $0.5 \leq M_\infty \leq 0.9$ and $\alpha \approx 4^\circ$ with $L/D_{max} \approx 9.5$, Fig. 7.12. This is also in contrast to the blunt capsules and re-entry vehicles where usually the maximum L/D occurs for low subsonic speeds. With growing Mach number L/D_{max} is shifted to higher angles of attack where values of around 7° are attained for hypersonic velocities ($M_\infty = 7$). There the maximum aerodynamic performance has the magnitude $L/D_{max} \approx 4.5$, Fig. 7.13.

The lower stage of the SAENGER system is longitudinal stable in the whole Mach number regime. The gradient $\partial C_m / \partial \alpha$, which is a measure for the degree of stability, has a maximum for transonic speeds and is lowest for hypersonic Mach numbers, Figs. 7.14 and 7.15. Trim for positive angles of attack obviously is not possible for the moment reference point $x_{ref} = 0.65 L_{ref}$. The pitching moment is primarily negative (pitch down effect). In order to allow for trim at an adequately positive angle of attack a pitch-up moment for all angles of attack must be generated. A shift of the moment reference point backwards reduces the pitch down moment in the case that the normal force C_Z is negative⁴. This indeed happens for angles of attack $\alpha \gtrsim 4^\circ$ to 5° . But for α values around zero degree C_Z changes sign and

⁴ Note that in the body fixed coordinate system the z-coordinate is directed downwards and the normal force C_Z is positive in this direction, Figs. 8.1 and 8.2.

becomes slightly positive. Therefore with a backward shift of x_{ref} trim cannot be attained as Figs. 7.16 and 7.17 demonstrate⁵.

The full SAENGER system, lower stage including the upper stage HORUS, has a very similar aerodynamic data base compared to the lower stage alone, Figs. 7.18 and 7.19. Nevertheless some minor differences in particular for $\alpha > 10^\circ$ remain. The lift is lower for subsonic-transonic speeds and the maximum L/D somewhat higher ($L/D_{max} \approx 9.8$). Further the pitching moment diagrams reveal a slightly reduced static stability for the full SAENGER system.

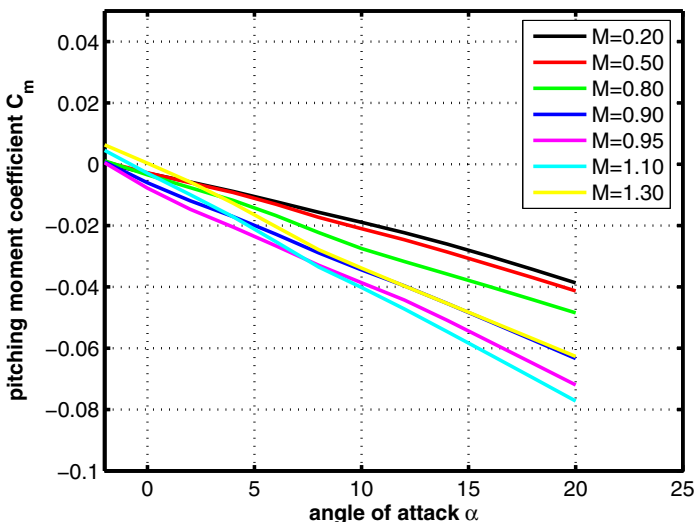


Fig. 7.14. Pitching moment coefficient C_m as function of the angle of attack α for the subsonic-transonic Mach number regime, [11]. Moment reference point $x_{ref} = 53.56\text{ m}$ ($\Rightarrow x_{ref} = 0.65 L_{ref}$), $z_{ref} = 1.2\text{ m}$.

Lateral Motion

The side force derivative $\partial C_Y / \partial \beta$ as function of Mach number is plotted in Fig. 7.20. Around sonic speed, $\partial C_Y / \partial \beta$ features a minimum and rises then again with increasing Mach number. The rolling moment derivative $\partial C_l / \partial \beta$ (roll stiffness coefficient) is always negative for the lower stage of the SAENGER system and decreases with increasing angle of attack, but

⁵ For the whole picture of course, the propulsion forces must be taken into account. Regarding longitudinal stability and trim two principally different approaches are possible: 1) autonomous airframe trim, 2) integrated airframe/propulsion trim, [18].

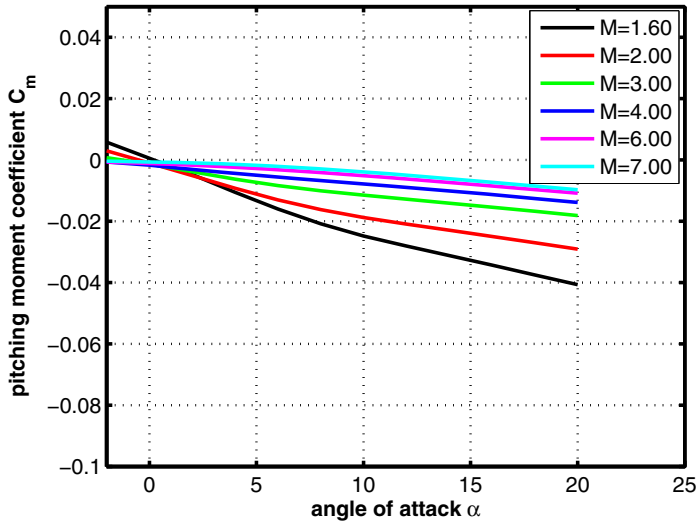


Fig. 7.15. Pitching moment coefficient C_m as function of the angle of attack α for the supersonic-hypersonic Mach number regime, [11]. Moment reference point $x_{ref} = 53.56 \text{ m}$ ($\Rightarrow x_{ref} = 0.65 L_{ref}$) , $z_{ref} = 1.2 \text{ m}$.

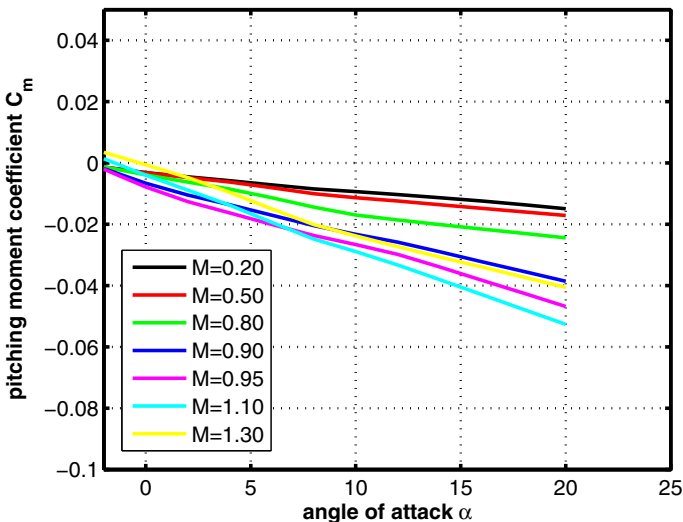


Fig. 7.16. Pitching moment coefficient C_m as function of the angle of attack α for the subsonic-transonic Mach number regime. The moment reference point has been shifted to $x_{ref} = 0.68 L_{ref}$ compared to Fig. 7.14.

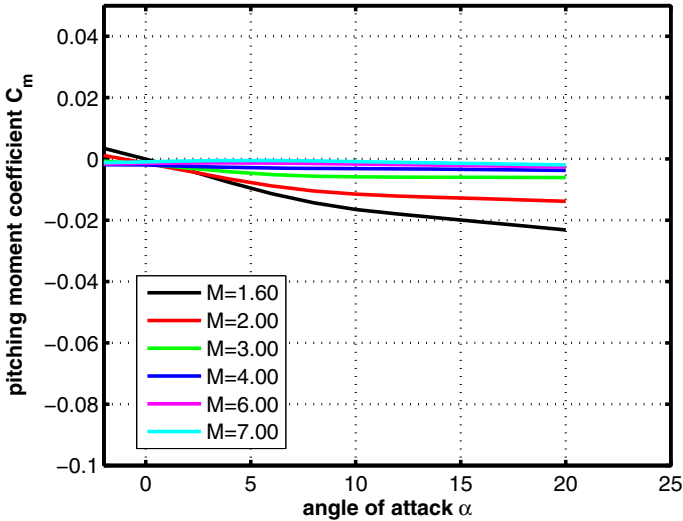


Fig. 7.17. Pitching moment coefficient C_m as function of the angle of attack α for the supersonic-hypersonic Mach number regime. The moment reference point has been shifted to $x_{ref} = 0.68 L_{ref}$ compared to Fig. 7.15.

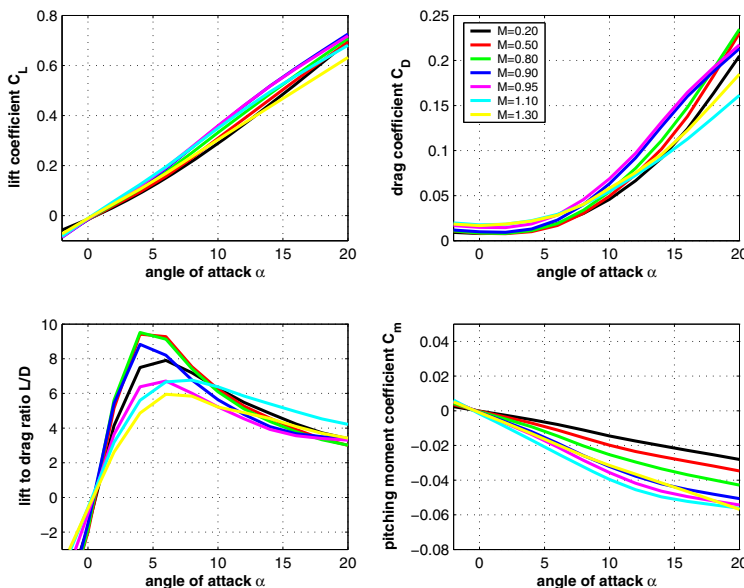


Fig. 7.18. Longitudinal motion of the SAENGER configuration with HORUS. Subsonic-transonic Mach numbers. Moment reference point $x_{ref} = 0.65 L_{ref}$.

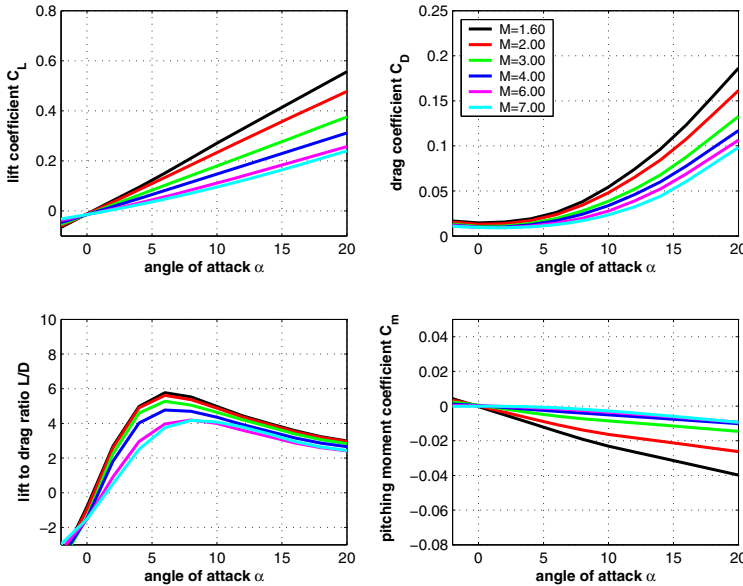


Fig. 7.19. Longitudinal motion of the SAENGER configuration with HORUS. Supersonic-hypersonic Mach numbers. Moment reference point $x_{ref} = 0.65 L_{ref}$.

increases with Mach number, Fig. 7.21. This behavior indicates that the roll motion is damped.

Directional stability is given if the yawing moment derivative $\partial C_n / \partial \beta$ (yaw stiffness coefficient) is positive, which is the case for the lower stage, where with increasing Mach number the magnitude of the stability decreases, Fig. 7.22. When an angle of yaw disturbance occurs the vehicle rotates always into the wind direction. This requires a negative side force C_Y and a line of action of this force lying behind the reference point. Both conditions are apparently true for this vehicle.

7.2.3 Aerodynamic Data of Unsteady Motion

Data of dynamic stability investigations are not available.

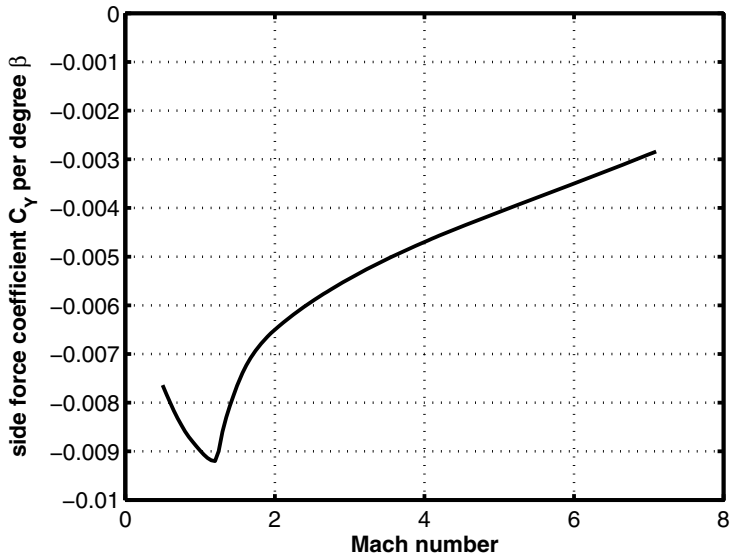


Fig. 7.20. Side force coefficient C_Y per degree of the yaw angle β as function of Mach number, [11]

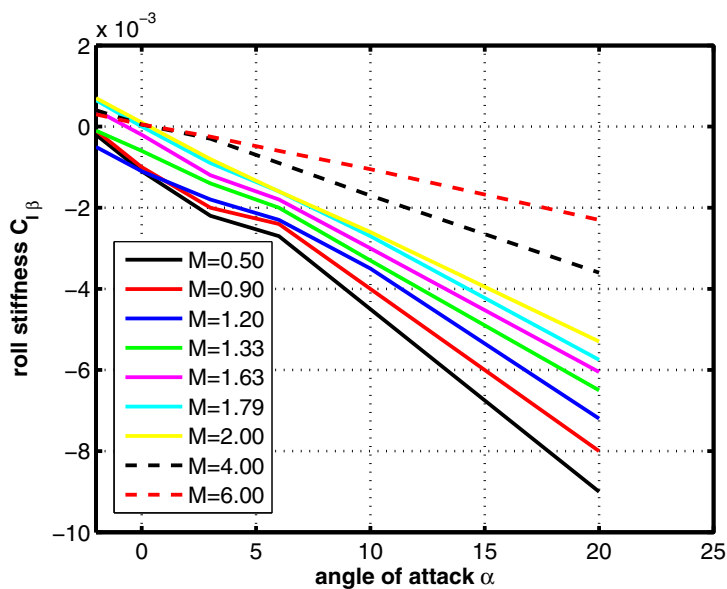


Fig. 7.21. Roll stiffness coefficient $\partial C_l / \partial \beta$ as function of the angle of attack α , [11]. Moment reference point $x_{ref} = 53.56 \text{ m}$ ($\Rightarrow x_{ref} = 0.65 L_{ref}$), $z_{ref} = 1.2 \text{ m}$.

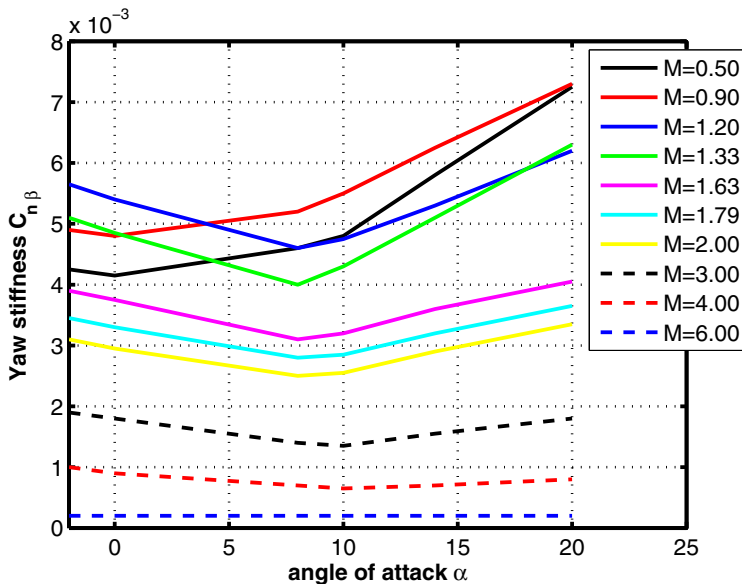


Fig. 7.22. Yaw stiffness coefficient $\partial C_n / \partial \beta$ as function of the angle of attack α , [11]. Moment reference point $x_{ref} = 53.56 \text{ m}$ ($\Rightarrow x_{ref} = 0.65 L_{ref}$), $z_{ref} = 1.2 \text{ m}$.

7.3 ELAC (Germany)

In Germany three Collaborative Research Centers (SFB), initialized 1989 by the Deutsche Forschungsgemeinschaft⁶, were established in order to bring forward the research on the basic principles necessary for a possible evolution of TSTO's. In that frame a reference concept was designed with the lower stage called ELAC (Elliptical Aerodynamic Configuration) and the upper stage called EOS (ELAC Orbital Stage), Fig. 7.23, [20].

Most of the work for establishing the aerodynamic data set was performed in wind tunnels. Fig. 7.24 shows ELAC models in the Large Low Speed Facility (LLF) of the German/Dutch organization DNW and in the shock tunnel TH2 of the RWTH Aachen. The photographs with the temperature sensitive liquid crystal image were prepared by the Institute of Aerospace Engineering at the RWTH Aachen and show the transition of the boundary layer flow from laminar to turbulent at the leeward side of the shape, Fig. 7.24, [3, 21, 22].

In the following subsections the aerodynamic data of the ELAC configuration are considered.

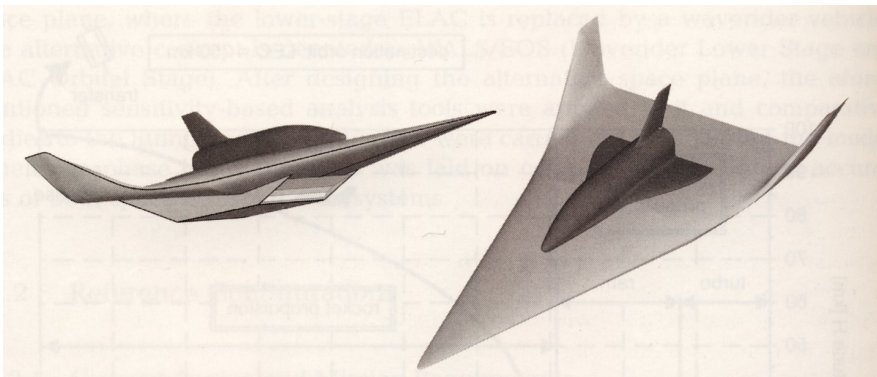


Fig. 7.23. Two-Stage-to-Orbit configuration ELAC/EOS, [20]

7.3.1 Configurational Aspects

The shape of the ELAC configuration is relatively simple, but was allowing for all research objects of the various scientific projects. It consists of a delta

⁶ The SFB's were at the RWTH Aachen, the Technical University Munich together with the University of the Armed Forces (Uni BW) and the University Stuttgart, all with participation of institutes of the German Aerospace Center (DLR), see [3, 19].

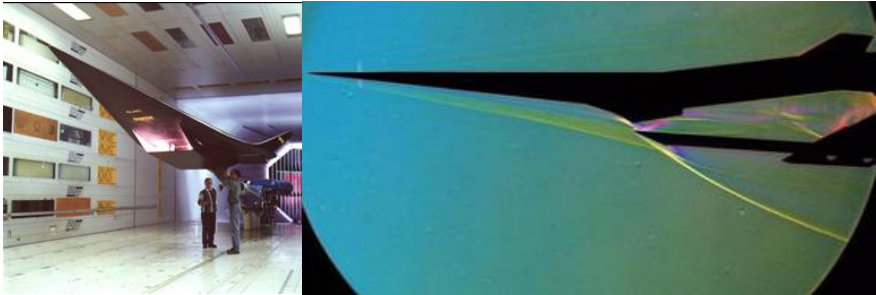


Fig. 7.24. ELAC model of 1:12 scale in the Large Low Speed Facility (LLF) of DNW, Germany/The Netherlands (left). Schlieren photograph of the ELAC model in the shock tunnel TH2 of the RWTH Aachen, [3, 22]. Test conditions $M_\infty = 7.9$, $h_o = 2.4 \text{ MJ/kg}$, $\alpha = 0^\circ$ (right).

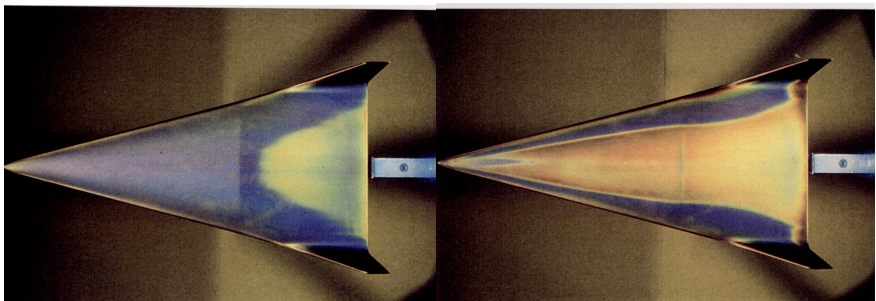


Fig. 7.25. ELAC model of 1:100 scale in the low speed wind tunnel of the Institute of Aerospace Engineering of the RWTH Aachen. Free-stream velocity $V_\infty = 50 \text{ m/s}$, $Re = 2.42 \cdot 10^6$. Temperature sensitive liquid crystal photographs on the leeward side visualizing the laminar-turbulent transition process (blue \Rightarrow laminar flow; yellow/green \Rightarrow turbulent flow). Angle of attack $\alpha = 0^\circ$ (left), angle of attack $\alpha = 4^\circ$ (right), [21].

wing form featuring rounded leading edges and a sweep angle of 75° . The reference length amounts to 72 m and the span to 38.6 m. The aspect ratio is 1.1. The cross-sections are made up of two half ellipses with an axis ratio of 1.4 for the upper part and 1.6 for the lower part of the shape. The maximum thickness of 5.36 m is reached at two thirds of the body length, [20, 21, 23]. Fig. 7.26 shows the engineering drawings of the ELAC configuration.

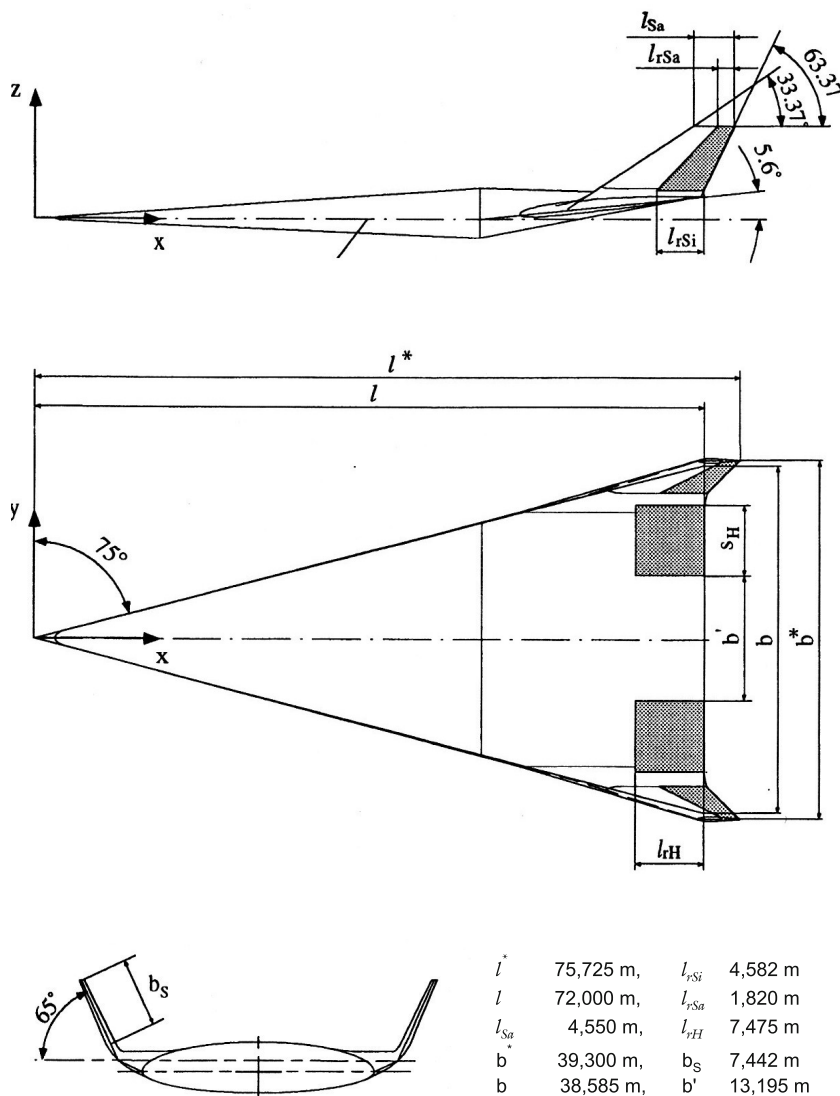


Fig. 7.26. Shape definition of ELAC configuration, engineering drawings with dimensions, [21]

7.3.2 Aerodynamic Data of Steady Motion

The aerodynamic data base of the ELAC configuration was essentially established by tests in wind tunnels. The Mach numbers covered the range from very low supersonic ($M_\infty < 0.1$) to hypersonic ($M_\infty = 7.9$) ones. Particular attention was payed to low subsonic flow ($M_\infty \approx 0.145$). There, intensive scientific work was conducted in order to reveal the effect of the Reynolds number on the surface pressure distributions and the aerodynamic coefficients. The investigated Reynolds numbers in the low speed regime range between $3.7 \cdot 10^6 \leq Re \leq 40 \cdot 10^6$, [21, 23, 24].

Longitudinal Motion

As mentioned above for the low speed regime wind tunnel experiments, but also numerical flow field computations were performed in order to investigate the influence of the Reynolds number on the longitudinal and lateral aerodynamic coefficients. The outcome of this investigation was that of course a slight Reynolds number dependency in this Mach number regime exists, but this does not change the general characteristics of the aerodynamic behavior of the ELAC configuration.

In the following four figures (Figs. 7.27 - 7.30) the aerodynamic coefficients with respect to the low speed regime ($M_\infty \approx 0.145$) are presented. The lift coefficient C_L shows the typical behavior of a delta wing, where a moderate non-linearity is generated when due to increasing angle of attack lee-side vortices arise, Fig. 7.27. Figs. 7.28 shows the drag coefficient C_D . The minimum drag value with $C_D \approx 0.007$ ensues around $\alpha \approx 3^\circ$. The aerodynamic performance L/D reaches its maximum with $L/D \approx 11$ for an angle of attack $\alpha \approx 8^\circ$, Figs. 7.29.

Static stability is secured for the longitudinal movement as the pitching moment diagram shows, Fig. 7.30. Moreover, for the moment reference point of $x_{ref} = 0.5 L_{ref}$ the vehicle can be trimmed at $\alpha \approx 4^\circ$. Interesting is the change of the gradient $\partial C_m / \partial \alpha$ at $\alpha \approx 10^\circ$ of the pitching moment. A possible explanation could be the incipient generation of the leeward side vortices, which cause this pitch-up of the vehicle.

The next four figures (Figs. 7.31 - 7.34) show the aerodynamic coefficients for the Mach number range $0.40 \leq M_\infty \leq 7.9$. These data were found by tests in the wind tunnel of the RWTH Aachen ($M_\infty = 0.4, 0.6, 0.83, 1.5, 2, 2.50$), the wind tunnel of the Institute of Theoretical and Applied Mechanics (ITAM) of the Russian Academy of Science in Novosibirsk ($M_\infty = 6$) and the shock tunnel TH2 of the RWTH Aachen ($M_\infty = 7.9$), [22, 25, 26].

The measured angles of attack lie between $-2^\circ \leq \alpha \leq 10^\circ$. All the curves of the lift coefficient show for this angle of attack regime a nearly linear behavior, which means that the generation of the leeward side vortices do not play a role yet. The general tendency for delta wing like configurations is, that $\partial C_L / \partial \alpha$ increases from subsonic speed on to a maximum at transonic

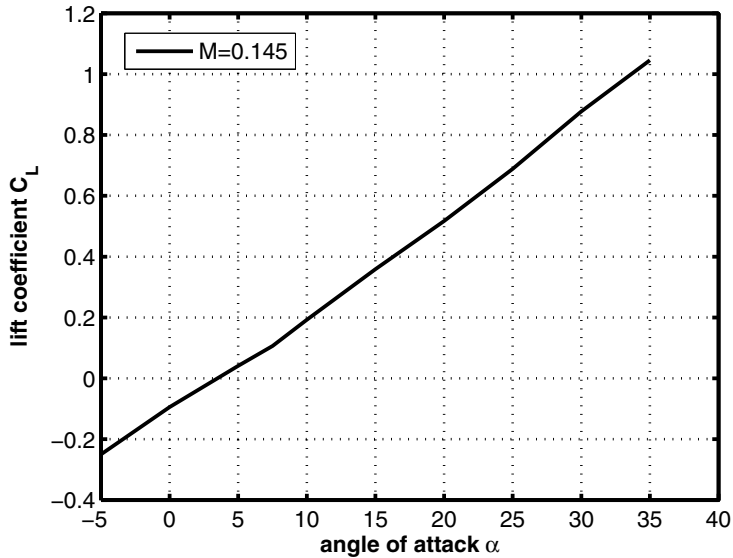


Fig. 7.27. Lift coefficient C_L as function of the angle of attack α for the free-stream velocity $V_\infty = 50$ m/s ($M_\infty \approx 0.145$), $Re = 3.7 \cdot 10^6$, [21, 23]

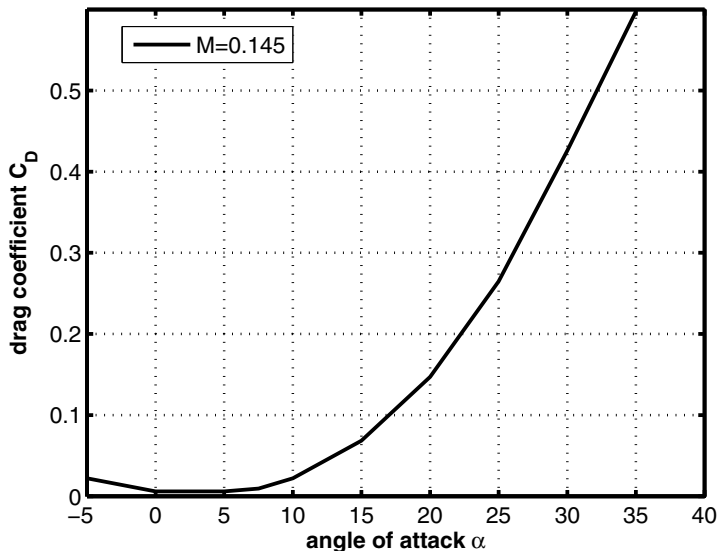


Fig. 7.28. Drag coefficient C_D as function of the angle of attack α for the free-stream velocity $V_\infty = 50$ m/s ($M_\infty \approx 0.145$), $Re = 3.7 \cdot 10^6$, [21, 23]

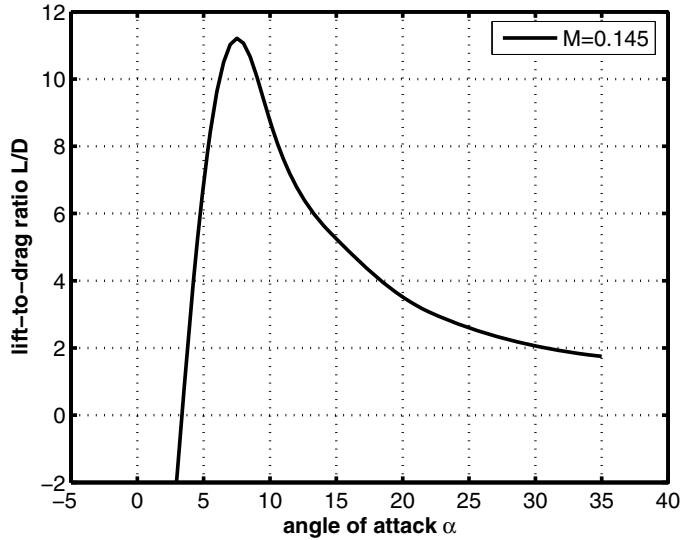


Fig. 7.29. Lift-to-drag ratio L/D as function of the angle of attack α for the free-stream velocity $V_\infty = 50$ m/s ($M_\infty \approx 0.145$), $Re = 3.7 \cdot 10^6$, [21, 23]

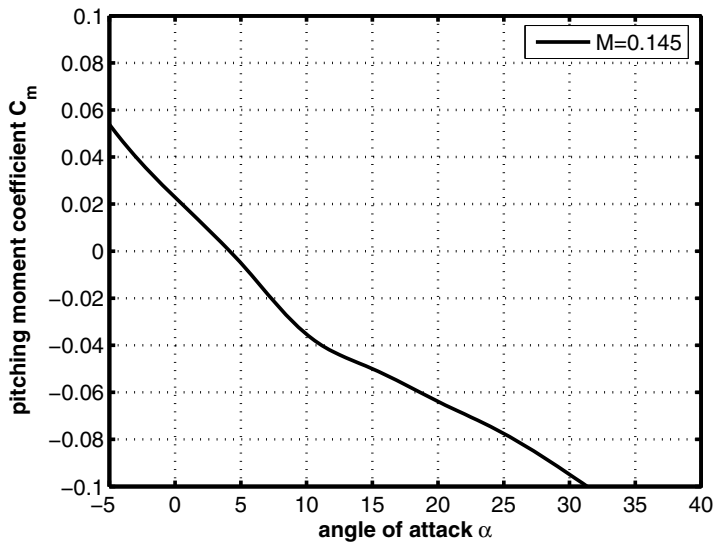


Fig. 7.30. Pitching moment coefficient C_m as function of the angle of attack α for the free-stream velocity $V_\infty = 50$ m/s ($M_\infty \approx 0.145$), $Re = 3.7 \cdot 10^6$, [21, 23]. Moment reference point $x_{ref} = 0.5 L_{ref}$.

speed in order to then decrease to a minimum at hypersonic speed, Fig. 7.31. This can also be observed for the SAENGER configuration, see Section 7.2.

For the moderate angles of attack considered here the drag coefficient C_D has relatively low values, Fig. 7.32. The minimal values occur in the angle of attack regime $1^\circ \lesssim \alpha \lesssim 4^\circ$. The lowest one with $C_D \approx 0.07$ is given for $M_\infty = 0.4$ and 0.6 at $\alpha \approx 3^\circ$, compare also with Fig. 7.28.

In subsonic flow the drag is lowest and the lift relatively high. Both has the effect that the lift-to-drag ratio L/D is highest there. It reaches a value of $L/D_{max} \approx 10.5$ at an angle of attack $\alpha \approx 7^\circ$, Fig. 7.33.

Static stability of the longitudinal motion with respect to the moment reference point $x_{ref} = 0.5 L_{ref}$ is assured for all Mach numbers, but the negative gradient of the pitching moment $\partial C_m / \partial \alpha$ decreases with increasing Mach number indicating a stability reduction, Fig. 7.34. Also trim is possible for all free-stream velocities. The trim angle of attack ranges from $\alpha \approx 2.5^\circ$ (subsonic) to $\alpha \approx 7^\circ$ (hypersonic).

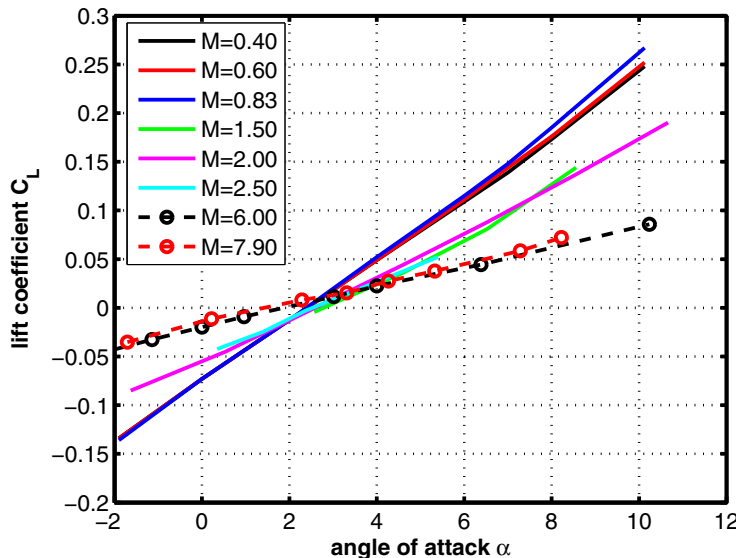


Fig. 7.31. Lift coefficient C_L as function of the angle of attack α for various Mach numbers, [22, 25]

Lateral Motion

Aerodynamic coefficients for the lateral motions are only available for subsonic speed with $V_\infty = 50$ m/s ($M_\infty \approx 0.145$), [21]. In Fig. 7.35 the side force coefficient C_Y is plotted versus the angle of yaw β . With increasing angle of

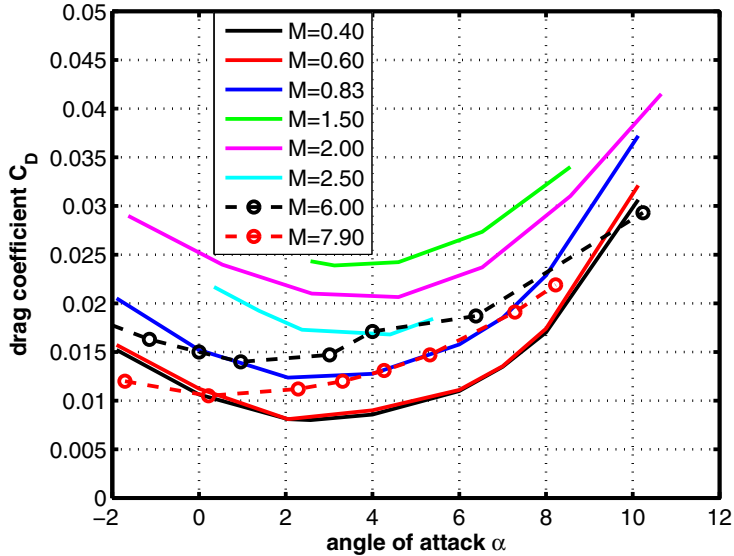


Fig. 7.32. Drag coefficient C_D as function of the angle of attack α for various Mach numbers, [22, 25]

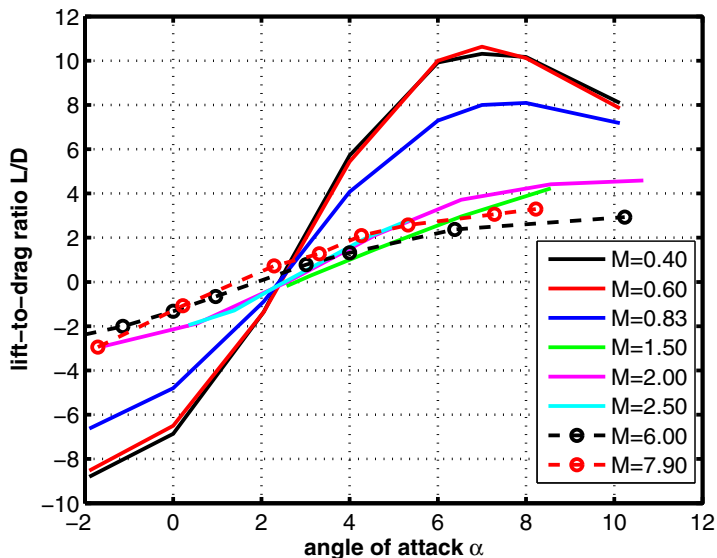


Fig. 7.33. Lift-to-drag ratio L/D as function of the angle of attack α for various Mach numbers, [22, 25]

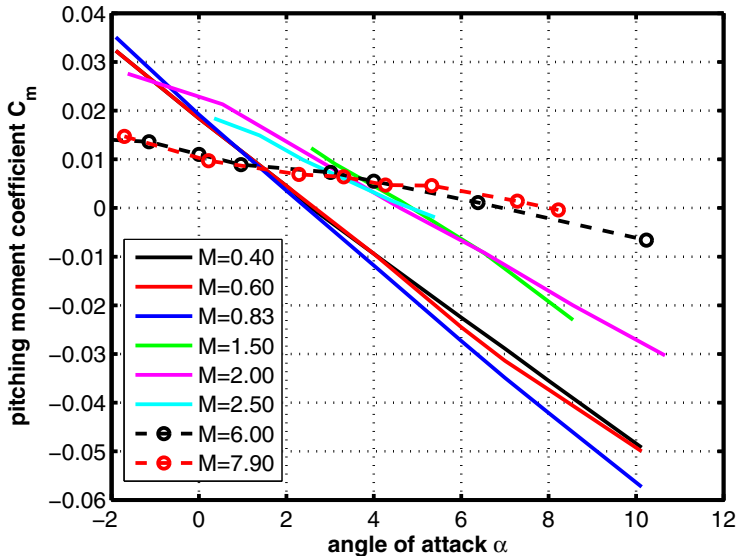


Fig. 7.34. Pitching moment coefficient C_m as function of the angle of attack α for various Mach numbers, [22, 25]. Moment reference point $x_{ref} = 0.5L_{ref}$.

yaw the negative side force increases essentially due to the different pressure distributions at the windward and the leeward sides of the fins (winglets). This effect is true for small angles of attack, as can be seen for $\alpha = 0^\circ$ and 10° . When the angle of attack rises, a second effect influencing the side force comes into play. The pressure distribution at the rearward part of the fuselage of ELAC generates due to the enforced development of the leeward side vortices a side force component, which acts in the opposite direction of the fin-induced side force, see the curve progression for $\alpha = 20^\circ$ in Fig. 7.35.

ELAC features a rolling moment C_l with a negative gradient $\partial C_l / \partial \beta$, which increases with increasing angle of attack, Fig. 7.36. Such a rolling moment behavior is desired since the vehicle after a disturbance has the tendency to automatically return to the level flight. The physical explanation is that when the body fixed x-axis and the direction of the free-stream velocity vector do not coincide (that is true when α and/or $\beta > 0$) a restoring rolling moment $C_{l\beta}\beta$ is generated, [27, 28], see also Fig. 7.37⁷.

The ELAC configuration is directional stable (weathercock stability). The diagram of the yawing moment coefficient C_n as function of the yawing angle β shows a positive gradient $\partial C_n / \partial \beta$ and only a low angle of attack dependency, Fig. 7.38. For a positive yaw stiffness coefficient $\partial C_n / \partial \beta$ the side force

⁷ Note that in this figure the moment reference point is $x_{ref} = 0.65 L_{ref}$. But this does not change substantially the rolling moment characteristics.

must be negative (Fig. 7.35) and the line of action of this force must lie behind the reference point, which apparently is given in this case. A change of the moment reference point from $x_{ref} = 0.50 L_{ref}$ to $x_{ref} = 0.65 L_{ref}$ obviously has the consequence that $\partial C_n / \partial \beta$ is no longer nearly constant, Fig. 7.39.

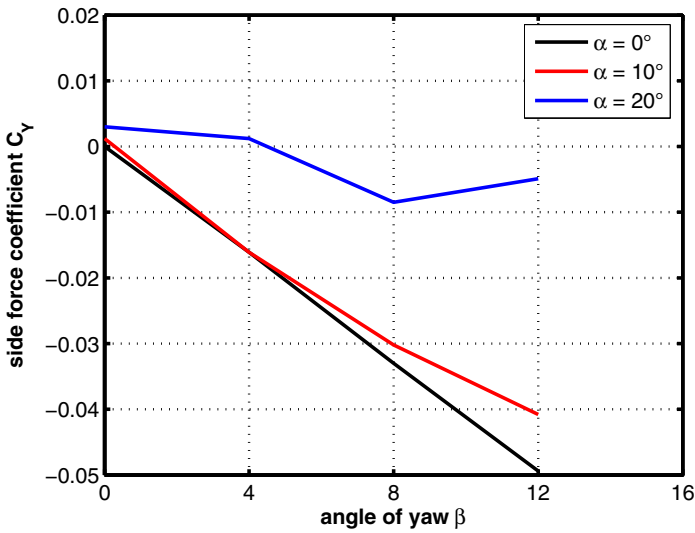


Fig. 7.35. Side force coefficient C_Y as function of the yaw angle β for three angles of attack α , [21]. Free-stream velocity $V_\infty = 50$ m/s ($M_\infty \approx 0.145$), $Re = 3.8 \cdot 10^6$.

7.3.3 Aerodynamic Data of Unsteady Motion

Data of dynamic stability investigations are not available.

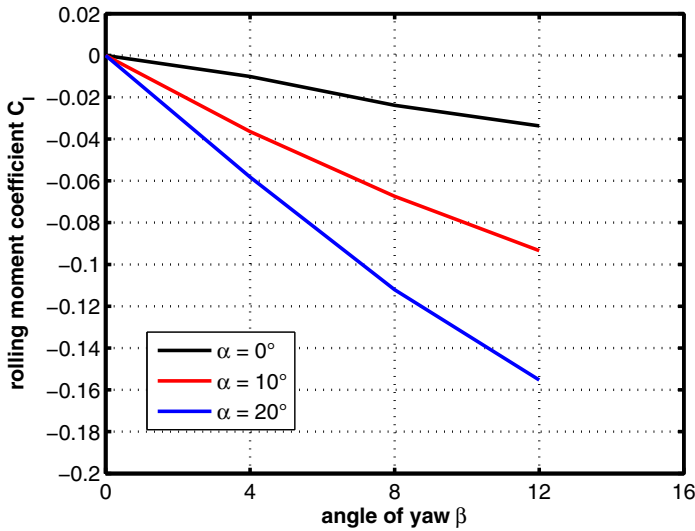


Fig. 7.36. Rolling moment coefficient C_l as function of the yaw angle β for three angles of attack α , [21]. Moment reference point $x_{ref} = 0.5 L_{ref}$. Free-stream velocity $V_\infty = 50$ m/s ($M_\infty \approx 0.145$), $Re = 3.8 \cdot 10^6$.

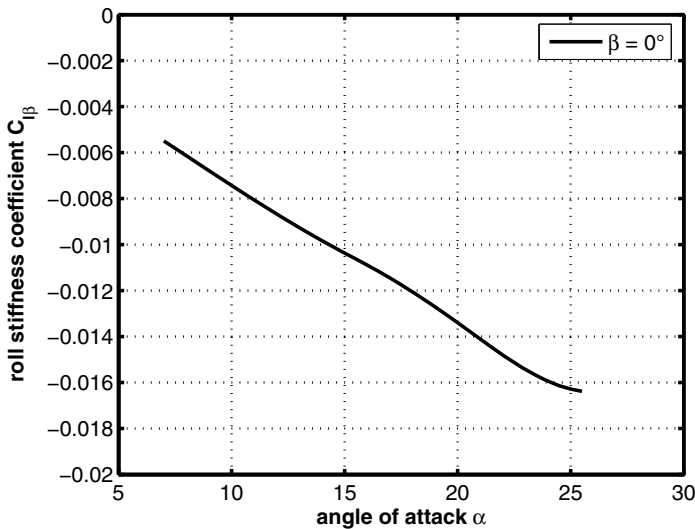


Fig. 7.37. Roll stiffness coefficient $C_{l\beta}$ in $[1/^\circ]$ as function of the angle of attack α , [21]. Moment reference point $x_{ref} = 0.65 L_{ref}$. Free-stream velocity $V_\infty = 50$ m/s ($M_\infty \approx 0.145$), $Re = 3.7 \cdot 10^6$.

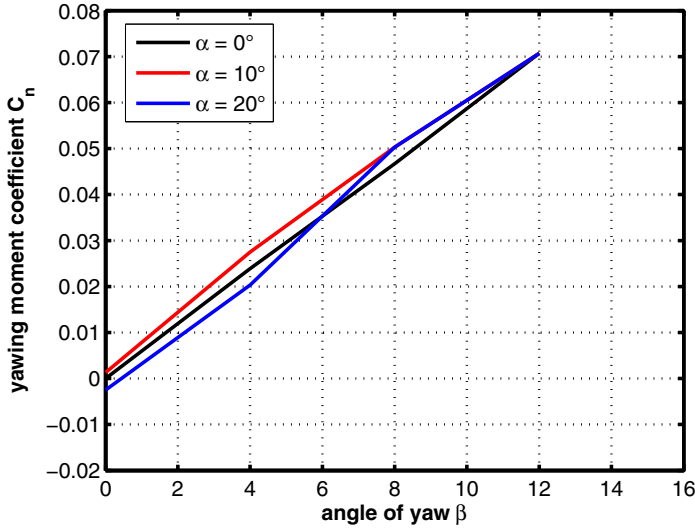


Fig. 7.38. Yawing moment coefficient C_n as function of the yaw angle β for three angles of attack α , [21]. Moment reference point $x_{ref} = 0.5 L_{ref}$. Free-stream velocity $V_\infty = 50$ m/s ($M_\infty \approx 0.145$), $Re = 3.8 \cdot 10^6$.

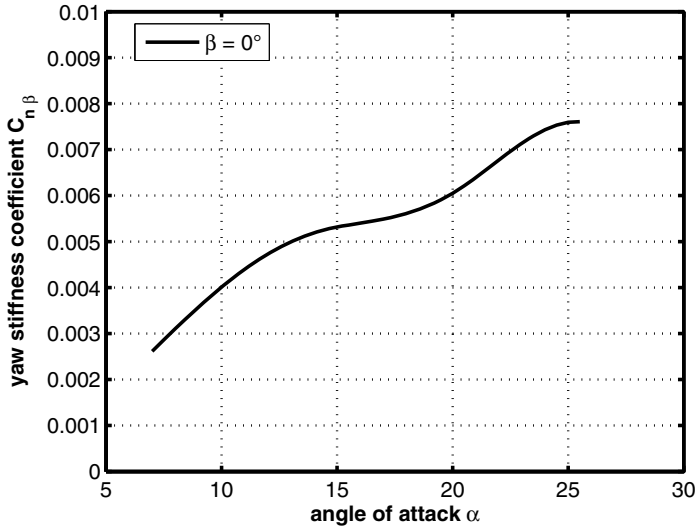


Fig. 7.39. Yaw stiffness coefficient $C_{n\beta}$ in $[1/^\circ]$ as function of the angle of attack α , [21]. Moment reference point $x_{ref} = 0.65 L_{ref}$. Free-stream velocity $V_\infty = 50$ m/s ($M_\infty \approx 0.145$), $Re = 3.7 \cdot 10^6$.

References

1. Hirschel, E.H., Weiland, C.: Selected Aerothermodynamic Design Problems of Hypersonic Flight Vehicles, vol. 229. Springer, Heidelberg; Progress in Astronautics and Aeronautics. AIAA, Reston (2009)
2. Kuczera, H., Sacher, P.: Reusable Space Transportation Systems. Springer, Heidelberg (2011)
3. Jacob, D., Sachs, G., Wagner, S. (eds.): Basic Research and Technologies for Two-Stage-To-Orbit Vehicles. Wiley-Vch-Verlag, Weinheim (2005)
4. Hirschel, E.H.: The Hypersonic Technology Development and Verification Strategy of the German Hypersonic Technology Programme. AIAA-Paper No. 93-5072 (1993)
5. Hirschel, E.H., Hornung, H.G., Mertens, J., Oertel, H., Schmidt, W.: Summary of the principal features and results of the BMFT study entitled: Determining Key Technologies as Starting Points for German Industry in the Development of Future Supersonic Transport Aircraft with a View to Possible Hypersonic Aircraft Projects. Final Report of the Study Group on Aerothermodynamics, BMFT Ref. No. LFF9694/8681 and LFF8682 (1987)
6. Kuczera, H., Krammer, P., Sacher, P.: SÄNGER and the German Hypersonic Technology Programme. IAF Congress Montreal, Paper No. IAF-91-198 (1991)
7. Krogmann, P., Schöler, H.: Windkanalversuche zur Sichtbarmachung des Strömungsfeldes und der Wärmeleitverteilung an der SÄNGER Konfiguration bei Mach 6.8. DFVLR Internal Report: IB - 222-88 C18 (1988)
8. Esch, H.: Kraftmessungen an einem 1:160 Modell des MBB - SÄNGER Konzepts im Überschall. DLR Internal Report: IB - 39113 - 89A03 (1989)
9. Esch, H.: Kraftmessungen an einem 1:160 Modell des MBB - SÄNGER Konzepts bei $Ma = 6$ im Hyperschallkanal H2K. DLR Internal Report: IB - 39113 - 89A08 (1989)
10. Esch, H.: Kraftmessungen an einem 1:160 Modell des MBB - SÄNGER Konzepts im Trisonikkanal TMK. DLR Internal Report: IB - 39113 - 90A05 (1990)
11. Kraus, M.: Aerodynamische Datensätze für die Konfiguration SÄNGER 4-92 (Aerodynamic Data Set for the SÄNGER Configuration 4-92). Technical Report: DASA-LME211-TN-HYPAC-290, Dasa, München/Ottobrunn, Germany (1992)
12. Weiland, C.: FESTIP Technology: Aerothermodynamics. Final Presentation, ESTEC Noordwijk (March 1997)
13. Schröder, W., Behr, R., Menne, S.: Analysis of Hypersonic Flow Around Space Transportation Systems via CFD Methods. AIAA-Paper No. 93-5067 (1993)
14. Schröder, W., Behr, R.: 3D Hypersonic Flow Over a Two-Stage Spacecraft. SPACE COURSE, Paper No. 14. Technical University of Munich, Germany (October 1993)
15. Weiland, C.: Stage Separation Aerothermodynamics. AGARD-R-813, pp. 11-1-11-28 (1996)

16. Esch, H.: Kraftmessungen zur Stufentrennung am MBB-SÄNGER Konzept bei $Ma = 6$ im Hyperschallkanal H2K. DLR Internal Report: IB - 39113 - 90C18 (1990)
17. Schröder, W., Mergler, F.: Investigation of the Flowfield over Parallel-Arranged Launch Vehicles. AIAA-Paper No. 93-3060 (1993)
18. Hirschel, E.H.: The Technology Development and Verification Concept of the German Hypersonic Technology Programme. Dasa-LME12-HYPAC-STY-0017-A, Dasa Ottobrunn, Germany (1995)
19. Krause, E.: German University Research in Hypersonics. AIAA-Paper 92-5033 (1992)
20. Raible, T., Jacob, D.: Evaluation and Multidisciplinary Optimzation of Two-Stage-to-Orbit Space Planes with Different Lower-Stage Concepts. In: Jacob, D., Sachs, G., Wagner, S. (eds.) Basic Research and Technologies for Two-Stage-To-Orbit Vehicles. Wiley-Vch-Verlag, Weinheim (2005)
21. Decker, F.: Experimentelle und Theoretische Untersuchungen zur Aerodynamik der Hyperschallkonfiguration ELAC-1 im Niedergeschwindigkeitsbereich (Experimental and Theoretical Investigations of the Aerodynamics of the Hypersonic Configuration ELAC-1 in Subsonic Flow). Doctoral Thesis, Institute of Aerospace Engineering, RWTH Aachen, Germany, 1996. Cuvillier Verlag, Göttingen (1997)
22. Bleilebens, M., Glössner, C., Olivier, H.: High Speed Aerodynamics of the Two-Stage ELAC/EOS-Configuration for Ascent and Re-entry. In: Jacob, D., Sachs, G., Wagner, S. (eds.) Basic Research and Technologies for Two-Stage-To-Orbit Vehicles. Wiley-Vch-Verlag, Weinheim (2005)
23. Neuwerth, G., Peiter, U., Jacob, D.: Low Speed Tests with an ELAC-Model at High Reynolds Numbers. In: Jacob, D., Sachs, G., Wagner, S. (eds.) Basic Research and Technologies for Two-Stage-To-Orbit Vehicles. Wiley-Vch-Verlag, Weinheim (2005)
24. Neuwerth, G., Peiter, U., Decker, F., Jacob, D.: Reynolds Number Effects on Low-Speed Aerodynamics of the Hypersonic Configuration ELAC 1. J. of Spacecraft and Rockets 36(2) (1999)
25. Schröder, W.: ELAC Aerodynamic Data. Private Communication, RWTH Aachen, Germany (2012)
26. Henze, A., Schröder, W., Meinke, M.: Numerical Analysis of the Supersonic Flow around Reusable Space Transportation Vehicles. ESA SP-487, pp. 191–197 (2002)
27. Etkin, B.: Dynamics of Atmospheric Flight. John Wiley & Sons, New York (1972)
28. Brockhaus, R.: Flugregelung. Springer, Heidelberg (2001)

Coordinate Systems

The coordinate systems used in aerodynamics and in flight mechanics as well as the directions in which the aerodynamic forces are counted positive, differ in the literature, but also from country to country and sometimes from aerospace company to aerospace company.

Therefore aerodynamicists and aerospace engineers have to check in each case precisely, which coordinate system is used and how the forces and moments are defined, [1] - [4].

We present in this chapter two often used coordinate frames including the definitions of the force directions. The first one is shown in Fig. 8.1 where the body-fixed coordinates x_f, y_f, z_f and the air-path coordinates x_a, y_a, z_a are plotted. In order not to overload this figure, we have drawn a second one, Fig. 8.2, with the definitions of the force coefficients C_X, C_Y, C_Z and the moment coefficients C_l, C_m, C_n in the body-fixed system and of the force coefficients C_D, C_{Y_a}, C_L in the air-path system. This frame is mostly applied to winged flight vehicles like civil and military aircraft as well as to winged space vehicles (RV-W, CAV).

The second frame, shown in Figs. 8.3 and 8.4, reflects the situation often given by the presentation of the aerodynamic data of non-winged space vehicles, like capsules, probes, blunted cones, etc. (RV-NW). As one can see the definitions in Figs. 8.3 and 8.4 are given for a negative angle of attack α . The reason is, that for capsules a positive lift can only be achieved by negative angles of attack. For the explanation of this fact see [2].

During project work the aerospace engineer often has to change between the body-fixed and the air-path systems. We know that in general this should not be a problem, but during the daily work it is frequently not clear if the signs of the various terms of the transformation equations are correct. For that reason we present for both of the above frames the transformation equations in full.

We consider the transformation of the aerodynamic coefficients C_D, C_{Y_a}, C_L of the air-path system with respect to the aerodynamic coefficients C_X, C_Y, C_Z given in the body-fixed system on the basis of the definitions in Figs. 8.1 and 8.2. A left-handed rotation around the z_a axis with the angle

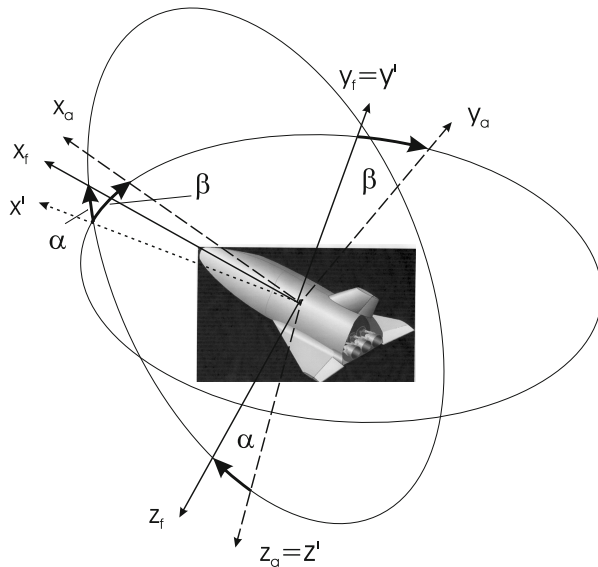


Fig. 8.1. Definition of the coordinate frame often used for winged aerospace vehicles, [2, 3]. Body-fixed system (x_f, y_f, z_f) , air-path system (x_a, y_a, z_a) .

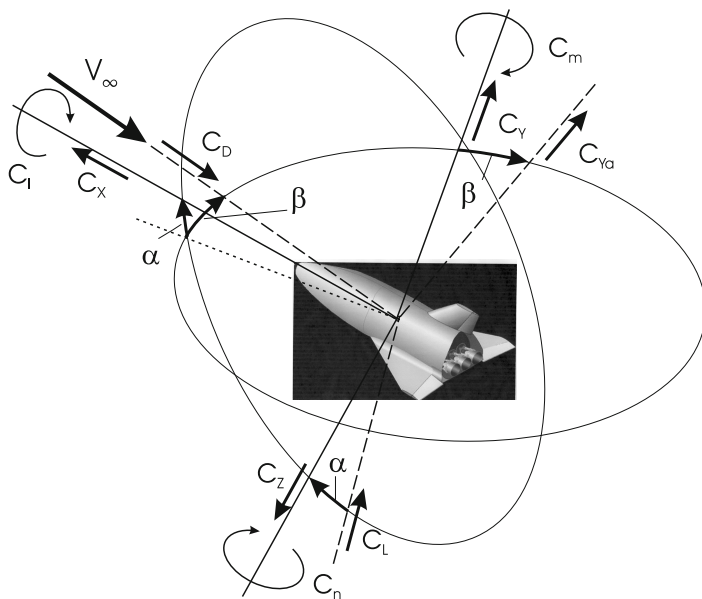


Fig. 8.2. Definition of the aerodynamic force and moment coefficients for winged aerospace vehicles with respect to the coordinate frame defined in Fig. 8.1, [2]

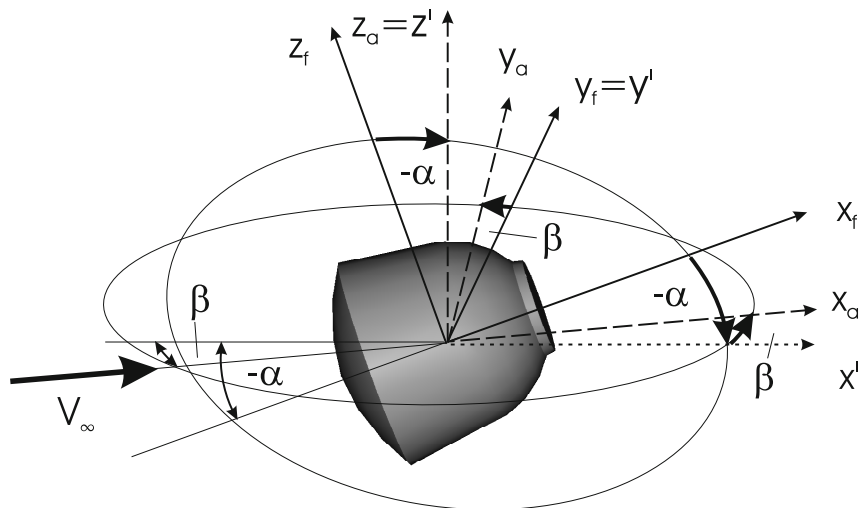


Fig. 8.3. Definition of the coordinate frame often used for non-winged space vehicles, [2]. Body-fixed system (x_f, y_f, z_f), air-path system (x_a, y_a, z_a).

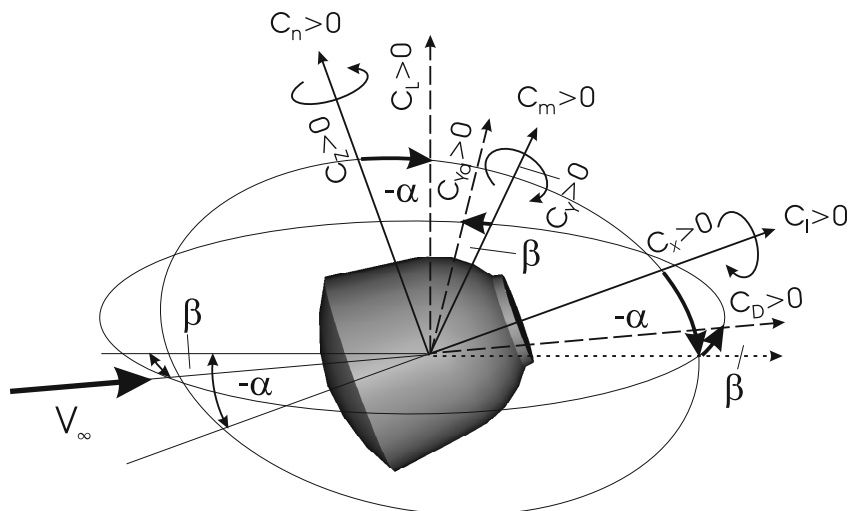


Fig. 8.4. Definition of the aerodynamic force and moment coefficients for non-winged space vehicles with respect to the coordinate frame defined in Fig. 8.3, [2].

β is followed by a right-handed rotation¹ around the $y' = y_f$ axis with the angle α . With the transformation matrix²

$$\begin{aligned} M_{ab} &= M^\alpha M^{-\beta} = \begin{pmatrix} \cos \alpha & 0 & -\sin \alpha \\ 0 & 1 & 0 \\ \sin \alpha & 0 & \cos \alpha \end{pmatrix} \begin{pmatrix} \cos \beta & -\sin \beta & 0 \\ \sin \beta & \cos \beta & 0 \\ 0 & 0 & 1 \end{pmatrix} \\ &= \begin{pmatrix} \cos \alpha \cos \beta - \cos \alpha \sin \beta & -\sin \alpha & 0 \\ \sin \beta & \cos \beta & 0 \\ \sin \alpha \cos \beta - \sin \alpha \sin \beta & \cos \alpha & \end{pmatrix}, \end{aligned}$$

we obtain the relation

$$\begin{pmatrix} C_X \\ C_Y \\ C_Z \end{pmatrix} = M_{ab} \begin{pmatrix} -C_D \\ C_{Y_a} \\ -C_L \end{pmatrix}, \quad (8.1)$$

or after resolving the eq. (8.1)

$$\begin{aligned} C_X &= -C_D \cos \alpha \cos \beta - C_{Y_a} \cos \alpha \sin \beta + C_L \sin \alpha, \\ C_Y &= -C_D \sin \beta + C_{Y_a} \cos \beta, \\ C_Z &= -C_D \sin \alpha \cos \beta - C_{Y_a} \sin \alpha \sin \beta - C_L \cos \alpha. \end{aligned} \quad (8.2)$$

The inverse of this transformation can be determined by

$$\begin{pmatrix} -C_D \\ C_{Y_a} \\ -C_L \end{pmatrix} = M_{ab}^{-1} \begin{pmatrix} C_X \\ C_Y \\ C_Z \end{pmatrix} = \begin{pmatrix} \cos \alpha \cos \beta & \sin \beta & \sin \alpha \cos \beta \\ -\cos \alpha \sin \beta & \cos \beta - \sin \alpha \sin \beta & 0 \\ -\sin \alpha & 0 & \cos \alpha \end{pmatrix} \begin{pmatrix} C_X \\ C_Y \\ C_Z \end{pmatrix}, \quad (8.3)$$

where we have made use of the orthogonality property of the matrix M_{ab} , viz. $M_{ab}^{-1} = M_{ab}^T$. Finally we obtain

$$\begin{aligned} C_D &= -C_X \cos \alpha \cos \beta - C_Y \sin \beta - C_Z \sin \alpha \cos \beta, \\ C_{Y_a} &= -C_X \cos \alpha \sin \beta + C_Y \cos \beta - C_Z \sin \alpha \sin \beta, \\ C_L &= C_X \sin \alpha - C_Z \cos \alpha. \end{aligned} \quad (8.4)$$

In the case of the coordinate frames of Figs. 8.3 and 8.4 the transformation from body-fixed to air-path coordinates reads

¹ For the definitions of right-handed and left-handed rotations see [3].

² Note that C_D and C_L are directed towards the negative x_a and z_a axes. That is the reason for the negative sign in eq. (8.1).

$$\begin{pmatrix} C_D \\ C_{Y_a} \\ C_L \end{pmatrix} = M_{ba} \begin{pmatrix} C_X \\ C_Y \\ C_Z \end{pmatrix}, \quad (8.5)$$

with

$$M_{ba} = M^\beta M^{-\alpha} = \begin{pmatrix} \cos \beta & \sin \beta & 0 \\ -\sin \beta & \cos \beta & 0 \\ 0 & 0 & 1 \end{pmatrix} \begin{pmatrix} \cos \alpha & 0 & \sin \alpha \\ 0 & 1 & 0 \\ -\sin \alpha & 0 & \cos \alpha \end{pmatrix}, \quad (8.6)$$

where M^β describes a right-handed rotation around the z' axis and $M^{-\alpha}$ a right-handed rotation around the y_f axis with the negative angle of attack $-\alpha$.

Finally we find

$$\begin{aligned} C_D &= C_X \cos \alpha \cos \beta + C_Y \sin \beta + C_Z \sin \alpha \cos \beta, \\ C_{Y_a} &= -C_X \cos \alpha \sin \beta + C_Y \cos \beta - C_Z \sin \alpha \sin \beta, \\ C_L &= -C_X \sin \alpha + C_Z \cos \alpha. \end{aligned} \quad (8.7)$$

The inverse of eq. (8.5) can be calculated by

$$\begin{pmatrix} C_X \\ C_Y \\ C_Z \end{pmatrix} = M_{ba}^T \begin{pmatrix} C_D \\ C_{Y_a} \\ C_L \end{pmatrix}, \quad (8.8)$$

$$\begin{aligned} C_X &= C_D \cos \alpha \cos \beta - C_{Y_a} \cos \alpha \sin \beta - C_L \sin \alpha, \\ C_Y &= C_D \sin \beta + C_{Y_a} \cos \beta, \\ C_Z &= C_D \sin \alpha \cos \beta - C_{Y_a} \sin \alpha \sin \beta + C_L \cos \alpha. \end{aligned} \quad (8.9)$$

Comparing eq. (8.2) with eq. (8.9) and eq. (8.4) with eq. (8.7) reveals that only the signs of some right-hand side terms are different. But just these signs sometimes cause confusions.

References

1. American National Standards Institute. Recommended Practice for Atmosphere and Space Flight Vehicle Coordinate Systems. American National Standard ANSI/AIAA R-0004-1992 (1992)
2. Hirschel, E.H., Weiland, C.: Selected Aerothermodynamic Design Problems of Hypersonic Flight Vehicles, vol. 229. Springer, Heidelberg; Progress in Astrodynamics and Aeronautics. AIAA, Reston (2009)
3. Weiland, C.: Computational Space Flight Mechanics. Springer, Heidelberg (2010)
4. Brockhaus, R.: Flugregelung. Springer, Heidelberg (2001)

Appendix A

Wind Tunnels

In the following the wind tunnels are listed, which were used for parts of the establishment of the aerodynamic data sets of the space vehicles considered in this book.

Table A.1. Wind tunnels in Germany referred to in this book

Wind tunnel	Institution	Location	Country	Flow regime	Page
TMK	DLR	Cologne	Germany	sub-,trans-, supersonic	144
H2K	DLR	Cologne	Germany	cold hypersonic	144
NWB	DLR	Braunschweig	Germany	low subsonic	235
TWG	DLR	Göttingen	Germany	sub-,trans-, low supersonic	235
HEG	DLR	Göttingen	Germany	shock tube high enthalpy	59
TH2	University of Aachen	Aachen	Germany	shock tube medium enthalpy	235 319
ILR	University of Aachen	Aachen	Germany	low subsonic	322

Table A.2. Wind tunnels in USA referred to in this book

Wind tunnel	Institution	Location	Country	Flow regime	Page
LaRC 20 Inch $M_\infty = 6$	NASA Langley	Hampton	Virginia (USA)	cold hypersonic	103, 200
LaRC 31 Inch $M_\infty = 10$	NASA Langley	Hampton	Virginia (USA)	cold hypersonic	103, 200
LaRC CF ₄ $M_\infty = 6$	NASA Langley	Hampton	Virginia (USA)	hypersonic	103, 200
LaRC 8-Foot	NASA Langley	Hampton	Virginia (USA)	transonic	112
LaRC 14-by-22 Foot	NASA Langley	Hampton	Virginia (USA)	subsonic	211
LaRC 16-Foot	NASA Langley	Hampton	Virginia (USA)	transonic	211
LaRC Unitary Plan WT	NASA Langley	Hampton	Virginia (USA)	supersonic	211
HFFAF ¹ Unitary Plan WT	NASA Ames	Mountain View	California (USA)	gun tunnel	104, 105

Table A.3. Wind tunnels in France referred to in this book

Wind tunnel	Institution	Location	Country	Flow regime	Page
S4	ONERA	Modane	France	cold hypersonic	179
F4	ONERA	Le Fauga	France	high enthalpy	59, 101

¹ HFFAF \Rightarrow Hypervelocity Free-Flight Aerodynamic Facility.

Table A.4. Wind tunnels in The Netherlands referred to in this book

Wind tunnel	Institution	Location	Country	Flow regime	Page
HST	NLR	Amsterdam	The Netherlands	sub-, trans-, low supersonic	81, 235
SST	NLR	Amsterdam	The Netherlands	supersonic	81, 235
LLF	DNW ²	Emmeloord	The Netherlands	low subsonic	235, 319

Table A.5. Wind tunnels in Russia referred to in this book

Wind tunnel	Institution	Location	Country	Flow regime	Page
T-313	ITAM	Novosibirsk	Russia	supersonic	166, 322
AT-303	ITAM	Novosibirsk	Russia	hypersonic	166, 322

Table A.6. Wind tunnel in Belgium referred to in this book

Wind tunnel	Institution	Location	Country	Flow regime	Page
S1	VKI	Brussels	Belgium	transonic	81

² DNW ⇒ is a German - Dutch organisation.

Appendix B

Abbreviations, Acronyms

ADB	Aerodynamic Data Base
AEDC	Arnold Engineering Development Center (United States)
AFE	Aeroassisted Flight Experiment (United States - Europe)
ALFLEX	Automatic Landing FLight EXperiment (Japan)
APOLLO	Capsule, first Moon landing (United States)
AOTV	Aeroassisted Orbital Transfer Vehicle
ARD	Atmospheric Re-entry Demonstrator (Europe)
ASTRA	Selected systems and technologies for future space transportation applications (Germany)
ASTV	Aeroassisted Space Transfer Vehicle
ARIANE V	Rocket launcher for heavy payloads (Europe)
BEAGLE2	Small Mars lander (Great Britain)
BURAN	Winged re-entry vehicle (Soviet Union/Russia)
CARINA	Capsule configuration of a flight demonstrator (Italy)
CAV	Cruise and Acceleration Vehicle
CFD	Computational Fluid Dynamics
CIRA	Aerospace research organization (Italy)
COLIBRI	Blunted cone configuration of a flight demonstrator (Germany)
CMC	Ceramic Matrix Composite
CRV	Crew Rescue Vehicle
CTV	Crew Transport Vehicle
DARPA	Defense Advanced Research Project Agency (United States)
DC-X	Delta Clipper EXperimental (United States)
DC-XA	Delta Clipper EXperimental Advanced (United States)
DLR	German Aerospace Center
EHTV	European Hypersonic Transport Vehicle
ELAC	TSTO technology demonstrator study (Germany)
EOS	ELAC Orbital Stage, upper stage of ELAC (Germany)
ESA	European Space Agency
ESTEC	European Space Research and Technology Center (The Netherlands)
EXPERT	European EXperimental Re-entry Testbed

FESTIP	F uture E uropean S pace T ransportation I nvestigation P rogramme
FOTON	Rocket launcher (Soviet Union/Russia)
GEMINI	Capsule configuration (United States)
GEO	Circular G eosynchronized O rbit
GNC	Guidance Navigation and C ontrol
GPS	Global Positioning S
GTO	Geostationary TO rbit
HALIS	simplified SPACE SHUTTLE Orbiter configuration
HERMES	Winged re-entry vehicle (Europe)
HOPE	H -II O rbiting P lan E (Japan)
HOPE-X	Redesigned HOPE system (Japan)
HOPPER	SSTO system concept (Europe)
HORUS	Upper stage of TSTO system SAENGER (Germany)
HOTOL	Horizontal TL concept (Great Britain)
HUYGENS	Titan probe (Europe)
HYFLEX	HFE (Japan)
HYPER-X	Testbed for scramjet demonstration flights (United States)
IBU	Inflatable BU
INKA	Configurational study of bent bicone shape (Germany)
IRDT	Inflatable Re-entry DT (Russia - Germany)
IRS	Institute for space systems, Stuttgart (Germany)
ISS	International Space Station
ITAM	Institute of Theoretical and Applied Mechanics, Novosibirsk (Russia)
JAXA	Japan's space agency (former NASDA)
KHEOPS	Configurational study in the frame of EXPERT program (Europe)
LEO	Low EO
MAJA	Subscale experimental vehicle of HERMES (Europe)
MERCURY	Capsule configuration (United States)
MIGAKS	TSTO system concept (Russia)
MIR	Space station of Soviet Union/Russia
MSRO	Mars Sample ROrbiter (Europe)
MSTP	Manned Space Transportation Programme (Europe)
MTFF	Manned Tended Free Flyer (Columbus module) (Europe)
NASA	National Aeronautics and Space Administration (United States)
NASP	National AeroSpace Plane Program (United States)
NEAT	North European Aerospace Test Range (Sweden)
NLR	National aerospace laboratory (The Netherlands)
NPO	Lavoschkin, Russian space research organization
OMS	Orbital Maneuvering System
ONERA	National aerospace research center (France)

OREX	Orbital Re-entry Experiment (Japan)
PHOENIX	Flight demonstrator for the SSTO system HOPPER (Germany)
PREPHA	TSTO system concept (France)
PRORA	Aerospace research program (Italy)
REV	Configuration as part of the EXPERT project (Europe)
RLV	Reusable Launch Vehicle
RCS	Reaction Control System
RV-NW	Re-entry Vehicle Non-Winged
RV-W	Re-entry Vehicle Winged
SAENGER	TSTO system study (Germany)
SALYUT	Space station of Soviet Union/Russia
SHEFEX	SHarp Edge Flight EXperiment (Germany)
SOYUZ	Capsule, transporter to and from ISS (Soviet Union/Russia)
SPACE – SHUTTLE	Winged re-entry vehicle (United States)
SPUTNIK	Capsule, first orbital flight (Soviet Union)
STARDUST	Space probe (United States)
STAR-H	TSTO system concept (France)
SSTO	Single-Stage-To-Orbit
TPS	Thermal Protection System
TSTO	Two-Stage-To-Orbit
TSAGI	Russian research institute for aerospace applications
TSNIIMASH	Russian aerospace research institute
USV	Unmanned Space Vehicle (Italy)
VIKING	Mars probe (United States)
VIKING-type	Capsule configuration of a system study (Europe)
VKI	von Kàrmàn institute, Brussels (Belgium)
VOLNA	Rocket launcher (Russia)
X-24A	Demonstrator vehicle (United States)
X-33	Demonstrator vehicle (United States)
X-34	Demonstrator vehicle (United States)
X-37	Demonstrator vehicle (United States)
X-38	Crew rescue vehicle for ISS (United States - Europe)
X-40	Demonstrator vehicle (United States)
X-43	Demonstrator vehicle (United States)
X-51A	Demonstrator vehicle (United States)

Name Index

- Adamov, N. P. 170
Aiello, M. 298
Akimoto, T. 119, 298
Alter, S. J. 296
An, M. Y. 118
Aoki, T. 298
Arrington, J. P. 296
- Baglioni, P. 169
Baillion, M. 119, 121
Bando, T. 119
Barth, T. 299
Behr, R. 297, 298, 331
Berry, S. A. 296
Bertin, J. J. 118
Best, J. T. 296
Blackstock, T. A. 169
Blanchet, D. 120
Bleilebens, M. 332
Bonetti, D. 299
Borrelli, S. 299
Borriello, G. 120
Bouilly, J. M. 118
Bouslog, S. A. 118, 121
Brauckmann, G. J. 297
Brockhaus, R. 21, 298, 332, 337
Brodetskay, M. D. 170
Brück, S. 296
Buhl, W. 298
Burkhart, J. 169
Burnell, S. I. 119
- Caillaud, J. 121
Campbell, C. H. 297
Caporicci, M. 299
Capuano, A. 120, 299
Caram, J. M. 118, 297
Cervisi, R. T. 297
- Chanelz, B. 120
Charbonnier, J. M. 120
Chen, Y. K. 119
Collinet, J. 119
Colovin, J. E. 121
Courty, J. C. 300
Curry, D. M. 121
- Davies, C. B. 169
De Zaiacomo, G. 299
Decker, F. 332
Decker, K. 297
Dieudonne, W. 120
- Eggers, T. 299
Erre, A. 120
Esch, H. 169, 298, 331, 332
Etkin, B. 21, 298, 332
- Felici, F. 118
Finchenko, V. 169
Fitzgerald, S. 297
Fossati, F. 299
Fraysse, H. 120
Fuhrmann, H. D. 297
Fujiwara, T. 119
- Gasbarri, P. 120
Giese, P. 298
Glößner, Ch. 332
Gockel, W. 298
Goergen, J. 297
Goodrich, W. D. 118
Graciona, J. 119
Grallert, H. 299
Griffith, B. F. 296
Gülhan, A. 297, 299
Gupta, R. N. 119

- Häberle, J. 298
 Hagmeijer, R. 119, 120
 Haidinger, F. A. 169
 Hartmann, G. 120, 296, 300
 Heinrich, R. 298
 Helms, V. T. 169
 Henze, A. 332
 Hirschel, E. H. 7, 21, 39, 118, 169,
 296, 298, 299, 331, 332, 337
 His, S. 118
 Hollis, B. R. 296
 Hornung, H. G. 331
 Hörschgen, M. 299
 Horvath, T. J. 296
 Hughes, J. E. 118
 Iliff, K. W. 296
 Inoue, Y. 119
 Isakowitz, S. J. 296
 Ishimoto, S. 298
 Ito, T. 119
 Ivanov, N. M. 118, 169
 Jacob, D. 331, 332
 Janovsky, R. 298
 Jategaonkar, R. 298
 Jones, J. J. 296
 Jones, T. V. 119
 Jung, G. 169
 Jung, W. 299
 Kassing, D. 169
 Kharitonov, A. M. 170
 Kilian, J. M. 120
 Kok, J. C. 120
 Kordulla, W. 118, 170
 Kouchiyama, J. 298
 Krammer, P. 331
 Kraus, M. 21, 331
 Krause, E. 332
 Krogmann, P. 331
 Kruse, R. L. 120
 Kuczera, H. 7, 39, 118, 296, 331
 Labbe, S. G. 297
 Lafon, J. 299
 Laux, T. 299
 Le Sant, Y. 120
 Lee, D. B. 118
 Leplat, M. 120
 Li, C. P. 297
 Liever, P. 119
 Longo, J. M. A. 297, 299
 Macret, J. L. 118
 Madden, C. B. 297
 Manley, D. J. 297
 Mansfield, A. C. 121
 Marini, M. 21, 299
 Marraffa, L. 119, 169
 Martin, L. 296
 Martino, J. C. 118
 Marzano, A. 120
 Masson, A. 120
 Matthews, A. J. 119
 Maus, J. R. 296
 Mazhul, I. I. 170
 Mazoue, F. 119
 McGhee, R. J. 120
 Mehta, R. C. 119
 Meinke, M. 332
 Menne, S. 120, 169, 296, 300, 331
 Mergler, F. 332
 Mertens, J. 331
 Micol, J. R. 120
 Midden, R. E. 169
 Miller, C. G. 169
 Molina, R. 297, 299
 Monnoyer, F. 300
 Mooij, E. 118
 Moore, R. H. 118
 Moseley, W. C. 118
 Moss, J. N. 119
 Mueller, S. R. 121
 Mundt, Ch. 300
 Murakami, K. 119
 Murphy, K. J. 296
 Muylaert, J. 118, 170
 Neuwerth, G. 332
 Northey, D. 170
 Nowak, R. J. 296
 Oertel, H. 331
 Olivier, H. 332
 Olynick, D. R. 119
 Oskam, B. 120
 Ottens, H. 170
 Palazzo, S. 21, 299

- Pallegoix, J. F. 119
 Pamadi, B. N. 297
 Paris, S. 120
 Park, C. 169
 Parnaby, G. 119
 Paulat, J. C. 118, 119, 170
 Peiter, U. 332
 Pelc, R. E. 120
 Pelissier, Ch. 290
 Perez, L. F. 297
 Pfitzner, M. 120, 169, 300
 Pilchkhadze, K. 169
 Pot, T. 120
 Prabhu, R. K. 296, 297
 Preaud, J.-Ph. 21
 Price, J. M. 119
 Radespiel, R. 296, 298
 Raible, Th. 332
 Ramos, R. H. 299
 Rapuc, M. 297, 299, 300
 Reimer, T. 299
 Requart, G. 299
 Riley, C. J. 296
 Riley, D. 170
 Rives, J. 120
 Rochelle, W. C. 121
 Rolland, J. Y. 118
 Roncioni, P. 21, 299
 Rufolo, G. C. 21, 299
 Russo, G. 299
 Ruth, M. J. 297
 Sacher, P. 7, 39, 118, 296, 331
 Sachs, G. 331, 332
 Sakamoto, Y. 298
 Sammonds, R. I. 120
 Sansone, A. 120
 Schöler, H. 331
 Schadow, T. O. 121
 Schettino, A. 299
 Schmidt, W. 331
 Schröder, W. 120, 300, 331, 332
 Scott, C. D. 121
 Serpico, M. 299
 Shafer, M. F. 296
 Siebe, F. 299
 Siemers, P. M. 120, 121
 Smith, A. J. 119, 169
 Solazzo, M. 120
 Spel, M. 120
 Stamminger, A. 299
 Staszak, P. R. 297
 Stojanowski, M. 298
 Tam, L. T. 118
 Tarfeld, F. 297, 298
 Tauber, M. E. 119
 Thompson, R. A. 296
 Throckmorton, D. A. 296
 Ting, P. C. 121
 Tournebize, F. 119
 Traineau, J. C. 120
 Tran, P. 119, 121
 Tsujimoto, T. 298
 Turner, J. 299
 Uselton, B. L. 121
 Vancamberg, Ph. 300
 Vaseniov, L. G. 170
 Venkatapathy, E. 120
 Verant, J. L. 120
 Votta, R. 21, 299
 Wagner, A. 298
 Wagner, S. 331, 332
 Walpot, L. 170
 Walther, S. 169
 Wang, K. C. 118
 Weber, C. 297
 Weihs, H. 299
 Weiland, C. 7, 21, 39, 118–120, 169,
 296, 297, 299, 300, 331, 337
 Wells, W. L. 120
 Whitlock, C. H. 121
 Wilde, D. 169
 Wong, H. 170
 Wood, W. A. 296
 Yamamoto, Y. 119
 Yates, L. A. 120
 Yoshioka, M. 119
 Zorn, Ch. 298
 Zvegintsev, V. I. 170

Subject Index

A

- Aeroassisted
 - flight 37
 - Flight Experiment 101
 - Orbital Transfer Vehicle 101
- Aeroassisted Orbital Transfer Vehicle 138
- Aerocapturing 103
- Aerodynamic
 - derivatives 14
 - model 15
 - performance 24
- Aerodynamic control
 - body flap 172, 186, 198, 202, 209, 222, 225, 243, 267, 281, 287
 - central fin 283
 - elevon 172, 186, 209, 270, 281, 287
 - flap 281
 - rudder 172, 281, 283
 - speed-brake 172
 - vertical tail 198
- Aerospike engine 173, 198, 217
- Aerospike rocket 37
- AFE 1, 26
- Air-launch 208
- Airbreathing propulsion 37
- ALFLEX 76
- APOLLO 1, 23, 26, 43, 58, 154
- Approximate design method 112, 124, 132, 305
- ARD 1, 26, 58
- ARIANE V 58, 280
- Autonomous landing 240

B

- Ballistic 24, 26

- entry 66
- factor 66
- flight 78, 159
- probe 67
- range facility 117
- Balloon 269
- Base drag 78, 273
- Base flow 270, 281
- BEAGLE2, 1, 26, 70
- BENT-BICONE 1, 30, 123, 138
- Bicone 1, 30, 123
- BLUFF-BICONE 1, 30, 123
- Boat-tailing 223
- BURAN 2, 176
 - features 172
 - system 172
- C
- Capsule 1, 24
 - features 171
- CARINA 1, 23, 26, 96
- Cassini
 - Orbiter 66
 - Saturn Orbiter 66
- Center-of-gravity 42, 50, 86, 98, 126, 133, 139, 154, 186, 225, 235, 240, 243, 244, 275
- Center-of-pressure 42, 227
- Coefficient
 - aerodynamic 10
 - aerothermodynamic 10
 - axial force C_X , 13
 - drag C_D , 13
 - lift C_L , 13
 - normal force C_Z , 13
 - pitching moment C_m , 13
 - rolling moment C_l , 13

- side force C_Y , 13
- side force C_{Ya} , 13
- yawing moment C_n , 13
- COLIBRI 1, 31, 142
- Composite structure 208
- Cone 1, 30, 123
- Coordinate system 333
 - air-path 11
 - body-fixed 11
- Coordinates
 - air-path 333
 - body-fixed 333
- Crew rescue vehicle 18, 123, 173, 220
- Crew transport vehicle 138
- Cross derivative 15
- Cross-range
 - capability 24, 30, 76, 123, 171, 220
 - capacity 302
 - margin 302
- Crossover 202

D

- DC-XA 207
- De-orbiting 149, 217, 238
- Delta wing 176, 200, 270, 282, 305, 309, 320
- Dihedral 15, 159, 202, 208, 248, 270, 305
- Drop test 76, 221
- Dynamic behavior 95, 233
- Dynamic derivative 48, 53, 57, 61
- Dynamic instability 48, 61, 117

E

- Earth
 - atmosphere 76, 103, 174
 - orbit 43, 51, 101, 103, 174
- ELAC 3, 23, 38, 319
- Emissivity coefficient 305
- Euler equations 59, 62, 81, 98, 126, 144, 151, 163, 179, 211, 221, 235, 238, 270, 281, 305
- European Hypersonic Transport Vehicle EHTV 303
- EXPERT 1, 32, 159
- Extra-terrestrial fly-by 1

F

- Facetted configuration 2, 33, 264
- FESTIP 2, 173, 235
- Flight
 - control 76, 269
 - control system 207
 - demonstration 76, 149, 166
 - demonstrator 34–36, 207, 235, 269
 - hypersonic 53, 76, 101, 123, 149, 182, 238, 269, 303
 - orbital 173, 217
 - qualification 149
 - suborbital 58, 76
 - test 208, 217, 270
- Flight
 - mechanical system 302
- Flow shadow 43, 58, 202, 209, 275, 283
- Forced oscillation technique 117
- Free oscillation technique 117

G

- GEMINI 43, 96
- Geostationary transfer orbit 179
- Geosynchronized orbit 179
- Global positioning system GPS 3, 208
- Gravity assist 66
- Guidance, navigation and control GNC 67, 76, 142, 217

H

- HALIS configuration 179
- HERMES 2, 23, 33, 58, 80, 96, 159, 172, 179, 280, 305
- HOPE 96
 - H-II Orbiting plane 76
- HOPE-X 2, 33, 172, 186, 253
- HOPPER 2, 37, 235
- HORUS 303
- HOTOL 2, 37, 173
- HUYGENS 23, 26, 66
- HYFLEX 76
- Hypersonic aircraft 303

I

- Inflatable braking unit 149

International Space Station 18, 142, 174, 220
 IRDT 1, 32, 149
 ISS 51, 96, 172

K

KHEOPS 159

L

Launch
 – costs 172
 Lift curve break 182, 211, 239
 Lifting body 173, 198, 220
 Loads
 – thermal 9
 Local inclination method 124
 Low Earth orbit 179

M

Mach number
 – independence 62, 105, 114, 127, 152, 182, 243, 287
 MAIA 280
 Mariner-Mark II Cassini 66
 Mars 111, 123
 – atmosphere 70, 112
 – express 70
 – lander 70
 – orbit 111
 – Sample Return Orbiter 101
 Mass 51, 67
 – capacity 179
 – gross 96
 – total 58, 142, 280
 MIGAKS 3
 MIR 51
 Moon
 – landing 43

N

NASP 2, 96, 173, 207
 Navier-Stokes equations 59, 64, 81, 82, 86, 98, 105, 163, 179, 200, 221, 233, 235, 238, 271, 281, 305
 Newton method 43
 – limit 273

– modified 81
 Numerical method 44, 58, 112, 281
 Numerical solution 57, 62, 86, 126, 151, 154, 200, 202, 221, 307

O

Orbital configuration 149
 Orbital Maneuvering System 174
 Orbital phase 217
 OREX 1, 26, 76
 Oryol program 3

P

Panel method 81, 124
 Parachute system 1, 25, 30, 149
 – landing 49
 Paraglider system 30, 149, 220, 223
 Payload 23, 149, 174, 198, 253
 – bay 179
 – costs 172, 173
 PHOENIX 2, 23, 33, 186, 235
 Piggy-back 96, 142, 303
 Pitch
 – damping 15, 157, 233
 PREPHA 3
 Probe 1, 24
 PRORA 2, 19, 23, 33, 269

R

Radiation
 – adiabatic wall 305
 – cooling 159
 Re-entry
 – atmospheric 269
 – capsule 142
 – configuration 264
 – demonstrator 58
 – flight 61, 159, 238, 269
 – gliding 280
 – mission 51
 – module 96
 – path 283
 – phase 78, 217
 – process 43, 49, 58, 76, 149, 174, 217, 264
 – technology 96
 – trajectory 76, 182

- vehicle 138, 222, 253
- Reaction control system RCS 171, 283
- Real gas effect 10, 59, 104, 105, 202, 238, 281
- R**Reusable
 - composite propellant tank 208
 - fully 198
 - launch vehicle 198, 207, 235
 - partly 172
 - space technology 173, 217
 - technology demonstrator 217
- Rocket 51, 96, 124, 171, 176, 253
 - aerospike motor 198
 - ARIANE V 58, 280
 - Atlas V 173, 217
 - Fastrac engine 208
 - H-II 76
 - Orbital Maneuvering System 176
 - propulsion system 198
 - solid booster 174, 269
 - sounding 264
 - SOYUZ 51, 142
 - SOYUZ Fregat 70
 - system 301
 - VOLNA 159
 - Vukcain 2 motor 235
- Roll
 - control 15
 - damping 15, 327
 - lateral force 15
 - motion 105, 202, 209, 227, 248, 255, 290
 - stiffness 15, 313
- S**
 - SAENGER 3, 16, 23, 38, 173, 303
 - SALYUT 51
 - Semi-reusable concept , 174
 - SHEFEX 264
 - Single-Stage-To-Orbit 2, 25, 173, 198, 217, 302
 - Skin friction line 179, 281, 305
 - SLENDER-BICONE 1, 30, 123
 - Solid rocket booster 24
 - SOYUZ 1, 23, 26, 51, 154
 - orbital module 51
 - re-entry module 51
 - service module 51
- Space
 - orbit 171, 173, 217, 238
 - SPACE SHUTTLE 23
 - Atlantis 174
 - Challenger 174
 - Columbia 174
 - Discovery 174
 - Endeavour 174
 - Enterprize 174
 - features 172
 - Orbiter 2, 33, 174, 208, 217, 253, 283
 - system 172, 174, 198, 301
 - Stability
 - directional 105, 144, 147, 190, 202, 209, 214, 227, 247, 260, 276
 - dynamic 13, 48, 53, 95, 96, 117, 221
 - lateral 14
 - longitudinal 14
 - roll 147, 270, 275
 - static 13
 - Stage
 - lower 303, 305, 308, 319
 - upper 303, 308, 319
 - Stage separation 303, 308
 - STAR-H 3, 25
 - STARDUST 70
 - Sub-orbit 24
- T**
 - Tank
 - expendable 174
 - Terminal approach and landing 220
 - Testbed 96, 142, 159, 217
 - Thermal protection system TPS 76, 142, 149, 172, 208, 217, 264, 269
 - Trajectory
 - flight 78, 105, 217, 275
 - point 57, 70, 83, 86, 105, 126, 133, 144, 154, 243
 - suborbital 235
 - Trim 126, 133, 154, 186, 202, 211, 255, 275, 287, 312
 - angle 46, 53, 58, 60, 86, 101, 105, 142, 224, 325
 - behavior 43
 - flight 139, 244
 - line 86

- parasite 43, 49
Two-Stage-To-Orbit 2, 25, 173, 302,
303, 308

V

Vehicle
- cruise and acceleration CAV 23, 37
- non-winged RV-NW 23, 25, 30
- winged RV-W 23, 33
VIKING 1, 23, 26, 111
- Orbiter 111
VIKING'1', 111
VIKING'2', 111
VIKING-type 1, 26, 80
VIKING1, 80
VIKING2, 80
Vortex 200, 211, 236, 271, 273, 305

W

Waverider 264
Winglet 253, 260, 283

X

X-24, 173
X-24A 220
X-33, 2, 33, 173, 198
X-34, 2, 33, 173, 207, 270
X-37, 2, 33, 173, 217
X-38, 2, 18, 33, 220
X-40, 217

Y

Yaw
- control 15
- damping 15
- lateral force 15
- stiffness 15, 316, 327

Z

z-offset 86, 98, 135, 154